Theoretical study of the geometrical, electronic and catalytic properties of metal clusters and nanoparticles

PhD degree on Sustainable Chemistry

INSTITUTO DE TECNOLOGÍA QUÍMICA

EXCELENCIA SEVERO OCHOA

UNIVERSITAT POLITÈCNICA DE VALÈNCIA

CSIC

Consejo Superior de Investigaciones Científicas

Estefanía Fernández Villanueva

Director: Dr. Mercedes Boronat Zaragozà

València, Setembre 2019

Te quise tanto.
El barro el cuello
el vino. A ver ahora.

A ver septiembre.

María Salgado, “XVIII”, *Ferias.*

Agradecimientos

Pense que ha arribat l'hora del teu cant a València.
Vicent Andrés Estellés, Llibre de meravelles.

En primer lugar me gustaría agradecer al Ministerio de Economía y Competitividad de España (MINECO) por la financiación de esta tesis mediante el programa Severo Ochoa (SVP-2013-068146), incluyendo los costes adicionales de mi estancia de investigación (EEBB-I-17-12057).

En segundo lugar, a mi directora de tesis, la Dra. Mercedes Boronat, por seleccionarme entonces, allá por octubre de 2013, pero también por todo lo compartido desde ese día. Por lo que me ha enseñado activamente y por lo que he aprendido con su ejemplo diario. Su profesionalidad, su presencia y su resolución en el trabajo despertaron pronto mi admiración, pero su humanidad llegó aún más lejos. No es ya sólo mi directora de tesis sino un gran referente para mí, tanto profesional como personalmente. Gracias por guiar mi trabajo, por preocuparte, y por mantener un ambiente de trabajo natural, alegre y honesto. I pel teu valencià :)

En tercer lugar, al Prof. Avelino Corma, fundador del ITQ y director del mismo hasta hace muy poco, por facilitar las oportunidades que se me han dado en este centro de excelencia, por tener en consideración mi trabajo y por lo aprendido en las discusiones sobre el mismo. Gracias por el buen trato y el tiempo dedicado.

I'd also like to acknowledge Prof. Joachim Sauer and Dr. Joachim Paier from the Humboldt Universität zu Berlin, for welcoming me at their theoretical chemistry group for a research stay. I specially thank Dr. Paier for his dedication and teachings along the three months.

Regarding those days im Berlin, if I remember them with a warm feeling in spite of the cold rainy weather, it is due to the now Dr. Maristella Alessio. She helped me with everything there, and she is such a clever, educated, strong woman. Thank you, Mari, for all the interesting talks both in and out of Adlershof, for your example of strength and determination, for your lovely italian accent and for the shared broken english that we perfectly understand. I wish you all the best in your new life at LA.

Hablando de ya-doctores, también me gustaría agradecer al Dr. Jordi Toda, mi compañero de doctorado durante cuatro años, el haber compartido alegrías y sufrimientos, congresos, trámites, debates políticos y científicos y por supuesto también sobre películas, cómics y videojuegos, muchas otras frikadas variadas, comidas al aire libre viendo pádel, zumos, bocadillos, donuts, vino y el jamón que faça falta. Gracias por hacerlo todo más compartido y llevadero.

A Reisel Millán, que también me ha acompañado buena parte del tiempo de este viaje, le agradezco que siempre comparta conmigo sus descubrimientos, y en particular que me haya mostrado que aprender a programar cosillas muy útiles no es tan difícil como yo pensaba. Asere, ¿qué bolá? Digo que igual tenemos que retomar las clases de salsa, ¡no sea cosa que lo de montar una empresa no nos salga tan bien…!

Al resto de compañeros de profesión con los que he trabajado en el ITQ, Dr. Antonio Leyva, Dra. Teresa Blasco, Dra. Patricia Concepción, Dr. Alejandro Vidal Moya, y a los ya doctores Miguel Ángel Crespo, Lichen Liu, Marta Moreno y Saray García, les agradezco las útiles discusiones y su colaboración en cada uno de los trabajos. A Teresa Blasco, además, me gustaría agradecerle su cercanía y simpatía.

No menos importante, quiero agradecer los buenos momentos compartidos a aquellos compañeros de profesión del ITQ que he conocido a pesar de no haber trabajado con ellos, coincidiendo bien en el despacho de los teóricos, bien en congresos u otros eventos, o bien en el pequeño comedor (todos apostando que estaría libre a la misma hora y desplazando las horas punta a poc a poc). En particular me gustaría mencionar a la Dra. Cristina Martínez, por su trato amable y atento y por la alegría que contagia, y a los becarios ya doctores Francine Bertella, Christian Wittee, Alejandro Cabrera, Victoria López y Vicente Juan Margarit, por interesarse siempre con una sonrisa.

En un plano más personal, me gustaría agradecer el apoyo de mis familiares. Sobre todo a mis padres, Félix y Pilar, que aceptaron, como yo, vivir desde entonces a distancia, esperando al fin de semana escogido que me traería de vuelta a Valladolid. Sin vosotros apoyando (y costeando) los inicios, nada de esto habría sido posible, pero además siempre habéis estado pendientes de que esté bien dónde sea que vaya. Gracias por vuestra comprensión, por preparar planazos cuando vuelvo a casa, ¡y por los tuppers! ;) Mis tíos Esther, Ramiro y Nines merecen también una mención especial que, en realidad, ya se habían ganado antes de que empezara la tesis, igual que mis padres. Me encanta que vengáis los cinco a Valencia, a llenarme la casa, a volverme loca con planes, que vayamos también a Palencia, que hagamos excursiones a vete-tu-a-saber dónde. Y siempre echaré de menos la partida de los domingos por la tarde en casa de la abu, que aún jugamos durante buena parte de esta tesis aunque tuviera que irme pronto a por el tren. ¡Menos mal que aún me aceptáis a las esporádicas de la treintaiuna cuando nos vemos! Me seguisteis a Berlín, y a la China iríais a visitarme si allí me fuera. Os quiero mucho, ¡muchas gracias!

A mi abu (la señora Basi, que diría mi madre), le debo un agradecimiento que igualmente trasciende la tesis. Siempre ha cuidado de mí, de todos sus nietos, e ir a casa de la abu siempre ha sido sinónimo de confortabilidad y diversión, de sitio seguro, de hogar. Su situación empeoró hace algún tiempo y ahora ya no vamos a verla a su casa sino a su residencia. Así que ya no me hace croquetas ni jugamos a las cartas, pero afortunadamente está bien, muy guapa, y sonríe al verme. Muchas gracias, abu.

A mi hermana, Silvia, que siempre ha estado abriendo camino por delante de mí, le agradezco su valentía y su apoyo, el entusiasmo a la hora de hacer cosas nuevas, que esté siempre ahí cuando la necesito y que de vez en cuando loqueemos juntas, ya sea en Almería, en Valencia o en Valladolid. Creo que necesitamos más de eso. Gracias también por estar siempre orgullosa de mí by default.

A todos los amigos que han dormido alguna vez en el piso que ha sido mi casa en Valencia, Vero y Ruger, Jesús, Emma, Jako y Sonya, Christopher y Bea, les doy las gracias por el tiempo compartido, pero sobre todo por esperarme de vuelta en sus respectivas ciudades o pueblos, y por hacernos ver (a Javi y a mí) el Oceanográfico como cinco veces en el mismo mes :D

A Javi, por recordarme que este día llegaría, y por ayudarme a llegar con el amor de cada día. Por las series y pelis y sus discusiones, por las meriendas, la vuelta del trabajo, las tortillas, los planazos. Pel jardí dels cirerers. Por Copenhague. Por el despacho, el mapa, las estanterías, los muebles, la cama, el sofá azul. Por los viajes Madrid-Valencia. Por los momentos de tirarnos en la cama, y también por los de bailar o cantar. Por los abrazos. Por la estabilidad. Por la paciencia y los ánimos. Por darme siempre fuerza, libertad y valentía para todo lo que quiera hacer, sentir o ser. Por escucharme. Por la comprensión, la amabilidad y la sonrisa, sobre todo por la sonrisa. Por emocionarte conmigo en las alegrías, grandes y pequeñas, y por darme serenidad y perspectiva en las tristezas. Por buscar siempre la manera de hacerme feliz. Por quererme tanto. Por poder quererte tanto. Viniste a descubrir Valencia conmigo, así que empezamos esto juntos y, tras haber vivido los dos cinco años entre Madrid y Valencia, me resulta casi poético que lo acabemos juntos desde Madrid. Ha sido un camino difícil para los dos, pero tú siempre has conseguido ponerlo más fácil. Muchas gracias, amor. Ha sido y es muy reconfortante saber que pase lo que pase tú vas a seguir ahí para abrazarme cuando todo acabe y todo empiece. Porque a ver ahora. A ver septiembre.

E. F. V.
Madrid, 15 de Septiembre de 2019.

Contents

Chapter 1
Introduction

The present dissertation covers our research efforts on the catalytic behavior of subnanometer transition metal *clusters*, that is, aggregates of a low number of atoms whose particle diameter is smaller than 1 nm.

While catalysis was initially a much more empirical *trial-and-error* science, it has evolved in the last decades into a directed interdisciplinary science that strives for fine rational design. As computational chemists, we participate in this goal employing theoretical modelling to simulate a chemical system as much realistically as possible, in order to obtain reliable information regarding its behavior. This way, the understanding of said behavior can be achieved, and suggestions for improvement or predictions for other systems may be derived.

Consolidated in the 20th century, both catalysis and computational chemistry are very wide specializations of chemistry nowadays. A summary of the key ideas of catalysis and subnanometer metal clusters as catalysts is presented in Chapter 1, whereas the foundations behind the computational approaches employed can be consulted in Chapter 2. Finally, the results and conclusions of our research are presented from Chapter 3 onwards.

1.1. Catalysis.

Catalysis is the process by which a material or compound called *catalyst* alters the reaction rate of a chemical reaction. It is therefore intimately related to chemical kinetics (section 2.8). While the name was coined in 1836 by Berzelius, the chemist that first noticed related phenomena, the catalytic process was not fully understood until the 20th century[1].

The difference between a catalyst and a reagent is that the former is not consumed in the process: it can change during reaction but in that case it eventually recovers its original state. Due to this, a catalyst can undergo the chemical reaction more than once, constituting what is called a *catalytic cycle*. Consequently, catalysts modify reactions dramatically even at very low concentrations.

Three main properties characterize the catalyst:

- The *activity* specifies how much the catalyst changes the rate of the reaction. A catalyst can also worsen the reaction rate; it is then called *inhibitor*.
- The *selectivity* specifies how much the catalyst changes the distribution of products, i.e. if a certain species is particularly favored or disfavored.
- Finally, the *stability* of the catalyst specifies how well the catalyst endures the reaction conditions and how fast it deactivates over time.

The stability of the catalyst is measured as the number of catalytic cycles that it can undergo before deactivation. The latter occurs due to the modification of the catalyst by harsh reaction conditions, simple mechanic wear or adsorption of unreactive species that are said to *poison* it. In the specific case of subnanometer clusters, deactivation due to sintering or aggregation of clusters into larger particles is always a concerning issue. Nevertheless, catalysts may be recoverable with appropriate treatments and, in the case of aggregated clusters, re-dispersion may be achievable.

The activity and selectivity originate in the modification the catalyst produces to the so-called *reaction mechanism*. The latter is the sequence of *elementary* i.e. irreducible reaction steps that yield the overall chemical reaction. Transition State Theory states that reactants form an intermediate unstable species prior to their decomposition into products, called *activated complex* or *transition state* (TS), and they need to obtain a certain amount of energy to reach it, the *activation* energy (Figure 1.1). As a result, each elementary reaction has an energetic *barrier* that needs to be overcome. If a specific elementary step has a much higher barrier than the others, it will limit the velocity of the reaction, hence constituting the *rate-determining step* (rds) (see also section 2.8).

Thus, a catalyst is said to be active if it decreases the barrier of the slowest reaction step/s significantly, leading to an increase in the reaction rate. This implies changes to the reaction mechanism, as exemplified in Figure 1.1. In practice, activity is measured with the so-called *Turnover Frequency* number (TOF), which is calculated as the number of molecules that react per amount of catalyst and hour. The larger the TOF, the more active the catalyst.

Selectivity implies modifications to the reaction rate of two or more competing steps of the reaction mechanism, thus favoring one over the other. Therefore, to achieve total selectivity the catalyst should not only increase the reaction rate of the steps leading to the desired products but also impede or severely decrease the rate of those that lead to undesired products.

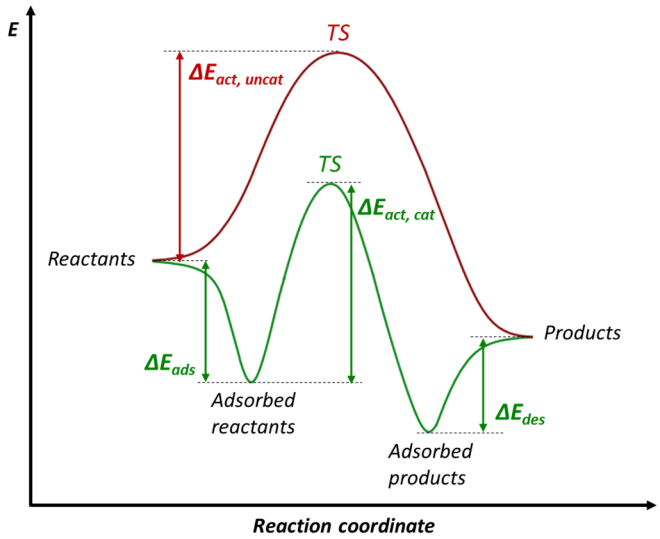

Figure 1.1. Schemes of the energy profiles of an uncatalyzed (red) and catalyzed (green) reaction. ΔE_{act}, ΔE_{ads} and ΔE_{des} stand for activation, adsorption and desorption energies, respectively (see also energy definitions in section 2.8).

Catalytic processes can be classified, depending on the number and type of the system phases involved, into homogeneous, heterogeneous or enzymatic:

- In *homogeneous* catalysis all the species (catalyst, reactants and products) are in the same phase, usually liquid. The catalysts are commonly organometallic species whose activity can be tuned through their ligands.

- In *heterogeneous* catalysis reactants and catalyst are in a different phase, usually with the former in a fluid and the latter in a solid phase. The reaction takes place at the interface of the two phases.

- *Enzymatic* catalysis takes place within living organisms, and the catalyst, called *enzyme*, is an organic substance usually formed by or containing proteins in a colloid. Their structure and mechanism are very complex, often unknown, but they exhibit higher activity and much higher selectivity than the other two groups. The latter is related to the key-lock mechanism that characterizes the interaction between catalyst and reactants, and to the almost perfect identification of reactive species by similar interactions.

Subnanometer metal clusters are heterogeneous catalysts, but their small size fills the gap between organic complexes or single atoms and larger nanoparticles and, consequently, they are often regarded as a bridge between heterogeneous and homogeneous catalysis[2] (see also section 1.3).

1.2. Heterogeneous catalysis.

As advanced, in heterogeneous catalysis reaction takes place at the interphase between catalyst and reactants. Since the catalyst is usually a crystalline or amorphous solid, such interphase is commonly the surface of the catalyst, but in the case of meso- or microporous catalysts, reagents rather react within specific cavities or, less often, in the channels. In any case, the complete reaction mechanism consequently includes the diffusion, adsorption and reaction of species (Figure 1.2):

- *Diffusion* determines how well the reactants or products reach or leave the catalyst. The accessibility of the catalyst to reactants is required and needs to be unimpeded by the diffusion of products (and viceversa). In addition, one can play with the latter to separate products, favor their production (Le Chatelier principle) or even reintroduce intermediate or secondary species that could still react. Diffusion mainly depends on the nature of the phase of reactants and products and their concentrations, but it becomes very important within meso- and microporous catalysts, where the mobility of species is more restricted. Surface diffusion, i.e. how easily do species move on a surface, may also be important in bimolecular reactions where reactants need to encounter each other.

- *Adsorption* reflects the interaction strength between the reactants or products and the catalyst. In principle, at least one reactant needs to be adsorbed on the catalyst for the reaction to occur, and thus a somewhat strong adsorption energy from a reactant is required. However, a too strong adsorption also means a very stable situation for the adsorbate, which then may not react. Thus, poisoning can be caused by reactants, products or any other present species under the same principle: a too strong adsorption energy.

- *Reaction* steps: As the activation energy of an elementary step depends on the energy of the transition state, achieving a good activity usually requires a better stabilization of the activated complex by the catalyst. The latter can be achieved both electronically, stabilizing unstable partial charges with compensating species, and geometrically, matching geometries with the catalyst in what would have been forced impossible geometries in gas phase.

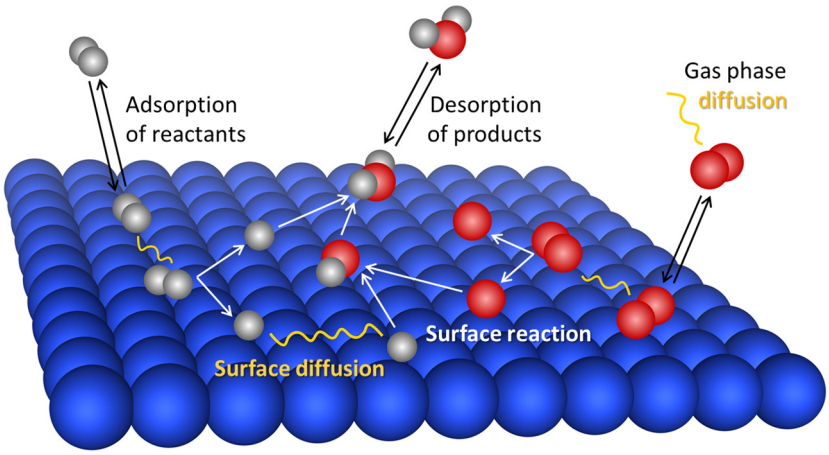

Figure 1.2. Scheme of possible reaction steps in heterogeneous catalysis. Adsorptions/desorptions and surface reactions are indicated by black and white arrows, respectively, and diffusions are shown in yellow curves. The metal surface is shown in blue, H atoms in white and O atoms in red.

However, and more importantly, the mentioned processes depend on the specific type of heterogeneous catalyst.

Atoms in crystalline solids pack in a specific arrangement, building their periodic crystalline structure. The surface exposed by these solids will thus depend on the symmetry plane their structure is cut at. Therefore, surfaces of different symmetry, i.e. exhibiting a different relative disposition of surface atoms and different broken bonds, can be obtained even for the same compound.
In addition to this, defects of different nature may disturb the otherwise perfect symmetry of the surface, such as steps (discontinued layers), vacancies (removed atoms) or kinks (low-coordinated atoms), as shown in Figure 1.3c.

Then, if the system is broken down into nanoparticles, more than one different surface or terrace can be exposed to reactants, and more edges too (Figure 1.3b).
Finally, reaching the size of subnanometer clusters terraces are lost and many more corners and edges are symmetrically inequivalent (Figure 1.3a).

Since all these sites are both geometrically and electronically different, it stands to reason that they present different catalytic activity, ranging from outstanding to none. The term *active site*, introduced by Taylor in 1929[3], is precisely reserved to indicate, among all, those sites that are catalytically active for the reaction of interest.
As many active sites can contribute with different activities, the TOF of a catalyst actually constitutes an average, and since the number of active sites per amount of catalyst may vary from one material to another, care must be taken in the TOF-based comparison of different catalysts.

Another source of complexity comes from the uncertainty regarding the *active species* that arises when different species are present in the catalyst. For instance, if the catalyst is composed of particles of different sizes, any one of them may be responsible for the catalytic activity, or the activity observed may be an average of the different activities of many of them (see also section 1.3.4).

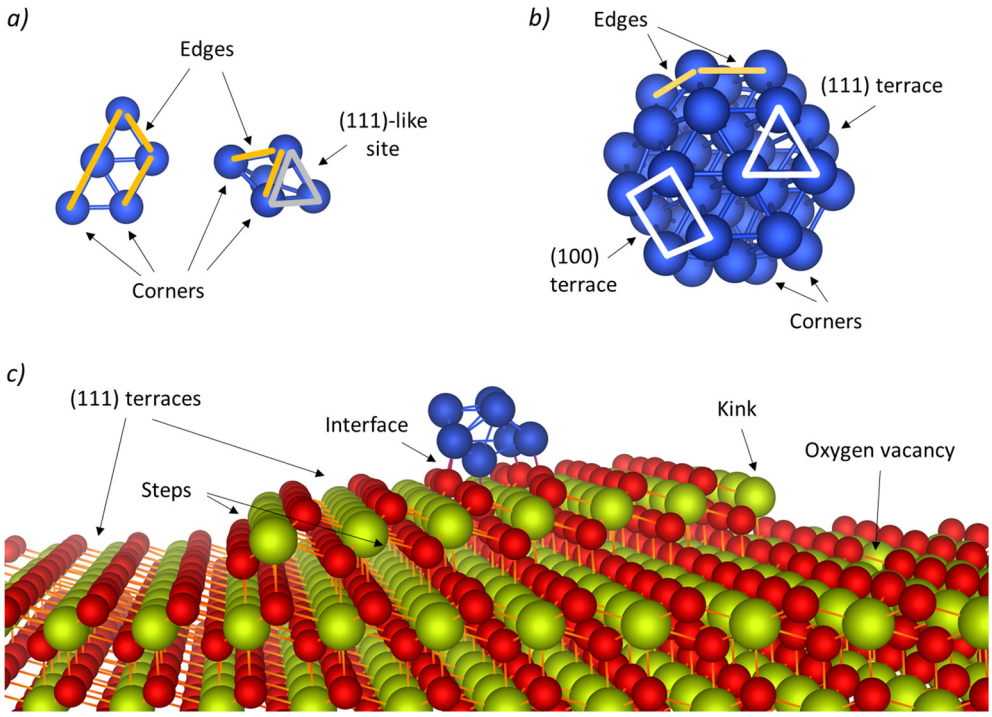

Figure 1.3. Schemes of possible active sites for a) clusters (two Cu_5 isomers are used as an example) b) nanoparticles (Cu_{38} is used as an example. Bear in mind that nanoparticles are typically bigger and exhibit larger terraces and edges) and c) surface (a $Cu_8/CeO_2(111)$ structure was modified to build the illustration). Cu atoms are in blue, Ce atoms in green and O atoms in red.

Therefore, to achieve the improvement or design of new catalysts, it is crucial to identify the active species and the particular active site/s, characterize them and their properties, and unravel the reaction mechanism they favor. It becomes apparent then why heterogeneous catalysis is such an interdisciplinary science, needing the cooperation of materials science, computational modelling and chemical kinetics.

1.3. Subnanometer metal clusters in catalysis.

The history of subnanometer metal clusters is somewhat difficult to track due to its recent and productive character, but also due to the broader use of the term *cluster*. In chemistry, the term is used to indicate ensembles of atoms with a particle size intermediate between that of a molecule and that of a bulk solid. This poses the additional difficulty of differentiating, in the literature, subnanometer metal clusters from metal *nanoparticles* (NPs), i.e. particles with a few nanometers of diameter size, which are also often addressed as clusters or nanoclusters. Moreover, the term is not exclusive of metals nor of the ligand-free clusters that we intend to focus on. Nevertheless, given the intermediate size of clusters in general, the separated areas of research dealing with larger and smaller species eventually converged into them, and all the mentioned materials share a past.

While nanoparticles have been used for years inadvertently to achieve the brilliant colors of stained glass, nanoparticle research started in 1857, with the study of the interaction of light with gold by Faraday, who was precisely trying to explain the appearance of the mentioned colors[4]. He found that gold had to be very finely divided in particles he could not see, and indeed it was not possible to actually see them until 1951, with electron microscopy, almost one century later[5].

In the meantime, industrial catalysis and many key aspects to chemistry and to our subject matter in particular were developed: Nobel prizes were awarded to Ostwald for his work on chemical kinetics (1909), to Max von Laue for the discovery of X-ray diffraction by crystals (1914) and to the Braggs (father and son) for finding out how to analyze the latter (1915), to Nernst for his work on thermochemistry (1920), to Langmuir for his work on surface chemistry (1932), to Heisenberg for the creation of quantum mechanics (1932) and to Schrödinger and Dirac for their new productive forms of atomic theory (1933).

In addition, the characterization of catalysts and active sites through the adsorption of molecules and IR-spectroscopy would not arrive until 1954[1], and scanning transmission electron microscopy (STEM) was to be developed in the 1970s[6]. Thus, it was not until the second half of the twentieth century that the study of nanoparticles and clusters flourished. In the 1960s and 1970s new cluster sources allowed the production of very small gas phase sodium clusters, but up to the early 1980s clusters were not considered to show any pattern with size in any property: since only clusters

of 12 or less atoms were studied and no order was observed, the bulk properties were supposed to be reached very soon in size, and the smallest clusters were rather thought of as molecules, each one being unique[7].

It is important to mention that during these years ligand-stabilized clusters were discovered from the study of organometallic complexes: In the 1960s Cotton, former PhD student of the soon-to-be Nobel prize winner Wilkinson (1973), coined the name "metal clusters compounds" for "those compounds or complex ions consisting of three or more metal atoms held together at least in part by metal–metal bonds"[8], thus distinguishing them from the metallic complexes that have metal atoms bridged by ligands. Carbonyl metal clusters, which he eventually started studying, are today among the most studied clusters of this type[9-12].

In 1983 ligand-free gas phase alkali clusters from 4 to 100 atoms were synthesized, and a certain order and trends were found related to their electronic structure[7]. This, together with the development of the jellium model by Ekardt in 1984[13] moved the focus towards the distinct electronic shell structure of clusters and nanoparticles. As a result, the quantum confinement or quantum size effect started to be discussed[14-16]. The influence of the geometric structure in catalysis was also pointed out, giving rise to the so-called *structure sensitive* reactions[17].

Computational modelling was also developed during the second half on the century, along with the hardware advances in supercomputing. Indeed, the first supercomputers where built in the late 1950s after the change from vacuum tubes to transistor technology that marked the second generation of computers and granted Schockley, Bardeen and Brattain the Nobel Prize in physics for their discovery (1956). Smaller personal computers arrived in the late 1970s, and from the 1980s onwards improvements on parallel design became a constant focus. Alongside this, the first systematic *ab initio* calculations on diatomic molecules was published in 1960[18], and the *ab initio* computer program Gaussian that we use in this dissertation was released in 1970[19]. Then, although the Density Functional Theory was presented in 1964, it became more popular in the 1990s with the improvements in the functionals, and in fact, Kohn and Pople were awarded the Nobel prize in chemistry in 1998. Indeed, the second program that we employ in the present work, VASP, which is DFT-based, was also developed in the 1990s[20-24].

The research efforts made from the 1990s on further consolidated the acknowledgement of the differential behavior of the smallest particles by the scientific community[25-27]. Indeed, in the last decades, clusters of different elements have been identified as the catalytically active species of many important reactions. Due to the *gold rush* that the gold nanoparticles of Haruta et al. initiated back in 1987, revealing their previously unseen catalysis of CO oxidation, small Au clusters have also been extensively studied. They have been shown to catalyze, among others, CO, alkane and

thiol oxidation reactions[28-32], C-C and C-heteroatom bond forming reactions[33], the hydration of alkynes[34] and the C-H bond dissociation of ethane[35]. Regarding other elements, Ag_3 clusters supported on Al_2O_3 catalyze the epoxidation of propene with O_2 with high activity and selectivity at low temperature[36], Cu clusters catalyze the chemoselective hydrogenation of carbonyl and olefin groups[37], the reduction of CO_2 to methanol with H_2[38,39], the oxidation of CO with N_2O[40], and C-C, C-N, C-O, C-S and C-P bond forming reactions[41], water stabilized Pd_3 and Pd_4 are highly active catalytic species in ligand free C-C cross-coupling reactions[42], and a clear size-dependent CO oxidation activity has been reported for Pd clusters supported on TiO_2[43], a reaction recently shown to be catalyzed by Pt/TiO_2 clusters as well[44]. Subnanometer Pt clusters are also active in the oxidative dehydrogenation of alkanes[45] and in the oxygen reduction reaction[46].

The list of studies just indicated is by no means complete: many more works can be found and several reviews have already been published covering differing aspects[47-54]. As a matter of fact, the Accounts of Chemical Research journal started a special issue "Toward atomic precision in nanoscience" the very last year, which evidences the current relevance of this area of research[12,55-60].

In the following subsection the unique electronic structure of clusters, responsible for their differential behavior and ultimately for their catalytic activity, is described, along with the interdependent properties of clusters. Then, section 1.3.2 presents the main synthesis procedures of metal clusters and their influence on the mentioned properties, while section 1.3.3 shows how the latter may be significantly affected by the support. One final subsection illustrates with selected examples the practical difficulty in identifying clusters as the active species.

1.3.1. Electronic structure of subnanometer metal clusters.

In the subnanometer regime, quantum confinement effects produce a discrete distribution of electronic states with a non-zero HOMO-LUMO gap. Their electrons are not fully delocalized as in the bulk metal, and therefore subnanometer metal clusters can be considered non-metallic[61,62]. Consequently, their behavior depends on geometric, electronic and size-dependent properties that are closely interrelated.

The geometries of transition metal clusters are determined by their *d* shell, which favors compact structures as a way to maximize the interaction between the rather localized *d* orbitals, and by the hybridization of the n*s*-(n-1)*d* orbitals induced by the relativistic contraction of the inner *s* and *p* shells, which favors planar structures and is stronger in heavier atoms like Pt and Au[63,64]. Since these effects are produced to a different extent for each element, the size-limit for the 2D to 3D transition differs from one metal to another. Thus, while the most stable isomers of Ni_4 and Pd_4 are tetrahedral[65,66], planar structures are the most stable configurations of Cu, Ag and

Pt clusters composed by up to 6 atoms[67-69] and of Au clusters of up to 7 atoms[70,71]. In general, there are often several low-lying isomers with only slightly different stability, especially as the cluster size increases[68,72]. This fact is important because the geometric and electronic structures of metal clusters are intimately correlated. The frontier orbitals (HOMO and LUMO) of small clusters usually consist of several lobes localized on the low coordinated metal atoms and fully accessible to interaction with reactant molecules. The shape and energy level of these orbitals depend not only on the atomicity of the metal cluster, but also on its morphology. As a consequence, reactants may preferentially adsorb and/or react on clusters with a specific morphology only.

As the number of atoms in the cluster increases and 3D structures become favored, more metal-metal bonds are formed, the surface atoms are more coordinated, and the contribution of the atoms inside the cluster to the composition of the frontier orbitals becomes more important, with a concomitant loss in the capability of orbital overlap with interacting molecules. In addition, as the atomicity increases the electronic distribution of clusters tends to the band structure of the bulk metal.

This change in the electronic structure of particles as the size decreases is reflected in their optical properties, as mentioned before[73,74]. Thus, larger metal nanoparticles present the so-called surface *plasmon* absorption bands under UV-visible radiation, produced from the resonance between the irradiating light and the oscillation of the electrons confined in their conduction band[75-77]. This resonance is strongest and shifted to the visible part of the electromagnetic spectrum for the noble metals (Cu, Ag, Au) due to the higher polarizability of their electrons, which provides them of characteristic colors and also gives rise to a sharper bandwidth compared to other transition metals[75]. In contrast, UV-visible absorption spectra of clusters are more similar to those of molecules, presenting thin peaks arising from the discretization of their electronic structure. In addition, the absorbed radiation is similarly emitted in the form of a transition, causing fluorescence[76-78]. Clusters hence behave like semiconductors, and while the surface plasmon of NPs changes mainly due to their shape, the UV-visible absorption spectra and the fluorescence emission wavelength of clusters changes severely with cluster size[76]. It is precisely due to this strong size-dependence that UV-visible and photoluminescence spectra are commonly employed to characterize the size of cluster samples. The atomicity is approximately obtained from the band gap of the cluster by applying a simple equation from a jellium model[7], and the band gap is at the same time obtained either from a Tauc plot of the UV-visible absorption spectra or from the emission wavelength of photoluminiscent spectra[79]. In the jellium model, the valence electrons are assumed to be delocalized and moving in the potential that the nuclei and core electrons produce, which are approximated to a uniform background of positive charge[7]. The model also provides a relatively simple explanation to the so-called magic numbers for transition metal clusters, which indicate cluster sizes that show larger HOMO-LUMO

gaps and a greater stability than the rest[80-82]. These extra-stable structures are achieved when a determined number of electrons is reached in the system and a closed-shell electronic configuration, a complete jellium level, is produced.

In a similar way, the s^1 electronic configuration of the three coinage metals (Cu, Ag and Au), albeit modified by the *sd* hybridization, produces stable closed-shell electronic configurations for even clusters, leading to a characteristic even-odd trend with size for certain properties like the HOMO-LUMO energy gap, the electron detachment energy or the ionization potential[67,69-71]. This behavior was also clearly evidenced in a comparative study of neutral, anionic and cationic Cu_n and Pt_n clusters with $2 \leq n \leq 14$ by Chaves et al.[67]. For example, the total magnetic moment of neutral Cu_n clusters oscillates between 0 μ_B and 1 μ_B for even and odd number of atoms, respectively, which can be explained by the $3d^{10}4s^1$ electronic configuration of Cu that results in an unpaired electron in clusters with an odd number of atoms. Accordingly, the trend for cationic Cu_n^+ and anionic Cu_n^- clusters is the opposite. The total magnetic moment of Pt_n clusters, in contrast, does not show any oscillatory trend, because it is due to the partial occupation of the 5*d* states. A similar oscillatory or zig-zag-like behavior was observed for the HOMO-LUMO energy gap, detachment energy and ionization potential of Cu_n clusters, but not for Pt_n clusters.

The strong interplay between electronic structure and geometry also explains the dramatic change in the shape of metal clusters with charge observed for some systems. Thus, the preferred triangular geometry obtained for neutral Pt_3, Cu_3, and Au_3 clusters turns into linear structures for anionic Pt_3^-, Cu_3^-, and Au_3^- clusters[67,71]. The distorted rhombus geometry preferred for neutral Pt_4 changes to a planar square upon addition of one electron forming Pt_4^-, and to a tetrahedron upon removal on one electron generating cationic Pt_4^+. And while 3D structures are also obtained for cationic Cu_5^+ and Pt_5^+, the corresponding neutral Cu_5 and Pt_5 and anionic Cu_5^- and Pt_5^- are 2D. As regards gold, the global minimum for the neutral Au_4 cluster is a rhombus, whereas two different degenerate structures were obtained by Häkkinen and Landman for anionic Au_4^- clusters, a Y-shaped geometry and a linear zig-zag structure. DFT calculations proposed a rhombus geometry for the most stable isomers of Au_4^+ and Ag_4^+ clusters, which was experimentally confirmed by photodissociation spectroscopy[83]. As explained before for neutral clusters, the relativistic *sd* hybridization is enhanced for the heavier elements, and the anionic Pt_n^- and Au_n^- also tend to be planar up to sizes larger than those found for other elements[67,84].

Even-odd trends are also sometimes reflected in the interaction of neutral and charged clusters with molecules. For example, early experiments detected a pattern in the adsorption of O_2 to negatively charged small gold clusters, where only anionic clusters with an even number of atoms, and therefore an odd number of valence electrons, showed significant O_2 uptake[85,86]. A density functional theory investigation

of the molecular and dissociative adsorption of O_2 on neutral and anionic Au_n clusters with $2 \leq n \leq 8$ confirmed this trend[87]. Indeed, in both systems binding energies exhibited odd-even oscillations, but molecular O_2 adsorption was found stronger on anionic clusters, with the calculated E_b values being larger for clusters with an odd number of electrons, that is, with an open electron-shell structure.

In summary, the main features that characterize the electronic structure of isolated metal clusters and therefore determine their catalytic properties are (Figure 1.4):

- Discrete energy levels (optical properties, molecular-like behavior).
- Presence of band gap (non-metallic character).
- Localized molecular orbitals (accessible lobes, overlap).
- Open-closed electronic shell (may exhibit even-odd properties).
- Morphology (alters all the others).
- Charge (changes electronic shell, may alter the morphology).

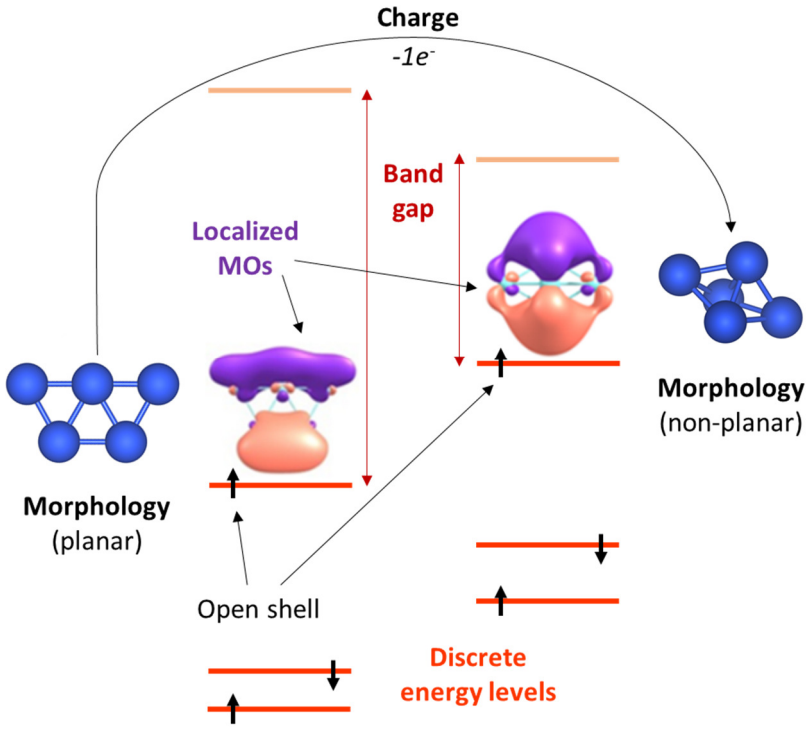

Figure 1.4. Scheme of the main features determining the electronic structure of isolated metal clusters. Energy diagrams of the frontier molecular orbitals of two Cu_5 isomers of different morphology are shown, along with the shape of their corresponding HOMO. Cu atoms are indicated in blue.

It is important to remark the last two features, as they are superimposed to all the others and can modify them. It thus stands to reason that clusters may change their properties along a reaction. Indeed, reactions involve transferences of charge and other interactions that may alter the morphology of the cluster and all of its properties with it. Such interconversions are also favored by the previously mentioned existence of many low-energy isomers. This is what is known as *fluxionality* of clusters, another current and complicated subject of research[88].

While the mentioned features provide clusters a high reactivity, they also confer them a low thermodynamic stability. Metal atoms prefer to surround themselves with more metal atoms, and the growing of clusters into increasingly larger particles is a common issue in their study and a great difficulty in their synthesis. Due to this, clusters need to be stabilized by external agents, usually protective ligands or the organic or inorganic support they are deposited in, especially in order to actually use them as catalysts of a chemical reaction.

From all of the above, it follows that the external agents and the method used for the synthesis and stabilization of transition metal clusters will necessarily have an impact on their catalytic properties. While this fact makes their study more involved, it also enriches the tuning possibilities of the resulting materials and hence expands their potential applications.

1.3.2. Synthesis of atomically precise subnanometer metal clusters.

The synthesis of catalysts containing size-controlled metal clusters is challenging, not only because of the intrinsic difficulties to generate these metallic entities with a particular atomicity, but also due to the problems associated to the anchoring of the clusters on the solid support, the removal of the stabilizing ligands and the possible sintering of the clusters into larger particles. Very generally, clusters can be generated in gas-phase or in solution, to be later stabilized by a variety of systems.

To generate clusters in gas-phase the most common procedures employ a piece of the solid metal as the source to be eroded (via laser vaporization, magnetron sputtering or arc discharge), but liquid metal or liquid precursors can also be used with the electrospray ionization technique, and metals of not very high boiling point (< 2000 K) can be directly vaporized via gas aggregation or supersonic expansion[89].

The cluster size selection among the wide size distribution that these techniques produce is achieved through mass spectrometers that separate the particles on the basis of their different charge and mass. This ability to discern cluster size has turned some of these spectrometries, such as electrospray ionization (ESI) and matrix-assisted laser desorption ionization (MALDI), into common techniques for cluster analysis[90-92].

Finally, the last step is cluster deposition, that is, to place the size-selected metal clusters on a surface. The velocity i.e. the kinetic energy that the gas-phase clusters approach the support with is very relevant, because with a high energy the cluster may suffer fragmentation, scatter or even implantate below the surface of the support[93]. A slight increase in energy may however be beneficial to anchor the cluster to a surface in what is known as *pinning*, where the cluster displaces some atoms of the support. Nevertheless, to produce the so-called model catalysts, where the nature and size of the deposited clusters are as controlled as possible (see further below), low-energy cluster deposition is preferred. This is known as *soft-landing*[89]. It is usually done in ultra-high vacuum conditions (UHV) and if gas phase clusters were ionized they become neutral losing their charge to the support upon deposition. Chemical vapor deposition (CVD) can be also applied, but soft-landing allows a higher control over the size of the clusters and their coverage of the support; CVD is usually employed to synthesize thin 2D films instead[94,95].

The generation of clusters in solution, also known as *wet-chemistry* approaches, include many different processes that generally involve the reduction of a salt or mononuclear precursor and produce clusters surrounded by stabilizers that prevent their agglomeration[61,96-101].

The electrochemical synthesis was first employed by Reetz et al. in 1994[102] to produce tetraalkylammonium-stabilized clusters of Pd of as low as 1.4 nm mean particle size. In this technique an anode of the desired metal is used as the source, producing metal cations that are reduced at the cathode and at the same time are stabilized by ligands from the solution[103]. The electrochemical method possess many advantages compared to the preparation of metal clusters by chemical reduction, as it requires low temperatures and cheaper materials, and the cluster size is more easily manipulated by tuning current, voltage, electrolyte and concentration of stabilizers[99,104]. Using this technique Vilar-Vidal et al. were able to synthesize Cu_n clusters of $n \leq 14$ stabilized by TBAN, able to be dispersed in both polar and apolar solvents[79,105] and the synthesis of ligand-free Cu_5 in water was recently achieved[106,107].

The Brust-Schriffin method owes its name to the scientists of the Shriffin group that proposed the method again back in 1994. Originally a two-phase method[108], in this synthesis a phase-transfer reagent is used to transfer a chloro-metal salt from an aqueous phase to an organic phase, from which the clusters are produced through reduction with a reducing agent (usually $NaBH_4$). One-phase variants were later developed[99]. Clusters synthesized this way are thiol-stabilized due to the thiols employed in the organic phase. Since the S-Au interaction is strong, many studies can be found on Au clusters synthesized by this method[97-99], but thiol-capping of Au clusters is also exploited in other synthesis procedures[98]. Nevertheless, there are also examples for Ag, Cu, Pt and Pd clusters synthesized by the Brust-Schriffin method[99]. The surface properties of the resulting material can be controlled by ad-

justing experimental parameters such as the nature of the protecting ligands and the reducing agent, the metal to ligand ratio or the pH of the solution[97,99]. Similar chemical reduction processes can be used to produce gold clusters stabilized by phosphines instead of thiols[99], generally by reduction of triarylphosphine Au(I) complexes. The weaker interaction of phosphines facilitates the removal or exchange of ligands after preparation and their use as stabilizers is not exclusive of gold: small silver clusters (Ag_{14}, Ag_{16}) were synthesized by Yang et al. through a combination of phosphine and thiol ligands[109,110].

It is worth noting that synthesis by chemical reduction can be carried out in a continuous flow as opposed to a batch, in what are called microfluidic, millifluidic or lab-on-a-chip procedures[111-114], also employed to produce other types of larger nanostructures for biomedical applications[115,116]. The main idea of this synthesis procedure is to inject the precursor and the reducing agent at specific flow rates that allow their reaction from their converging point onwards. This way, the selected flow rate, capillar or channel length and/or reaction time can change the final size and morphology of the particles synthesized.

The ligand-protected clusters obtained as described could in principle be directly employed in homogeneous catalysis, but the strong interaction with the ligand molecules and their high surface coverage usually impedes the interaction with reactants, hence leading to a low activity. It is thus more common to deposit the clusters on a solid support and employ them as heterogeneous catalysts instead, for clusters are then stabilized by the surface of the material and ligands are no longer necessary[98]. While clusters can be deposited after generation in solution, the synthesis in solution directly on the support by impregnation with precursors (salts or organometallic complexes) is one of the most common ways to obtain supported metal clusters[117].

The decarbonylation of supported metal carbonyl clusters constitutes one of the first efforts that lead to Ir and Pt clusters along this line[10,100,118]. Thus, mononuclear metal carbonyl precursors (or preformed metal carbonyl clusters) on MgO or γ-Al_2O_3 metal oxides produce dispersed metal carbonyl clusters of the $M_n(CO)_m$ form, from which supported clusters are obtained after the removal of CO ligands by heating in He or H_2. Stronger ligands such as thiolates and phosphines may require harder treatments for their elimination[98,117], the most common of which is calcination. It eliminates organic ligands effectively, but entails the risk of cluster aggregation due to heat. Redox reactions and solvent extraction are softer and simpler treatments that can be used for ligands with determined reactivities or solubilities, respectively, while inorganic salt anions can be removed through washing and centrifugation. Besides, the nature of the support will also affect the final material upon these treatments; for instance, if the metal-support interaction (MSI) is not strong enough not only cluster aggregation but also cluster encapsulation by the support may be produced.

Metal oxides are the most common materials used as supports, both unreducible, when properties of the clusters are meant to be preserved as unmodified as possible (MgO, Al_2O_3) and reducible, when a certain MSI effect is pursued (CeO_2, TiO_2). However, mesoporous solids such as metal-organic-frameworks (MOFs) and zeolites (crystalline aluminosilicates) are also increasingly employed due to their advantageous confinement restrictions.

Indeed, the so-called *template* methods are another synthesis alternative where the metal clusters are formed within the interior of systems that act as a template or nanoreactor, which can precisely be MOFs or zeolites. Other systems include polymers, dendrimers and even microemulsions. The encapsulation favors the production of clusters with well-controlled size, while the various configurations and sites of the different templates can produce clusters with a certain desired morphology[99]. The procedure generally involves the incorporation or exchange of metal ions from solution to specific sites of the stabilizers, from which the clusters are produced in a subsequent reduction[119]. As the protons from solution can compete with the metal ions for the sites, the pH of the solution is an important variable here. This otherwise simple synthesis method has the potential advantages of cluster size control, stability against cluster sintering and ligand-free surfaces of the clusters[99].

Microemulsions, which are produced in the mixture of two immiscible liquids, also behave like nanoreactors, but the method takes advantage of the exchange of material that occurs between different droplets of an emulsion to synthesize clusters by chemical reduction: one emulsion is prepared containing the metallic salt and another one with the reducing agent[61]. While the droplet size can be controlled, obtaining small clusters is difficult and requires the optimization of several variables, such as the water-surfactant molar ratio or the concentrations of the salt and the reducing agent. Nevertheless, using this technique very small clusters of Ag ($n < 10$) and Cu ($n < 13$) were successfully synthesized[61,74].

As the interaction of metal clusters with metal oxides is less specific than with the organic ligands of MOFs or the supporting polymers, a heterogeneity in the size, morphology and electronic nature of metal species usually exists in solid catalysts that employ metal oxides as support. Seeking to minimize this complexity, *model* catalysts consist of size-controlled metal clusters deposited, at well-defined surface coverages, on clean, vacuum-annealed or thin films of metal oxides or on carbon-based materials. They are used to identify the parameters governing catalytic activity, to confirm proposals from theory, to accurately characterize the properties of the true active sites, or to analyze separately the effect of every variable relevant for the catalytic process, such as metal cluster size, morphology, charge state of the metal or the support, and presence of defects or adsorbed species. The actual understanding of catalysis by clusters is largely based on studies performed on model catalysts.

Finally, it is important to mention that the strong interaction between metal atoms and stabilizing ligands can cause the etching of particles, which can be purposely used to synthesize clusters from larger nanoparticles[98,99]. These types of methodologies where clusters are produced from preformed larger systems are also classified as *top-down*, whereas those where clusters are obtained through aggregation and reduction are called *bottom-up*. The term *ship-in-the-bottle* is also used to differentiate template-based procedures from the other two approaches.

1.3.3. The metal-support interaction (MSI).

A strong metal-support interaction can change the properties of a metal cluster substantially. At the very least, the electronic structure is modified and the system may become partially charged. Then, MSI can be large enough to stabilize the clusters in otherwise very unstable hence strange geometries.

For instance, cluster charging was found to be key in the catalytic activity of size-selected Au_n clusters with $n \leq 20$ for CO oxidation[29,120]. Clusters were soft-landed on thin films of MgO epitaxially grown on a Mo(100) surface and annealed at different temperatures to generate different densities of oxygen vacancies (F centers), and it was theoretically shown that the charge transfer from these electron-rich F centers in defective MgO to the supported gold clusters is necessary to bind and activate O_2. Clusters deposited on close-to-perfect MgO surfaces remained chemically inert. In addition, these defect sites anchored strongly the supported gold clusters, inhibiting their sintering into larger and inactive particles.

Many more variables related to the MSI were studied for the CO oxidation by gold clusters, such as particle morphology or the oxidation/hydration state of the support. Indeed, it was found that although clusters bind more strongly to the oxygen vacancy defects of TiO(110), a gold bilayer structure is significantly more active than the monolayer or than other 2D clusters[121-123]. In addition, it was theoretically found that strong Au-O bonds are only formed on the oxidized TiO_2(110), explaining the experimental result of sintering resistance only observed in that case[124].

In another example, $[Pd_4]^{2+}$ clusters were found to be stabilized in a linear zig-zag structure on a particular MOF. Bader analysis of the charge distribution revealed a mixed-valence state $Pd^+Pd^0Pd^0Pd^+$, with the positive charge preferentially located on the terminal Pd atoms. Such stable Pd^+ species render the material active for several carbene-mediated reactions of diazoacetates, such as the Buchner reaction[125].

More dramatic examples of the importance of the MSI involve those in which the interface is the active site. This is well illustrated by the selective catalysis of propene epoxidation by subnanometer Ag_3 clusters (and Ag nanoparticles formed from their

sintering under reactions conditions) deposited on an amorphous alumina support[36,126]. Simplified, the reaction can produce the desired propene epoxide or follow a secondary reaction path that leads to undesired CO_2. The very same silver species deposited on Ultrananocrystalline Diamond (UNCD) were not selective, as it also happened with previous attempts on different silver facets[127] or small clusters[128]. In addition, DFT calculations showed lower activation energies leading to propene epoxide at interfacial sites and, although the unselective route leading to CO_2 is also energetically favored, it was shown to require a high oxygen coverage and therefore propene epoxide formation becomes competitive. All of it proved that the active sites were at the interface between the silver clusters and the alumina.

Many other examples can be found in the literature[100,117,125,129]. It is thus clear that the MSI is determinant for the catalytic properties of the final material and it needs to be carefully considered for each particular case study.

1.3.4. Identification of the active species.

The fact that metal clusters can be formed in solution from the corresponding metal salts or metal organic complexes under certain reaction conditions raised concerns about the true nature, homogenous or heterogeneous, of the active species in reactions catalyzed by transition metal complexes in solution[130-137]. Indeed, the combination of experimental and computational techniques has often allowed the identification of metal clusters as the true catalytically active species.

One of the most challenging cases reported was the identification of the kinetically dominant active species in the classic hydrogenation of benzene and cyclohexene with molecular H_2, using a specific rhodium complex as starting catalyst. Using a methodology that combines kinetic studies, poisoning experiments, TEM measurements and other operando spectroscopic characterization techniques, it was established that at the milder reaction conditions employed for cyclohexene hydrogenation (22ºC and 3.7 atm H_2) the catalyst was a monometallic homogeneous complex. In contrast, the harsher conditions required to hydrogenate the more stable benzene molecule (50-100ºC, 50 atm H_2) led to the formation of traces of soluble $Rh(0)_n$ nanoparticles and large amounts of sub nanometer Rh_4 clusters, the latter being the true heterogeneous catalyst[138,139].

As another example, a combination of detailed kinetic studies with adsorption/emission UV-Vis spectroscopy and MALDI-TOF characterization led Corma et al. to identify small Au_3-Au_{10} clusters formed from several Au^+ and Au^{3+} salts and complexes in solution as the true catalytically active species in different organic reactions. Thus, small Au_3-Au_5 clusters are formed in the presence of alkynes and catalyze their ester-assisted hydration, while Au_8-Au_9 clusters are specifically active for the bromination of arenes[34].

Formation under reaction conditions of gold clusters that are the catalytically active species also happens in the oxidation of thiophenol to disulfide with molecular O_2 using as starting catalyst a solid material consisting of isolated gold atoms supported on functionalized carbon nanotubes[32,140]. The initial sample showed an induction period, and the study of the reaction at different times showed the aggregation of atoms first into clusters then into nanoparticles, with the highest activity shown by an intermediate sample containing gold clusters of 4 to 13 atoms (and presenting no induction period). DFT calculations showed that O_2 is only efficiently activated by small gold clusters such as Au_3 and Au_5, and that the co-adsorption of the two reactants enhances the charge transfer from thiolate to oxygen, making possible the formation of the S-S bond. In contrast, the Au^+ complex is not able to activate O_2 due to a poor overlap between the LUMO of O_2 and the HOMO of the gold species, and is not able to form the S-S bond either due to the formation of a negatively charged dithiolate gold complex. Finally, nanoparticles deactivate due to poisoning by strong adsorption of thiolates.

The key role of small clusters composed by three or four palladium atoms has been recently demonstrated in cross-coupling reactions such as Heck, Suzuki, Sonogashira or Stille[42]. These reactions involve the activation of an aryl halide reactant and lead to the formation of a new C-C bond, and are typically and efficiently catalyzed by palladium salts and complexes in homogeneous phase[141-143], but also by metallic nanoparticles as heterogeneous solid catalysts[133,134,137,144]. The knowledge derived from the former study allowed the ex situ preparation of sub nanometer Pd clusters, their storage in aqueous solution for long periods, and their subsequent use in cross-coupling reactions without loss of catalytic properties.

The latter constitutes an uncommon success, because an important and usual limitation of these systems for industrial application is precisely that the extremely active clusters are formed in situ under reaction conditions, and despite their excellent performance they usually evolve to larger non-active species that cannot be recovered nor reused in subsequent cycles. This is another reason why the heterogenization of metal clusters by supporting them on solid carriers is usually pursued.

The complexity of heterogeneous catalysts, however, makes the identification of the true active species among the many present in the material challenging too. As already mentioned, different sites or species may have catalytic activity, which can lead to seemingly opposed results in *a priori* equivalent tests.

For instance, after studying many gold species in a series of Au/FeO_x samples for the CO oxidation reaction using high-angle annular dark-field scanning transmission electron microscopy (HAADF-STEM) to accurately determine particle size, Herzing et al. identified bilayer gold clusters of ~ 0.5 nm diameter and ~10 atoms as the true catalytic species[30], whereas Liu et al. found high activity from gold NPs with diam-

eter in the 2-5 nm range only two years later[145]. These results along with those recently presented by He et al.[146] indicate that each of the different species present can have a non-equivalent catalytic activity indeed, and that a size-dependent activity hierarchy must exist, at least in the Au/FeO_x catalyst for CO oxidation.

Finally, it is important to mention that the formation of the true catalytic species under reaction conditions is not exclusive of homogeneous catalysis. For example, in the study of small linear $[Pd_4]^{2+}$ clusters on a MOF presented in section 1.3.3, the MOF precatalyst containing only Pd^{2+} species is also active at a similar rate after an induction period, in which a reactant acts as a reducing agent leading to the cluster formation, just as $NaBH_4$ does in the external preparation of the catalyst.

1.4. Motivation.

As seen in the previous section, subnanometer metal clusters currently constitute a vast area of research, ever increasingly studied yet still largely unexplored. Given their potential, fundamental computational studies are not uncommon, especially in the past due to the traditional difficulty in the controlled synthesis, stabilization and characterization of clusters. These studies are commonly guided by previous results on bigger systems or on similar size systems but of different elements, and aim to obtain information regarding the potential behavior of the clusters in broader terms, in order to discern the applicability of clusters for related reactions at a later stage. As the synthesis and handling of clusters has become increasingly feasible, much more specific studies combining experimental and computational techniques have been increasingly reported, as shown in the previous section, and the use of clusters in the rational design of new materials for catalysis is currently pursued.

The present dissertation collects works belonging to both types. On the one hand, a fundamental study on the oxygen dissociation by Cu clusters was carried out guided by previous results to evaluate, among others, their potential catalysis of oxidation reactions in general[68]. Then, experimental results corroborated the conclusions of that study and the results of further work[107], and the knowledge generated was finally used to study the viability of more specific reactions and the effect of a support (Chapters 3-5). On the other hand, more specific problems were directly tackled from a computational point of view in the case of Pt and Pd clusters[147,148] (Chapters 6-7).

While in all cases the studies were motivated by the potential catalytic activity of the species, based on either previous literature, experimental results or both, the literature background and the specific motivation of each study is properly presented in the introductory section of each chapter.

Chapter 2
Theoretical background

In computational chemistry, the first broad classification of methods differentiates *molecular mechanics*, which make use of the classical laws of physics, from *electronic structure methods,* which employ those of quantum mechanics.

Molecular mechanics do not treat electrons explicitly. Instead, their effect is included in the so-called *force fields*, and only the interaction among nuclei is calculated. As a result, it is inexpensive and allows the study of systems of thousands of atoms. However, they only work well for systems similar to those for which the force fields were parameterized and cannot describe bond breaking and formation processes, where electronic effects predominate.

Thus, electronic structure methods are the ones employed for mechanistic studies. Most of these approaches make use of the Born-Oppenheimer approximation (see below) to separate electronic and nuclear interactions. This way, and as opposed to molecular mechanics, the properties of the system depend on the nuclei only parametrically and the electronic interactions are more determinant. Since the number of electrons per nucleus can be large and the electronic interactions are more complex, these calculations are costly and limit the treatable size of the system. In the present work we employed different levels of the electronic structure method Density Functional Theory (DFT), which is briefly reviewed below.

Some aspects regarding the models, basis sets and optimization algorithms used, the analysis of stationary or steady states and the theoretical approaches employed for the thermodynamic and kinetic studies subsequently follow.

2.1. The Schrödinger equation.

Quantum mechanics state that the energy and many other properties of a system can be obtained by solving Schrödinger equation. The time-independent Schrödinger equation is, in general:

$$\hat{H}\Psi = E\Psi \tag{2.1}$$

Where Ψ is the wave function, which contains all the information of the system, and $\hat{H}$ is the Hamiltonian operator, which contains the kinetic $\left(\hat{T}\right)$ and potential $\left(\hat{V}\right)$ energy terms:

$$\hat{H} = \hat{T} + \hat{V} = \hat{T}_n + \hat{T}_e + \hat{V}_{ee} + \hat{V}_{nn} + \hat{V}_{ne} \tag{2.2}$$

Here *n* and *e* are labels for nuclear (**R**) and electronic (**r**) coordinates, respectively.

However, this equation can be solved exactly only for two-body systems, which limits its applicability to hydrogenoid atoms. Due to this, mathematical approximations need to be introduced in order to treat any other system.

Since nuclei are much heavier than electrons, the latter move much faster and they can barely feel the movement of the nuclei. Because of this, we can decouple nuclear and electronic velocities, in what is known as the Born-Oppenheimer (BO) approximation. Within this approach, an electronic Hamiltonian is defined by separating the term of the kinetic energy of the nuclei:

$$\hat{H}_{el} = \hat{T}_e + \hat{V}_{ee} + \hat{V}_{nn} + \hat{V}_{ne} \tag{2.3}$$

$$\hat{H}_{el}\Psi\left(\vec{r},\vec{R}\right) = E_e\Psi(\vec{r},\vec{R}) \tag{2.4}$$

This means that the Hamiltonian depends now only parametrically on the coordinates of the nuclei. For a system of N electrons and M nuclei, we can write the electronic Hamiltonian as follows:

$$\hat{H}_{el} = \sum_{i=1}^{N} -\frac{\hbar^2}{2m_e}\nabla_i^2 + \sum_{i}^{N}\sum_{j>i}^{N}\frac{e^2}{4\pi\varepsilon_0\left|r_i - r_j\right|} + \sum_{k}^{M}\sum_{l>k}^{M}\frac{Z_k Z_l e^2}{4\pi\varepsilon_0\left|R_k - R_l\right|} - \sum_{k}^{M}\sum_{i}^{N}\frac{Z_k e^2}{4\pi\varepsilon_0\left|R_k - r_i\right|} \tag{2.5}$$

Where *e* and m_e are the charge and mass of an electron, Z_k and Z_l the charge of the nuclei, ε_0 is the vacuum permittivity and $\hbar$ is the reduced Planck's constant.

Since equation (2.1) is an eigenvalue problem, for a certain given geometry many eigenvalues E_k will be obtained. The lowest E_k corresponds to the ground state, while higher ones correspond to excited states.

Thus, we can obtain the electronic energy from the Schrödinger equation as the expectation value of the electronic Hamiltonian:

$$\hat{H}_{el}\Psi\left(\vec{r},\vec{R}\right)=E_e\Psi(\vec{r},\vec{R}) \tag{2.6}$$

$$E_e=\left\langle\Psi\left(\vec{r},\vec{R}\right)\middle|\hat{H}_{el}\middle|\Psi\left(\vec{r},\vec{R}\right)\right\rangle \tag{2.7}$$

Even with the BO approximation, the equation is still complicated and there are different approaches to its resolution, which gave rise to a subclassification of electronic structure methods. *Semi-empirical* methods use parameters derived from experimental data whereas *ab initio* methods rely fully on the laws of quantum mechanics (use no parameters). Then, *density functional* methods constitute a third approach that is more similar to that of *ab initio* methods but with an important difference: while *ab initio* (and semi-empirical) methods find the solution by obtaining the wavefunction of the system, in Density Functional Theory the energy is obtained as a functional of the electron density.

2.2. Density Functional Theory.

The Density Functional Theory (DFT) owes its name to the use it makes of functionals, i.e. functions of another function, of the electron density. Early advances were introduced by Thomas, Fermi and Dirac in the late 20s[149-151], but Hohenberg and Kohn proved the applicability and provided the first key mathematical ideas from which Kohn and Sham finally developed the DFT methodology.

The Hohenberg-Kohn theorems.

The first Hohenberg-Kohn theorem (1964)[152] states that, for non-degenerate ground states (the same was later demonstrated for degenerate ground states), the external electron-nuclei potential is a unique functional of the electron density (ρ).
Since that potential and the number of electrons completely define the Hamiltonian of the system, and the electron density determines the potential and the number of electrons, then the electron density determines all the electronic properties of the ground state of the system. In other words, the theorem proves that any observable of a stationary non-degenerate ground state can be written as a functional of the electron density of the ground state and be calculated exactly. Therefore, there is a direct relation between the density and the wavefunction:

$$\rho(\vec{r})\rightarrow v(\vec{r})\rightarrow\hat{H}\rightarrow\Psi \tag{2.8}$$

Indeed, by substituting in equation 2.7 the expression for the electronic Hamiltonian (2.5), we can arrive to an expression of the electronic energy that includes terms that depend on the electron density:

$$E_e = \hat{T}_e(\rho) + \hat{V}_{ne}(v,\rho) + \hat{J}(\rho) + \hat{E}_{NC}(\rho) + \hat{E}_{nuc} \tag{2.9}$$

Where $\hat{T}_e(\rho)$ accounts for the kinetic energy of the electrons, $\hat{V}_{ne}(\hat{v},\rho)$ is the electron-nuclear potential energy, $\hat{J}(\rho)$ corresponds to the classical Coulomb electron repulsion, $\hat{E}_{NC}(\rho)$ represents the non-classical electronic exchange-correlation energy and $\hat{E}_{nuc}$ stands for the nuclear coulombic repulsion, which is constant in the BO approximation.

The electronic terms of equation (2.9) that do not depend directly on the external potential (v) are called universal and are gathered, to simplify, in what is called the Hohenberg-Kohn functional $F_{HK}(\rho)$:

$$E_v(\rho) = \int \hat{v}(\vec{r})\rho_1(\vec{r})d\vec{r} + F_{HK}(\rho) + E_{nuc} \tag{2.10}$$

In this expression it is clear that for a specific external potential the energy is a functional of the density.

The missing mathematical pieces, then, are the expressions for such functional, which the theorem does not provide, and of the function of the electron density itself.

The second theorem provided a first step towards those. It states that the electron density of a non-degenerate ground state can be calculated as that which minimizes the energy functional. Any other density will provide a higher energy, and thus this constitutes a variational principle. Therefore, to obtain the exact density of the ground state we have to find the density that minimizes the energy:

$$\frac{\partial E_v(\rho)}{\partial \rho} = 0 \tag{2.11}$$

However, to ensure the N-representability of the density, i.e., the fact that the density must be positive in all space and its integral must provide the total number of electrons, a μ undetermined Lagrange multiplier is introduced, resulting in a constrained minimization:

$$E_v(\rho) - \mu\left(\int \rho(\vec{r})d\vec{r} - N\right) \tag{2.12}$$

Where, as we said, $\int \rho(\vec{r})d\vec{r} - N = 0$.

Minimizing equation 2.12 and given that the differential of a functional has the form $\partial F = \int \frac{\partial F(f)}{\partial f(x)} \partial f(x) dx$, one arrives to:

$$\partial\left[E_v(\rho) - \mu\left(\int \rho(\vec{r})d\vec{r} - N\right)\right] = \int \frac{\partial E_v(\rho)}{\partial \rho(\vec{r})} \partial\rho(\vec{r})d\vec{r} - \mu \int \partial\rho(\vec{r})d\vec{r} = 0 \qquad (2.13)$$

$$\int \left(\frac{\partial E_v(\rho)}{\partial \rho(\vec{r})} - \mu \right) \partial\rho(\vec{r})d\vec{r} = 0 \qquad (2.14)$$

And introducing the expression of the energy of equation 2.10:

$$\mu = \frac{\partial E_v(\rho)}{\partial \rho(\vec{r})} = \hat{v}(\vec{r}) + \frac{\partial F_{HK}(\rho)}{\partial \rho(\vec{r})} + \frac{\partial E_{nuc}(\rho)}{\partial \rho(\vec{r})} = \hat{v}(\vec{r}) + \frac{\partial F_{HK}(\rho)}{\partial \rho(\vec{r})} \qquad (2.15)$$

This constitutes the so-called *fundamental equation of density functional theory*. The very important consequence of these theorems (and the herein developed DFT) is the introduction of an alternative way to finding the solution of the Schrödinger equation, avoiding the inherent many-body problem of N electrons with 3N spatial coordinates that arises looking for the wavefunction. Instead, DFT only deals with a single-body problem of three spatial coordinates: those of the electron density.

While the mathematical derivations are so far exact, the problem is that the exact expression between the functional and the density, of the $\hat{T}_e(\rho)$ term specifically, is unknown. And here is where Kohn and Sham proposed a solution.

The Kohn-Sham method[153].

While the exact form of the electronic kinetic energy as a function of the density is not known, it is easily calculated as a function of the wavefunction. This lead Kohn and Sham to try to divide the electronic kinetic energy into a term that would be known and easily calculated from the wavefunction and an unknown term. The first one would be equivalent to the kinetic energy of a reference system with the same electron density but where electron-electron interactions are not accounted for, whereas the second one would be subjected to electron correlation and calculated from the electron density. In doing so, they found that equation 2.15 provided the same structural expression for the real system than for the reference system if the unknown term is introduced into the potential ones providing an effective potential.

Consequently, the equations were solvable in a way very similar to that of the reference system, i.e. to the Hartree-Fock (HF) method[154].

Mathematically:

$$\hat{T}_e = \hat{T}_r + \hat{T}_c \tag{2.16}$$

Where $\hat{T}_r$ is the HF exact value for the kinetic energy of the reference system and the other term, $\hat{T}_c$, accounts for some electron correlation and remains inexact.

Therefore, from equation 2.9:

$$E_v(\rho) = \hat{T}_r(\rho) + \int \hat{v}(\vec{r})\rho_1(\vec{r})d\vec{r} + E_{nuc} + \hat{J}(\rho) + \hat{E}_{NC}(\rho) + \hat{T}_e(\rho) - \hat{T}_s(\rho) \tag{2.17}$$

Since the unknown term accounts for some electron correlation, it can be added to $\hat{E}_{NC}(\rho)$ in what constitutes the exchange-correlation energy:

$$E_v(\rho) = \hat{T}_r(\rho) + \int \hat{v}(\vec{r})\rho_1(\vec{r})d\vec{r} + E_{nuc} + \hat{J}(\rho) + \hat{E}_{XC}(\rho) \tag{2.18}$$

Applying the fundamental equation of DFT we have:

$$\frac{\partial E_v(\rho)}{\partial \rho(\vec{r})} = \frac{\partial T_r(\rho)}{\partial \rho(\vec{r})} + \hat{v}(\vec{r}) + 0 + \int \frac{\rho(\vec{r}_2)}{|\vec{r}_1 - \vec{r}_2|} d\vec{r}_2 + \frac{\partial E_{XC}(\rho)}{\partial \rho(\vec{r})} = \mu \tag{2.19}$$

We can simplify this expression by defining the following potentials:

The first one is the sum of the nuclear-electron potential energy and the electron repulsion term. Both appear due to Coulomb forces, and the potential is known as the Coulomb potential. The second one is called exchange correlation potential and the final effective potential is the sum of the previous two.

$$\hat{v}_C(\vec{r}) = \hat{v}(\vec{r}) + \int \frac{\rho(\vec{r}_2)}{|\vec{r}_1 - \vec{r}_2|} d\vec{r}_2 \tag{2.20}$$

$$\hat{v}_{XC}(\vec{r}) = \frac{\partial E_{XC}(\rho)}{\partial \rho(\vec{r})} \tag{2.21}$$

$$\hat{v}_{eff}(\vec{r}) = \hat{v}_C(\vec{r}) + \hat{v}_{XC}(\vec{r}) \tag{2.22}$$

Finally, the compact equation we obtain is:

$$\frac{\partial \hat{T}_r(\rho)}{\partial \rho(\vec{r})} + \hat{v}_{eff}(\vec{r}) = \mu \tag{2.23}$$

As advanced, this result only differs from the result of the non-interacting system in the expression for the potential. Therefore, we will have a very similar equation for the Kohn-Sham (KS) Hamiltonian which can be solved through very similar HF equations:

$$\hat{h}_{KS} = -\frac{1}{2}\nabla^2 + \hat{v}_{eff}(\vec{r}) \tag{2.24}$$

A set of Kohn-Sham orbitals can be written to define a Slater determinant that allows obtaining the electron density, and are solutions to the Schrödinger equation:

$$\rho(\vec{r}) = \sum_{i=1}^{N_{oc}} |\chi_i(\vec{r})|^2 \tag{2.25}$$

$$\hat{h}_{KS}\chi_i = \varepsilon_i \chi_i \tag{2.26}$$

Then, much like HF, the most precise solution for the energy and wavefunction of the system is obtained through an iterative procedure until results converge to the same value, which makes DFT belong to the so-called Self-Consistent Field (SCF) methods. The exact procedure is as follows:

1. An initial guess for the Kohn-Sham molecular orbitals χ_i is selected.
2. The electron density ρ is calculated from them (eq. 2.25).
3. The Coulomb potential $\hat{v}_C$ and the exchange-correlation potential $\hat{v}_{XC}$ are calculated from the electron density (eq. 2.21 and 2.22), and the effective potential $\hat{v}_{eff}$ is calculated as their sum (eq 2.23).
4. The Hamiltonian is now known (eq. 2.24) and the KS equations (eq. 2.26) can be written and solved. A new set of KS orbitals are obtained.
5. The electron density is calculated again with the new orbitals (eq. 2.25). If the result is the same as the one obtained in step 2, then convergence is reached and the orbitals and energy obtained in this cycle are the most precise ones the method can give (to the selected energy difference threshold). If the results differ, the cycle is repeated from step 3 until they converge.

It is important to point out that while in HF the molecular orbitals and their energies have physical meaning, KS orbitals and their energies do not. The KS wave function belongs to the set of wavefunctions whose integral yields the electron density, but it constitutes a not-so-good approximation to the wavefunction. Due to this, using it to calculate values of observables is not strictly correct. However, the shape, symmetry and energetic order of KS orbitals is very similar to that of the HF ones, and therefore they can be useful for qualitative analysis[155].

Besides, unlike HF, DFT is able to take into account all correlation energy if the exchange-correlation functional is appropriate, providing a much greater degree of accuracy at roughly the HF cost. Indeed, notice that whereas in HF the main source of error comes from employing a Slater determinant, in DFT, although an approximate Hamiltonian is used, the electron density is potentially exact and the only source of error comes from the expression of the exchange-correlation potential.

Therefore, in DFT the exchange-correlation functional is the key to obtain the most accurate results. However, one of the main disadvantages of the method is that there is no systematic way of improving the results because it is impossible to know in advance which exchange-correlation functional is going to give better results for a given system. Nevertheless, the low cost of the approach is attracting and there is always active research being done to find new or improved density functionals.

Exchange-Correlation functionals.

There are lots of different exchange-correlation functional types. Most of them have separated expressions to account for exchange and to account for correlation, and also many exchange and many correlation functionals have been developed independently. All of them can be combined, which gives rise to many possibilities.

They are traditionally classified by the locality of their approximation, that is, by which quantities of the density they employ at each point (the density, its gradient, etc), and whether they include HF exchange in the functional. Since long-range interactions are not well treated by the conventional approaches, long-range or dispersion-corrected functionals have also been developed in the last years (see Dispersion correction below).

Local Density Approximation (LDA).

In this approximation the energy depends only on the density at each point, and therefore the exchange-correlation functional is strictly *local*, as the name indicates. The energy is divided into exchange and correlation energy, with the homogeneous gas constant density taken as a model for the exchange part:

$$E_{XC}^{LDA}(\rho) = E_{X}^{LDA}(\rho) + E_{C}^{LDA}(\rho) \tag{2.27}$$

LDA works very well in systems in which the density does not change much, but the results are not very good for real molecules. The overall results for geometries are similar to HF ones, but the distances are underestimated, overestimating the bond energy. They have been used to study extended systems like metals where the description of a constant electron density can be valid. The VWN functional of Vosko, Wilk and Nusair[156] is one of the most known of this type.

Generalized Gradient Approximation (GGA) and meta-GGA functionals.

This approximation is semi-local, because the exchange-correlation energy is described in terms of the density and density gradient, i.e., considering the value of the density and its variation around the point.

$$E_{XC}^{GGA} = E_X^{GGA} + E_C^{GGA} \tag{2.28}$$

$$E_{XC}^{GGA}(\rho) = \int f(\rho, \nabla\rho) d\vec{r} \tag{2.29}$$

The PW91 of Perdew-Wang[157] and the PBE of Perdew-Burke-Ernzerhof[158] functionals employed in this dissertation belong to this GGA approximation.

Although there are empirical and non-empirical approaches to implement GGA functionals, they employ certain parameters usually adjusted to experimental data.

This approximation successfully improves the values for the geometries, frequencies and charge densities with respect to the results of the LDA functional and even work well for hydrogen bonds, but they still fail to describe weaker interactions. They also overestimate adsorption energies and underestimate band gaps.

Meta-GGA functionals improve GGA functionals by adding higher order derivatives of the density. Therefore, the exchange-correlation energy does not only contain the density and its gradient but also the Laplacian of the density.

$$E_{XC}^{meta-GGA}(\rho) = \int f(\rho, \nabla\rho, \tau, \nabla^2\rho) d\vec{r} \tag{2.30}$$

Hybrid functionals and hybrid meta-GGA functionals.

Since some properties are overestimated by HF but underestimated by GGA, such as the band gap, the so-called hybrid functionals were developed, including part of the exact exchange energy from a HF calculation in GGA functionals. One of the most famous is the three parameters method B3PW91[159,160]:

$$E_{XC}^{B3PW91} = E_{XC}^{LSDA} + a_0\left(E_X^{exact} - E_X^{LSDA}\right) + a_X \Delta E_X^{B88} + a_C \Delta E_C^{PW91} \tag{2.31}$$

Where a_0, a_x and a_c are parameters fitted to experimental thermochemical data, and the best fitted values for them are 0.20, 0.72 and 0.81 respectively.

There are also *hybrid-meta-GGA* functionals, based in including HF exchange energy to some extent in meta-GGA functionals. To this type belongs the M06 series family, for instance.

Dispersion correction.

As mentioned, one of the main problems of DFT is that conventional correlation-exchange functionals are not able to properly treat the dispersion energy. The failure lies in the impossibility of the local or semi-local functionals to describe an interaction whose nature is non-local. The problem is generally partially but sufficiently solved in practice by correcting the final value of the energy. For some weakly bonded systems, however, if the weak interaction is important and therefore needed, such correction may be included throughout the optimization, or a functional that includes dispersion terms may be employed, such as the B97D[161].

We have mostly relied on the D2 approach by Grimme, where dispersion interactions are taken into account by atom pair 1/R6 terms. For the C and R0 parameters that it employs, default values were used except for Ce, for which values of 20.00 and 1.860, respectively, were chosen according to previous tests[161,162].

Self-Interaction Error (SIE) and the Hubbard approximation (DFT+U).

Another problem of DFT is that the Coulomb electron-electron repulsion term (eq. 2.20) is not zero for the same electron. As a result, the inexistent interaction of one electron with itself is added, hence the name Self-Interaction Error[163]. In HF the exchange term cancels this effect exactly, and that is why hybrid functionals generally perform better as regards to the SIE.

The artificial repulsion of an electron with itself causes it to artificially delocalize, hence favoring more delocalized solutions for the density. Thus, covalent bonding is enhanced, band gaps are underestimated, and electrons that are known to be localized in specific atomic orbitals can be lost (delocalized).

Since hybrid functionals are costly for periodic calculations, a pragmatic tweak is usually applied to the GGA functional to overcome this problem. A U term, called Hubbard term, is added to modify the coulombic repulsion of those orbitals.

The immediate consequences of the Hubbard approximation are that all properties become dependent on the U value and therefore the method becomes non-universal, because different systems will require different values of U. As a result, one needs to choose the U term carefully, and indeed research studies can be found devoted to find which value provides overall better agreement with experiment, or better agreement with respect to the one and only selected property.

In this dissertation, we have employed the DFT+U method introduced by Dudarev et al.[164] to correctly localize the electrons on ceria, with U_{eff}=4.5[165,166].

2.3. Models.

In computational chemistry, the selection of an adequate model of the system is as important as the selection of the theoretical level at which it will be treated. The model heavily depends on the real system that we want to represent and the properties that we are more interested in (which often determines the appropriate theoretical level as well). In fact, in this dissertation we have employed finite and periodic models for both finite and periodic systems.

Finite models.

A finite model is composed by the minimum amount of atoms needed to represent the material. It is defined by the positions of said atoms in a coordinate system, which can be expressed in the traditional (x, y, z) directions of space (cartesian) or referred to an internal coordinate system.

Molecular or finite systems such as gas phase clusters or nanoparticles are naturally perfectly described by this model. However, a finite model can also be applied to periodic systems by cutting or limiting the model to a certain region of the material. These are known as *cluster models*. In that case, boundary effects need to be minimized. Thus, for covalent solids such as zeolites, dangling bonds need to be saturated, which is usually done adding final hydrogen atoms or hydroxide groups in those positions. The electronic structure of ionic materials may require a series of fixed point charges surrounding the cluster in the model. Finally, for metals the situation can become unrepresentable, as the effect of the cut-out atoms cannot be taken into account in the model and the electronic structure changes into the discrete levels characteristic of metallic clusters (see section 1.3). In addition, one needs to be sure that whatever property one aims to simulate is not affected by the cut, for example by studying its convergence with cluster size.

The smaller size of a finite model allows the application of any quantum chemistry method, and consequently it is sometimes the only way to properly perform studies that require higher accuracy. Since the maximum system size to carry out calculations in a practical amount of time is limited by the accuracy and computational cost of the method chosen, mixed alternatives to overcome this size limit were developed, which define smaller internal regions to which a higher computational level is applied, while the external region is treated at a lower level. For transition metal clusters and nanoparticles there are no regions eligible to be treated at a lower level, however. Approximations in this case can only be done to the wavefunction, that is, a smaller basis set may be chosen or pseudopotentials may be used (see section 2.4).

In this work, we have employed a finite model mainly for gas-phase clusters and nanoparticles (Figure 2.1a), as well as for the isolated molecules involved.

Periodic models.

Crystalline solids are periodic, and thus can be completely represented by a unit that is repeated in all directions of space. The repeating unit is tridimensional and constitutes a cell. Thus, a *unit cell* contains a series of points that upon infinity replication by translational symmetry expand the crystalline solid. As a result, certain patrons are produced and solids are classified as belonging to a specific *crystalline structure*, which are also known as Bravais lattices. The smallest irreducible unit cell is called *primitive* cell and is characterized by *primitive* vectors $\boldsymbol{a_i}$. The translational vectors $\boldsymbol{R}$ can then be expressed in terms of these lattice vectors:

$$\boldsymbol{R} = n_1\boldsymbol{a_1} + n_2\boldsymbol{a_2} + n_3\boldsymbol{a_3} \tag{2.32}$$

Larger unit cells known as *supercells* can be built as multiples of the primitive cell. This is indicated in the model with a (MxNxZ) nomenclature, hence specifying the times the first (M), second (N) and third (Z) lattice vectors, respectively, are replicated. The position of the atoms within the resulting unit cell can be expressed in traditional (x, y, z) coordinates (cartesian) or in relative values with respect to the length of the unit cell sides, also called *unit cell parameters* (direct).

In this dissertation we have employed periodic models for two types of systems, as exemplified in Figure 2.1:

- Finite systems: Mainly gas-phase clusters and nanoparticles (Figure 2.1b), both to compare with other methods on finite models and with supported clusters in periodic models and to carry out calculations faster, but also isolated molecules when needed.

  As the real system is not periodic in any direction, the model consists of a cubic box of a cell parameter sufficiently large to avoid any fictitious interaction of neighboring clusters from different cells.

- Supported clusters (Figure 2.1c), to evaluate the effect of the support in the properties of the clusters studied before.

  For this, the surface of the support is modelled in what is also known as *slab*. Slabs are created from the replication of the optimized bulk unit cell, by cutting the supercell through a selected symmetry plane that determines the symmetry of the slab and of the surface exposed to reactants.

  A surface is periodic in two dimensions of space, whereas in the remaining other a vacuum space is built with the purpose of leaving space for adsorbates to interact with the surface. Such model then, being periodic, has two

surfaces, when the real system would only show one. As a consequence, the atoms of the bottom surface are usually fixed at the positions characteristic of the bulk material, and subsequent layers are added towards the upper surface, some of which are allowed to relax upon optimization. The more free layers added the more expensive but the more realistic the calculation.

Also, the vertical symmetry of the slab, i.e. where to cut (at which atomic layer) once the plane is selected, is important if the system is ionic, presents particular dipoles or a specific magnetic structure. The replication of such properties in the model may lead to computational instabilities, which is also the reason why anionic systems are generally not well-treated by periodic calculations. A common approach is to cut the slab with an odd number of layers so that dipoles are compensated. These are known as *symmetric* slabs.

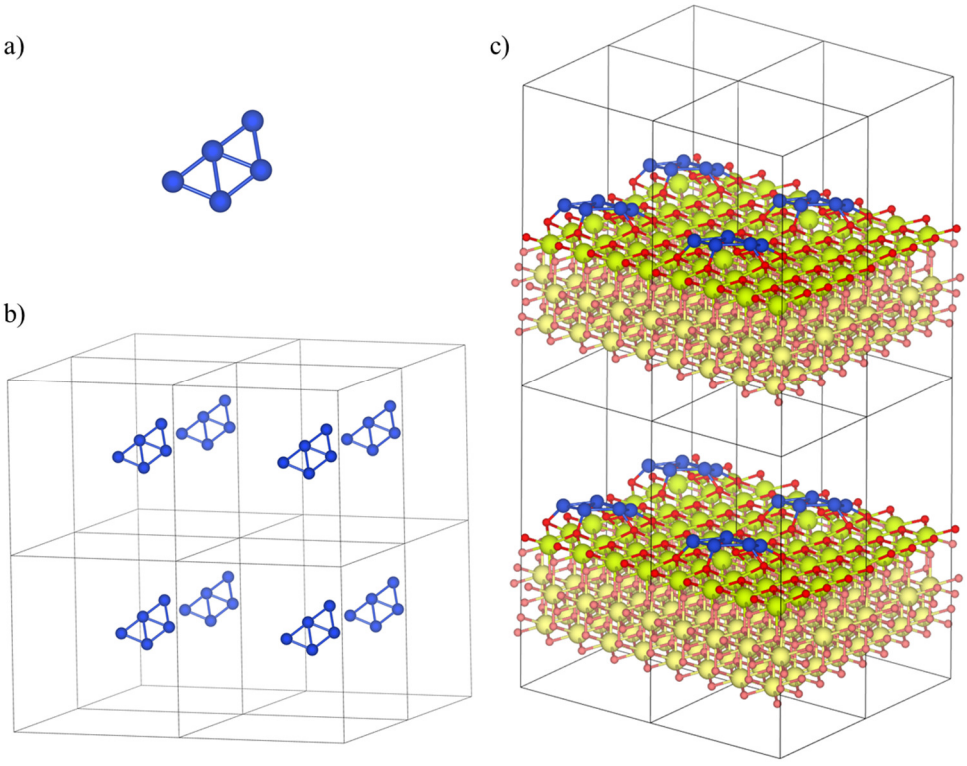

Figure 2.1. Models employed throughout this work: a) finite model of a Cu_5 cluster, b) periodic model of a Cu_5 cluster, c) periodic model of a Cu_5 cluster supported on the $CeO_2(111)$ surface. The unit cells are specified by black lines in all periodic models. Cu atoms are depicted in dark blue, O atoms in red (subsurface O atoms in pink), Ce atoms in green (subsurface Ce atoms in yellow).

2.4. Basis sets.

In quantum chemistry methods, the wavefunction of the system is mathematically expressed as a linear combination of certain *basis* functions. These basis functions constitute the *basis set*. If the basis set is complete, any mathematical function can be exactly represented with it, but achieving this would involve an infinite number of functions, which is not possible computationally. Therefore, a finite basis is used as an approximation. The type and size of the chosen basis can determine the accuracy of the calculation.

For calculations on finite systems, basis sets are usually built using atom-centered Gaussian functions. However, for periodic systems wavefunctions are mathematically described as planewaves in order to preserve the periodicity of the model.

Atom-centered basis set.

Minimal basis set.

Two of the first and simplest basis sets initially proposed were Slater Type Orbitals (STO)[167] and Gaussian Type Orbitals (GTO)[168], which were later combined to constitute the so-called STO-NG basis, the most common of *minimal* basis sets[169]:

$$\phi_{STO-NG} = \sum_i a_i \varphi_{i,GTO} \tag{2.32}$$

$\varphi_{i,GTO}$ is a gaussian function called *primitive* and the STO-NG is called *contracted*.

In a minimal basis set the amount of functions used is the minimum to describe the core and valence orbitals of the atoms, but not any virtual orbitals. As a consequence, a minimal basis set is not flexible enough to describe correctly the atoms in a molecular environment and the results obtained are very rough.

Split-valence basis set.

Since valence electrons are the ones that usually participate in chemical bonds, in these basis sets the valence atomic orbitals are described with more than one basis function. If the split is in two basis functions, the basis is called double zeta, DZ. Similarly, we can have a triple zeta (TZ), quadruple zeta (QZ) and so on. The coefficients of each of these functions can be varied and thus the size of the orbital changes, allowing the adjustment to a particular molecular environment.

The most common basis sets of this type are Pople and Watchers-Hay basis sets[170-172]. The notation of these basis sets states its type and composition. For instance, we have employed the standard 6-311+G(d,p), in which each core atomic orbital is de-

scribed by a function with 6 Gaussian primitive functions. Then, the valence atomic orbitals are split in three (since three digits are indicated), each of which is described by two functions (as per definition). These two functions are described by 3 Gaussian primitives for the first part, whereas the remaining four are described by 1 primitive each. In addition, heavy atoms are described with a diffuse function (+), and for heavy atoms and hydrogen atoms a *d* and *p* polarization function, respectively, is included. The hyphen implies its split-valence character and G stands for Gaussian.

The polarization and diffuse functions mentioned are employed to provide additional mathematical flexibility for the correct description of the system. Polarization functions are orbitals with higher angular momentum than the ones an atom has in its ground state. It owes its name to the fact that it provides the atom with new directions that can accommodate the electron density in cases where it is deformed such as in polarization processes. Diffuse functions are needed when the atomic orbitals reach farther distances from the nuclei due to it having more charge, as in ionic atoms, or in the case of weakly bonded systems. In general, they are included as an *s* function and a set of *p* functions for each atom of the system, with the exponents obtained variationally for the anion or hydride anion of the corresponding atoms.

The Def2TZVP is another all-electron split-valence basis set we employed, based on the TZVP from Ahlrichs and co-workers. It is less computationally demanding and yet has been reported to be close to the basis set limit for DFT calculations[173,174].

Finally, we have also used the LANL2DZ basis set, which is the only one that does not include all electrons: it combines Los Alamos effective core potential to account for the electrons of the core with a DZ set for valence electrons. This makes it much less expensive and, due to that, widely used for transition metals[175,176].

Planewaves as basis set.

In a periodic system the wavefunction has to be periodic as well:

$$\Psi(\boldsymbol{r}) = \Psi(\boldsymbol{r} + \boldsymbol{R}) \quad | \, \boldsymbol{R} = n_1\boldsymbol{a_1} + n_2\boldsymbol{a_2} + n_3\boldsymbol{a_3} \tag{2.33}$$

Where **R** is the translation vector of the unit cell, n_i are integers and $\boldsymbol{a_i}$ are primitive vectors that span the lattice in their direction (see section 2.3).

The Bloch theorem limits the wavefunction to the number of electrons in the unit cell by stating that each one-electron wavefunction, also known as Bloch state, can be expressed as the product of a periodic part and a wave-like part:

$$\psi_i(\boldsymbol{r}) = f_i(\boldsymbol{r})e^{i\boldsymbol{k}\boldsymbol{r}} \quad | \, f_i(\boldsymbol{r}) = f_i(\boldsymbol{r} + \boldsymbol{R}) \tag{2.34}$$

Every periodic function can be expanded as a linear combination of planewaves, which means that the periodic part of these Bloch functions can be written as a Fourier series. The latter is interesting because it allows the use of the Fast Fourier Transform to speed up calculations.

This mathematical process leads to the expression of the wavefunction in terms of the so-called *reciprocal lattice* vectors (**G**):

$$\psi_i(\boldsymbol{r}) = \sum c_{i,\boldsymbol{K}}\, e^{i\boldsymbol{K}\boldsymbol{r}} = \sum c_{i,\boldsymbol{k}+\boldsymbol{G}}\, e^{i(\boldsymbol{k}+\boldsymbol{G})r} \quad | \boldsymbol{G} = m_1\boldsymbol{b_1} + m_2\boldsymbol{b_2} + m_3\boldsymbol{b_3} \qquad (2.35)$$

Where $\boldsymbol{k}$, $\boldsymbol{K}$ are wave vectors and the $\boldsymbol{k} + \boldsymbol{G}$ notation is employed to specify that vectors that differ by a reciprocal lattice vector are equivalent.

The reciprocal lattice is, as any lattice, a periodic set of points. However, since it constitutes the Fourier transform of the real lattice (and vice versa), its points belong to the *reciprocal space*. The points are usually characterized by (k_1, k_2, k_3) coordinates or a $\boldsymbol{k}$ vector, due to which the reciprocal space is also called *k-space*. The real lattice is also called *direct* lattice, and its primitive vectors $\boldsymbol{a_i}$ are related to the reciprocal primitive vectors $\boldsymbol{b_i}$ by:

$$\boldsymbol{b_1} = 2\pi\frac{\boldsymbol{a_2}\times\boldsymbol{a_3}}{\boldsymbol{a_1}\cdot(\boldsymbol{a_2}\times\boldsymbol{a_3})};\quad \boldsymbol{b_2} = 2\pi\frac{\boldsymbol{a_1}\times\boldsymbol{a_3}}{\boldsymbol{a_2}\cdot(\boldsymbol{a_1}\times\boldsymbol{a_3})};\quad \boldsymbol{b_3} = 2\pi\frac{\boldsymbol{a_1}\times\boldsymbol{a_2}}{\boldsymbol{a_3}\cdot(\boldsymbol{a_1}\times\boldsymbol{a_2})} \qquad (2.36)$$

Since the wavefunction needs to be periodic and fulfill the boundary conditions, only certain values of $\boldsymbol{k}$, also called *k-points*, are allowed in each of the lattice directions. Due to the solid extension, in principle there is an infinite number of k-points to evaluate in eq. 2.35, but Bloch realized that, thanks to translational symmetry, many were equivalent. Indeed, he found that all Bloch states are accounted for without redundancy if one includes all the k-points belonging to the so-called first Brillouin zone, which is the name given to the primitive cell in the reciprocal space. However, in practice, when k-points are close in k-space the wavefunctions are almost identical, and an even lower number of k-points can be selected.

Since coordinates in the reciprocal space are inversely proportional to those in real space (eq 2.36), when the unit cell of the system is sufficiently large even a single k-point can be enough. In such case the one employed is generally the so-called gamma point, Γ (0, 0, 0), that is located at the center of the Brillouin zone. Usually, nevertheless, one needs to make an energetic scan of the system with respect to the number of k-points to find the minimum amount needed to obtain accurate results, i.e. convergence. There are several methods to produce the k meshes from the number of k-points selected per unit cell side, which is also known as *k-point sampling*. When the Γ point was not enough, we employed the sampling by Monkhorst and Pack[177].

In principle an infinite number of planewaves should be used in the Fourier series, but Bloch realized that the expansion coefficients $c_{i,\boldsymbol{k+G}}$ tend to zero when the kinetic energy of the planewaves is high enough. Thus, an *energy cutoff* can be established to only include the significant ones, that is, those up to a selected restricted value.

Pseudopotentials and the Projector Augmented Wave method (PAW).

Real wavefunctions are smooth in bonding regions but exhibit rapid oscillations near the nuclei. As a result, expressing the wavefunction in terms of planewave expansions converges rapidly for bonding regions and very badly for the atoms, where a much higher number of planewaves are required.

One approach to overcome this is the use of *pseudopotentials*, which avoid the oscillations of the core electrons by removing them from the model. In this approximation the all-electron potential is thus substituted by an effective potential and the valence electrons are described by *pseudowavefunctions* that are smoother, i.e. have significantly fewer nodes. This way, planewaves can be efficiently used to describe the system. A core cut-off radius is used to determine how far from the nucleus is the pseudopotential approximation applied, so that the larger the radius, the softer the pseudopotential and the less accurate.

In a related but different approach, the so-called *augmented* planewave methods use functions different to planewaves to describe atom-centered regions.

In the particular case of PAW[178], the all-electron wavefunction near the nuclei Ψ is built using a modified pseudowavefunction $\widetilde{\Psi}$. The conceptual idea is to apply a transformation operator to each one-electron or partial pseudowavefunction $\tilde{\phi}_i$, so that a more appropriate function to represent it, ϕ_i, is obtained. Thus, the transformation operator is usually constructed using partial waves that are solutions to the KS Schrödinger equation of the isolated atom. Mathematically, this is achieved through *projector* operators, p_i, that introduce these orbitals or partial waves. To avoid repetition, the corresponding partial pseudowavefunctions are projected out:

$$|\Psi\rangle = |\widetilde{\Psi}\rangle + \sum_i |\phi_i\rangle\langle p_i|\,\widetilde{\Psi}\rangle - \sum_i |\tilde{\phi}_i\rangle\langle p_i|\,\widetilde{\Psi}\rangle \tag{2.37}$$

The part of space where the transformation is non-zero is delimited by a spherical augmentation region enclosing each atom. Therefore, out of this space, i.e. between atoms, the usual planewave expansion is used unchanged, whereas within the atom the true all-electron wavefunction is produced from the mentioned modification to the pseudowavefunction. At the frontier, the modified pseudowavefunction is equal to the all-electron wavefunction from unmodified planewaves. This way, the PAW method reintroduces the lost nodes of the wavefunctions and provides more accurate results than pseudopotentials.

The approach is compatible with the frozen core approximation and is usually employed along with it (VASP uses it). The latter assumes that the core states are not affected by the environment and can be kept fixed or *frozen* in the calculation.

2.5. Optimization algorithms.

Through the DFT method reviewed in section 2.2, the lowest electronic energy for a given position of the nuclei can be obtained. However, the total energy depends on the relative positions of the nuclei. Therefore, the latter must be allowed to move in order to explore the most stable geometry of the whole system. The procedures that aim to obtain these stable geometries are called *optimization algorithms*. Each calculation program has a default procedure and usually offers the user the possibility of changing it in the input.

Potential Energy Surface (PES).

A potential energy surface is the representation of the *potential energy* as a function of certain parameters, which are usually the relative positions of the atoms. If all the relative positions of the atoms are taken into account, then a *hypersurface* is obtained. The latter has a 3N dimensionality (where N is the number of atoms) due to the three-dimensionality of space (x, y, z) (or 3N-6 after the removal of 3 rotational and 3 translational degrees of freedom). However, as the system can be also represented by internal coordinates (bond distances and angles), *reduced* PESs can be built employing only some selected coordinates. Thus, the *PES of a reaction* can be built plotting the energy with respect to the coordinates that change upon the elementary reaction (Scheme 2.1a). In this surface, a trajectory can be defined from the initial state or reactants to the final state or products following the minimum energy reaction path (MERP). The energy profile of the MERP is said to follow the *reaction coordinate*, and shows that to reach one state from the other the system must pass through an unstable transition state (TS) and therefore needs certain activation energy to overcome an energetic barrier (Scheme 2.1b, see also section 1.1).

Initial and final states correspond to minima in the PES, while the TS corresponds to a saddle-point. Mathematically, this means that they are critical points on the surface. For all of them the derivative of the energy with respect to the coordinates, i.e. the *gradient* or *forces*, are zero, which is why they are also called *stationary* or *steady* states. However, the saddle-point is a minimum in all directions except that of the reaction coordinate, on which it is a maximum. It can be characterized by one negative value of the second derivative of the energy, the *curvature*, or, equivalently, by a negative eigenvalue in the *Hessian matrix*, which is the square matrix of second order partial derivatives of the energy. The Hessian is positive at a minimum.

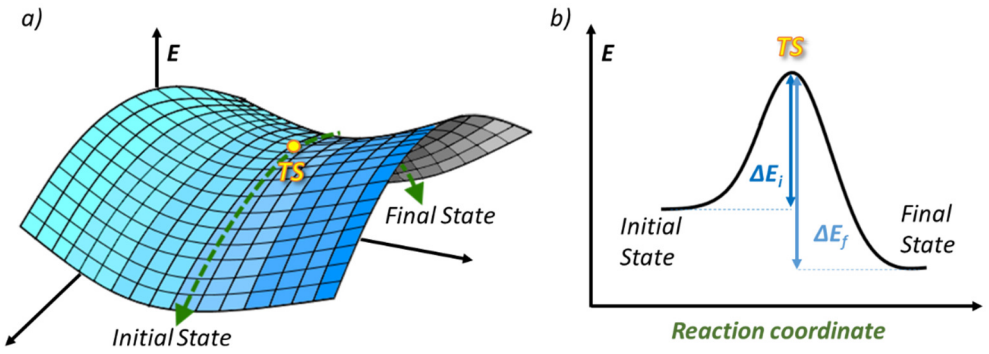

Scheme 2.1. a) Section of the PES of a reaction and b) energy profile along the reaction coordinate. The transition, initial and final states are indicated. The MERP is shown in a dashed green line and the energetic barriers in blue.

Aided by these mathematical definitions, optimization algorithms decide where to move the nuclei of any input structure, so that the system follows a path on the PES that leads it to a minimum or a saddle-point with the lowest number of steps. In general, they involve the computation of forces in one way or another, for the gradient of a surface at any point is a vector that points to the direction of greatest increase.

Finding minima.

In Gaussian, we always employed the default Berny algorithm[179]. It constructs an approximate Hessian for the system and optimizes the structure using it and the forces on the atoms, from which the Hessian is subsequently updated. Optimizations stop by satisfying four convergence criteria: the maximum remaining force on any atom of the system, the average (root mean square, RMS) force on all atoms, the maximum displacement, i.e. the maximum structural change of one coordinate in the last two iterations and the average (RMS) change over all structural parameters in the last two iterations.

In VASP, we have mainly relied on the Limited-memory Broyden-Fletche-Goldfarb-Shanno (LBFGS) force-based optimizer provided by the VTST tools[180]. It belongs to quasi-Newton methods, in which the Hessian matrix is also not calculated but approximated through the gradient. In addition, we have also used the residual minimization scheme, direct inversion in the iterative subspace (RMM-DIIS)[181], and the conjugate-gradient[182] algorithms. The former is better when the structure already has a geometry close to that of a local minimum, while the latter is generally more robust and converges rapidly to the minimum structure. Optimizations stop when the energy change between steps or the forces per ion are less than the selected threshold.

It is important to notice that these algorithms are meant to find any minima and are thus bound to find those that are close to the input structure. Therefore, finding the global minimum of the system heavily depends on the optimization of many different input structures to compare their energies, and one needs to be sure that the options explored, if not all, are sufficiently representative of the system.

Finding Transition States.

In Gaussian, we also employed the default Berny algorithm mentioned in the previous section[179]. It is an eigenvector-following algorithm, but the default options will stop the optimization if more than one negative eigenvalue is found in the Hessian matrix. Since strictly obtaining a single negative eigenvalue from a trial structure seldom happens, skipping this test is common procedure. This is not a problem as long as the unstable mode of the TS has the largest negative eigenvalue, which is the one the algorithm will follow. Therefore, the input structure needs to be close enough to the real TS, and it is better to force the program to calculate the Hessian matrix through proper derivation at least in the first optimization step so that the direction of the unstable mode is clear. The algorithm then steps uphill in that direction while minimizing the energy gradient, and the Hessian is updated using the previous Hessian and the gradient of the last two points.

Energetic scans and constrained optimizations varying and/or fixing only certain coordinates were also employed to explore the PES in complicated cases, and the Synchronous Transit-guided Quasi-Newton method was also sometimes used, both in the QST2 and QST3 versions[183,184]. The initial and final state structures are needed as input in both, whereas QST3 additionally requires a guess structure for the TS.

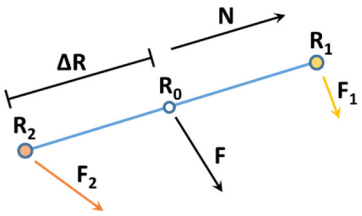

Scheme 2.2. Definition of the dimer and the corresponding forces (***F***) on each point (***R***). ***N*** is a unitary vector along the dimer axis.

Similarly, while we have mainly used the Dimer (or Improved Dimer) method[185,186] to find TSs in VASP, the Nudge Elastic Band (or Climbing Image Nudge Elastic Band)[187] was employed when the direct application of the former was not successful. Nevertheless, a Dimer calculation was always carried out to refine NEB results.

In the Dimer method the TS is found with two images of a very similar geometry to the one used as input, $\boldsymbol{R_0}$. These images, $\boldsymbol{R_1}$ and $\boldsymbol{R_2}$, are displaced in the 3N dimensional space a fixed distance from $\boldsymbol{R_0}$, $\boldsymbol{\Delta R}$, and constitute a *dimer* (Scheme 2.2).

The method does not require the computation of the second derivatives of the energy; the curvature is obtained from finite differences on the forces:

$$C = \frac{(\boldsymbol{F}_2 - \boldsymbol{F}_1)\cdot \boldsymbol{N}}{2\Delta R} = \frac{E - 2E_0}{(\Delta R)^2} \tag{2.38}$$

If E_0, the energy at the $\boldsymbol{R_0}$ point, and $\boldsymbol{\Delta R}$ are constant, then the energy of the dimer $E = E_1 + E_2$ is directly related to the curvature C. Such a situation arises when the dimer is rotated keeping $\boldsymbol{R_0}$ fixed. In such case, minimizing the energy of the dimer is equivalent to minimizing the curvature. Consequently, the direction of the dimer axis after the rotation that minimizes its energy is also along the minimum curvature mode. The method takes advantage of this fact and optimizes the structure following two general steps: rotation and translation. The rotation identifies the lowest curvature mode, which characterizes the TS. Then, a translational step in the direction of the resulting net force on $\boldsymbol{R_0}$, $\boldsymbol{F}$, would move the dimer towards a minimum. Thus, a modified force is employed where the force along the dimer axis is inverted, hence moving the dimer towards the saddle point instead. If the dimer wrongly reaches a region where the curvature is positive (leading to minima in the PES), the force is only this inverted force along the dimer axis, so that it leaves this region faster.
The key of the dimer method thus lies in the efficiency of the rotation step in finding the lowest curvature mode. The rotational plane is spanned by the dimer axis and a normalized vector orthogonal to it, but there are many ways to obtain the latter, such as by a steepest descent method or by using a conjugate gradient. The improved dimer method is based on the same procedure but employs a more efficient algorithm that results in a better scaling with system size and is more robust.

Finally, the Nudge Elastic Band (NEB) method tries to find a TS between known initial and final states, as the QST2 and QST3 methods of Gaussian. The method optimizes a selected number of structures, intermediate between the reactants and products, called *images*. The optimization is constrained, so that the images maintain an equal spacing between one another along the reaction coordinate, called *band* in the method. This is achieved by defining a driving vector or direction along the reaction coordinate and so-called *spring forces* between the images. For each image, the direction along the reaction coordinate can be described as a vector from the coordinates of the previous and next images. Then, the total force on each image can be split into one parallel to the path, i.e., to the mentioned vector, and one perpendicular to it. Therefore, if the image is correctly aligned in the reaction coordinate, the perpendicular force component should be zero. The algorithm thus moves each image along this perpendicular force in small steps until the force gets close to zero. As in each of these steps the coordinates change, each step of an image modifies the vector direction of the previous and next images. Consequently, the optimization of all the images is interdependent and done simultaneously. Spring forces are added to the parallel force to avoid all images from falling to minima in the optimization.

The method thus implies a sampling of the reaction coordinate, and additional high-energy images could arise if the path from the initial to the final state is not an elemental step, indicating the existence of more than one TS along the path that connects the two minima. The more images optimized, the better the sampling, but also the more expensive. The climbing image NEB (CI-NEB) is a modification where this spring is not used for the highest energy image. Instead, its normal net force along the band is inverted, so that it goes uphill in energy in the direction of the band, while being still minimized in all other directions. As a result, this image is moved towards the saddle-point and provides a better result than conventional NEB.

2.6. Steady state analysis.

Additional analyses of the steady states are usually required after their optimization. Thus, a normal mode analysis confirms the nature of the structure (as a minimum or a transition state) and further allows the study of changes to the vibrational frequencies of reactants upon adsorption. Then, the analysis of atomic charges, frontier orbitals or density of states plots provides a better understanding of the atomic interactions and of the behavior or reactivity of the material.

Normal mode analysis. Vibrational frequencies.

Nuclei are constantly in motion in steady states, vibrating, a feature that is ignored in optimization calculations. These vibrations contribute to the energy of the steady states and the system can be identified by the Infra-Red (IR) or Raman spectra that are produced by transitions between its different vibrational energy levels.

In the framework of the Born-Oppenheimer approximation, it is also possible to solve the Schrödinger equation for nuclear motion:

$$\left[-\sum_i^N \frac{1}{2m_i}\nabla_i^2 + V(\boldsymbol{R})\right]\Psi_{nuc}(\boldsymbol{R}) = E\,\Psi_{nuc}(\boldsymbol{R}) \tag{2.39}$$

Where N is the number of atoms, m_i the atomic masses, $V(\boldsymbol{R})$ the potential energy of the PES, $\boldsymbol{R}$ the nuclear coordinates and $\Psi_{nuc}(\boldsymbol{R})$ the nuclear wavefunction.

Vibrations are usually well approximated by a harmonic oscillator. The potential energy V($\boldsymbol{r}$) can be expressed as a Taylor expansion truncated at second order. For the diatomic case:

$$V(\boldsymbol{r}) = \frac{1}{2}k(\boldsymbol{r} - \boldsymbol{r}_{eq})^2 \tag{2.40}$$

Where k is the second derivative of the energy with respect to $\boldsymbol{r}$ at $\boldsymbol{r}_{eq}$. It is also known as the bond force constant.

The eigenvalues of eq. 2.39 with eq. 2.40 for the potential are the energies:

$$E = \left(n + \frac{1}{2}\right) h\omega = \left(n + \frac{1}{2}\right) \frac{h}{2\pi} \sqrt{\frac{k}{\mu}} \tag{2.41}$$

Where n is the vibrational quantum number and μ the reduced mass. Therefore, any energy separation between two consecutive levels is $h\omega$. Also, in order to calculate this frequency of vibration ω, k needs to be known.

For a polyatomic case, and since we are at steady states where the gradient is zero:

$$V(\boldsymbol{R}) = V + V' + V'' = V(0) + 0 + \sum_{i,j} \frac{1}{2} H_{i,j} x_i x_j \tag{2.42}$$

Where $H_{i,j}$ is the mass-weighted Hessian. After a mathematical transformation of coordinates, this generalization of the harmonic approximation to the polyatomic case leads to a matrix eigenvalue problem where the Hessian matrix needs to be calculated, in analogy with the requirement of k in the diatomic case. The resulting eigenvectors of this problem are the so-called *normal modes*. In each of them all atoms of the system are moving sinusoidally in phase with the same frequency of vibration and pass by the equilibrium geometry at the same time. The frequency is characteristic of the normal mode and is obtained from the eigenvalue.

Since all 3N coordinates are used, three modes are additionally obtained that actually correspond to translations and another three for rotations. Their frequencies should be as close to zero as possible, otherwise the structure may not have been well optimized. Also, all frequencies must be positive for minima. For TSs, since they are characterized by one negative value of the Hessian matrix and the eigenvalues are expressed in terms of square roots, one imaginary frequency should be obtained.

Gaussian calculates the Hessian matrix analytically for frequency calculations, that is, the second derivatives of the potential are calculated explicitly from the potential. VASP calculates them numerically instead, from finite differences of the forces. We used central differences, for which small displacements (h) are firstly made for each atom along each cartesian coordinate in the forward (*1*) and backward (*-1*) directions. Single-point calculations are carried out to evaluate the forces (F) of the modified geometry, and the second derivatives are obtained from them as:

$$V''(0) = \frac{F_1 - F_{-1}}{2h} \tag{2.43}$$

Finally, note that the vibrations of a solid material can be considered decoupled and not affecting that of the adsorbates, which allows a substantial reduction of the computational time by fixing the coordinates of the material in the frequency calculation.

Atomic charges.

The transfer of charge is a feature that aids in the characterization of produced or broken bonds, and in understanding or predicting the behavior of the systems. In Gaussian, we have calculated charges with the Natural Bond Orbitals (NBO) program by Weinhold et al.[188] whereas in VASP we have used the Bader program[189-191].

Natural Bond Orbitals (NBO).

Natural Orbitals (NO) are called *natural* because, due to their mathematical description, they can be seen as those orbitals that the wavefunction itself would choose as optimal for its own description of the electron density.

Mathematically, the NOs Θ_k of a wavefunction Ψ can be defined as the orbitals that are eigenfunctions of the first-order reduced density matrix, also called first-order reduced density operator:

$$\rho_1(\vec{x}_1';\vec{x}_1) = \hat{O} \Rightarrow \hat{O}\Theta_k = p_k\Theta_k \tag{2.44}$$

Where the eigenvalue p_k represents the population i.e. the occupancy of Θ_k.

Indeed, NOs can be characterized as maximum occupancy orbitals, and can be calculated by a variational maximization of their occupancy. The inclusion of electron correlation causes these populations to lose their integer character: some virtual orbitals participate in the wavefunction, obtaining some occupation, and some occupied orbitals participate in excitations to virtual orbitals, losing some occupation.

It is important to know that natural orbitals are independent of the particular basis set chosen to describe the wavefunction: natural orbitals are intrinsic and unique to the wavefunction of the system, while the basis orbitals are simply general fitting functions numerically convenient.

Natural Bond Orbitals (NBO) are localized natural orbitals whose N/2 leading members give the most accurate Lewis-like description of the total N-electron density. The program searches all possibilities of assorting the bonds and lone pairs of the system to reproduce the variationally optimal bonding pattern which places the electron density precisely in the leading N/2 Lewis type NBOs. These Lewis-type NBOs are the ones that determine the Natural Lewis Structure (NLS) representation of the wavefunction, and the rest of the NBOs, the non-Lewis type, complete the basis and account for residual delocalization effects. This way, NBOs provide a valence bond-like description of the wavefunction, linking it to classical Lewis structure concepts.

NBOs have also a unique association to the wavefunction of the system, and are practically insensitive to the variation of the basis set and method. They are composed of Natural Hybrid Orbitals (NHO), which at the same time are optimized linear combinations of Natural Atomic Orbitals (NAO) in a given center. Natural Atomic Orbitals are localized 1-center orbitals and are defined as the effective natural orbitals of a certain atom in the molecular environment.

The output of the NBO program displays information regarding the nature of the NBOs. For instance, core NBOs, usually of nearly pure NAO character, are labeled as CR, and 1-center lone pairs are labeled LP, whereas two-center bonds are shown as BD and are constituted by a linear combination of two NHOs, whose coefficients are a measure of the covalent or ionic nature of the bond.

In addition, natural atomic charges are also provided in the output, calculated as the subtraction of the summed natural populations of the NAOs on the atom to the nuclear charge characteristic of the element.

Finally, NBOs are orbitals that are easy to understand qualitatively and can be plotted to obtain information regarding their shape and extension. We have often done so in order to explain preferential sites for the interaction between catalysts and reagents.

Atoms In Molecules (AIM) and Bader charges.

The Quantum Theory of Atoms in Molecules (QTAIM), developed by Bader and coworkers[192,193], is based on the idea that, since atoms, bonds, electron lone pairs, etc., are concepts that have been proved to be very useful in the understanding of chemistry and its predictions, they should be representable from the electron density.

According to this theory, the electron density, together with the gradient paths of the electron density, reveals the structure of the system through its stationary points. In addition, it allows the calculation of some physical properties by dividing them into terms of only one nucleus, thus justifying the additive character of those properties.

The gradient path is the trajectory the gradient follows considering the maximum increase in the density. When the gradient paths of the whole molecule are calculated, the gradient vector field is obtained, and it can be seen that every trajectory starts and ends at a critical point where the derivative of the density is zero, such as at nuclei. As a result, nuclei are referred to as point attractors of the gradient vector field. The *basin* of the attractor is defined as the region that contains all the trajectories of the gradient that end into the attractor. Therefore, the space the molecular density is distributed in can be separated into atomic basins, separated regions that contain only one point attractor or nucleus. Thus, in this theory an atom is defined as a point attractor and the associated gradient paths that constitute its atomic basin.

Between an atom and a bonded other there is an interatomic surface, and that makes possible another definition of an atom in terms of the limits of its basin with that of the other atoms, i.e. delimited by one or more interatomic surfaces. Since the trajectories of the gradient of the density never cross and terminate at a critical point, in this interatomic surface the flux of the gradient of the density is zero, i.e. no gradient path crosses it or exists within it.

As a consequence, finding the surface around each atom on which the charge density is minimum, which is usually what happens between atoms, turns out to be a way to separate them naturally. Then, the electronic charge on the atom can be calculated as the electron density contained in the volume that such surface encloses.

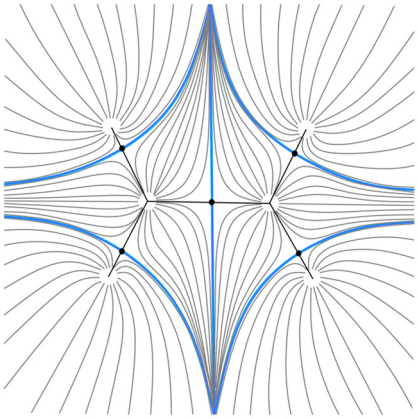

Scheme 2.3. Gradient paths of the C_2H_4 molecule within the plane that contains its nuclei, illustrating the separation of space into atomic basins. Trajectories that end at a nucleus or attractor are shown in grey. The molecular graph, constituted by the bond critical points (black dots) and bond paths (black lines) is also shown. The intersection of the interatomic surfaces with the plane are indicated in blue.

Density of states (DOS).

Much like atomic charges, the density of states helps characterizing the bonds and the behavior of systems. As the name implies, it indicates the number of states (occupied or empty) at a given energy value, hence serving as a measure of how dense are the latter. Due to this, it is more commonly used for extended systems where the energy levels form bands instead of thin discrete levels. It thus constitutes a Molecular Orbital (MO) diagram counterpart. Indeed, and resembling the Highest Occupied and the Lowest Unoccupied Molecular Orbitals (HOMO and LUMO) of MO diagrams, in a DOS plot there are usually a valence and a conduction band, separated at the Fermi level, of which the former contains all occupied states whereas the latter has the unoccupied ones.

The DOS, as a density, is calculated as the number of states within a selected energy range divided by the same energy range. As explained in section 2.4, the first Brillouin zone is enough to represent the whole material, and both the number of states and the possible energy values are given by the number of acceptable k-points within it. For a certain differential amount of k-space $d\boldsymbol{k}$, the two observables can be expressed as integrals.

The occupancies of the states can be determined by different methods involving functions of probability. This is linked to smearing methods, especially in metals, for mathematical reasons: they have several close to degenerate states at the Fermi level and it is hence possible to get convergence problems, as very small perturbations may change the electron occupation. Thus, a fictitious smearing function is used to avoid them: fractional occupancies are allowed and electrons are smeared along more states, higher but close to the Fermi level. The approach is equivalent to increasing the energy of the system, and therefore the temperature and entropy introduced are removed later by extrapolation to 0 K. We have mostly relied in the Gaussian smearing since it is appropriate for both conductors and insulators.

Finally, to extract some orbital-like information one needs to project the DOS onto adequate orbital functions. We have employed the default projection onto spherical harmonics, which are centered at the position of the ions and are non-zero within the so-called Wigner-Seitz radius (which is different for each element). This approach also provides the magnetization density in the output, which, if calculations are spin polarized, is the difference between that of the up and down spins. The resulting DOS are then called Projected DOS (PDOS). They can show specific contributions to certain bands, which is particularly interesting in the identification of peaks or defects that arise upon changes to the material.

2.7. Thermodynamic properties.

In the macroscopic regime observables are obtained for large amounts of molecules and depend on thermodynamic variables. In contrast, the energies that we obtain in our calculations, also known as *electronic* energies, do not include the Zero-Point Vibrational Energy (ZPVE) nor any thermal contribution. However, these energy contributions can be approximately calculated from optimized structures and added to electronic energies so that comparison with experiment becomes possible[155].

Zero-Point Vibrational Energy (ZPVE).

As mentioned in section 2.6, nuclei are constantly vibrating in steady states, even at 0 K, and these vibrations imply an additional energy contribution. Within the harmonic approximation, the energy of the lowest vibrational level for each normal mode can be determined from eq 2.41. The ZPVE is defined as the sum of the lowest vibrational energies of all the normal modes of a system. Then, the so-called *internal* energy at 0 K, U_0, is simply the sum of the ZPVE plus the electronic energy:

$$U_0 = E_{elec} + ZPVE = E_{elec} + \sum_i^{modes} \frac{1}{2} h\omega_i \qquad (2.45)$$

Statistical Mechanics.

In statistical mechanics one usually deals with a so-called *ensemble* of molecules upon which some external conditions are constant. In a canonical ensemble, the total number or particles N, the volume V and the temperature T are constant, and its corresponding *partition function* Q is given by:

$$Q(N,V,T) = \sum_i e^{-E_i(N,V)/k_B T} \tag{2.46}$$

Where *i* are the all states of the system and k_B is Boltzmann's constant.
The partition function characterizes the ensemble much like the wavefunction characterizes the microscopic system, i.e. contains all the information needed to calculate any thermodynamic property of the ensemble. It is called partition function because it arises from Boltzmann's distribution of the occupation of energy levels, and thus indicates how is the population distributed or partitioned among the energy levels. It is also called sum of states, for straightforward reasons (eq. 2.46). Within the canonical ensemble thermodynamic variables can be obtained from Q:

$$U = k_B T^2 \left(\frac{\partial lnQ}{\partial T}\right)_{N,V} \tag{2.47}$$

$$H = U + PV \xrightarrow{ideal\ gas} U + RT \tag{2.48}$$

$$S = k_B lnQ + k_B T \left(\frac{\partial lnQ}{\partial T}\right)_{N,V} \tag{2.49}$$

$$G = H - TS \tag{2.50}$$

Where H is enthalpy, P is pressure, R is the ideal gas constant, S is entropy and G is free energy. The calculation of these thermodynamic properties becomes much easier if the energy is separable into a sum of electronic, translational, rotational and vibrational terms. In such case, Q is expressed as a product of the corresponding partition functions:

$$Q = q_{elec} q_{trans} q_{rot} q_{vib} \tag{2.51}$$

Electronic contribution.

The contribution to the electronic partition function of excited states at low temperature is negligible, and thus only the groundstate contributes. In our approach the electronic energy from the groundstate is already considered (eq. 2.45). Thus it should be zero now and q_{elec} equal to the degeneracy of the groundstate (the number or states that have zero electronic energy) (eq. 2.46). Then, as such q_{elec} does not change with temperature, the additional U_{elec} is also zero (eq. 2.47).

However, the contribution to the entropy is not zero. From eq. 2.49:

$$S_{elec} = k_B ln q_{elec} + k_B T \left(\frac{\partial ln q_{elec}}{\partial T}\right)_{N,V} = k_B ln q_{elec} + 0 = k_B \ln (2S_M + 1) \quad (2.52)$$

Where S_M is the spin multiplicity, so that $2S_M+1$ is the degeneracy of the groundstate.

Translational contribution.

To evaluate this contribution for the partition function it is assumed that the system acts as a particle in a three-dimensional cubic box. Since in a macroscopic box the energy levels are very close the partition sum over the corresponding energy levels is substituted by an integral, for which an easier analytical expression can be found. The resulting expressions for the internal energy and the entropy are:

$$U_{trans} = \frac{3}{2} RT \quad (2.53)$$

$$S_{trans} = R \left\{ ln \left[\left(\frac{2\pi M k_B T}{h^2} \right)^{3/2} \frac{k_B T}{P} \right] + \frac{5}{2} \right\} \quad (2.54)$$

Where M is the molecular mass.

Rotational contribution.

The rotational contribution to the partition function is obtained from the energy solutions to the rigid-rotor nuclear Schrödinger equation. Then, again, an analytical expression that substitutes the integral over the rotational energy levels is used. The solutions are different for linear and not-linear molecules, since the former possess one less degree of freedom:

$$U_{rot}^{linear} = RT \quad (2.55)$$

$$S_{rot}^{linear} = R \left[ln \left(\frac{8\pi^2 I k_B T}{\sigma h^2} \right) + 1 \right] \quad (2.56)$$

$$U_{rot}^{non-linear} = \frac{3}{2} RT \quad (2.57)$$

$$S_{rot}^{non-linear} = R \left\{ ln \left[\frac{\sqrt{\pi I_A I_B I_C}}{\sigma} \left(\frac{8\pi^2 k_B T}{h^2} \right)^{3/2} \right] + \frac{3}{2} \right\} \quad (2.58)$$

Where I is the moment of inertia for the linear molecule, I_A, I_B, I_C the principal moments of inertia of the non-linear system and σ is a symmetry number that depends on the symmetry point group of the system.

Vibrational contribution.

As seen for the ZPVE and in section 2.6, vibrational contributions are obtained from the solutions to the vibrational nuclear Schrödinger equation in the harmonic approximation. Since the ZPVE has already been taken into account it must not be considered here, i.e. the energy of the zeroth vibrational energy level of each normal mode must be zero here. The resulting expressions for the vibrational contributions to the internal energy and the entropy are:

$$U_{vib} = R\sum_{i=1}^{3N-6}\frac{h\omega_i}{k_B\left(e^{h\omega_i/k_BT}-1\right)} \tag{2.59}$$

$$S_{vib} = R\sum_{i=1}^{3N-6}\left[\frac{h\omega_i}{k_B\left(e^{h\omega_i/k_BT}-1\right)} - ln\left(1-e^{-h\omega_i/k_BT}\right)\right] \tag{2.60}$$

Where the upper limit of the summation would be 3N-5 for a linear molecule.

From all of the above it can be seen that one only needs the optimized geometry of the system and the frequencies of its normal modes to calculate enthalpies or free energies from eq. 2.48 and 2.50 at the selected temperature and pressure.

2.8. Kinetics and reaction mechanism.

A *reaction mechanism* is the sequence of *elementary* i.e. single-step reactions that ultimately lead to the products of the formal chemical reaction. Elementary steps can imply adsorption/desorption processes or a chemical change of species. The former are characterized by an adsorption/desorption energy $\Delta E_{ads/des}$, whereas the latter needs an activation energy ΔE_{act}, as seen in section 2.5:

$$\Delta E_{ads} = E_{Molec/Cat} - E_{Molec} - E_{Cat} \tag{2.61}$$

$$\Delta E_{des} = -E_{Molec/Cat} + E_{Molec} + E_{Cat} \tag{2.62}$$

$$\Delta E_{act} = E_{TS} - E_R \tag{2.63}$$

Where $E_{Molec/Cat}$ is the energy of the adsorption complex of a molecule on the catalyst, E_{Molec} and E_{Cat} are those of the isolated molecule and catalyst, respectively, E_{TS} is the energy of the transition state and E_R is that of the reactants or initial state. Although the notation just employed is E for energy, it is better to employ free energies so that the entropy is accounted for, especially for adsorption/desorption processes.

The rate of a reaction (r) is defined as the velocity of disappearance or consumption of reactants or, equivalently, as the rate of appearance of products:

$$aA + bB \overset{k}{\rightarrow} cC \tag{2.64}$$

$$r = -\frac{1}{a}\frac{\delta[A]}{\delta t} = -\frac{1}{b}\frac{\delta[B]}{\delta t} = \frac{1}{c}\frac{\delta[C]}{\delta t} \tag{2.65}$$

Where k is the rate constant and concentrations can be substituted by partial pressures if the reaction is in gas phase. If eq. 2.64 were an elementary step:

$$r = k[A]^a[B]^b \tag{2.66}$$

And the rate constant can be determined using the Eyring equation, which is derived from Transition State Theory:

$$k(T) = \frac{k_B T}{h} e^{-\Delta G^{\ddagger}/RT} \tag{2.67}$$

Where $\Delta G^{\ddagger}$ is the free energy difference between the reactants and the so-called *activated complex*, the TS.

Another reaction rate analogous to eq. 2.65 and 2.66 can be defined for the opposite reaction of eq. 2.64. In this case, eq. 2.64 is called *forward* reaction and its rate constant is usually denoted k_1, while the opposite is called *reversed* or *backward* reaction, and its rate constant is denoted k_{-1}. The overall rate in the forward direction would then be given by the rate constant $K = k_1/k_{-1}$. When the rate of the forward and backward reactions are equal, an equilibrium is said to be stablished, and this K is called *equilibrium constant*.

From thermodynamics, adsorption/desorption processes are in equilibrium and their equilibrium constant can be calculated as:

$$\Delta G_{ads/des} = -RTlnK_{ads/des} \Rightarrow K_{ads/des} = e^{-\Delta G_{ads/des}/RT} \tag{2.68}$$

The total rate of the reaction will depend on the rate constants of the elementary steps, the equilibrium constants of adsorption of reactants and of desorption of products and on the concentration of all species, including the catalyst and the active sites available on it.

If a particular step has a lower rate constant than the others, it will limit the velocity of the overall reaction and will constitute the rate-determining step (rds). If there is only one clear rds, then the overall reaction may be well described by the Arrhenius equation with an *apparent* activation energy. Otherwise, a microkinetic study with different approximations may be required in order to obtain a fitting expression for the rate of the reaction in terms of reagent concentrations and rate constants.

Chapter 3
O_2 dissociation by gas phase Cu clusters

Our studies on copper clusters began with the dissociation of the O_2 molecule as a fundamental study, following the idea that although copper nanoparticles deactivate soon in their application to oxidation reactions, small clusters may behave differently and be potentially good catalysts for these reactions.

Since there are computational difficulties in the calculations of systems with transition metals, we used this very first study to, in addition, provide a comparison for copper of a few approaches with orbital-based wavefunctions and planar wavefunctions, by employing both the Gaussian and VASP codes.

In the present chapter we have gathered this study[68] and the subsequent work on the dissociation of the molecule in the presence of water, including a collaboration with other colleague researchers at the ITQ, who were able to synthesize and characterize small Cu clusters, and whose experimental results corroborated ours[107].

3.1. Introduction.

Copper nanoparticles are good catalysts for important industrial processes such as alcohol synthesis[194,195], water gas shift[196], deoxygenation of biomass-derived molecules[197], selective alkyne hydrogenation[198], or CO electroreduction to liquid fuels[199] and, as mentioned in section 1.3, some publications have appeared of late reporting improved catalytic performance of subnanometer Cu clusters[37]. The scientific interest in the catalytic properties of copper clusters has increased in the last years[200,201], and several quantum chemical studies concerning the structure and electronic properties of small copper clusters, in some cases combined with photoelectron spectroscopy measurements, can be found in the literature[67,69,72,202,203].

When we published the first paper corresponding to this chapter[68], reports on the reactivity of naked gas phase copper clusters were limited to the interaction of CO and O_2 with Cu_n clusters with $n \leq 10$ atoms and the dissociative chemisorption of H_2 on Cu_n clusters of up to 15 atoms[204-210]. Similarly, regarding mechanistic studies, only the dissociation of H_2O on Cu_7[211] and the mechanism of CO oxidation on Cu_6 and Cu_7 clusters[212] were reported in the literature. Since then, a few more studies have been published on the interaction with NO[213], CO_2[214,215], NO_2 and SO_2[216], CH_4 and CH_3[217,218], as well as mechanistic studies on the acetylene selective hydrogenation[219], CO_2 hydrogenation to methanol[220], syngas conversion[221] and the N_2O + CO reaction[222]. However, with the remarkable exception of the latter, the sizes studied in each work are few, and thus the evolution of the reactivity of gas phase clusters with their atomicity has been less investigated.

The activation of molecular O_2 with metal particles and clusters is a most relevant case hence widely studied. In a sustainable chemistry context, the possibility to carry out oxidation reactions using molecular O_2 as the oxidant species, and generating water as the only byproduct, is one of the great challenges of catalysis. In addition, larger copper-based catalysts have shown good initial catalytic activity in the selective oxidation of CO in fuel cells and in the selective epoxidation of alkenes, but the activity is rapidly lost as the material oxidizes[223,224] (see also Chapter 4). The potentially different behavior of smaller clusters in the same situations is appealing and further motivated the studies of this chapter. Thus, we carried out a systematic theoretical study of O_2 adsorption and dissociation on Cu_n clusters with n=3-8, 13, and 38 atoms, this last model being considered here the size limit between clusters and nanoparticles, with the objective of finding a trend with particle size in the reactivity of copper clusters for oxidation reactions.

In addition, we wanted to address the methodological issue that exists in the study of metal clusters of increasing size, related to the scaling of the computational cost with the number of electrons in the system. Density functional theory (DFT) based methods are usually chosen because they provide reasonable accuracy at a relatively

moderate computational cost. However, the cost of a DFT calculation based on atom-centered Gaussian orbitals scales with N^3, being N the number of functions in the basis set[225-227]. This means that even when using effective core potentials (ECP) to account for the core electrons of transition metals instead of an all-electron basis set, a limit will be eventually reached from which further increasing the system size is impractical. A different approach consists of performing periodic calculations in which the isolated clusters or nanoparticles are placed in a unit cell that is periodically repeated in the three dimensions of space, and that employ plane wave basis sets within a reciprocal space representation that lead to a reduction in the computational scaling to N^2 or even N[22,24,178]. A key advantage of this approach is that small, intermediate size and large transition metal clusters or nanoparticles, as well as the upper size limit represented by extended surfaces, can be studied using a single methodology[228-230]. However, its accuracy when describing molecular systems may be lower than that of DFT methods using atom-centered functions as basis sets. On the other hand, it is not clear whether the results obtained employing both methodological approaches can be directly compared without any other consideration. For these reasons, the subject that we wanted to investigate, i.e. the adsorption and dissociation of molecular O_2 on copper clusters of increasing size, was carried our using both atom-centered Gaussian-type orbitals in molecular calculations and plane-wave basis sets in periodic calculations[68].

Soon after this first study, Dr. Patricia Concepción and Dr. Saray García, fellow researchers at the ITQ, were able to synthesize very small clusters of copper of specific sizes. To aid with the characterization and to confirm their experimental results, we revisited our previous results and continued our research by studying the effect of water on copper clusters of selected sizes[107].

3.2. Computational details.

3.2.1. Models.

The initial systematic theoretical study of O_2 adsorption and dissociation was carried out on Cu_n clusters with n=3-8, 13, and 38 atoms, whereas only certain cluster sizes were selected for the upcoming studies. The first n=3-8 series is sufficiently small to be simulated by atom-centered basis sets, whereas n=13 is a more case limit for that methodology and the last size model was only affordable at a periodic level, added to the study as the size limit between clusters and nanoparticles.

The initial models for the copper clusters were built *ad hoc*, following the reports already available in the literature for copper and also for silver and gold clusters. Several isomers were optimized for the n=3-8 series, but for Cu_{13} and Cu_{38} only the cuboctahedral isomers of Cu_{13} and Cu_{38} (and a more stable yet irregular isomer for Cu_{13}) were considered.

Similarly, for each atomicity –or even isomer- of the copper clusters, the different unequivalent adsorption modes for all the pertinent molecules were also considered *ad hoc* and from literature results when available.

3.2.2. Methods.

Molecular calculations based on atom-centered Gaussian orbitals were performed with the Gaussian 09 program package[19], while the Vienna Ab-initio Simulation Package (VASP)[22,231] was used for periodic calculations with plane-wave basis sets.

All calculations in this chapter are based on density functional theory (DFT). The functional by Perdew and Wang within the gradient corrected approach (GGA) was chosen to perform the computational study[159]. Periodic calculations were carried out with the PW91 exchange-correlation functional as implemented in the VASP code, and are labelled as p-PW91 throughout the manuscript[157]. In molecular calculations using the Gaussian software, the equivalent approach consists of combining the PW91 correlation functional with the B88 exchange functional by Becke[232] and is labelled as BPW91. Since hybrid functionals that include a certain amount of the exact Hartree-Fock exchange are usually chosen due to their superior performance and improved accuracy[226,227], Becke's hybrid three-parameter exchange functional[160] in combination with the PW91 correlation functional was also used in the study of section 3.3.1, and the method is labelled as B3PW91.

In the case of molecular calculations using atom-centered Gaussian orbitals, to correctly simulate the system behavior it is crucial to select a sufficiently large basis set. Thus, the standard 6-311+G(d,p) basis set by Pople was always used for non-copper atoms[233]. For Cu atoms, the all-electron triple zeta (TZ) 6-311+G(d,p) Watchers-Hay basis set[171,172] with added polarized and diffuse functions, was selected as reference for benchmark calculations with other less expensive basis sets, namely the LANL2DZ and the Def2TZVP sets. The LANL2DZ basis set combines Los Alamos effective core potential with a double zeta (DZ) set for valence electrons, and it is widely used for transition metals due to its low computational cost[175,176]. The Def2TZVP basis set constitutes a relatively recent reformulation of the split-valence triple zeta basis set (TZVP) from Ahlrichs and co-workers, and it has been reported to be close to the basis set limit for DFT calculations[173,174]. In section 3.3.1 a comparative study of the three basis sets was performed using the hybrid B3PW91 functional, and the data obtained are labelled as B3PW91/6-311+G(d,p), B3PW91/LANL2DZ and B3PW91/Def2TZVP, respectively. As it will be shown in the same section, the B3PW91/Def2TZVP was the level of theory chosen for future calculations with the Gaussian code, i.e. those of the following sections.

In the periodic calculations using the VASP code, the valence density was expanded in a plane wave basis set with a kinetic energy cutoff of 450 eV, and the effect of the core electrons in the valence density was taken into account by means of the projected augmented wave (PAW) formalism[178]. The copper clusters and O_2 molecules were placed in a 20x20x20 $Å^3$ cubic box, large enough to avoid spurious interactions between periodically repeated clusters or adsorbates, and integration in the reciprocal space was carried out at the Γ k-point of the Brillouin zone.
In all cases the positions of all atoms in the system were fully optimized without any restriction. Regarding spin, the periodic calculations with VASP program were always spin polarized, while for molecular calculations using the Gaussian code the two lowest possible multiplicities for each system were always considered. In addition, all stationary points were characterized by pertinent frequency calculations, which were obtained numerically for VASP calculations. When using the Gaussian code, transition states were determined through potential energy surface (PES) scans along with the subsequent optimizations, whereas the DIMER algorithm[185,186] was employed to locate transition states with VASP. Atomic charges and molecular orbital distributions were calculated using the natural bond order (NBO) approach[188]. The Basis Set Superposition Error (BSSE) in molecular calculations was determined using the counterpoise method[234] and dispersion interactions were taken into account by means of the B97D functional[161].

3.3. Results.

3.3.1. O_2 dissociation and comparison of methodologies.

3.3.1.1. Isolated copper clusters.

In general, different isomers with energies close to the ground state structures are usually found for metal clusters, especially as the particle size increases. The equilibrium geometries of the lowest energy isomers of Cu_n clusters with $3 \leq n \leq 8$, and their relative stability at the different levels of calculation considered in this work are shown in Figure 3.1, together with the optimized structures of the cuboctahedral isomers of Cu_{13} and Cu_{38}, and a more stable *distorted* Cu_{13} system. The planar structure for Cu_7 was included to confirm the size at which copper clusters become preferentially three-dimensional, although it is not the third most stable structure for this atomicity. The lowest spin multiplicity, that is, singlet for even values of n and doublet for odd values of n, was found to be the most stable at each cluster size.
The corresponding relative energies and average Cu-Cu bond distances at all the theoretical levels are collected in Table 3.1. In agreement with previous studies[67,69,72,202,203], all methods indicate that planar (2D) isomers are the most stable up to n = 6, and three-dimensional (3D) structures are clearly preferred for clusters containing 7 or more atoms. For Cu_4, Cu_6 and Cu_7 clusters, the difference in energy between the two most stable isomers for each atomicity does not depend on the theoretical method used, with relative energies differing by less than 1.5 kcal mol^{-1}.

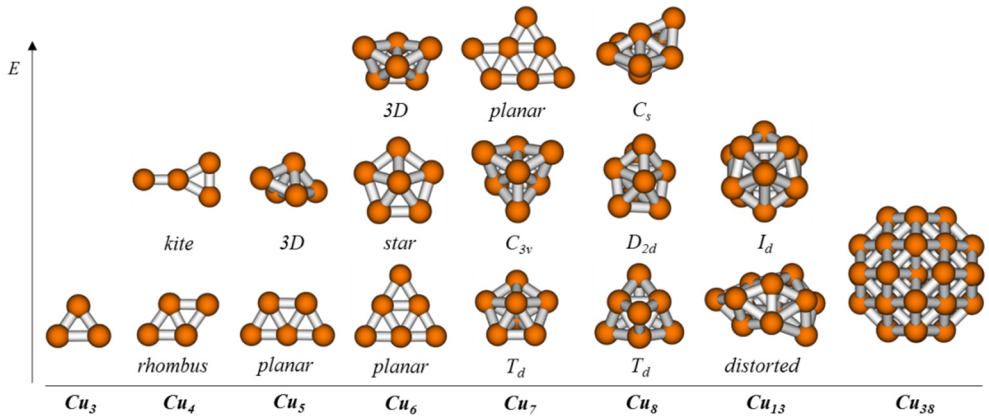

Figure 3.1. Optimized structures of the lowest energy isomers of Cu_n clusters with n = 3-8, 13 and 38.

Table 3.1. Relative electronic energies (in kcal mol^{-1}) and average Cu-Cu bond distances of the isolated copper clusters at all the theoretical levels studied, namely, B3PW91/6-311+G(d,p) (TZ), B3PW91/LANL2DZ (LANL2DZ), B3PW91/Def2-TZVP (Def2TZVP), BPW91/Def2TZVP (BPW91) and periodic PW91 (p-PW91).

		TZ		LANL2DZ		Def2TZVP		BPW91		p-PW91	
Size	Geometry	ΔE_{rel}	$R_{Cu,av}$	ΔE_{rel}	$R_{Cu,av}$	ΔE_{rel}	$R_{Cu,av}$	ΔE_{rel}	$R_{Cu,av}$	ΔE_{rel}	$R_{Cu,av}$
Cu_3		0.00	2.42	0.00	2.45	0.00	2.43	0.00	2.40	0.00	2.36
Cu_4	*rhombus*	0.00	2.40	0.00	2.42	0.00	2.41	0.00	2.39	0.00	2.35
	kite	7.77	2.37	7.56	2.39	8.34	2.39	8.90	2.36	8.91	2.32
Cu_5	*planar*	0.00	2.41	0.00	2.43	0.00	2.42	0.00	2.40	0.00	2.36
	3D	7.38	2.46	9.86	2.50	7.08	2.46	5.16	2.45	6.25	2.41
Cu_6	*planar*	0.00	2.41	0.00	2.43	0.00	2.42	0.00	2.40	0.00	2.36
	star	2.67	2.44	3.44	2.46	2.53	2.45	2.47	2.43	3.14	2.39
	3D	8.02	2.46	10.99	2.50	7.36	2.47	4.83	2.45	6.57	2.42
Cu_7	T_d	0.00	2.46	0.00	2.50	0.00	2.46	0.00	2.45	0.00	2.43
	C_{3v}	4.89	2.45	4.44	2.49	5.16	2.46	5.61	2.44	4.94	2.42
	planar	23.13	2.42	20.24	2.44	24.33	2.43	26.56	2.41	24.24	2.37
Cu_8	T_d	0.00	2.46	0.00	2.50	0.00	2.47	0.00	2.46	0.00	2.42
	D_{2d}	1.76	2.46	1.06	2.50	1.95	2.47	-0.18	2.46	-0.96	2.42
	C_s	2.54	2.48	3.80	2.52	2.08	2.48	2.81	2.47	-0.88	2.42
Cu_{13}	*distorted*	0.00	2.53	0.00	2.57	0.00	2.54	0.00	2.59	0.00	2.46
	I_d	15.58	2.52	15.34	2.55	15.16	2.51	15.76	2.50	23.31	2.47

In other cases, however, the influence of the computational level employed is non-negligible. Thus, for Cu_5 and Cu_6, the difference in energy between the 2D and 3D isomers (notice that the second most stable isomer of Cu_6, labelled Cu_6-star, is not absolutely planar, but it is composed by one layer of atoms and therefore we do not consider it 3D) is slightly larger when the hybrid B3PW91 functional is used, with the largest deviation being obtained with the less accurate LANL2DZ basis set. In the case of the Cu_8 cluster the order of stability of the two lowest energy isomers is reversed when some Hartree-Fock exchange is included in the hybrid functional, although the difference in stability between them is less than 3 kcal mol^{-1} in all cases. It is important to remark that the co-existence of both isomers is supported by experimental results by Lecoultre et al.[72], who showed that both isomers contribute to the measured UV-visible absorption spectra of Cu_8. As regards the difference between molecular and periodic calculations, the most remarkable result is the larger stabilization of the irregular Cu_{13} structure at the p-PW91 level.

Also consistent with the previous studies mentioned, the average Cu-Cu distances are clearly shorter for planar clusters and increase as systems become 3D, for the coordination of the atoms increases (Figure 3.2a).

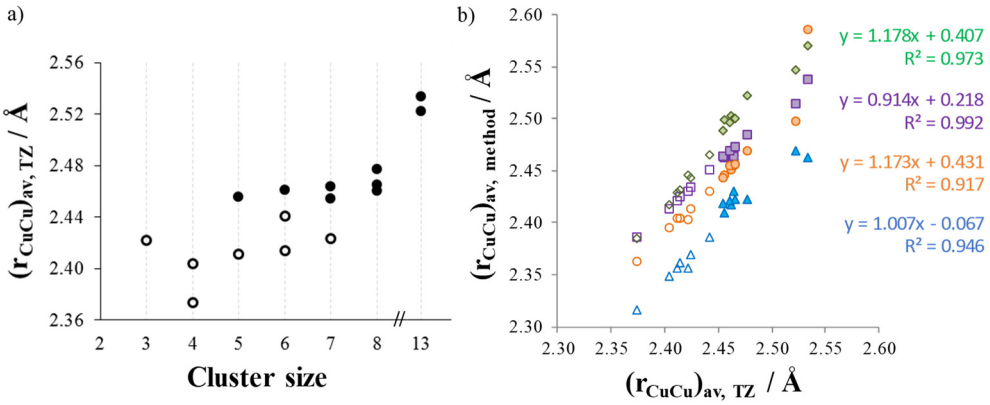

Figure 3.2. a) Average Cu-Cu distances (in Å) per size of gas phase clusters at the B3PW91/6-311+G(d,p) level and b) same distances (in Å) at all computational levels considered (B3PW91/LANL2DZ (green diamonds), B3PW91/Def2TZVP (purple squares), BPW91/Def2TZVP (orange circles) and p-PW91 (blue triangles)) against those obtained with the reference method B3PW91/6-311+G(d,p). The respective regression lines are shown. Empty points correspond to planar clusters.

In order to compare the optimized geometries further, the average Cu-Cu distance in each cluster at the several computational levels considered in this work was plotted in Figure 3.2b against the same parameter obtained with the reference B3PW91/6-311+G(d,p) method. In all cases a linear relationship is clearly observed. While the

best correlation is found at the B3PW91/Def2TZVP level, the slope is in turn best for the p-PW91 method. Non-hybrid methods yield systematically shorter Cu-Cu distances, a trend that is more pronounced in the case of periodic p-PW91 calculations. The only exception corresponds to the irregular Cu_{13} cluster at the BPW91/Def2TZVP level, and is due to the fact that the optimized structure at this level is not exactly equivalent to those obtained with the other methods. It is important to remark that the average Cu-Cu distances are clearly shorter for planar clusters, and increase as systems become 3D.

3.3.1.2. O_2 adsorption and activation.

The optimized structures of the most stable adsorption complexes formed by interaction of molecular O_2 with Cu_n copper clusters with n = 3-8 are depicted in Figure 3.3, and the most relevant parameters describing this interaction (adsorption energies, optimized O-O bond lengths, O-O vibrational frequencies and net charge transferred to O_2) computed at the B3PW91/6-311+G(d,p) level are summarized in Table 3.2. The corresponding values obtained at the B3PW91/LANL2DZ, B3PW91/Def2TZVP, BPW91/Def2TZVP and p-PW91 levels of theory are listed in the analogous Tables 3.3-3.6.

Adsorption of molecular O_2 over copper clusters leads to several different types of complexes (Figure 3.3). In the case of small planar clusters, and in a similar way to what was previously found for gold and silver[28,128,235], O_2 interaction preferentially occurs at their edges and corners, and the possible adsorption modes are labeled as *mono*, when only one bond is formed between a O atom of molecular O_2 and a low coordinated Cu atom (see structure **10** for instance); *top*, when the two O atoms of molecular O_2 are directly attached to the same low coordinated Cu atom (as in structure **2**), and *bridge*, when each of the two O atoms in the molecule is directly attached to one Cu atom in the cluster (structure **1**). In the case of 3D copper clusters (and nanoparticles), O_2 can also occupy hollow positions on the (111) and (100) facets, and the complexes obtained are labeled according to the facet where they adsorb: *h-111* or *h-100* (see structures **12** and **28**, respectively, for instance).

In agreement with a previous study by Yuan et al.[208], the *bridge* conformation is the most stable for planar Cu_3, Cu_4 and Cu_5 clusters, (structures **1, 3, 7-9** in Figure 3.3), followed by *top* (structures **2** and **4**) and *mono* modes (structures **5** and **10**), and the interaction is stronger with the clusters having an odd number of electrons (Cu_3 and Cu_5). Thus, the calculated adsorption energies at the B3PW91/6-311+G(d,p) level are larger than -37 kcal mol^{-1} for the most stable *bridge* conformers on Cu_3 and Cu_5, and significantly lower, -21 kcal mol^{-1}, for the *bridge* conformation on Cu_4 (see Table 3.2). When O_2 was initially placed above the planar Cu_4 cluster, geometry optimization without any restriction led to structure **6**, which corresponds to O_2 adsorbed on a 111 facet of a tetrahedral Cu_4 cluster, adopting the *h-111* conformation. This

complex is only 1,6 kcal mol^{-1} less stable than structure **3**. It was not possible however to optimize the geometry of the 3D Cu_4 cluster in the absence of an adsorbed O_2 molecule, and all attempts finally ended in the most stable planar isomer shown in Figure 3.1. As mentioned in the computational details section, two spin states were initially considered for each adsorption complex. A doublet state was found to be the most stable for all structures obtained by adsorption of O_2 on planar Cu_3 and Cu_5, but in the case of Cu_4 a triplet state was found for O_2 adsorbed on the 2D cluster while structure **6** was obtained as singlet.

The interaction of molecular O_2 with the two bi-dimensional isomers of Cu_6 (structures **14-17** in Figure 3.3) is really weak, with calculated adsorption energies lower than -5 kcal mol^{-1} (see Table 3.2). In these systems molecular O_2 adsorbs on low coordinated copper atoms of Cu_6 adopting a *mono* conformation, except in structure **15** in which a *bridge* complex is formed and a small deformation of the cluster geometry occurs. The most stable spin state for these four structures is triplet.

When 3D structures are considered for Cu_5 and Cu_6, the *h-111* adsorption mode is obtained, in which one O atom is directly attached to a copper atom and the other O atom is occupying a bridge position between two copper atoms (see structures **12** and **18** in Figure 3.3). The *h-111* complex is 3.5 kcal mol^{-1} less stable than the *bridge* mode on Cu_5,and 5 kcal mol^{-1} more stable than the *bridge* mode on Cu_6. Moreover, the formation of three Cu-O bonds in structure **18** modifies its electronic distribution and the most stable spin state is singlet, in agreement with Yuan et al.[208].

As the atomicity of the clusters increases, the number of adsorption complexes with similar stability becomes larger, and the calculated adsorption energy values decrease. Thus, six different adsorption complexes with interaction energies ranging from -21 to -7 kcal mol^{-1} are shown for Cu_7 (structures **22** to **27** in Figure 3.3), all of them doublet in nature. The most stable systems involve O_2 adsorbed in a *bridge* mode, either on top of the cluster or at its edge, followed by a *h-111* conformer, and *mono* or *top* modes at different positions.

In the case of the Cu_8 cluster we initially considered the adsorption of O_2 at different positions on the two most stable Cu_8 isomers described before, whose co-existence has been experimentally demonstrated as already mentioned[72]. However, the formation of copper-oxygen bonds modifies the geometry of the metal clusters in such a way that it is not always possible to clearly identify the initial structure of the isolated Cu_8 cluster. Therefore, only six stable adsorption complexes with interaction energies ranging between -16 and -10 kcal mol^{-1}, some of them previously reported by Yuan et al.[208], are described here (structures **28** to **33** in Figure 3.3). In the most stable system obtained (structure **28**), each of the two oxygen atoms in O_2 molecule is directly attached to two Cu atoms that are situated forming the square planar arrangement characteristic of the (100) facet, labeled as *h-100*. Structure **29**, with O_2 adsorbed on a (111) facet of the cluster, is less than 1 kcal mol^{-1} higher in energy.

The calculated adsorption energies obtained for structures **30** to **33**, in which O_2 adopts either *h-111* or *bridge* conformations, differ by less than 2 kcal mol^{-1} (see Table 3.2), suggesting that several different adsorption geometries may co-exist on 3D copper clusters. It is important to remark that while the most stable spin state for all *bridge* conformers formed on Cu_8 is triplet, the *h-111* and *h-100* modes lead to a singlet spin state of the system.

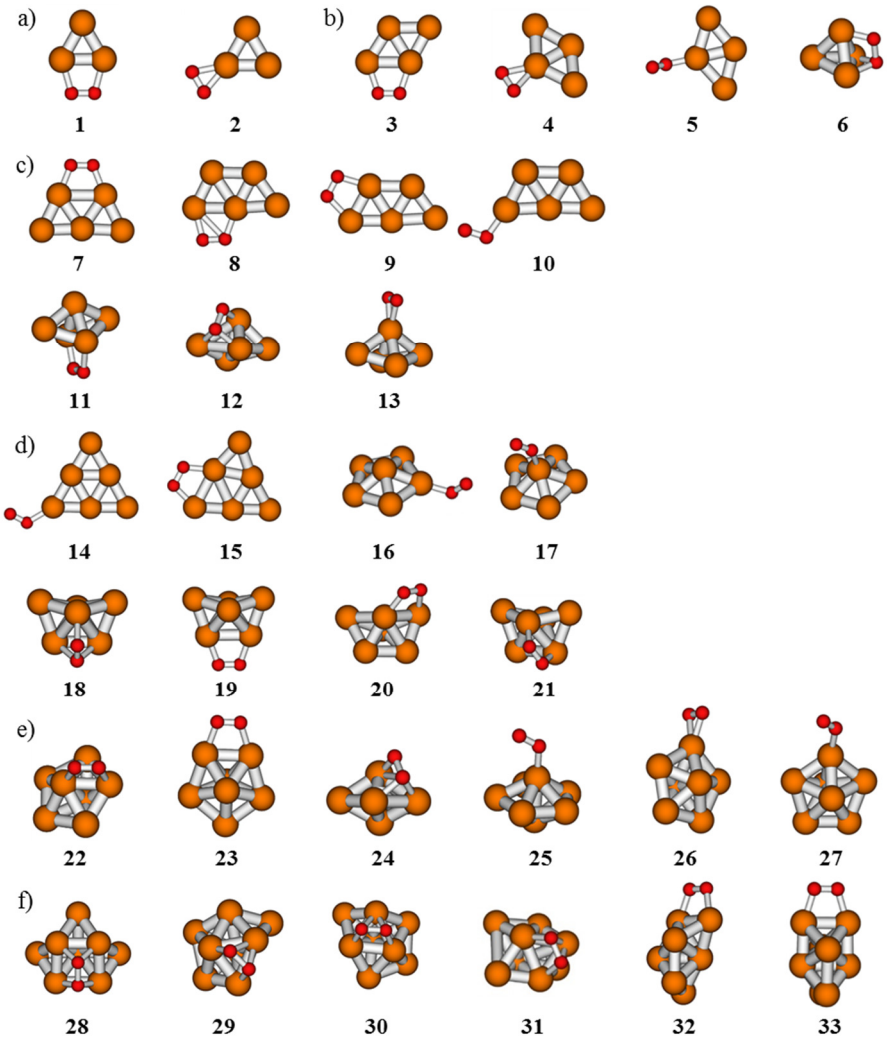

Figure 3.3. Optimized structures for the adsorption of one O_2 molecule on a) Cu_3, b) Cu_4, c) Cu_5, d) Cu_6, e) Cu_7 and f) Cu_8 clusters.

Table 3.2. Calculated values at the B3PW91/6-311+G(d,p) level of theory of the most relevant parameters describing the interaction of molecular O_2 with Cu_n (n = 3-8) clusters, namely, adsorption mode, energy of adsorption (ΔE_{ads}), O-O bond length (r_{OO}), O-O vibration frequency (ν_{OO}) and net charge transferred to O_2 (qO_2).

Cluster atomicity	Structure (Fig. 3.3)	Adsorption Mode	ΔE_{ads} (kcal mol^{-1})	r_{OO} (Å)	ν_{OO} (cm^{-1})	qO_2 (e$^-$)
Cu_3	1	*Bridge*	-38.4	1.323	1171	-0.684
	2	*Top*	-29.0	1.320	1172	-0.564
Cu_4	3	*bridge*	-21.2	1.326	1157	-0.673
	4	*Top*	-13.9	1.291	1217	-0.385
	5	*mono*	-10.2	1.242	1317	-0.248
	6	*h-111*	-19.6	1.481	778	-1.283
Cu_5	7	*bridge*	-37.2	1.330	1172	-0.692
	8	*bridge*	-24.0	1.331	1164	-0.765
	9	*bridge*	-13.1	1.316	1166	-0.644
	10	*mono*	-10.7	1.273	1213	-0.426
Cu_5-3D	11	*bridge*	-22.5 (-29.9)[a]	1.315	1183	-0.602
	12	*h-111*	-19.0 (-26.4) [a]	1.467	763	-1.210
	13	*Top*	-15.1 (-22.5) [a]	1.310	1173	-0.460
Cu_6	14	*mono*	-4.5	1.234	1383	-0.201
	15	*bridge*	-3.1	1.325	1158	-0.671
Cu_6-star	16	*mono*	-2.4 (-5.0)[b]	1.238	1353	-0.230
	17	*mono*	-0.8 (-3.4) [b]	1.219	1476	-0.056
Cu_6-3D	18	*h-111*	-22.7 (-30.7) [a]	1.479	779	-1.198
	19	*bridge*	-17.3 (-25.4) [a]	1.330	1172	-0.651
	20	*bridge*	-14.7 (-22.7) [a]	1.326	1168	-0.641
	21	*bridge*	-10.8 (-18.8) [a]	1.318	1161	-0.599
Cu_7	22	*bridge*	-20.6	1.323	1180	-0.618
	23	*bridge*	-18.2	1.324	1185	-0.678
	24	*h-111*	-15.1	1.413	788	-0.958
	25	*mono*	-12.8	1.283	1167	-0.463
	26	*Top*	-9.9	1.300	1172	-0.452
	27	*mono*	-6.8	1.254	1248	-0.333
Cu_8	28	*h-100*	-16.3	1.521	720	-1.346
	29	*h-111*	-15.6	1.514	756	-1.241
	30	*h-111*	-11.9	1.487	784	-1.191
	31	*h-111*	-11.4	1.502	770	-1.218
	32	*bridge*	-11.1	1.320	1166	-0.641
	33	*bridge*	-10.3	1.318	1154	-0.634

[a]Values in parenthesis have been calculated with respect to the Cu_n-3D isomer.
[b]Values in parenthesis have been calculated with respect to the Cu_6-star isomer.

Table 3.3. Calculated values at the B3PW91/LANL2DZ level of theory of the most relevant parameters describing the interaction of molecular O_2 with Cu_n (n = 3-8) clusters, namely, adsorption mode, energy of adsorption (ΔE_{ads}), O-O bond length (r_{OO}), O-O vibration frequency (ν_{OO}) and net charge transferred to O_2 (qO_2).

Cluster atomicity	Structure (Fig. 3.3)	Adsorption Mode	ΔE_{ads} (kcal mol^{-1})	r_{OO} (Å)	ν_{OO} (cm^{-1})	qO_2 (e$^-$)
Cu_3	1	*Bridge*	-39.4	1.318	1188	-0.678
	2	*Top*	-27.9	1.318	1169	-0.575
Cu_4	3	*bridge*	-21.1	1.320	1171	-0.780
	4	*Top*	-13.8	1.285	1228	-0.380
	5	*mono*	-10.6	1.241	1323	-0.257
	6	*h-111*	-17.4	1.461	803	-1.247
Cu_5	7	*bridge*	-36.6	1.326	1192	-0.761
	8	*bridge*	-24.0	1.327	1181	-0.754
	9	*bridge*	-13.3	1.310	1174	-0.625
	10	*mono*	-10.7	1.265	1247	-0.396
Cu_5-3D	11	*bridge*	-[c]	-[c]	-[c]	-[c]
	12	*h-111*	-[c]	-[c]	-[c]	-[c]
	13	*Top*	-11.8 (-21.6)[a]	1.307	1170	-0.466
Cu_6	14	*mono*	-5.0	1.229	1413	-0.182
	15	*bridge*	-2.4	1.317	1161	-0.656
Cu_6-star	16	*mono*	-2.3 (-5.8)[b]	1.234	1382	-0.207
	17	*mono*	-1.4 (-4.9)[b]	1.215	1501	-0.043
Cu_6-3D	18	*h-111*	-19.6 (-30.6)[a]	1.465	800	-1.182
	19	*bridge*	-14.0 (-25.0)[a]	1.327	1190	-0.715
	20	*bridge*	-11.9 (-22.9)[a]	1.322	1182	-0.640
	21	*bridge*	-9.4 (-20.4)[a]	1.310	1169	-0.584
Cu_7	22	*bridge*	-21.6	1.320	1191	-0.624
	23	*bridge*	-17.5	1.320	1199	-0.674
	24	*h-111*	-[c]	-[c]	-[c]	-[c]
	25	*mono*	-13.6	1.276	1188	-0.441
	26	*Top*	-9.5	1.289	1193	-0.430
	27	*mono*	-7.3	1.248	1278	-0.305
Cu_8	28	*h-100*	-14.8	1.508	754	-1.327
	29	*h-111*	-12.7	1.508	764	-1.241
	30	*h-111*	-9.0	1.478	794	-1.181
	31	*h-111*	-[c]	-[c]	-[c]	-[c]
	32	*bridge*	-10.0	1.314	1172	-0.625
	33	*bridge*	-9.8	1.310	1152	-0.604

[a]Values in parenthesis have been calculated with respect to the Cu_n-3D isomer.
[b]Values in parenthesis have been calculated with respect to the Cu_6-star isomer.
[c]Structure not found at this level of theory.

Table 3.4. Calculated values at the B3PW91/Def2TZVP level of theory of the most relevant parameters describing the interaction of molecular O_2 with Cu_n (n = 3-8) clusters, namely, adsorption mode, energy of adsorption (ΔE_{ads}), O-O bond length (r_{OO}), O-O vibration frequency (ν_{OO}) and net charge transferred to O_2 (qO_2).

Cluster atomicity	Structure (Fig. 3.3)	Adsorption mode	ΔE_{ads} (kcal mol^{-1})	r_{OO} (Å)	ν_{OO} (cm^{-1})	qO_2 (e$^-$)
Cu_3	1	*bridge*	-38.6	1.321	1177	-0.686
	2	*top*	-28.8	1.319	1172	-0.572
Cu_4	3	*bridge*	-20.9	1.324	1160	-0.675
	4	*top*	-13.8	1.290	1220	-0.400
	5	*mono*	-9.9	1.242	1313	-0.271
	6	*h-111*	-19.3	1.481	778	-1.281
Cu_5	7	*bridge*	-36.6	1.330	1173	-0.693
	8	*bridge*	-23.7	1.330	1167	-0.776
	9	*bridge*	-12.9	1.315	1167	-0.647
	10	*mono*	-10.3	1.270	1223	-0.428
Cu_5-3D	11	*bridge*	-23.0 (-30.0)[a]	1.314	1197	-0.614
	12	*h-111*	-18.7 (-25.8)[a]	1.468	762	-1.199
	13	*top*	-15.4 (-22.5)[a]	1.310	1172	-0.480
Cu_6	14	*mono*	-4.4	1.231	1396	-0.201
	15	*bridge*	-2.9	1.324	1161	-0.765
Cu_6-star	16	*mono*	-2.4 (-5.0)[b]	1.237	1363	-0.240
	17	*mono*	-0.9 (-3.4)[b]	1.217	1487	-0.078
Cu_6-3D	18	*h-111*	-22.8 (-30.2)[a]	1.476	781	-1.190
	19	*bridge*	-17.9 (-25.3)[a]	1.330	1174	-0.656
	20	*bridge*	-15.4 (-22.7)[a]	1.325	1171	-0.647
	21	*bridge*	-11.4 (-18.7)[a]	1.317	1161	-0.608
Cu_7	22	*bridge*	-20.4	1.322	1180	-0.629
	23	*bridge*	-18.2	1.323	1187	-0.674
	24	*h-111*	-14.7	1.403	819	-0.925
	25	*mono*	-12.6	1.281	1173	-0.486
	26	*top*	-10.1	1.298	1176	-0.660
	27	*mono*	-6.7	1.252	1254	-0.345
Cu_8	28	*h-100*	-15.5	1.520	723	-1.307
	29	*h-111*	-15.2	1.514	754	-1.217
	30	*h-111*	-11.5	1.486	784	-1.163
	31	*h-111*	-10.5	1.502	770	-1.192
	32	*bridge*	-11.5	1.319	1168	-0.639
	33	*bridge*	-10.4	1.317	1194	-0.629

[a]Values in parenthesis have been calculated with respect to the Cu_n-3D isomer.
[b]Values in parenthesis have been calculated with respect to the Cu_6-star isomer.

Table 3.5. Calculated values at the BPW91/Def2TZVP level of theory of the most relevant parameters describing the interaction of molecular O_2 with Cu_n (n = 3-8) clusters, namely, adsorption mode, energy of adsorption (ΔE_{ads}), O-O bond length (r_{OO}), O-O vibration frequency (ν_{OO}) and net charge transferred to O_2 (qO_2).

Cluster atomicity	Structure (Fig. 3.3)	Adsorption mode	ΔE_{ads} (kcal mol^{-1})	r_{OO} (Å)	ν_{OO} (cm^{-1})	qO_2 (e$^-$)
Cu_3	1	*bridge*	-41.7	1.357	1002	-0.662
	2	*Top*	-33.7	1.342	1084	-0.499
Cu_4	3	*bridge*	-24.1	1.359	969	-0.631
	4	*Top*	-18.1	1.317	1137	-0.370
	5	*mono*	-17.1	1.274	1239	-0.300
	6	*h-111*	-23.5	1.511	664	-1.170
Cu_5	7	*bridge*	-39.4	1.375	973	-0.692
	8	*bridge*	-26.4	1.371	979	-0.661
	9	*bridge*	-17.9	1.338	1027	-0.556
	10	*mono*	-17.7	1.294	1178	-0.402
Cu_5-3D	11	*bridge*	-27.5 (-32.6)[a]	1.342	1034	-0.560
	12	*h-111*	-25.2 (-30.4)[a]	1.496	673	-1.071
	13	*Top*	-22.5 (-27.6)[a]	1.332	1102	-0.403
Cu_6	14	*mono*	-11.7	1.270	1260	-0.285
	15	*bridge*	-8.7	1.318	1052	-0.448
Cu_6-star	16	*mono*	-10.2 (-12.6)[b]	1.274	1244	-0.317
	17	*mono*	-7.3 (-9.8)[b]	1.260	1291	-0.199
Cu_6-3D	18	*h-111*	-29.4 (-34.2)[a]	1.500	687	-1.060
	19	*bridge*	-23.0 (-27.8)[a]	1.373	980	-0.644
	20	*bridge*	-20.7 (-25.5)[a]	1.358	981	-0.599
	21	*bridge*	-16.4 (-21.3)[a]	1.341	1009	-0.534
Cu_7	22	*bridge*	-22.8	1.355	1010	-0.595
	23	*bridge*	-20.6	1.355	1028	-0.641
	24	*h-111*	-21.4	1.467	699	-0.945
	25	*mono*	-18.3	1.292	1174	-0.403
	26	*Top*	-15.9	1.322	1120	-0.404
	27	*mono*	-14.1	1.279	1214	-0.345
Cu_8	28	*h-100*	-18.2	1.610	494	-1.256
	29	*h-111*	-21.5	1.562	622	-1.120
	30	*h-111*	-18.1	1.521	673	-1.061
	31	*h-111*	-16.3	1.546	646	-1.095
	32	*bridge*	-16.6	1.341	1016	-0.553
	33	*bridge*	-16.5	1.329	1037	-0.493

[a]Values in parenthesis have been calculated with respect to the Cu_n-3D isomer.
[b]Values in parenthesis have been calculated with respect to the Cu_6-star isomer.

Table 3.6. Calculated values at the p-PW91 level of theory of the most relevant parameters describing the interaction of molecular O_2 with Cu_n (n = 3-8) clusters, namely, adsorption mode, energy of adsorption (ΔE_{ads}), O-O bond length (r_{OO}), O-O vibration frequency (ν_{OO}) and net charge transferred to O_2 (qO_2).

Cluster atomicity	Structure (Fig. 3.3)	Adsorption mode	ΔE_{ads} (kcal mol^{-1})	r_{OO} (Å)	ν_{OO} (cm^{-1})	qO_2 (e$^-$)
Cu_3	1	*bridge*	-50.9	1.376	966	-0.695
	2	*top*	-41.9	1.351	1099	-0.574
Cu_4	3	*bridge*	-32.5	1.376	943	-0.671
	4	*top*	-24.1[c]	1.330	1151	-0.481
	5	*mono*	-20.5	1.269	1212	-0.431
	6	*h-111*	-30.6	1.515	669	-1.049
Cu_5	7	*bridge*	-49.4	1.393	939	-0.751
	8	*bridge*	-34.7	1.399	944	-0.729
	9	*bridge*	-26.2	1.332	1008	-0.610
	10	*mono*	-24.5	1.288	1181	-0.442
Cu_5-3D	11	*bridge*	-34.1 (-40.4)[a]	1.360	1011	-0.630
	12	*h-111*	-33.2 (-39.5)[a]	1.504	674	-1.032
	13	*top*	-28.5 (-34.7)[a]	1.340	1129	-0.530
Cu_6	14	*mono*	-17.4	1.287	1261	-0.373
	15	*bridge*	-17.1	1.340	1024	-0.583
Cu_6-star	16	*mono*	-15.1 (-18.2)[b]	1.292	1247	-0.401
	17	*mono*	-11.8 (-15.0)[b]	1.276	1301	-0.333
Cu_6-3D	18	*h-111*	-33.2 (-39.8)[a]	1.552	695	-1.063
	19	*bridge*	-26.3 (-32.9)[a,c]	1.390	952	-0.726
	20	*bridge*	-[d]	-[d]	-[d]	-[d]
	21	*bridge*	-[d]	-[d]	-[d]	-[d]
Cu_7	22	*bridge*	-30.4	1.416	983	-0.699
	23	*bridge*	-27.8	1.413	990	-0.712
	24	*h-111*	-31.2	1.537	690	-1.001
	25	*mono*	-23.5	1.305	1192	-0.481
	26	*top*	-22.0	1.332	1141	-0.524
	27	*mono*	-19.5	1.295	1217	-0.432
Cu_8	28	*h-100*	-25.0	1.642	492	-1.271
	29	*h-111*	-29.8	1.551	633	-1.113
	30	*h-111*	-25.3	1.525	680	-1.094
	31	*h-111*	-24.3	1.549	660	-1.127
	32	*bridge*	-22.8	1.357	993	-0.654
	33	*bridge*	-29.9	1.345	1033	-0.599

[a]Values in parenthesis have been calculated with respect to the Cu_n-3D isomer.
[b]Values in parenthesis have been calculated with respect to the Cu_6-star isomer.
[c]Singlet state was slightly more stable, but the triplet was kept for consistent comparison.
[d]Structure not found at this level of theory.

In order to bring some light into the relative stability of the O_2 adsorption complexes described above, the electronic structure of copper clusters of different size and shape was analyzed in more detail. The interaction of molecular O_2 with transition metal clusters and nanoparticles involves a transfer of electron density from the metal to the anti-bonding π^* molecular orbital of O_2. Taking into account that the degree of electron density transfer depends on the difference in stability and the spatial overlap between the orbitals involved, the composition and stability of the highest occupied molecular orbital (HOMO) of the Cu clusters considered in this work are plotted in Figure 3.4.

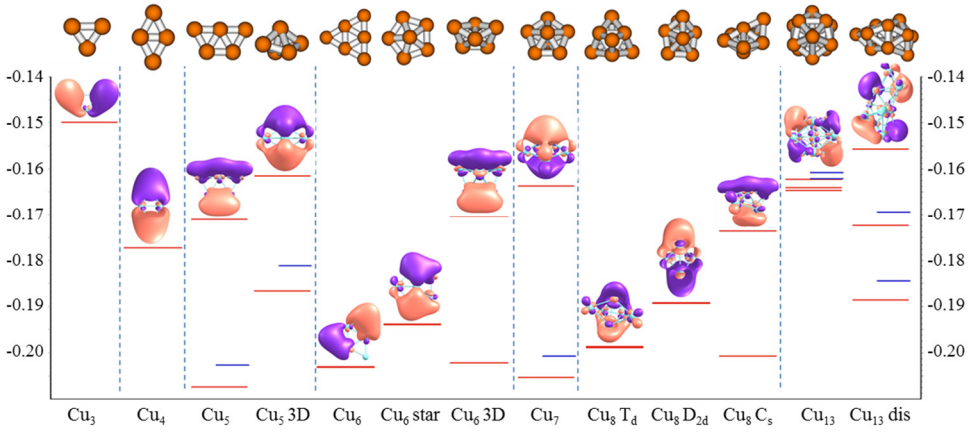

Figure 3.4. Stability and composition of the highest occupied molecular orbitals (HOMOs) of Cu_n clusters (n=3-8, 13) calculated at the B3PW91/6-311+G(d,p) level. Optimized structures of copper clusters are also shown. E_{homo} in hartrees.

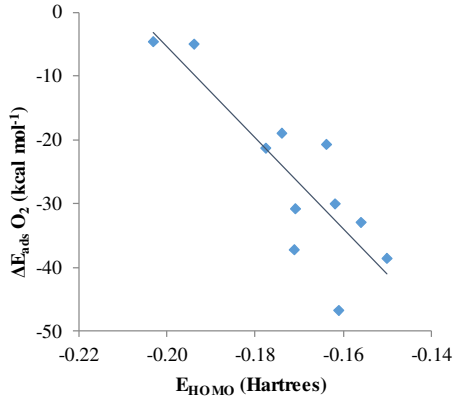

Figure 3.5 Adsorption energies of O_2 on copper clusters vs HOMO stability of the corresponding cluster at the B3PW91/6-311+G(d,p) level.

In all cases, the HOMO consists of several lobes fully accessible to interaction with reactant molecules. The strong interaction of O_2 with Cu_3, Cu_5, Cu_5-3D, Cu_6-3D or Cu_{13} (see Table 3.11 for ΔE_{ads} values on Cu_{13}) is related to the low stability and therefore better accessibility of the electrons in the HOMOs of these systems. In contrast, the extremely low reactivity of 2D Cu_6 clusters is due to the high stability of their corresponding HOMOs. Interestingly, O_2 adsorption on Cu_8 tends to modify the structure of the cluster towards the isomer with the higher E_{HOMO} to facilitate interaction.

The direct relationship between the stability of the HOMO and the adsorption energy of the most stable complex found on each Cu cluster can be observed in Figure 3.5.

The electron density transfer from the HOMO of the metal to the anti-bonding π* molecular orbital of O_2 causes a lengthening of the O-O bond distance and consequently a shift in the calculated ν_{OO} vibrational frequency. As described before for gold and silver[28,128,235], the degree of charge transfer and activation of the O-O bond depends directly on the mode of adsorption, and not so much on the size of the metal clusters. Thus, when molecular O_2 adsorbs adopting a *mono* mode, the amount of charge transferred from the copper cluster is always lower than -0.5 e. The optimized O-O distances are between 1.22 and 1.28 Å, and consequently the calculated stretching vibrational frequencies are usually larger than 1200 cm^{-1}. In the few structures corresponding to a *top* conformation there is a charge transfer of -0.4 – -0.6 e, and consequently the optimized O-O distances are in the 1.29–1.32 Å range, and the ν_{OO} frequencies are around 1170 cm^{-1}. A similar degree of activation is found for O_2 molecules adsorbed in a *bridge* mode. Although the degree of charge transferred is slightly larger (between -0.6 and -0.8 e), the optimized O-O bond lengths are within 1.31–1.33 Å, and the calculated stretching frequencies take values around 1160–1180 cm^{-1}. On the other hand, adsorption of molecular O_2 on the 100 and 111 facets of 3D clusters of any atomicity allows a charge transfer larger than -1.0 e that leads to a higher degree of molecular activation reflected in optimized O-O distances in the 1.41–1.52 Å range and calculated vibrational frequencies between 700 and 800 cm^{-1}.

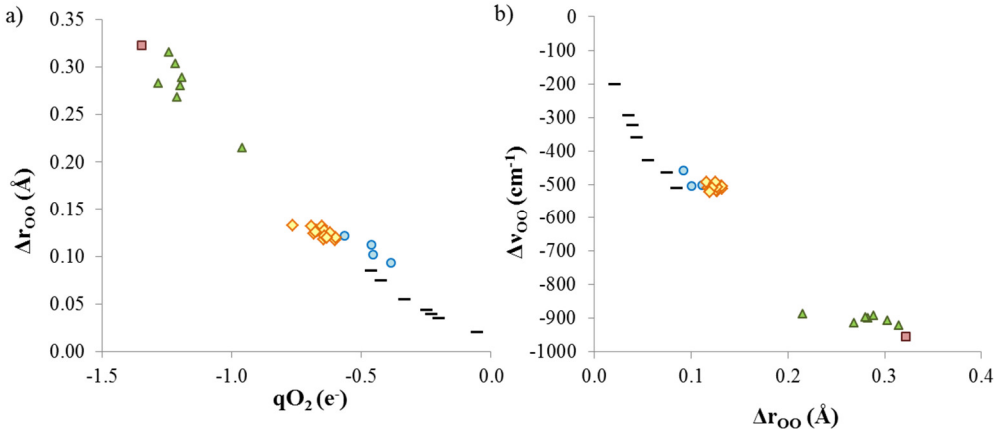

Figure 3.6. Relationship between a) the bond length variation Δr_{OO} and the charge transferred qO_2 and between b) the shift in the ν_{OO} vibrational frequency and the bond length variation Δr_{OO} obtained at the B3PW91/6-311+G(d,p) level of theory per adsorption mode: *mono* (black lines) *top* (blue circles) *bridge* (yellow diamonds) *h-111* (green triangles) and *h-100* (red squares).

Figure 3.6 clearly shows the direct relationship existing between charge transferred and activation of the O-O bond, and the key role of the mode of adsorption of O_2 on this activation. The correlation between the net charge on O_2 after adsorption and the increase in the r_{OO} bond lengths with respect to the gas phase value is almost linear (see Figure 3.6a). The black lines corresponding to *mono* conformations lie in the right bottom part of the plot, while the largest qO_2 and Δr_{OO} values are found for the red square and green triangles describing the *h-100* and *h-111* adsorption modes respectively. In a similar way, the large increase in the r_{OO} bond lengths found for *h-100* and *h-111* adsorption modes leads to shifts of more than 800 cm^{-1} in the calculated ν_{OO} vibrational frequencies. On the contrary, no clear trend was found for adsorption energies when they were plotted against the charge transferred (see Figure 3.7).

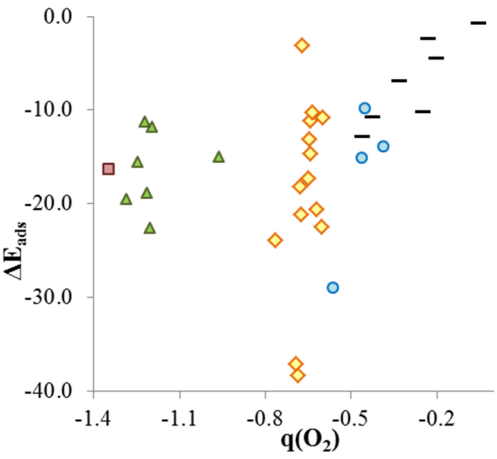

Figure 3.7. Adsorption energies vs charge transferred to O_2 obtained at the B3PW91/6-311+G(d,p) level per adsorption mode: *mono* (black lines) *top* (blue circles) *bridge* (yellow diamonds) *h-111* (green triangles) and *h-100* (red squares).

Regarding the computationally cheaper methods considered, the same structures with the same order of stability are obtained (see Tables 3.3-3.6). The only exceptions are the three lowest energy isomers of O_2 adsorbed on Cu_7 cluster, whose relative stability order changes when non-hybrid functionals are used (22 > 24 > 23 at the BPW91/def2tzvp level, and 24 > 22 > 23 at the p-PW91 level), and four isomers of O_2 adsorbed on Cu_8 (structures **30** to **33**) whose stability differ by less than 2 kcal mol^{-1} and their relative ordering can therefore easily change with the methodology employed. To facilitate the comparative analysis of results, the adsorption energy ΔE_{ads}, net charge transferred qO_2, increase in the OO bond length Δr_{OO} and shift in the ν_{OO} vibrational frequency values provided by the different computational levels considered are plotted in Figure 3.8 against the same parameters obtained with the reference B3PW91/6-311+G(d,p) method. The slopes, ordinate at the origin, and correlation coefficients for all regression lines are summarized in Table 3.7. In the case of adsorption energies, a linear relationship is clearly observed for all computational levels, with the best correlation being found for the B3PW91/Def2TZVP method (r^2 = 0.998). Non-hybrid methods yield systematically larger adsorption energies, this trend being more pronounced in the case of periodic p-PW91 calculations with a deviation of -13 kcal mol^{-1} (see Figure 3.8a).

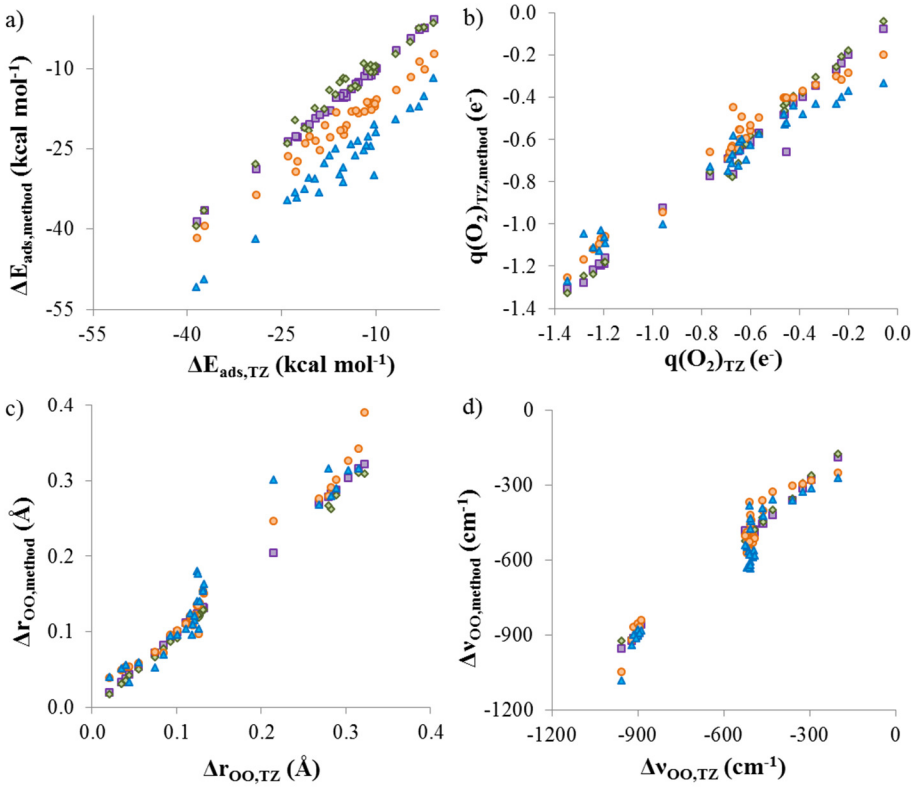

Figure 3.8. Relationship between the values of a) O_2 adsorption energies, ΔE_{ads}, b) charge transferred to O_2 molecule, qO_2, c) increase in the O-O bond length, Δr_{OO}, and d) shift in the O-O vibrational frequency, $\Delta \nu_{OO}$, calculated at different theoretical levels (B3PW91/LANL2DZ (green diamonds), B3PW91/Def2TZVP (purple squares), BPW91/Def2TZVP (orange circles), p-PW91 (blue triangles)) and those obtained using the reference B3PW91/6-311+G(d,p) method.

The different performance of hybrid and non-hybrid methods is more evident in the calculation of charge distributions. The correlation coefficients, R^2, for the BPW91/Def2TZVP and p-PW91 levels are not so good, 0.97 and 0.96, respectively, and the slopes of the regression lines are less than unity, 0.84 and 0.72, respectively. This means that the degree of charge transfer is underestimated for small clusters and overestimated for the largest systems. The poorer behavior of non-hybrid methods is also observed in the optimized O-O distances and calculated vibrational frequencies. For these properties, the slope of the correlation line is always close to unity, but the R^2 values for p-PW91 method are 0.93 for Δr_{OO} and 0.90 for $\Delta \nu_{OO}$ (see Table 3.7). In contrast, the overall performance of the hybrid B3PW91/Def2TZVP method is excellent in all cases.

Table 3.7. Regression parameters (correlation coefficient R^2, slope m and ordinate at the origin n) for the regression lines y = mx + n corresponding to the data plotted in Figure 3.8.

Data from	Method	R^2	m	n
Fig. 3.8a, ΔE_{ads}	B3PW91/Def2TZVP	0.998	0.997	+0.034
	B3PW91/LANL2DZ	0.977	0.986	+0.601
	BPW91/Def2TZVP	0.970	0.874	-7.177
	p-PW91	0.939	0.956	-12.91
Fig. 3.8b, qO_2	B3PW91/Def2TZVP	0.986	0.950	-0.044
	B3PW91/LANL2DZ	0.991	1.000	+0.003
	BPW91/Def2TZVP	0.968	0.844	-0.057
	p-PW91	0.961	0.723	-0.204
Fig. 3.8c, Δr_{OO}	B3PW91/Def2TZVP	1.000	1.002	-0.002
	B3PW91/LANL2DZ	0.999	0.970	-0.003
	BPW91/Def2TZVP	0.977	1.077	-0.002
	p-PW91	0.932	1.089	-0.001
Fig. 3.8d, $\Delta \nu_{OO}$	B3PW91/Def2TZVP	0.998	1.005	+8.054
	B3PW91/LANL2DZ	0.997	1.000	+15.306
	BPW91/Def2TZVP	0.935	1.004	+13.334
	p-PW91	0.904	0.988	-31.576

The effect of including Zero-Point Vibrational Energies (ZPVE) and correcting for the Basis Set Superposition Error (BSSE) was checked at the B3PW91/Def2-TZVP level, and the results are summarized in Table 3.8. Both corrections are destabilizing, and take values between 0.2 and 1.2 kcal mol^{-1} in the case of ZPVE and are slightly larger for BSSE corrections, in the 1.2 – 2.8 kcal mol^{-1} range except for one largest value of 3.4 kcal mol^{-1}. The order of stability of the structures investigated is not altered by these corrections, except again for the four isomers of O_2 adsorbed on Cu_8 whose relative stability differs by less than 2 kcal mol^{-1}.

Finally, the influence of dispersion interactions was taken into account by using the B97D functional as implemented in the Gaussian09 software and, again, the difference between the B97D and B3PW91 calculated adsorption energies is in most cases less than 2 kcal mol^{-1}, except for the molecules adsorbed in a *mono* conformation that are stabilized by around 4 kcal mol^{-1} (see Table 3.8.)

Table 3.8. Adsorption energy (ΔE_{ads}), Zero-Point Vibrational Energy (ZPVE), ZPVE-corrected adsorption energy ($\Delta E_{ads,ZPVE}$), Basis Set Superposition Error (BSSE), BSSE-corrected adsorption energy ($\Delta E_{ads,BSSE}$) and ZPVE + BSSE-corrected adsorption energy of molecular O_2 on Cu_n (n = 3-8) clusters at the B3PW91/Def2-TZVP level, and for the adsorption energy including dispersion interactions at the B97D/ Def2-TZVP level (in kcal mol^{-1}).

Cluster atomicity	Structure (Fig. 3.3)	ΔE_{ads}	ZPVE	$\Delta E_{ads,ZPVE}$	BSSE	$\Delta E_{ads,BSSE}$	$\Delta E_{ads,ZPVE+BSSE}$	B97D/ Def2-TZVP
Cu_3	1	-38.6	1.2	-37.4	1.7	-36.9	-35.7	-37.1
	2	-28.8	0.7	-28.1	1.3	-27.5	-26.8	-29.3
Cu_4	3	-20.9	0.8	-20.1	1.7	-19.2	-18.4	-19.3
	4	-13.8	0.4	-13.4	1.3	-12.5	-12.1	-14.5
	5	-9.9	0.4	-9.5	1.3	-8.6	-8.2	-14.6
	6	-19.3	0.6	-18.7	2.6	-16.7	-16.1	-16.8
Cu_5	7	-36.6	1.0	-35.5	1.9	-34.7	-33.7	-35.6
	8	-23.7	0.9	-22.8	1.8	-21.9	-21.0	-22.9
	9	-12.9	0.7	-12.2	1.6	-11.3	-10.6	-14.1
	10	-10.3	0.3	-10.0	1.2	-9.1	-8.8	-15.2
Cu_5-3D	11	-23.0	1.1	-21.9	1.9	-21.0	-20.0	-21.5
	12	-18.7	0.8	-17.9	2.6	-16.0	-15.2	-20.2[a]
	13	-15.4	0.6	-14.8	1.5	-13.9	-13.2	-15.5
Cu_6	14	-4.4	0.4	-4.0	1.2	-3.2	-2.8	-8.9
	15	-2.9	0.6	-2.2	1.9	-1.0	-0.4	-5.1
Cu_6-star	16	-2.4	0.4	-2.1	1.3	-1.2	-0.8	-7.4
	17	-0.9	0.4	-0.5	1.4	0.5	0.9	-6.4
Cu_6-3D	18	-22.8	1.1	-21.7	2.8	-20.0	-19.0	-19.3
	19	-17.9	1.1	-16.8	2.1	-15.8	-14.7	-11.6
	20	-15.4	1.1	-14.3	1.9	-13.5	-12.4	-10.5
	21	-11.4	0.9	-10.4	1.9	-9.5	-8.6	-10.7
Cu_7	22	-20.4	0.8	-19.6	2.0	-18.5	-17.6	-21.3
	23	-18.2	0.8	-17.4	1.9	-16.2	-15.4	-17.3
	24	-14.7	0.3	-14.4	2.7	-12.0	-11.7	-18.8
	25	-12.6	0.3	-12.3	1.7	-10.9	-10.6	-19.7
	26	-10.1	0.3	-9.7	1.5	-8.6	-8.3	-13.1
	27	-6.7	0.2	-6.5	1.4	-5.3	-5.1	-12.4
Cu_8	28	-15.5	0.9	-14.5	3.4	-12.1	-11.1	-16.2
	29	-15.2	0.7	-14.4	2.8	-12.3	-11.6	-14.5
	30	-11.5	0.7	-10.8	2.8	-8.7	-8.0	-11.3
	31	-10.5	0.7	-9.8	2.8	-7.7	-7.0	-[b]
	32	-11.5	0.8	-10.7	1.9	-9.6	-8.8	-[b]
	33	-10.4	0.7	-9.7	2.0	-8.5	-7.7	-12.2

[a]The geometry of the structure is different.
[b]Structure not found at this level of theory.

3.3.1.3. O_2 dissociation.

Taking as starting point the most stable O_2 adsorption complex found for each atomicity of the copper cluster, the transition state for the dissociation of the O-O bond and the reaction product consisting of two O atoms adsorbed on the cluster have been optimized, and their nature characterized by means of frequency calculations. Given the large adsorption energies obtained for O_2 complexes on 3D Cu_5 and Cu_6 clusters, dissociation on these isomers has also been considered. Following the same reasoning, the study on 2D Cu_6 clusters was discarded due to the very low adsorption energies found for them. It is important to mention at this point that, although the *bridge* conformers **11** and **22** were initially taken as starting point for O_2 dissociation over 3D Cu_5 and Cu_7 clusters, calculations always led to dissociation paths involving structures **12** and **24**, where the O_2 molecule is adsorbed in a *h-111* mode. This is justified by the larger activation of O_2 molecule when adsorbed in such mode, and by the relative low difference in energy between the *bridge* and *h-111* conformers. So, the reaction paths starting from *h-111* structures are described below for 3D Cu_5 and Cu_7 clusters. The optimized structures of reactant (R), transition state (TS), and product (P) for each process are depicted in Figure 3.9 along with the corresponding energy profiles, while the B3PW91/6-311+G(d,p) calculated adsorption (ΔE_{ads}), activation (ΔE_{act}) and reaction (ΔE_{reac}) energies, together with the optimized values of the O-O distance in the TS are summarized in Table 3.9. The corresponding values obtained at the less computationally demanding B3PW91/LANL2DZ, B3PW91/ Def2TZVP, BPW91/ Def2TZVP and p-PW91 levels are summarized in Table 3.10.

Table 3.9. Adsorption (ΔE_{ads}), activation (ΔE_{act}) and reaction (ΔE_{reac}) energies and O-O distance in the TS at the B3PW91/6-311+G(d,p) level.

Cluster atomicity	Path (Fig. 3.9)	ΔE_{ads} (kcal mol^{-1})	ΔE_{act} (kcal mol^{-1})	r_{OO} in TS (Å)	ΔE_{reac} (kcal mol^{-1})
Cu_3	1-[34]-35	-38.4	54.2	2.123	-22.8
Cu_4	3-[37]-38	-21.2	39.3	1.734	-30.4
Cu_5	7-[39]-40	-37.2	40.8	1.849	-41.7
Cu_5-3D	12-[41]-42	-19.0 (-26.4)[a]	14.8	2.004	-54.1
Cu_6-3D	18-[43]-44	-22.7 (-30.7)[a]	14.9	2.020	-51.7
Cu_7	22-[45]-46	-15.1	17.6	1.997	-58.2
Cu_8	28-[47]-48	-16.3	15.2	2.172	-78.1

[a]Calculated with respect to the corresponding isolated Cu_n-3D isomer.

Dissociation of molecular O_2 over planar Cu_3 and Cu_4 clusters follows a pathway similar to that previously described for small gold and silver clusters.[15, 72] Starting from O_2 adsorbed in a *bridge* conformation, the rupture of the O-O bond occurs via transition state structures (**34** and **37** in Figure 3.9a) in which only one of the O atoms can be stabilized through formation of new Cu-O bonds. As a consequence, the calculated activation energies are really high, 54.2 and 39.3 kcal mol^{-1} for Cu_3 and Cu_4

clusters, respectively. After dissociation, however, the two O atoms occupy bridge positions between two copper atoms, so that both processes are clearly exothermic. It is important to remark that the optimized geometry of the reaction product P over a Cu_3 cluster varies with the computational method used. Thus, while the hybrid B3PW91 functional yields structure **35** in which one of the three Cu-Cu bonds initially present in the cluster is broken, with the non-hybrid BPW91/ Def2TZVP and p-PW91 methods structure **36** is obtained.

Two different initial reactant structures were considered to investigate the dissociation of O_2 over clusters containing five copper atoms, the *bridge* conformer **7** over planar Cu_5, which is the most stable adsorption complex found for this atomicity, and the *h-111* conformer **12** over Cu_5-3D cluster, with the highest degree of molecular O_2 activation. In the transition state obtained over planar Cu_5 (structure **39** in Figure 3.9a), one of the O atoms is in the cluster plane forming a bridge between two copper atoms, while the other O atom is placed on the cluster forming three new Cu-O bonds. However, this situation is not stable and the calculated activation energy is really high, 40.8 kcal mol^{-1}. Moreover, the process involves important structural changes in the Cu_5 cluster that, in the product structure **40**, has evolved to a 3D system. The global process is clearly exothermic, suggesting that planar Cu_5 clusters might be converted to 3D structures by reaction with O_2, although a high activation barrier should be overcome. Another pathway involves structure **12** as initial reactant R, which is 18,2 kcal mol^{-1} less stable than structure **7**. As described before, this *h-111* adsorption mode facilitates the charge transfer necessary to activate the O-O bond. As a consequence, the optimized r_{OO} distance in structure **12** is already 1.467 Å, and increases to 2.004 Å in the transition state structure **41**. The calculated activation energy for this pathway is only 14.8 kcal mol^{-1} and the process is again highly exothermic.

As previously mentioned, 2D Cu_6 clusters interact weakly with O_2 and are not able to efficiently activate the O-O bond, and therefore we studied the dissociation of O_2 over the 3D Cu_6 isomer, starting from the most stable structure **18** in which the O_2 molecule is adsorbed on the 111 facet. The geometry of the transition state (structure **43**) is similar to that found over Cu_5-3D (structure **41**). The optimized O-O distance is 2.0 Å, and the disposition of the O atoms is equivalent, with both of them sharing one low coordinated copper atom and being stabilized via formation of two other Cu-O bonds. Accordingly, the calculated activation energy is nearly the same, 14.9 kcal mol^{-1}.

Further increase of cluster atomicity does not significantly change the reaction pathway described for 3D Cu_5 and Cu_6 clusters. The geometry of the transition state obtained for O_2 dissociation over Cu_7 cluster (structure **45**) is equivalent to those previously described, and the calculated activation energy is only slightly higher, 17.7

kcal mol^{-1}. In the most stable adsorption complex found over Cu_8 cluster, O_2 is adsorbed over a 100 facet, with each oxygen atom forming two bonds with two copper atoms. The number of Cu-O bonds present in the system does not change in the transition state **47**, and the reaction coordinate is only associated to the elongation of the O-O bond and to some deformation of the cluster geometry. Again, the calculated activation barrier is low, 15.2 kcal mol^{-1}.

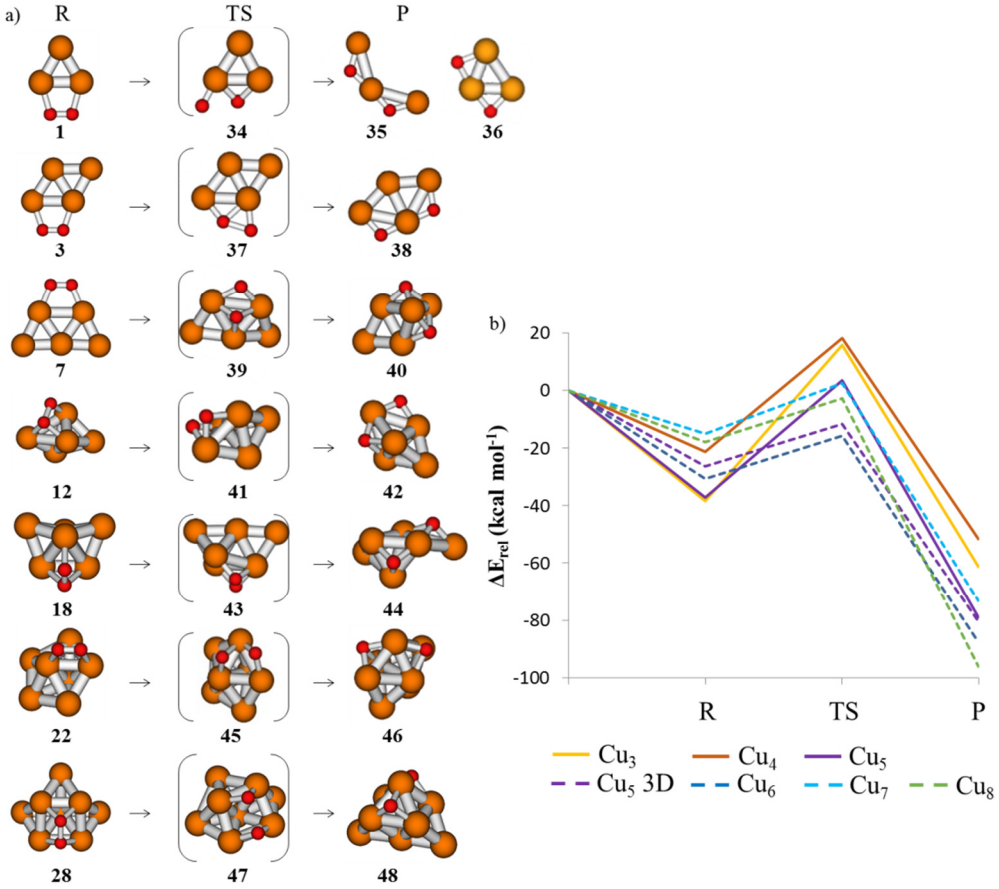

Figure 3.9. a) Structures of reactants (R), transition states (TS) and products (P) for the process of dissociation of one oxygen molecule by Cu_n clusters with n = 3-8 and b) corresponding energy profiles for n = 3 (yellow), 4 (orange), 5 (purple), 6 (dark blue), 7 (light blue) and 8 (green) at the B3PW91/6-311+G(d,p) level. Solid and dashed lines correspond to 2D and 3D clusters, respectively.

Table 3.10. Adsorption (ΔE_{ads}), activation (ΔE_{act}) and reaction (ΔE_{reac}) energies and O-O distance in the TS at different levels of theory.

Cluster atomicity	Path (Fig. 3.9-10)	ΔE_{ads} (kcal mol^{-1})	ΔE_{act} (kcal mol^{-1})	r_{OO} in TS (Å)	ΔE_{reac} (kcal mol^{-1})
B3PW91/LANL2DZ					
Cu_3	1-[34]-35	-39.4	64.7	2.253	-9.0
Cu_4	3-[37]-38	-21.1	42.6	1.773	-18.3
Cu_5	7-[39]-40	-36.6	44.9	1.916	-34.2
Cu_5-3D	12-[41]-42	-[b]	-[b]	-[b]	-[b]
Cu_6-3D	18-[43]-44	-19.6 (-30.6)[a]	21.0	2.140	-44.6
Cu_7	22-[45]-46	-[b]	-[b]	-[b]	-[b]
Cu_8	28-[47]-48	-14.8	22.4	2.226	-69.2
B3PW91/Def2TZVP					
Cu_3	1-[34]-35	-38.6	56.0	2.145	-18.6
Cu_4	3-[37]-38	-20.9	39.8	1.741	-27.4
Cu_5	7-[39]-40	-36.6	41.3	1.856	-40.5
Cu_5-3D	12-[41]-42	-18.7 (-25.8)[a]	15.5	2.021	-52.9
Cu_6-3D	18-[43]-44	-22.8 (-30.2)[a]	16.1	2.038	-50.0
Cu_7	22-[45]-46	-14.7	18.2	2.014	-56.7
Cu_8	28-[47]-48	-15.5	16.3	2.178	-76.9
BPW91/Def2TZVP					
Cu_3	1-[34]-36	-41.7	38.1	2.096	-25.7
Cu_4	3-[37]-38	-24.1	25.3	1.811	-35.8
Cu_5	7-[39]-40	-39.4	32.2	1.850	-43.2
Cu_5-3D	12-[41]-42	-25.2 (-30.4)[a]	6.4	1.869	-53.9
Cu_6-3D	18-[43]-44	-29.4 (-34.2)[a]	7.2	1.931	-49.4
Cu_7	22-[45]-46	-21.4	10.3	1.948	-57.2
Cu_8	28-[47]-48	-18.2	1.7	1.968	-79.8
p-PW91					
Cu_3	1-[34]-36	-50.9	35.8	2.053	-29.5
Cu_4	3-[37p]-38	-32.5	19.8[c]	2.165[c]	-41.9
Cu_5	7-[39p]-40	-49.4	30.8[d]	1.969[d]	-42.3
Cu_5-3D	12-[41]-42	-33.2 (-39.5)[a]	6.2	1.874	-55.6
Cu_6-3D	18-[43]-44p	-33.2 (-39.8)[a]	5.7	1.900	-45.2[e]
Cu_7	22-[45]-46	-31.2	9.7	1.912	-57.4
Cu_8	28-[47]-48p	-25.0	1.0	1.822	-82.6[e]

[a]Calculated with respect to the corresponding isolated Cu_n-3D isomer.
[b]Structure not found at this level of theory.
[c]Different TS with a different spin (singlet) (structure 37p in Figure 3.10).
[d]Different TS (see Figure 3.10).
[e]Different product (see Figure 3.10).

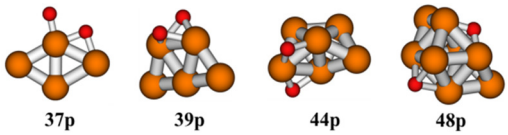

Figure 3.10. Structures **37**, **39**, **44** and **48** obtained at the p-PW91 level.

These results suggest that it is not cluster atomicity but cluster morphology the main parameter determining the catalytic activity of copper towards O_2 dissociation, a proposal that is clearly confirmed by comparing the two energy profiles obtained over 2D and 3D Cu_5 clusters with those calculated over the planar Cu_3 and Cu_4 and the 3D Cu_6 Cu_7 and Cu_8 systems in Figure 3.9b. The four energy profiles corresponding to 3D clusters are similar, and involve activation barriers significantly lower than those found over planar clusters, regardless the stability of the initial adsorption complex formed. It is also important to remark that the adsorption mode of the reactant R is also different on 2D and 3D clusters. Thus, *bridge* conformations are found over planar clusters, while *h-111* modes, which lead to a higher degree of molecular activation, are usually found over 3D clusters.

To gain insight into the influence of cluster morphology and mode of adsorption on the reactivity of copper clusters, the complete reaction path for dissociation of an O_2 molecule over a 3D Cu_4 cluster (structure **6**) and adsorbed in a *h-111* mode over a Cu_3 cluster (structure **53** in Figure 3.11b) have been calculated, and the energy profiles and structures involved are plotted in Figure 3.11.

The reaction mechanism over a 3D Cu_4 cluster is not completely equivalent to those previously described, and involves two consecutive elementary steps with very low activation energies. In the transition state for the first step (structure **49** in Figure 3.11a), the O-O bond length increases to 1.56 Å while the 3D Cu_4 cluster flattens. An IRC calculation from this transition state **49** leads to intermediate species **50**, in which the O_2 molecule is not dissociated but inserted into the cluster, with an optimized O-O distance of 1.56 Å. Then, through transition state **51** that resembles those found over Cu_5, Cu_6 and Cu_7 3D clusters, the O-O bond is finally broken and species **52**, with two O atoms adsorbed on a planar Cu_4 cluster, is obtained. The activation energy for this pathway is only 9.1 kcal mol^{-1}, and the process is clearly exothermic. It should be mentioned at this point that all species involved in the mechanism are singlet, except for the reaction product **52** that is more stable in the triplet state. Therefore, the reaction energy ΔE_{reac} for the global process is -29.7 kcal mol^{-1} considering the singlet state for structure **52** and -39.0 kcal mol^{-1} considering the triplet state.

Going one step further, the dissociation of O_2 adsorbed in a *h-111* conformation over the smallest system exposing a 111 facet, that is, the Cu_3 cluster, was theoretically investigated (Figure 3.11b).

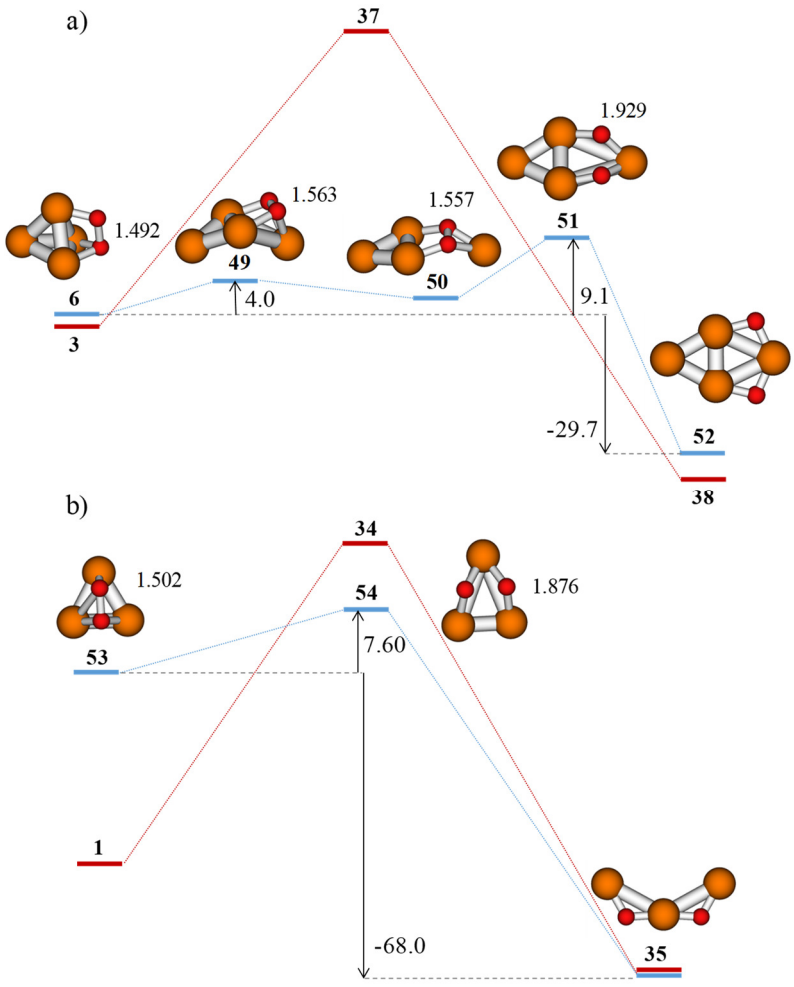

Figure 3.11. Energy profile (in blue) and structures involved in the dissociation of O_2 a) over a 3D Cu_4 cluster and b) adsorbed in a *h-111* conformation over Cu_3. The optimized O-O bond lengths (in Å) are shown for each structure, and the B3PW91/6-311+G(d,p) calculated activation and reaction energies (in kcal mol^{-1}) are written beside the arrows. The energy profiles starting from bridge conformations over planar Cu_3 and Cu_4 clusters are included (in red) for comparison.

In structure **53** (Figure 3.11b), like in other *h-111* adsorption complexes, the large amount of charge transferred to O_2 (-1.325 e^-), causes a high degree of activation of the O-O bond, reflected in a long r_{OO} value and a calculated ν_{OO} vibrational frequency of 749 cm^{-1}. In the transition state **54** the O-O bond lengthens to 1.876 Å, and the geometry of the whole system resembles that of the transition states previously described for 3D Cu_5, Cu_6 and Cu_7 clusters (structures **41**, **43** and **45** in Figure 7). From this transition state, structure **35** with the two O atoms forming symmetrical bridges between two Cu atoms is obtained in a highly exothermic process. Since O_2 in adsorption complex **53** is already highly activated, the energy barrier for its dissociation is really low, only 7.6 kcal mol^{-1}, suggesting the possibility to dissociate the O-O bond through this pathway. However, although the adsorption of O_2 on Cu_3 in a *h-111* mode is exothermic with an adsorption energy value of -6.8 kcal mol^{-1}, the stability of this conformer is considerably lower than that of the *bridge* conformer **1**, as depicted in Figure 3.11b. Considering the possibility that the most stable conformer **1** could evolve to the *h-111* mode and then follow the pathway through transition state **54** instead of via **34**, the global activation barrier for the process would be still very high, 39.2 kcal mol^{-1}.

It can then be concluded from this part of the study that adsorption of O_2 in a *h-111* or *h-100* modes leads to higher activation of the O-O bond and, as a consequence, to lower activation energy barriers for its dissociation. It is also found that 3D clusters preferentially stabilize the more activating *h-111* and *h-100* modes, in contrast to 2D isomers that prefer *bridge* conformations. Altogether, this results in an enhanced reactivity for 3D clusters, but it also implies a higher stability against oxidation of small 2D copper clusters.

The performance of the computationally less demanding B3PW91/LANL2DZ, B3PW91/Def2TZVP, BPW91/Def2TZVP and p-PW91 methods in reactivity studies has been addressed by comparing the activation and reaction energies for O_2 dissociation obtained with these methods and summarized in Table 3.10 (recall Table 3.9 for the B3PW91/6-311+G(d,p) values). The activation ΔE_{act} and reaction energies ΔE_{reac} provided by the computationally cheaper methods listed above are plotted against the same parameter obtained with the reference B3PW91/6-311+G(d,p) method in Figure 3.12. As discussed before in relation to O_2 adsorption and activation, the overall performance of the B3PW91/Def2TZVP method is excellent, with correlation coefficients of 0.999 for both activation and reaction energies, followed by B3PW91/LANL2DZ. Non-hybrid methods on the other hand yield systematically lower activation barriers and reaction energies. It has to be therefore concluded that it is not possible to directly compare results obtained with hybrid and non-hybrid functionals. However, taking into account the considerably lower computational cost of periodic p-PW91 calculations and its suitability to study larger clusters and nanoparticles, the trends in adsorption, activation and reaction energies with cluster size, at the five theoretical levels considered, are compared in Figure 3.13. It is important

to remark that, despite the different energy values obtained with the different methods, their variation with increasing cluster size is almost equivalent. Thus, O_2 adsorption energies over planar Cu_3 and Cu_5 are systematically larger than over 3D systems, while activation and reaction energies for O_2 dissociation decrease with increasing cluster size.

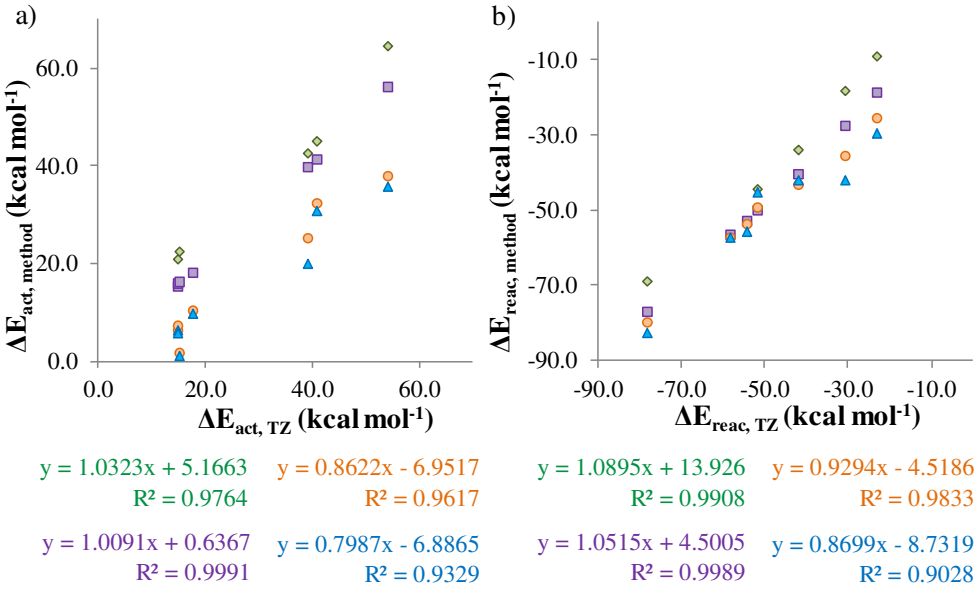

Figure 3.12. Relationship between the values of a) activation energies ΔE_{act} and b) reaction energies ΔE_{reac} calculated at the different theoretical levels and those obtained using the reference B3PW91/6-311+G(d,p) method, with B3PW91/LANL2DZ as green diamonds, B3PW91/Def2TZVP in purple squares, BPW91/Def2TZVP in orange circles and p-PW91 as blue triangles.

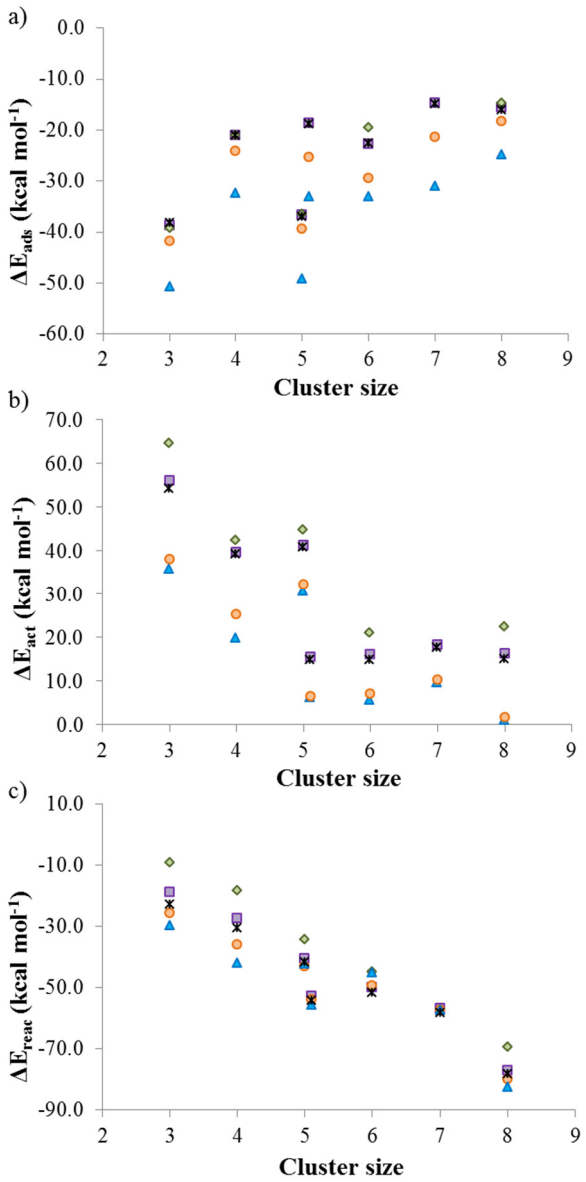

Figure 3.13. a) O_2 adsorption energies, ΔE_{ads}, b) activation energies for O_2 dissociation, ΔE_{act}, and c) reaction energies, ΔE_{reac}, with cluster size at the different theoretical levels considered, with B3PW91/6-311+G(d,p) values in black stars, B3PW91/LANL2DZ in green diamonds, B3PW91/Def2TZVP in purple squares, BPW91/Def2TZVP in orange circles and p-PW91 as blue triangles.

O_2 dissociation over larger clusters and nanoparticles.

Real catalysts usually consist of nanometric metal particles containing from tenths to hundreds of atoms, and can only be treated using periodic plane-wave based methods, like p-PW91. In order to extend this comparative study to more realistic systems, we included the two cuboctahedral M_{13} and M_{38} models previously used in our group to investigate the reactivity of gold and silver nanoparticles[28,128,235,236] as the largest systems that can be computationally treated with DFT methods based on atom-centered Gaussian orbitals. Based on previous theoretical studies on the size dependence of the reactivity of gold nanoparticles with 38, 55, 79, 116 and 147 atoms,[73] the differences in reactivity expected for systems larger than Cu_{38} should be less important than those found in the subnanometric regime.

Both the *h-100* and *h-111* adsorption modes were considered on the Cu_{13} and Cu_{38} models. The energy profile over Cu_{13} was obtained at the B3PW91/6-311+G(d,p), B3PW91/Def2TZVP and p-PW91 levels, but for computational reasons geometry optimizations on the Cu_{38} nanoparticle were only performed at the p-PW91 level, and single point calculations at the B3PW91/Def2TZVP level were carried out on the p-PW91 optimized geometries for comparison. The optimized structures of reactants R, transition states TS and products P are depicted in Figure 3.14, and Table 3.11 summarizes the calculated adsorption, activation and reaction energies.

Table 3.11. Adsorption (ΔE_{ads}), activation (ΔE_{act}) and reaction (ΔE_{reac}) energies for the dissociation of O_2 over Cu_{13} and Cu_{38} clusters calculated at the B3PW91/6-311+G(d,p), B3PW91/Def2TZVP (in parenthesis) and p-PW91 levels of theory. The corresponding optimized structures are depicted in Figure 3.14.

Cluster atomicity	Ads. mode	ΔE_{ads} (kcal mol^{-1})		ΔE_{act} (kcal mol^{-1})		ΔE_{reac} (kcal mol^{-1})	
		B3PW91	p-PW91	B3PW91	p-PW91	B3PW91	p-PW91
Cu_{13}	*h-111*	-45.6 (-45.9)	-62.5	13.8 (14.7)	4.1	-80.3 (-78.5)	-77.1
Cu_{13}	*h-100*	-46.7 (-46.0)	-58.5	8.9 (9.4)	0.8	-74.6 (-74.1)	-77.8
$Cu_{13\text{-dis}}$	*h-100*	-48.5 (-47.4)	-64.0	6.0 (6.6)	1.8	-68.1 (-66.8)	-64.4
Cu_{38}	*h-111*	(-23.7)	-39.7	(8.3)[a]	3.8	(-53.1)[a]	-50.1
Cu_{38}	*h-100*	(-34.9)	-50.2	(10.3)[a]	2.4	(-40.3)[a]	-39.1

[a]From B3PW91/Def2TZVP//p-PW91 single point calculations.

O_2 adsorption over Cu_{13} cluster is always highly exothermic, with the p-PW91 adsorption energy values being systematically larger than the B3PW91/6-311+G(d,p) ones by ~ -14 kcal mol^{-1}, the same deviation previously found for the Cu_n clusters with n = 3-8. The optimized geometry of O_2 adsorbed in a *h-111* mode is not exactly equivalent at all theoretical levels discussed.

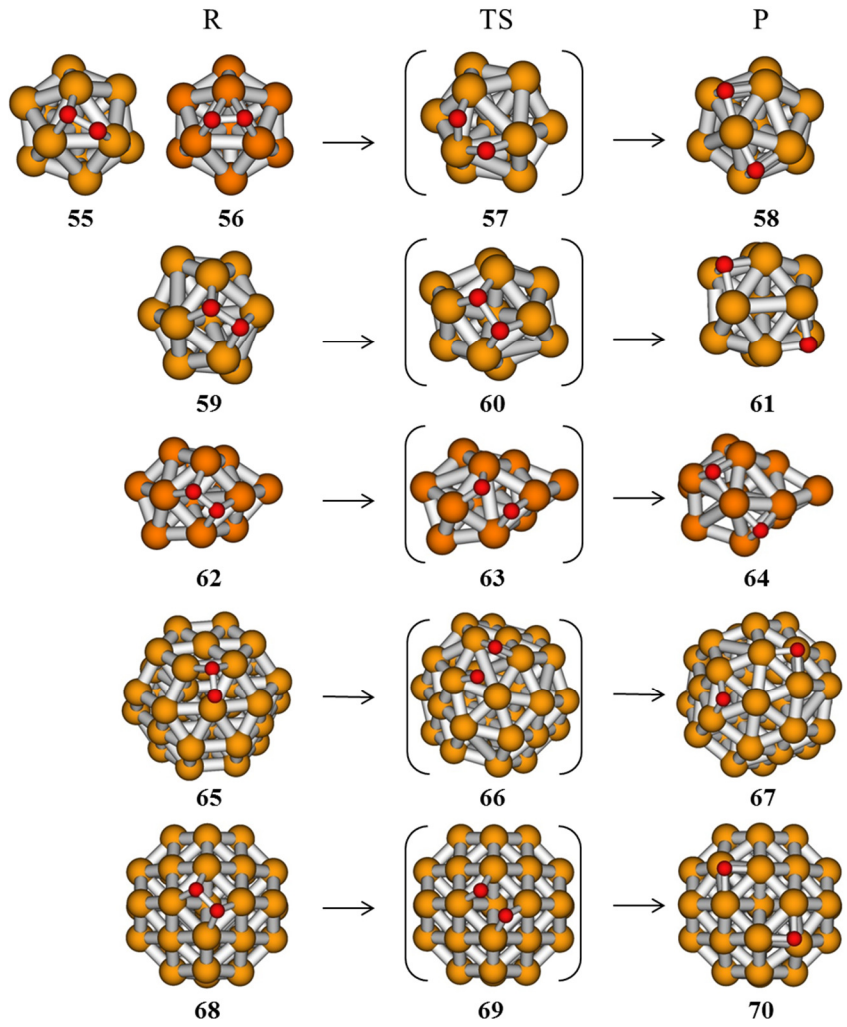

Figure 3.14. Structures of reactants (R), transition states (TS) and products (P) for the dissociation of one oxygen molecule by Cu_{13} and Cu_{38} clusters.

Structure **55** in Figure 3.14 with one oxygen atom on top of a copper atom is obtained with the p-PW91 method, while the hybrid methods yield structure **56** with the two oxygen atoms occupying bridge positions between two copper atoms. O_2 dissociation occurs through transition state **57** with an activation energy of 13.8, 14.7 and 4.1 kcal mol^{-1} at the B3PW91/6-311+G(d,p), B3PW91/Def2TZVP and p-PW91 levels, respectively, and the process is exothermic by ~ -80 kcal mol^{-1}. When O_2 adsorbs on a 100 facet of the Cu_{13} cluster the degree of molecular activation is higher, and consequently the calculated activation energy for dissociation of the O-O bond is lower, around 9 kcal mol^{-1} with the hybrid B3PW91 methods and only 0.8 kcal mol^{-}

$^{-1}$ at the p-PW91 level. It is important to remark that structure **60** is not a true stationary point on the B3PW91 potential energy surfaces, and could only be obtained in an approximate way by stopping the geometry optimizations that finally converged to transition state **63**. Two imaginary frequencies were obtained for structure **60** at the B3PW91/6-311+G(d,p) level, one of -815 cm^{-1} associated to rupture of the O-O bond, and another one of only -16 cm^{-1} associated to cluster deformation. This small value justifies the characterization of structure **60** as the transition state for O-O dissociation over a cuboctahedral Cu_{13} cluster in order to compare with the corresponding p-PW91 pathway. On the other hand, only one imaginary frequency of -792 cm^{-1} associated to O-O rupture was obtained for the structure **63** that connects adsorption complex **62** with structure **64**. These species are involved in a reaction path that starts with O_2 adsorbed in the same *h-100* conformation over a distorted Cu_{13} cluster. The process in this case requires an activation barrier of ~ 6 kcal mol^{-1} at the B3PW91 levels and only 1.8 kcal mol^{-1} at the p-PW91 level. Notice that, as discussed before for Cu_n clusters with n = 3-8, activation energies at the p-PW91 level are systematically lower than those provided by hybrid methods, although the difference between the computed ΔE_{act} values seems to decrease as particle size increases.

Finally, O_2 dissociation over a cuboctahedral Cu_{38} nanoparticle was explored at the p-PW91 level, and single point calculations with the B3PW91/Def2TZVP method were performed on the p-PW91 optimized geometries. The *h-111* and *h-100* adsorption complexes and the corresponding transition states for O-O dissociation over Cu_{38} are geometrically similar to those found over Cu_{13}. Adsorption and dissociation of O_2 are clearly exothermic, and the activation barriers involved are not high, 2-4 kcal mol^{-1} at the p-PW91 level and slightly higher, 8-10 kcal mol^{-1} at the B3PW91/Def2TZVP//p-PW91 level.

These results indicate that while periodic non-hybrid p-PW91 methods yield systematically larger adsorption energies and lower activation barriers for O_2 dissociation when compared to the reference B3PW91/6-311+G(d,p) computational level, the structures involved in the reaction mechanisms and the trends found as particle size increases are similar, and therefore the same chemical conclusions can be obtained irrespectively of the methodology employed.

Finally, it is interesting to compare the results obtained here for copper clusters and nanoparticles with those previously reported for gold and silver analogous systems at the same p-PW91 computational level[28,128,235,236]. The calculated activation barriers for O_2 dissociation on small planar clusters are extremely high in all cases (45.4 kcal mol^{-1} on Au_3[28], 60.9 kcal mol^{-1} on Ag_3[128] and 35.8 kcal mol^{-1} on Cu_3), but the O atoms interact more strongly with copper than with the other metals, as indicated by reaction energies that are endothermic for Au_3 and Ag_3 (3.0 and 23.9 kcal mol^{-1}, respectively) and clearly exothermic for Cu_3 (-29.5 kcal mol^{-1}, see Table 3.6). As

particle size increases the process becomes energetically accessible and thermodynamically favorable on all systems, but with remarkable differences between the three metals considered. The calculated adsorption energies on gold and silver clusters or nanoparticles composed by 13 or 38 atoms range from -18.3 to -23.6 kcal mol^{-1}, while they are larger than -50 kcal mol^{-1} on copper systems. The calculated activation energies for O_2 dissociation are lower than 10 kcal mol^{-1}on Au_{13} and Au_{38}, almost negligible on Cu_{13} and Cu_{38} (~2 kcal mol^{-1}, see Table 3.11) and as high as ~20 kcal mol^{-1} on Ag_{13} and Ag_{38}. Finally, the dissociation process is exothermic on gold and silver systems, with reaction energies ranging from -12.5 to -42.3 kcal mol^{-1}, and it is extremely favorable on Cu_{13} for instance with a calculated reaction energy of -64.4 kcal mol^{-1}. These results indicate that although copper is more active towards O_2 dissociation than the other two coinage metals previously studied, the oxidized copper systems are so stable that their activity in oxidation reactions might be hindered by the energy cost required to transfer the adsorbed oxygen atoms to reactant molecules.

3.3.2. O_2 dissociation kinetics and comparison with experiment.

From the results shown in the past section on the dissociation of O_2 on Cu_n clusters of increasing size, a clear reactivity trend with cluster atomicity is stablished: calculated activation energies for O-O bond dissociation increase from less than 10 kcal/mol on small copper nanoparticles of ~1 nm diameter, to 15-20 kcal/mol on 3D clusters composed by 7-10 atoms, and to more than 40 kcal/mol on planar Cu_n clusters with $n \leq 5$. The question remains whether there is also a trend in the further reducibility of these copper clusters composed by a few atoms, which is key to stabilize metallic copper species and to produce efficient and long-lasting oxidation catalysts. In order to address this question, the computed Gibbs free energies have been used to calculate equilibrium constants and kinetic constants for adsorption, dissociation and recombination processes.

The optimized structures of reactant ($Cu_n - O_2$), transition state (TS) and product ($Cu_n - 2O$) of O_2 dissociation reaction over Cu_5, Cu_8 and Cu_{13} model clusters are depicted again in Figure 3.15 together with the corresponding Gibbs free energy profiles. These sizes are representative of small, medium and larger clusters, and directly comparable to the samples of a narrow size distribution synthesized by our ITQ colleagues[107].

The oxidation of clusters by reaction with molecular O_2 could be described by:

$$Cu_n + O_2 \overset{K_{ads}}{\longleftrightarrow} Cu_n - O_2 \overset{k_{dis}}{\longrightarrow} Cu_n - 2O \qquad \text{(Eq 3.3.1-1)}$$

Where K_{ads} is the equilibrium constant for O_2 adsorption on the Cu_n clusters and k_{dis} is the kinetic constant for dissociation of the O-O bond in adsorbed O_2.

They can be calculated as: $K_{ads} = e^{\frac{-\Delta G_{ads}}{RT}}$, and $k_{dis} = \frac{k_B T}{h} e^{\frac{-\Delta G^{\ddagger}_{dis}}{RT}}$, respectively, with the Boltmann constant k_B = 1.38065·10^{-23} J K^{-1} and the Planck constant h = 6.62607·10^{-34} J·s.

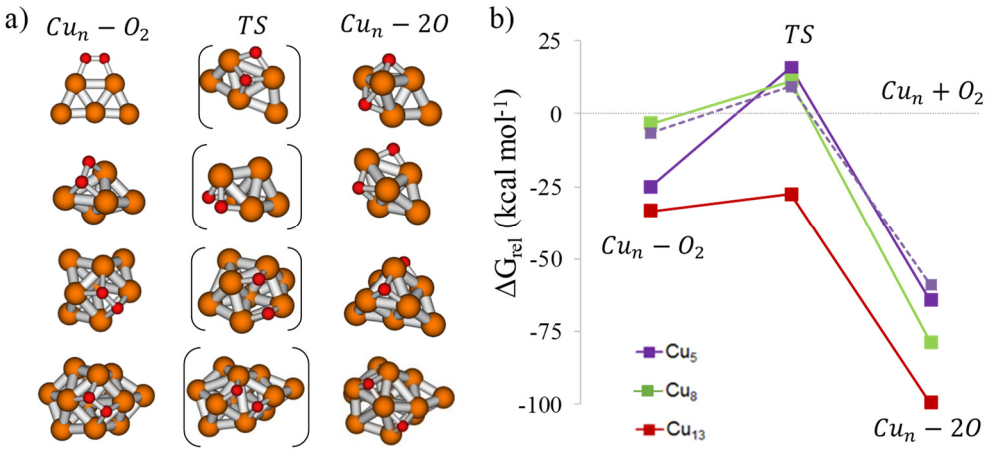

Figure 3.15. a) Optimized structures of reactant, transition state and product and b) calculated Gibbs free energy profile for dissociation of molecular O_2 into two adsorbed O atoms over Cu_5 (purple), Cu_5-3D (purple, dashed lines), Cu_8 (green) and Cu_{13} (red) clusters.

From equation (3.3.1-1), the amount of dissociated $Cu_n - 2O$ species will depend on the product $K_{ads}·k_{dis}$, whose variation with temperature is plotted in Figure 3.16b, as well as that of k_{dis}. As suggested by the activation free energy barriers, the kinetic k_{dis} constant and therefore the rate of O_2 dissociation increases with temperature and follows the order $Cu_{13} > Cu_8 > Cu_5$. But when O_2 adsorption is also taken into account, the difference between Cu_{13} and the smaller clusters widens, and the rate of oxidation of Cu_{13} becomes twenty orders of magnitude larger (Figure 3.16a,b), a difference that should be clearly observable experimentally.

In a similar way, the reduction of the oxidized systems could be described by:

$$Cu_n - 2O \xrightarrow{k_{rec}} Cu_n - O_2 \xleftrightarrow{K_{des}} Cu_n + O_2 \qquad \text{(Eq. 3.3.1-2)}$$

Where k_{rec} is the kinetic constant for recombination of two O atoms into adsorbed O_2 and K_{des} is the equilibrium constant for O_2 desorption from the Cu_n clusters. They can be calculated as $k_{rec} = \frac{k_B T}{h} e^{\frac{-\Delta G^{\ddagger}_{rec}}{RT}}$ and $K_{des} = e^{\frac{-\Delta G_{des}}{RT}}$, respectively.

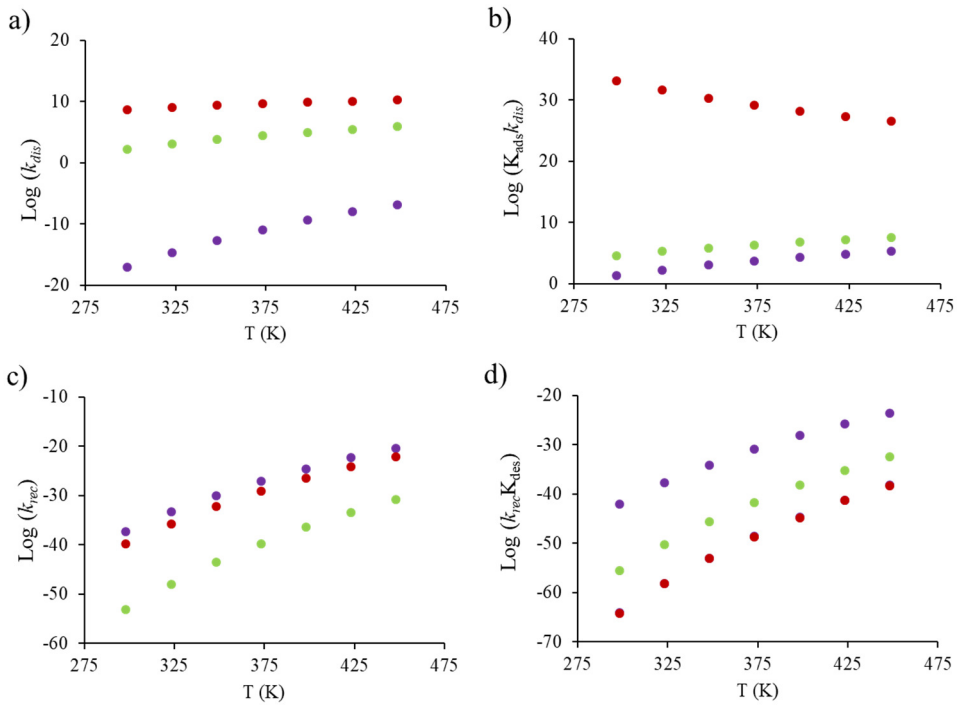

Figure 3.16. Logarithm of calculated a) kinetic constant for O_2 dissociation, k_{dis}, b) product of equilibrium constant for O_2 adsorption by k_{dis}, $K_{ads} \cdot k_{dis}$, c) kinetic constant for recombination of two O atoms forming adsorbed O_2, k_{rec}, and d) product of equilibrium constant for O_2 desorption by k_{rec}, $K_{des} \cdot k_{rec}$, as a function of temperature over Cu_5 (purple) Cu_8 (green) and Cu_{13} (red) clusters.

Notice that O_2 dissociation over Cu_5 causes a morphological change of the cluster from planar to 3D, and as a consequence a different pathway exists for the recombination step on Cu_5 (purple dotted lines in Figure 3.15b) that involves a lower Gibbs free activation energy barrier and produces a less stable adsorbed O_2 system. Again, the k_{rec} and $k_{rec} \cdot K_{des}$ calculated using the DFT Gibbs free energy values were plotted as a function of temperature (Figure 3.16c,d). While the trend in the kinetic constant k_{rec} for recombination of two O atoms over Cu_5 and Cu_{13} is not too different, when desorption of the formed O_2 molecule leaving the naked cluster is taken into account the global process is clearly favored on Cu_5 cluster, suggesting an easier reduction of the smallest copper clusters.

Finally, the strength of the interaction between copper clusters and atomic oxygen was measured by the interaction energy, ΔG_{int}, calculated as:

$$\Delta G_{int} = G(Cu_n - O) - G(Cu_n) - \tfrac{1}{2}\, G(O_2) \qquad \text{(Eq. 3.3.1-3)}$$

The values obtained, -25.1, -32.1 and -36.1 kcal·mol^{-1} for Cu_5, Cu_8 and Cu_{13} clusters respectively, are in line with the relative stability of the Cu_n – 2O systems shown in Figure 3.15, and suggest that the O atoms adsorbed on small clusters should be easier to transfer to other molecules than those adsorbed on larger three-dimensional copper clusters.

Thus, the higher ability of copper clusters of increasing atomicity to be oxidized leading to a relatively stable copper oxide compound agrees with literature data[18-22] and explains the observed catalytic behavior of conventional copper catalysts. In opposite to that behavior, we found high activation barriers for O_2 dissociation and an easier reduction of oxidized Cu_5 clusters allowing stabilization of metallic copper under oxidizing reaction conditions.

In order to confirm the trends arising from the DFT study, the oxidation-reduction behavior of synthesized copper clusters of controlled atomicity was evaluated by means of surface sensitive spectroscopic tools, namely, X-ray Photoelectron Spectroscopy (XPS) and Surface Enhanced Raman Spectroscopy (SERS). XPS was used to determine the chemical state of the copper species, while SERS provides information about the interaction of copper samples with O_2.

The evolution of the Cu $2p_{3/2}$ XPS core level binding energies (BE) and Cu L_3VV Auger electron kinetic energies (KE) of the Cu_5, Cu_8 and Cu_{20} samples under controlled atmospheres (N_2 and O_2) at different temperatures are shown in Figure 3.17.

The BE value of 934.3 eV and the Cu L_3VV Auger peak at 917.5 eV of the as-synthesized Cu_{20} correspond to Cu^{2+} ions in a CuO like structure. The oxidized state was stable under N_2 atmosphere up to a temperature of 250°C and only partially reduced at 300°C, as revealed by the growth of a new component at a BE of 932.8 eV. After exposing the sample to molecular O_2, this peak decreased again in intensity due to a re-oxidation of the Cu_{20} clusters (Figure 3.17e,f).

Cu_5 and Cu_8 clusters were pre-activated in N_2 at 120°C prior to each study, in order to remove any adsorbed species remaining from the synthetic procedure. After this pre-treatment, a similar Cu $2p_{3/2}$ BE peak at 932.7 eV was observed in the XPS spectra of both samples (Figure 3.17a,c), but the Cu L_3VV Auger kinetic energies were different: 916.0 eV for Cu_5 and 914.2 eV for Cu_8 (Figure 3.17b,d). After exposing the clusters to N_2 and O_2 atmospheres, only modifications in the Cu L_3VV Auger electron KE were detected, due to the higher sensitivity to chemical environment effects of Auger peaks as compared to core level XPS values[237,238].

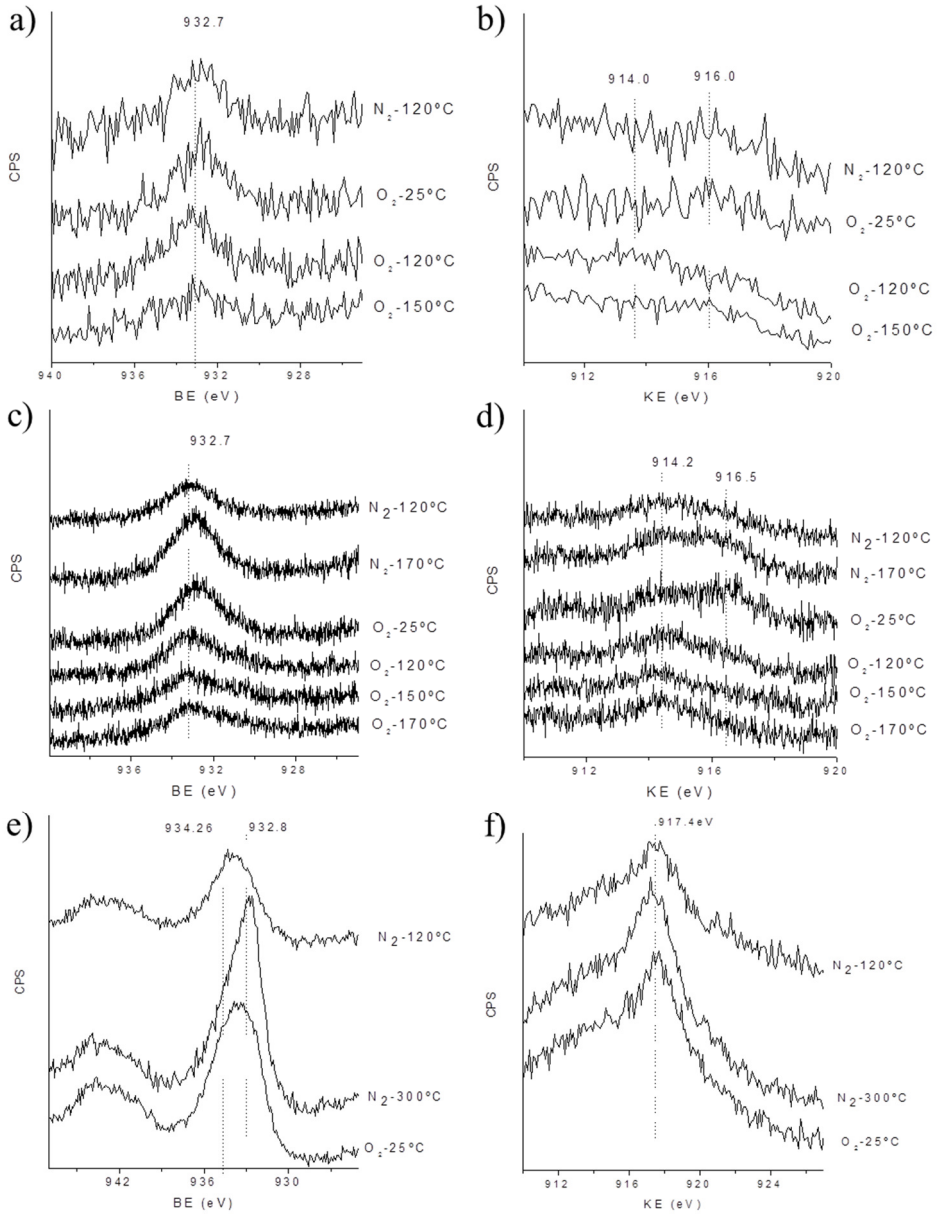

Figure 3.17. XPS study of Cu_5 (a-b), Cu_8 (c-d) and Cu_{20} (e-f) samples under N_2-O_2 treatments at different temperatures. a,c,e) Cu $2_{p3/2}$ XPS peak and b,d,f) CuL_3VV Auger peak.

For the Cu_8 sample, a peak at 916.5 eV appears when increasing temperature to 170°C in N_2 (Figure 3.17d), similar to the one previously observed in the Cu_5 sample (at 120°C in N_2). At this state, replacing N_2 with O_2 at a temperature of 25°C did not lead to any change. When temperature rose to 120°C under O_2 atmosphere, this peak was lost again restoring the initial 914.2 eV peak, and it remained stable even after further increasing temperature to 150 and 170°C in the presence of O_2.

For the Cu_5 sample, however, a peak at 914.0 eV was only partially observed at 120°C under O_2 atmosphere, but it evolved again to the original 916.0 eV peak with further increase of the temperature to 150°C (in the same O_2 atmosphere).

Considering these shifts and comparing with the trends reported in the literature for copper compounds[239,240], the peak at 914 eV was assigned to oxidized copper species and the peak at 916 eV to copper species in a metallic state. In that case, the XPS studies would indicate that Cu_8 clusters were initially oxidized, then reduced at 170ºC in N_2, and then reoxidized at 120ºC in O_2, whereas Cu_5 would be initially reduced, partially oxidized at 120ºC in O_2 and reduced again at 150ºC in O_2. Thus, XPS results would show a lower ability of Cu_5 clusters to interact with oxygen as compared to Cu_8 clusters, in agreement with the DFT results.

To confirm this behavior, the Cu-O interaction in Cu_5 and Cu_8 samples under N_2 or O_2 atmospheres was also followed by SERS (Figure 3.18). In order to assist in the assignation of the bands in the SERS spectra, the interaction of O atoms, O_2 and H_2O molecules, OH and OOH groups on Cu_5 and Cu_8 clusters was modelled by means of DFT calculations. The optimized structures are collected in Figures 3.19 – 3.22, and the calculated vibrational frequencies, organized according to the chemical system and the vibrational modes considered, are summarized in Table 3.12.

In the Cu_5 sample, the main Raman bands after N_2 treatment at 120°C appear in the 1035-1370 cm^{-1} frequency range, and are usually ascribed in the literature to different types of ν(O-O) stretching modes[241,242]. A signal at 270 cm^{-1} and a small peak at 388 cm^{-1}, which are in general related to Me-O stretching modes associated to atomic oxygen species and/or hydroxyl groups[243] were also observed. However, all these peaks were completely removed at 150°C under N_2 atmosphere, indicating a weak Cu-O interaction that leads to O_2 desorption from the metallic Cu_5 clusters.

Changing the gas flow from N_2 to O_2 at 25°C resulted in the appearance of bands at 1045, 1185, 1295, 1335 and 1390 cm^{-1}, associated to the O-O bond stretching frequency in O_2 adsorbed in mono-coordinated or bridge conformations, and at 270 cm^{-1} which can be unambiguously ascribed to stretching of the Cu-O bond in molecularly adsorbed O_2. These bands were stable at 80°C, but increasing the temperature to 120°C under O_2 flow caused a decrease in the intensity of all signals, which was especially visible in the disappearance of the 270 cm^{-1} band. Since XPS data pointed

to a partial oxidation of the Cu_5 clusters at this stage, some O_2 dissociation may occur. In fact, two small Cu-O stretching signals at 355 and 650 cm^{-1}, corresponding to atomic O, were observed at 80°C (green line in Figure 3.18b).

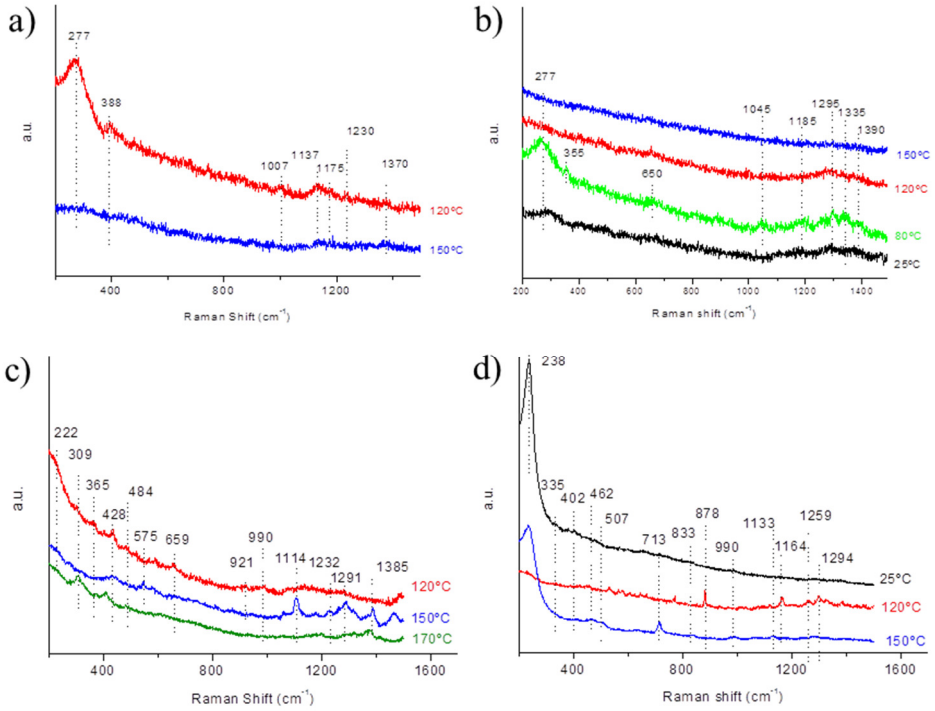

Figure 3.18. SERS spectra of Cu_5 (a,b) and Cu_8 (c,d) under N_2 flow at increasing temperatures (a,c) and after switching to O_2 flow at different temperatures (b,d).

In the Raman spectra corresponding to Cu_8 sample, not only bands at high frequencies (1061, 1127, 1291 and 1430 cm^{-1}) but also lower frequency peaks were observed, ranging from 220 cm^{-1} to 922 cm^{-1}, which indicate the presence of atomic O. These bands decreased in intensity under N_2 flow at increasing temperatures, but they were not completely removed even at 170°C (Figure 3.18c). By changing the N_2 flow to O_2 flow at 25°C, no change in the SERS spectra could be observed. However, when increasing the temperature to 120°C in the presence of O_2 flow, new bands in the 250-700 cm^{-1} frequency range started to appear (Figure 3.18d) which, according to the DFT values reported in Table 3.12, are related to Cu-O stretching modes. These bands remained stable at 150°C, and confirm the higher stability of oxidized Cu_8 clusters as compared to Cu_5 clusters, in agreement with DFT and XPS results.

Therefore, XPS and SERS data under the different atmospheres confirm the DFT conclusions and subsequent kinetic results by proving that indeed small Cu_5 clusters are easier to reduce and more difficult to oxidize than Cu_8, with Cu_{20} nanoparticles being much less reducible and much more easily re-oxidized (at 25°C).

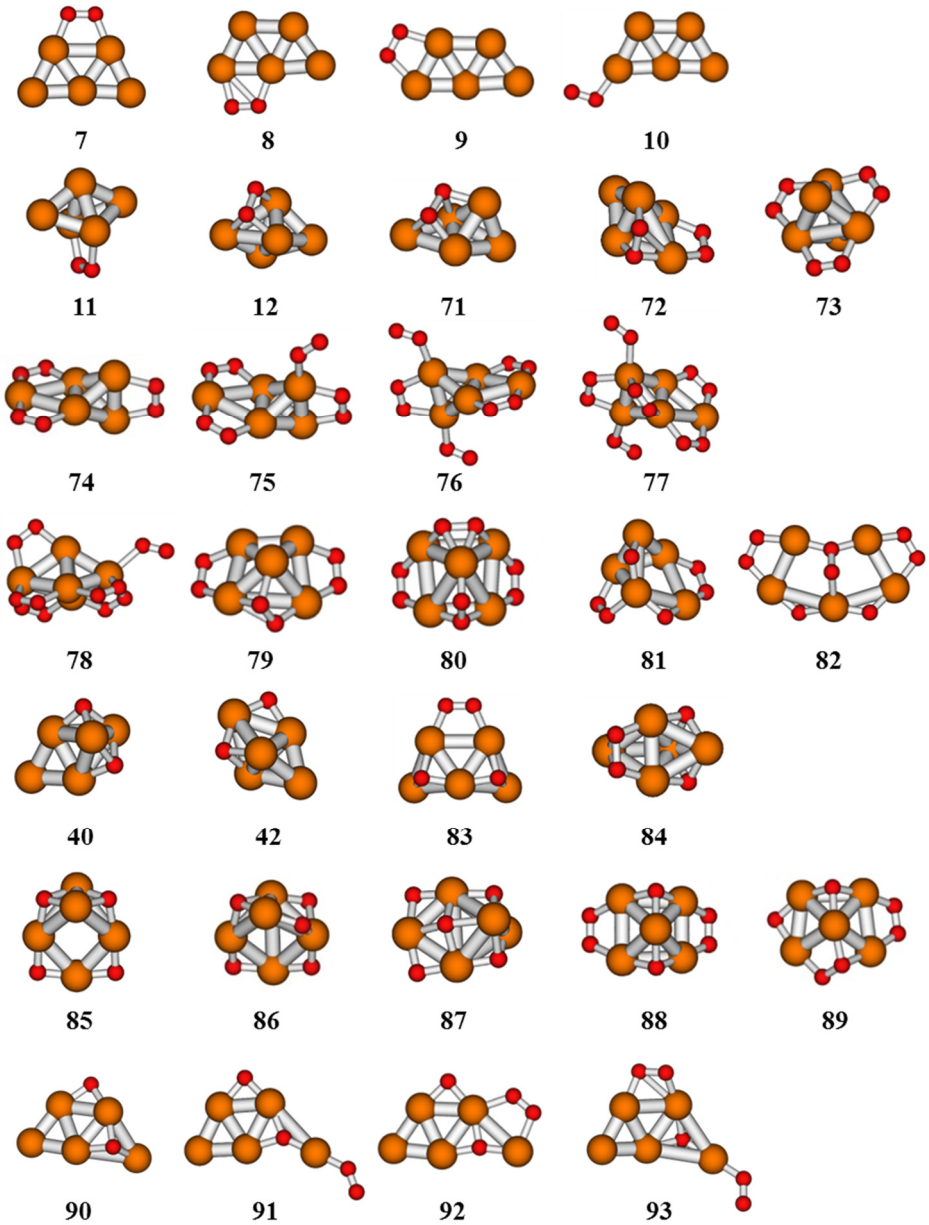

Figure 3.19. Optimized geometries of Cu_5-nO_2 and Cu_5-nO systems used to calculate the vibrational frequencies summarized in Table 3.11.

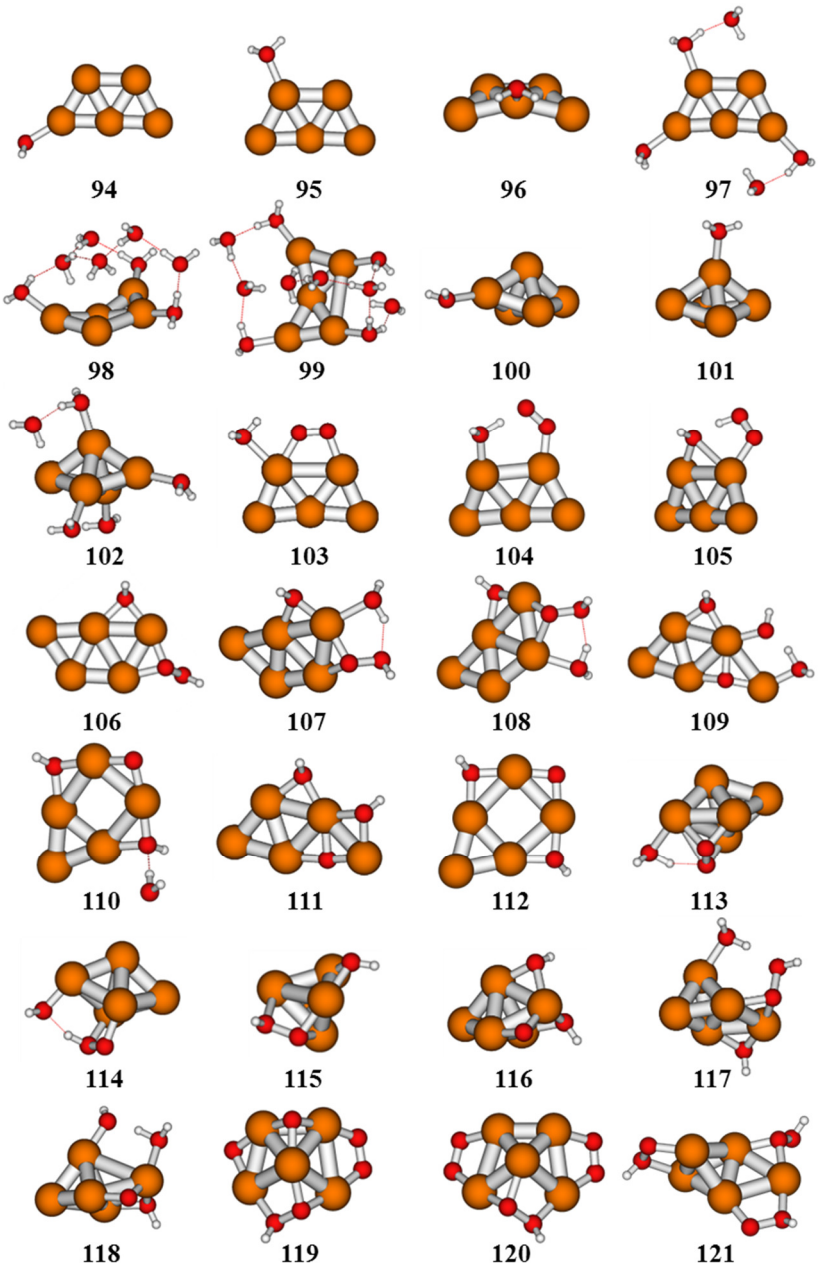

Figure 3.20. Optimized geometries of Cu_5-nH_2O and Cu_5-nO_2-mH_2O systems used to calculate the vibrational frequencies summarized in Table 3.12.

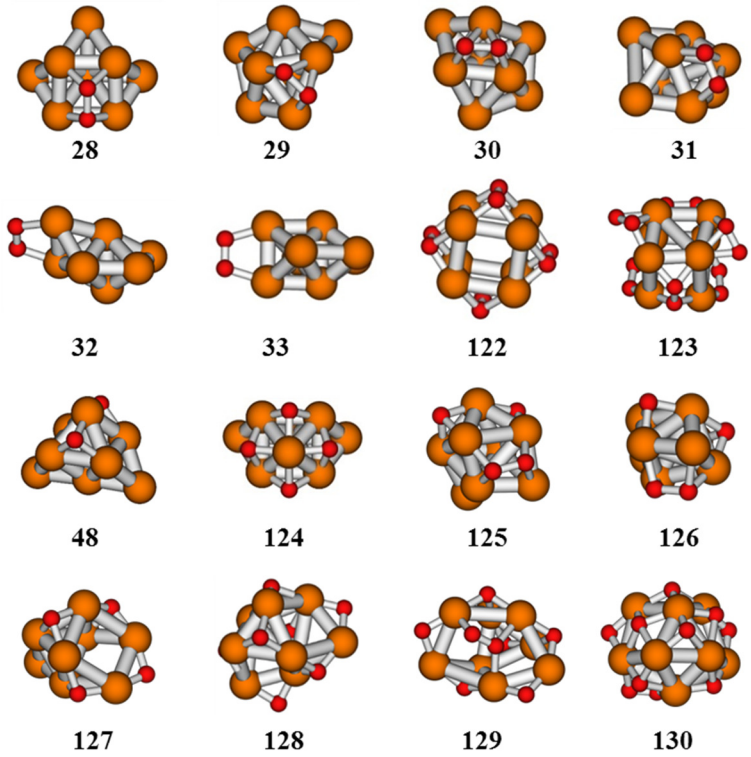

Figure 3.21. Optimized geometries of Cu_8-nO_2 and Cu_8-nO systems used to calculate the vibrational frequencies summarized in Table 3.12.

Table 3.12. Calculated vibrational frequencies (in cm^{-1}) for selected vibrational modes in the adsorption complexes depicted in Figures 3.19 – 3.22.

System	Vibrational mode		Cu_5	Cu_8
$Cu_n + O_2$	O-O stretching	*mono*	1180 – 1440	
		bridge	1080 – 1260	1040 - 1130
		h-111	730 – 880	730 - 810
	Cu-O stretching	*atomic O*	300 – 670	300 - 650
		molecular O_2	220 – 580	240 - 570
$Cu_n + O_2$ + H_2O	O-OH stretching	*mono*	1175	-
		bridge	780 – 870	780 - 850
		h-111	730 – 760	690 - 810
	O-OH bending	*OOH*	1190 – 1300	1160 - 1490
	Cu-O stretching	*OOH or OH*	330 – 510	340 - 530
		H_2O	240 - 360	220 - 350
	Cu-OH bending	*OH*	470 - 720	440 - 740

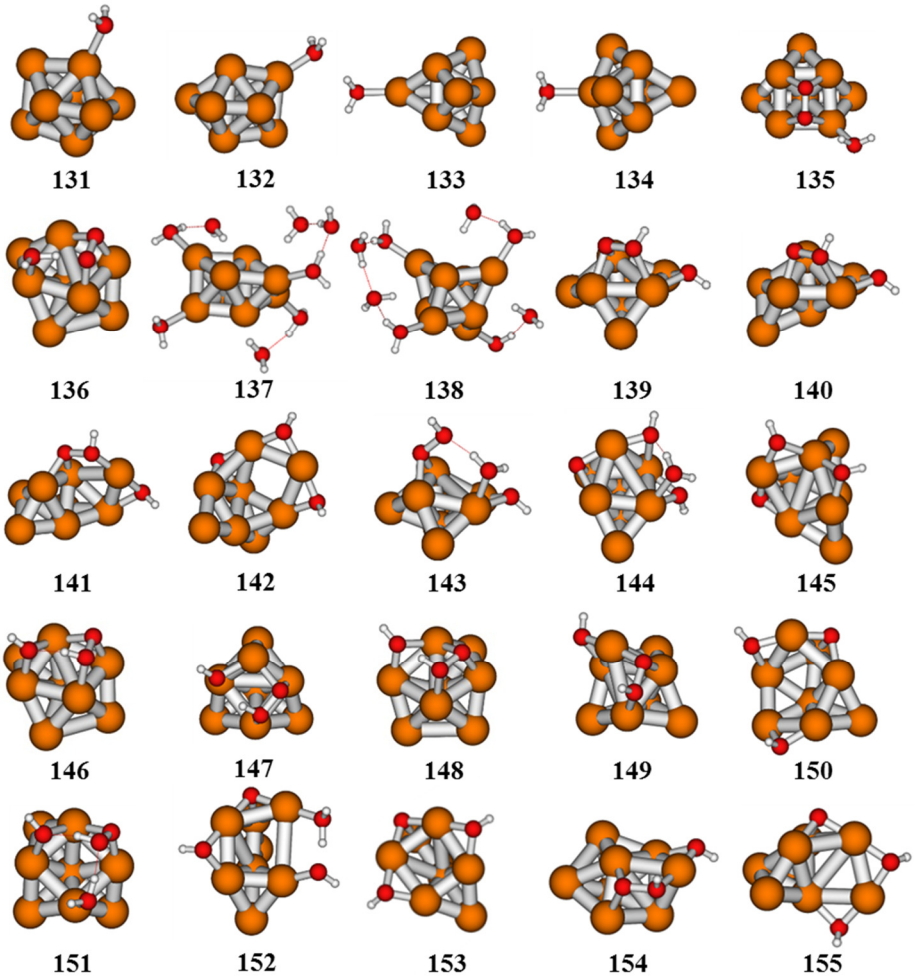

Figure 3.22. Optimized geometries of Cu_8-nH_2O and Cu_8-nO_2-mH_2O systems used to calculate the vibrational frequencies summarized in Table 3.12.

3.3.3. Influence of H_2O in the O_2 dissociation by Cu clusters.

While the high energetic barrier for O_2 dissociation on planar Cu_5 clusters could hinder the global oxidation activity of Cu_5, the presence of other reactant molecules may modify the energetic profile and, accordingly, cluster reactivity[244]. For this reason the role of water on O_2 dissociation, which is present in many reactions as a reactant, product or solvent, has been evaluated and discussed. Thus, the complete reaction path for O_2 dissociation over Cu_5 and Cu_8 clusters in the presence of co-adsorbed water was theoretically investigated in this section, at the same DFT level.

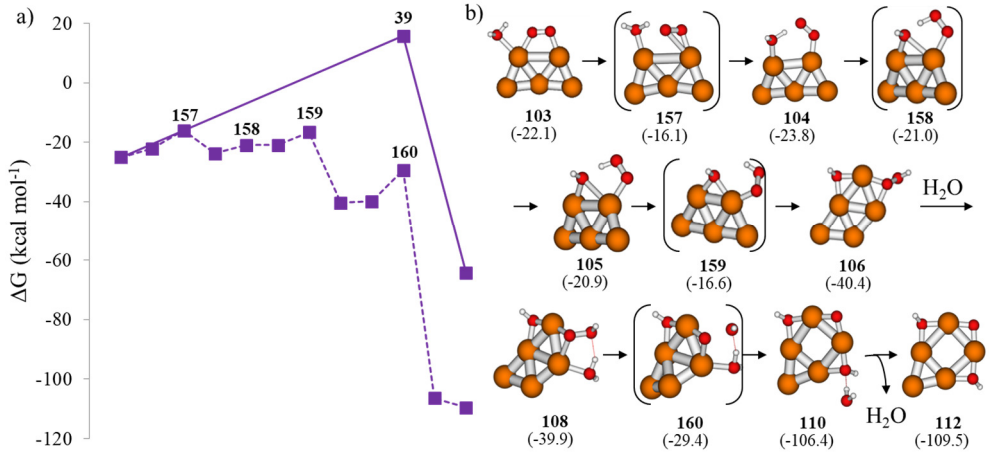

Figure 3.23. a) Calculated Gibbs free energy profiles for O_2 dissociation in the absence (solid lines) and presence (dashed and dotted lines) of water over planar Cu_5 clusters and b) optimized structures of all species involved in the water-assisted dissociation of O_2 over the planar Cu_5 cluster.

Figure 3.23 shows the calculated Gibbs free energy profiles for dissociation of one molecule of O_2 over Cu_5 planar clusters in the absence (solid line) and presence (dashed line) of water, and the optimized geometries of the structures involved in these processes. As previously shown, molecular O_2 adsorbs in a bridge conformation over the most stable isomer of planar Cu_5 and dissociates with a high activation free energy barrier of 40.7 kcal mol^{-1}, yielding a 3D cluster with two adsorbed O atoms (see Figure 3.15). Co-adsorption of a water molecule close to O_2 on planar Cu_5 facilitates the rupture of a copper-oxygen bond to produce, through transition state **157** with a free energy activation barrier as low as 6.0 kcal mol^{-1}, a system in which a hydrogen atom stabilizes the now mono-coordinated oxygen. It is easy from this point to generate co-adsorbed hydroxyl and hydroperoxyl groups (structure **105**) in a process that involves a very low activation barrier of 2.7 kcal mol^{-1}. The mono-

coordinated OOH group tends to form a more stable bi-coordinated fragment, thus causing a rearrangement of the copper atoms in the cluster which ultimately produces the highly stable structure **106** with an activation energy of only 4.3 kcal mol^{-1}. There is not a direct pathway for dissociation of the O-O bond in this system, but addition of a second water molecule yields structure **108**, with the H_2O molecule attached to the Cu atom in contact with the OOH ligand. A proton transfer from the adsorbed water to the OOH group breaks the O-O bond and generates intermediate **110** with an activation free energy barrier of 10.6 kcal mol^{-1}. Finally, water desorption leaves a Cu_5 cluster with two hydroxyl groups and one O atom, the three of them adsorbed in concatenated edge modes that deform the cluster to a planar square capped geometry. As clearly observed in the energy profile, the rate determining step in the global process is the dissociation of the O-O bond in structure **108** through transition state **160**, with a calculated activation energy of only 10.6 kcal mol^{-1}, which is much lower as compared to the 40.7 kcal mol^{-1} obtained in the absence of water. The lowering of the barrier by 30 kcal mol^{-1} when water is present increases the calculated rate constant for O_2 dissociation k_{dis} by 20 orders of magnitude. So, the presence of water in the reaction media would considerably enhance the ability of Cu_5 clusters to activate molecular O_2.

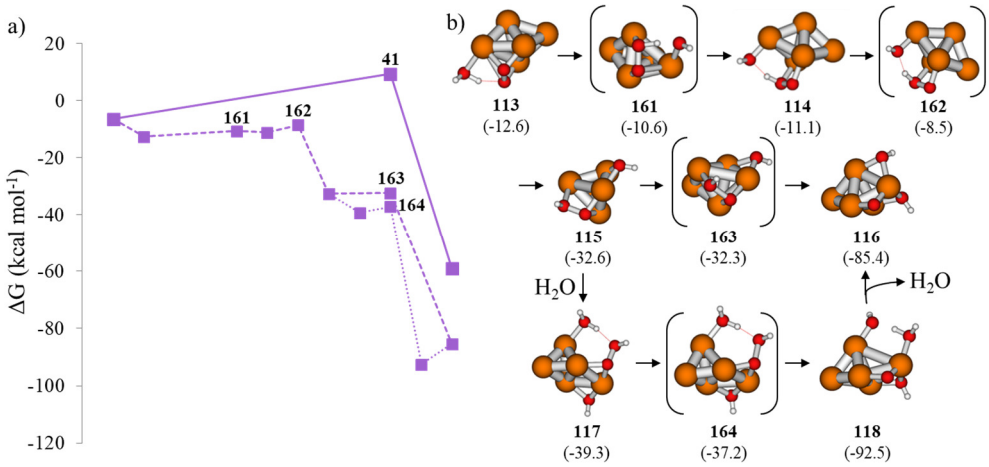

Figure 3.24. a) Calculated Gibbs free energy profiles for O_2 dissociation in the absence (solid lines) and presence (dashed and dotted lines) of water over 3D Cu_5 clusters and b) optimized structures of all species involved in the water-assisted dissociation of O_2 over the 3D Cu_5 cluster.

Similar results are obtained when evaluating the H_2O-assisted dissociation of O_2 in 3D Cu_5 and Cu_8, whose energy profiles are shown in Figures 3.24-26. As the barriers for O_2 dissociation in absence of water are lower on these 3D clusters, the decrease

in the activation energy of the O-O bond dissociation is less pronounced. Nevertheless, in all cases the barriers are now lower than 8 kcal mol^{-1}. It is important to notice that in these 3D clusters the preferential adsorption on the *h-111* and *h-100* modes is again found here for the OOH species. As a consequence, there is no need to adsorb a second water molecule to facilitate de dissociation of the O-O bond, which easily breaks on these facets where the molecule is more activated (structures **115**, **141** and **171** in Figures 3.24, 3.25 and 3.26, respectively). As it can be seen in the same figures, the adsorption of the second water molecule mentioned does not change the mechanisms significantly.

TS **167** shows a 0.3 kcal mol^{-1} lower energy than its previous minimum **141** (Figure 3.25). The two structures are correctly characterized as a TS and a minimum, i.e. with a single imaginary frequency mode corresponding to the breaking of the O-O bond and no imaginary frequencies, respectively. In fact, when only electronic energy is considered, the TS is 0.3 kcal mol^{-1} higher in energy than the minimum. As soon as vibrational contributions are considered, through ZPVE or entropy, the order is reversed. The net difference is thus less than 1 kcal mol^{-1}, hence fully within both the mean error of the computational level employed. As we are not pursuing chemical accuracy and given that the structures are characterized correctly, we did not dwell further in other treatments to obtain more precise free energy values.

In addition, as indicated in the captions of Figures 3.25 and 3.26, the paths shown for Cu_8 clusters start from structures **135** and **136**, respectively. Said structures were obtained from the adsorption of a water molecule in the two different copper sites near the oxygen molecule in structure **28**. However, we were not able to find the transition state structures leading from **135** and **136** to **139** and **146**, respectively. Scans along the O-H distance showed an ever decreasing energy as the hydrogen moved from the water molecule to the O_2. It can therefore be safely concluded that the transition state is going to be much more similar to the initial minimum and the step can be assumed as essentially barrierless.

A higher number of steps are found in the mechanisms for Cu_8 clusters as opposed to those of Cu_5 clusters, and the additional ones are related to changes in the position of the copper atoms with activation energies that are generally lower than 3 kcal mol^{-1}. This fact further illustrates the fluxionality of small metallic clusters, which on the one hand provides them of interesting additional options in catalysis and on the other hand difficults their study.

The easier reducibility of smaller 3D Cu_5 clusters is again observed here, for their recombination barrier is almost 20 kcal mol^{-1} lower than that of Cu_8 or planar Cu_5 clusters (76, 53 and 70 kcal mol^{-1} for planar Cu_5, 3D Cu_5, and Cu_8, respectively, see Figures 3.23-3.26).

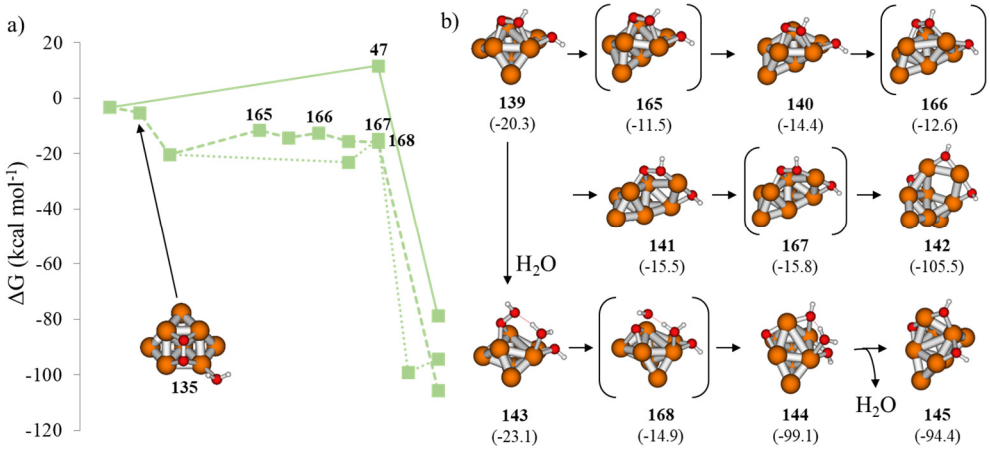

Figure 3.25. a) Calculated Gibbs free energy profiles for O_2 dissociation in the absence (solid lines) and presence (dashed and dotted lines) of water (starting from structure **135**) over Cu_8 clusters and b) optimized structures of all species involved in the water-assisted dissociation of O_2 over the Cu_8 cluster starting from structure **135**, which is shown on the left within the graph.

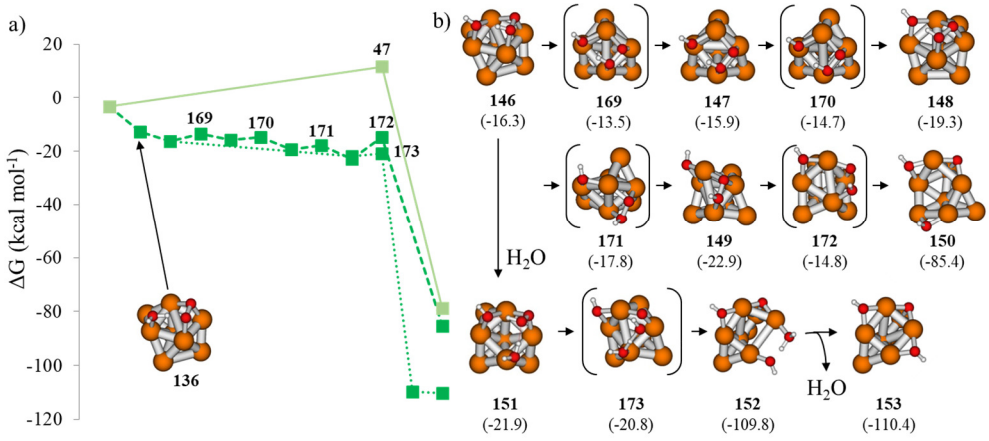

Figure 3.26. a) Calculated Gibbs free energy profiles for O_2 dissociation in the absence (solid lines) and presence (dashed and dotted lines) of water (starting from structure **136**) over Cu_8 clusters and b) optimized structures of all species involved in the water-assisted dissociation of O_2 over the Cu_8 cluster starting from structure **136**, which is shown on the left within the graph.

These results were experimentally confirmed by SERS and XPS spectroscopic studies of the interaction of fully reduced Cu_5 clusters (after N_2 treatment at 120ºC) with pure water and with a mixture of water and O_2 (Figure 3.27).

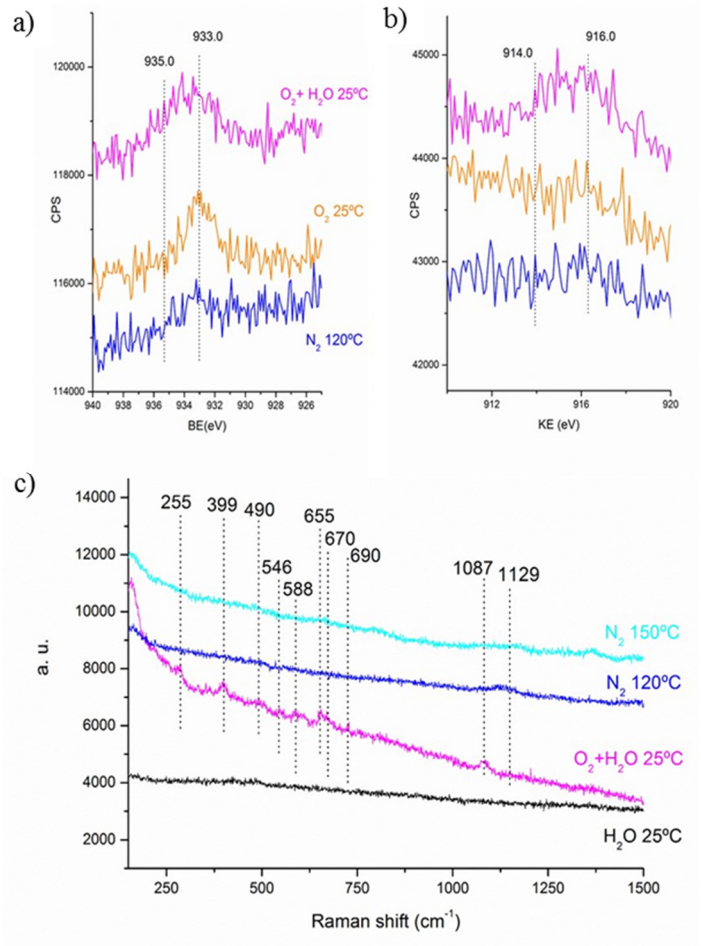

Figure 3.27. a) Cu $2_{p3/2}$ XPS peak and b) CuL3VV Auger peak of the XPS spectra of fully reduced Cu_5 cluster after N_2 treatment at 120°C, followed by subsequent O_2 flow at 25°C and 3%H_2O/O_2 flow at 25°C, and c) SERS spectra of fully reduced Cu_5 cluster (after N_2 treatment at 120°C) exposed to 3% H_2O/N_2 flow at 25°C, 3%H_2O/O_2 flow at 25°C, N_2 flow at 120°C and N_2 flow at 150°C.

As discussed before, only bands associated to molecularly adsorbed O_2 were detected in the SERS spectra of Cu_5 under O_2 atmosphere at 25°C (see Figure 3.18b).

In a similar experiment in the presence of only water (3wt% H_2O in N_2 flow) at 25°C, no bands were observed (Figure 3.27c, black line), which demonstrates that Cu_5 clusters are not able to activate neither O_2 nor H_2O separately at 25°C. However, in the presence of a mixture of both O_2 and H_2O, (3wt% H_2O in O_2 flow) besides the bands at 255, 1087 and 1129 cm^{-1} corresponding to molecular O_2 adsorbed in a bridge conformation, several peaks at 399, 490, 546, 588, 655, 670 and 690 cm^{-1}, are clearly observed in Figure 3.27c, pink line. According to literature and to the data presented in Table 3.12, the peaks between 580 and 670 cm^{-1} are associated either to Cu-O stretching modes of atomic O or to bending modes of Cu-OH bonds, which demonstrate the promoting effect of water in dissociating O-O bonds, in agreement with the calculated mechanisms.

Similar behavior could be deduced from the XPS spectra. As discussed before, after N_2 treatment at 120°C Cu_5 clusters appear in a metallic state which remains stable even after O_2 treatment at 25°C (Cu $2_{p3/2}$ XPS BE of 932,7 eV and Cu L_3VV KE of 916.0 eV). However, in the presence of 3% water in O_2 flow a broadening of the Cu L_3VV peak toward higher KE (914.5 eV) could be observed, indicating the formation of oxidized copper species.

As regards the reducibility of the partially oxidized system, it was found that increasing temperature to 120° and 150°C under N_2 atmosphere leads again to a clean SERS spectra due to complete desorption of all species (Figure 3.27c, blue lines), much like what was already observed in the previous experiments after the synthesis of the Cu_5 clusters and fully in agreement with the computational results.

3.4. Conclusions.

Firstly, the comparison of the results on the adsorption and dissociation of the O_2 molecule in Cu_n clusters of size n=3-8, 13 and 38 at different computational levels shows that the absolute values of adsorption, activation and reaction energies are not directly comparable. However, the species involved in the reaction mechanisms and the trends found with particle size and shape are similar, thus ultimately reaching the same qualitative conclusions.

Regarding O_2 interaction with copper clusters, as with other metal clusters it involves a transfer of electron density from the metal HOMO to the anti-bonding π^* of O_2, and the calculated adsorption energies correlate with the HOMO energy of the isolated clusters. The electron density transfer resulting from this interaction weakens and hence activates the O-O bond, facilitating its dissociation. The degree of O-O

bond activation, indicated by the optimized r_{OO} distances or the shifts in the ν_{OO} vibrational frequencies, directly correlates with the net charge on adsorbed O_2, and is determined by the mode of adsorption of O_2 on the copper clusters. Thus, adsorption on 100 or 111 facets allows a larger degree of electron density transfer than adsorption at corners or edges adopting *bridge*, *mono* or *top* conformations.

The role of particle morphology is thus key because it determines the preferential mode of adsorption of O_2, with the most activating *h-100* and *h-111* modes being preferentially stabilized over 3D clusters. The influence of particle size is partly related to particle shape. Small Cu_3, Cu_4 and Cu_5 clusters are planar, and the electronic activation energies needed to dissociate O_2 are larger than 40 kcal mol^{-1}. Activation barriers around ~ 15 kcal mol^{-1} are found for 3D clusters with n = 5-8, and still decrease to 6-10 kcal mol^{-1} over larger Cu_{13} or Cu_{38} nanoparticles. These results indicate that small planar 2D copper clusters are less active towards O_2 dissociation than larger 3D clusters or nanoparticles, but it also means that they should be more stable against oxidation, a feature that might be relevant when trying to stabilize metallic copper systems. Similarly, the high stability of the oxidized 3D clusters and nanoparticles might have a negative impact into their reactivity in oxidation reactions, due to the energy cost required to transfer the adsorbed oxygen atoms to reactant molecules.

Theoretical kinetic studies for Cu_5, Cu_8 and Cu_{13} further show the differential behaviour of small Cu_5 clusters, being less susceptible to be oxidized with respect to larger clusters, and also more easily reduced back to metallic copper. Experimental XPS and SERS studies under different atmospheres on comparable samples of Cu_5, Cu_8 and Cu_{13} clusters confirm these results. Therefore, it seems possible to stabilize metallic copper clusters under oxidizing reaction conditions by adjusting the atomicity of the copper cluster. Thus, Cu_5 clusters can be considered as very promising candidates for catalytic applications where stabilization of metallic copper species is strongly required, as in oxidation reactions.

Finally, both theoretical and experimental data have shown that the reactivity of Cu_5 (and Cu_8) clusters toward oxygen dissociation is strongly enhanced in the presence of water. The more dramatic effect is observed for planar Cu_5 clusters, where the calculated electronic barrier for the O_2 dissociation is almost 30 kcal mol^{-1} lower. Besides, in the case of 3D Cu_5 the interaction of the resultant oxygen species with the copper cluster is lower than for the rest, favouring oxygen recombination and O_2 desorption. Indeed, experiments observe the easy reduction of the Cu_5 sample even after the presence of water. This translates as well into a high reactivity of the O atomic species with other reactant molecules, and altogether these results situate Cu_5 clusters as very promising catalysts for catalytic applications where oxidation of copper species has to be avoided.

Chapter 4
Oxidation reactions on gas phase Cu clusters

This chapter continues the research line of Chapter 3. Firstly, the oxidation of CO is studied as another test for the viability of a catalytic cycle in oxidation reactions by Cu_n clusters of n = 5 and n = 8. As we further explain below, the catalytic activity in these reactions is usually assigned to either Cu^+ or Cu^0, but hardly to Cu^{2+}, which is why larger particles of copper, easily and irreversibly oxidized, are inactive.

Consistent with the results from Chapter 3, we will show that the largest differences in this reaction involve the planar morphology of the most stable isomer of Cu_5, whereas the 3D Cu_5 and Cu_8 exhibit a more similar behavior towards CO oxidation. Consequently, the final study on the selective oxidation of propene to propene epoxide is only carried out for both isomers of Cu_5, planar and 3D, considered representative enough of the smaller (planar) and medium (3D) copper clusters. Competing reactions are additionally explored to state whether the application of such clusters has a beneficial impact on selectivity, the key to the successful catalysis of propene epoxidation.

4.1. Introduction.

The CO oxidation is a prototypical reaction that has been extensively studied both fundamentally, in order to explore the oxidation capabilities of potential catalysts, and industrially, being very interesting for the selective oxidation of CO in fuel cells, preventing the oxidation of their valuable H_2[245,246], and for the catalytic conversion of automobile exhaust[247,248]. Since CO is an important pollutant, such processes are, in addition, convenient and interesting green routes. Small Au particles with less than 10 atoms have already been identified as the catalytically active species in this reaction[29,30], but cheaper alternatives would be industrially desirable, and copper seems a good candidate provided that it has a similar electronic configuration to gold. In this direction, copper nanoparticles display an excellent initial activity for CO oxidation, but deactivate under reaction conditions due to the easy oxidation of metallic Cu to cationic Cu^+ and Cu^{2+}[223,224]. Besides, a recent in situ study of CO oxidation over a Cu(111) model catalyst showed that even under highly reducing conditions with a $CO:O_2$ ratio of 99:1 and room temperature, the presence of O_2 induces surface reconstructions related to the oxidation/reduction of metallic copper/copper oxide domains[224]. It seems therefore really challenging to avoid the formation of oxide phases under reaction conditions, with the concomitant decrease in catalytic activity and selectivity. The resistance to oxidation shown by the smallest copper clusters, however, may be enough to overcome this problem.

Regarding propene epoxidation, propene or propylene oxide (PO) is an important industrial precursor of polyurethane and hence it is applied to produce commercial products such as foams or adhesives, among others[249-252]. The industrial processes to synthesize it are broadly divided into those employing chlorohydrin compounds and those employing hydroperoxides[252]. Since the former produce toxic chlorinated organic compounds as by-products, several approaches improving the latter exist. However, they still have problems: using organic hydroperoxides produces too large amounts of by-products that are useful but exceed the demand, and using H_2O_2 consumes H_2 for its generation and has the risk of potential explosion of the mixture of H_2 and O_2. Besides, all of them require several reaction steps. Thus, it would be better to find an alternative that does not need H_2 and reacts in fewer steps, preferably in a one-step reaction using only O_2.

Propene epoxidation using both H_2 and O_2 is achieved with high selectivity (< 80%) in Ag and Au nanoparticles supported on Ti-containing metal oxides, with a conversion of 2.0 and 5.3-9.8%, respectively[252]. For the direct oxidation of O_2, however, it was found that while all coinage metals can form PO, the size of the particle seems to be key, for the cases reported with more than 80% selectivity involve very small clusters of Ag and Au[36,252,253]. For Cu, in line with the previous statements, both Cu^0 and Cu^+ can catalyze the reaction (with up to 60% selectivity), but not Cu^{2+}, whereas for Ag and Au only the metallic state is active[252].

In addition, the reaction mechanism may be different on each coinage metal and particle size, and, if they are supported, the support material may participate. Such is the case for the Au/Ti-containing oxides catalysts that work well with H_2 and O_2, where the hydroperoxide is produced at the coinage metal whereas epoxidation takes place at Ti sites[252], and also for the direct epoxidation by subnanometer Ag_3 clusters and Ag aggregates of ~3.5 nm diameter on amorphous alumina, for which the active sites lie at the interface between the silver clusters and the support[36,126].

For copper-based catalysts it has been found that the formation of copper oxide domains under reaction conditions strongly affects their catalytic performance. In the alkene epoxidation a certain surface coverage of oxygen is needed for the reaction to proceed, and it has been reported that metallic copper exhibits a high selectivity to the epoxide that drops when the catalyst surface becomes oxidized[254]. Taking advantage of the light-induced reduction of Cu by photoexcitation of its localized surface plasmon resonance, Linic et al. succeeded in the stabilization of metal copper species under propene epoxidation reaction conditions, which resulted in an increase in the selectivity to PO from 20% to 50%[255].

It is therefore clear that to catalyze both oxidation reactions copper needs to avoid its oxidized Cu^{2+} state. Thus, in the present chapter we test the catalysis of CO and propene oxidation reactions by subnanometer copper clusters, following the results of Chapter 3 that conclude that metallic or Cu^+ species should be stabilized for Cu_5.

4.2. Computational details.

4.2.1. Models.

The two lowest energy isomers of Cu_5 (planar and 3D) and Cu_8 (T_d and D_{2d}) from the previous study were considered, and the most stable structures with O_2 adsorbed or dissociated were also taken from those of Chapter 3.

For each isomer, the different non-equivalent adsorption modes for all the pertinent molecules were built *ad hoc* and from literature results when available.

4.2.2. Methods.

All calculations in this work are based on density functional theory (DFT) and were carried out employing the Gaussian 09 program package[19]. The B3PW91 functional was employed, which combines the PW91 correlation functional by Perdew and Wang with Becke's hybrid three-parameter exchange functional[160]. Since in the previous study it was concluded that the Def2TZVP[173,174] basis set shows a very good performance at an affordable cost for Cu, it was used for Cu atoms whereas the standard 6-311+G(d,p) basis set by Pople was employed for the rest[233].

In all cases, the positions of all atoms in the system were fully optimized without any restriction, and all stationary points were characterized by pertinent frequency analysis calculations. Transition states were determined through potential energy surface (PES) scans along with the subsequent optimizations and vibrational frequency calculations. Atomic charges and molecular orbital distributions were calculated using the natural bond order (NBO) approach[188].
In addition, the MOLDEN[256], Jmol[257] and ChemCraft[258] programs were used throughout the work to visualize the systems and their frequencies and to obtain a graphical representation of their molecular orbitals.

4.3. Results.

4.3.1. CO oxidation on Cu_n (n = 5, 8) clusters.

4.3.1.1. Adsorption of CO and O_2 on Cu_n (n = 5, 8) clusters.

The adsorption of one molecule of carbon monoxide was studied on the two lowest isomers of Cu_5 and Cu_8 in three possible modes, classified by the number of interactions between the carbon atom and the copper atoms: monocoordinated on top of one Cu atom (*mono*), bicoordinated on the edge between two copper atoms (*bridge*), and on the hollow site of a (111) facet, with the carbon atom bonded to three Cu (*hcp*). A *mono* mode was obtained as preferential in all cases, with the bicoordinated mode being stable only for Cu_5 clusters (Figure 4.1a). Attempts to adsorb the CO in hollow sites always ended with the molecule moved to another position.

In addition, situations with higher CO coverage were considered for each cluster. Firstly, structures **4**, **8** and **14** were built with one CO molecule per copper atom in the most stable *mono* mode. The corresponding structure for the Cu_8-D_{2d} isomer was not stable and evolved into structure **14**. Secondly, the maximum amount of CO molecules that each cluster can adsorb was investigated. For planar Cu_5 clusters, the addition of more CO molecules produced a deformation of the cluster to the tridimensional isomer.

From Figure 4.1, it can be seen that interaction energies are somewhat stronger for Cu_5 than for Cu_8 clusters, consistent with previous studies[204,205], with structure **6** of the Cu_5-3D isomer as especially stable. The addition of one CO molecule per copper atom averages the interaction energy on all available sites, better showing the overall interaction of the clusters with CO. Hence, it can be seen that the interaction is best for Cu_5-3D clusters, whereas planar Cu_5 show the weakest interaction, and Cu_8 clusters have a somewhat stronger interaction than the latter. The strong interaction with the 3D isomer of Cu_5 compared to the weak interaction in its planar isomer can explain the deformation of the latter to the 3D one with the addition of even more CO molecules. As to the Cu_8-D_{2d} deformation, the very close energies of the Cu_8 isomers

allow their easy transformation into each other, even though the strength of the interaction in each one is not as different as between the two Cu_5 isomers. Finally, as it can be observed from the comparison of structures **8** and **14** with **9** and **15**, respectively, the addition of more CO molecules halves the average interaction energy, meaning that at least the last adsorption is not thermodynamically favored.

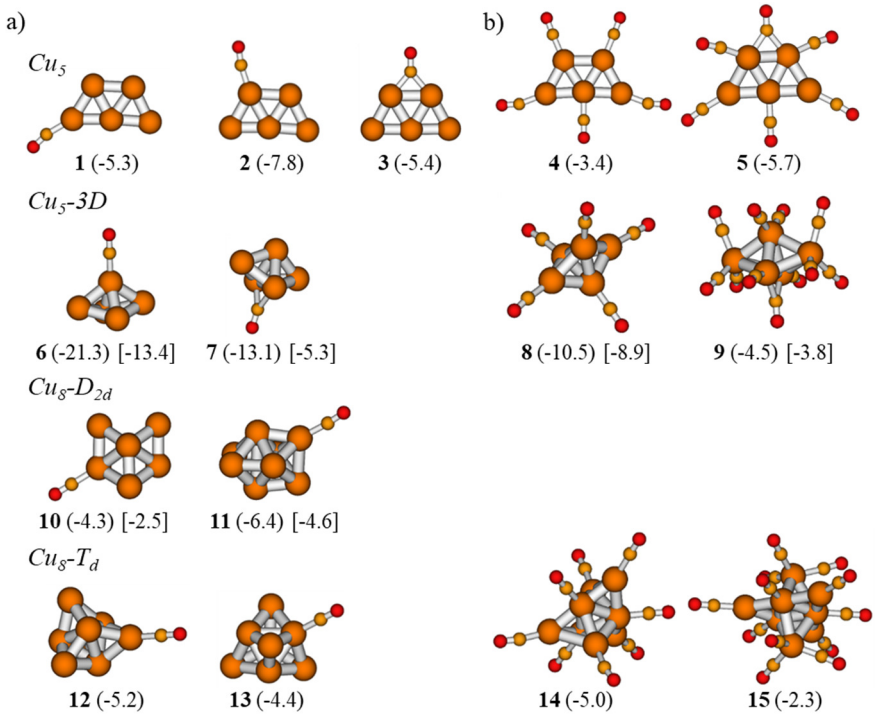

Figure 4.1. Optimized structures for the adsorption of a) one CO molecule and b) more than one CO molecules in Cu_n clusters. Adsorption free energies in kcal mol^{-1} are indicated in parenthesis, averaged in the case of more than one CO. Values in brackets are calculated w.r.t. the most stable isomer per cluster size.

The bonding with CO is the result of two main interactions: on the one hand, the charge transferred from the HOMO of the cluster to the anti-bonding $2\pi^*$ LUMO of the molecule and, on the other hand, the back-bonding from the HOMO of the molecule to the LUMO of the cluster. In addition to the energy of these orbitals, the strength of the interaction may depend on their shape and degeneracy, for a more fitting shape produces a better overlap. Because of this, it is difficult to assess which property has the major contribution and determines the interaction. Nevertheless, the charge transferences described are favored when the HOMO of the cluster is higher and its LUMO lower in energy, and it can be seen that the order found on the adsorption energies (Cu_5-3D > Cu_5 > Cu_8) do indeed correlate qualitatively with the HOMO-LUMO gap found for these orbitals (Figure 4.2).

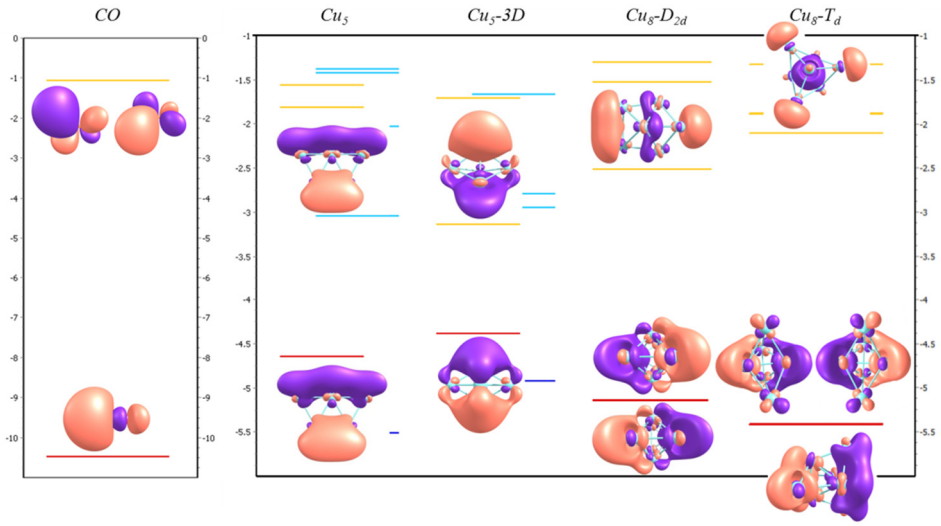

Figure 4.2. Stability and composition of the highest occupied and lowest unoccupied molecular orbitals (HOMOs and LUMOs) of Cu_n clusters (n=5, 8) and the CO molecule, calculated at the B3PW91/6-311+G(d,p) level (eV).

From Chapter 3 we know the most stable structures for a O_2 molecule adsorbed on planar Cu_5, 3D Cu_5 and Cu_8, which are structures **7**, **11** and **28** in Figure 3.3 (page 76), respectively. Their corresponding adsorption free energies are -25.0, -18.5 (-10.7 with respect to the planar isomer) and -3.3 kcal mol^{-1}. Therefore, for planar Cu_5 the interaction of the clusters with O_2 is always stronger than with CO, whereas for 3D Cu_5 they are similar and for Cu_8 the interaction is similarly weak. With this in mind, the co-adsorption was considered through the adsorption of a CO molecule in the structures with O_2 adsorbed mentioned, labelled here as **3-7**, **3-11** and **3-28** to avoid confusion (Figures 4.3-4.5).

Since we also know that the dissociation of the more strongly adsorbed O_2 in the 3D Cu_5 and Cu_8 clusters is easy (free activation energies of 15.8 and 14.9 kcal mol^{-1}, respectively), the reaction mechanism from CO adsorbed on a cluster with pre-dissociated O_2, i.e. with two oxygen atoms, is also studied for them. For planar Cu_5, given the large Gibbs free energy barrier involved (40.1 kcal mol^{-1}), the reaction of CO with pre-dissociated oxygen is unlikely.

Several Langmuir-Hinshelhood (LH) or Eley-Rideal (ER) mechanisms can be stated depending on whether the reactants are previously adsorbed (LH) or one of them is not (ER). In principle, a high activation of the O_2 molecule upon adsorption should facilitate an ER mechanism for the O_2 + CO reaction. Following this reasoning, 3D Cu_5 and Cu_8 should prefer an ER path to a larger extent than planar Cu_5. Similarly, for the reaction of adsorbed O atoms with CO, less stable O atoms should be easily captured through an ER mechanism.

4.3.1.2. CO oxidation by molecular O_2.

Planar Cu_5 (Figures 4.3-4.4). Attempts to obtain an ER pathway from structure **3-7**, i.e with the CO molecule coming from gas phase, did not succeed. As mentioned, the activation of O_2 in **3-7** is not high and the ER mechanism is unlikely, which explains the CO moving away or adsorbing on the cluster during the optimizations. The CO molecule adsorbs in the same copper atom the oxygen is bonded to with a

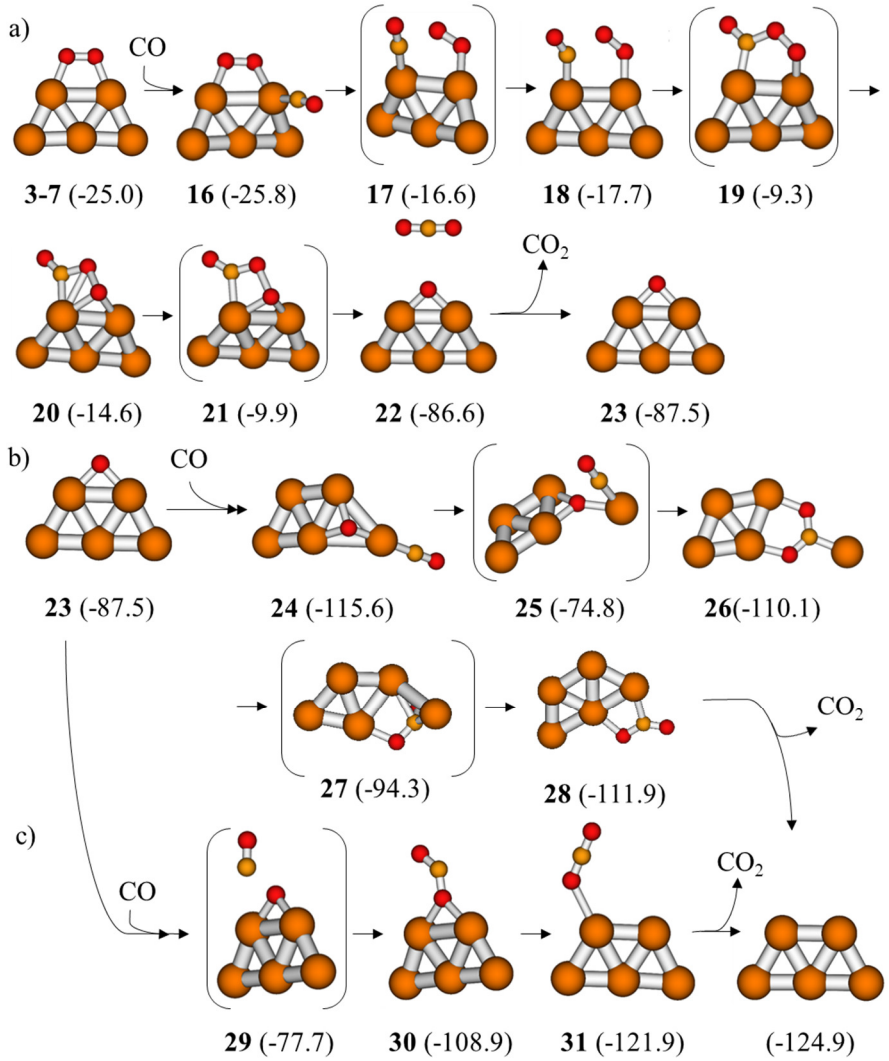

Figure 4.3. Mechanism for the CO oxidation by molecular O_2 in planar Cu_5. a) and b,c) correspond to the first and second part of the catalytic cycle, respectively. Relative Gibbs free energies with respect to separate planar $Cu_5 + O_2 + 2CO$ in kcal mol^{-1} are given in parenthesis. Cu in orange, C in amber, O in red.

very small adsorption energy (structure **16**). The approaching of CO to the O_2 molecule produces the breaking of one of the bonds that tied the latter to the cluster, which can be seen in the imaginary frequency of -100 cm^{-1} that characterizes transition state **17**, and ultimately leads to intermediate **18**, where both molecules are monocoordinated to copper and closer to each other. This first step has an activation energy of 9.2 kcal mol^{-1}. The free oxygen atom of the O_2 molecule binds then to the close carbon atom of the CO molecule in a process that requires another 8.4 kcal mol^{-1} (TS **19**), and produces the OO-CO species **20** as intermediate. From here, the dissociation of the oxygen molecule through TS **21** is easy, leading to the formation of a CO_2 molecule with an activation energy of 4.7 kcal mol^{-1} only in a very exothermic process (ΔG_{reac}= -72.0 kcal mol^{-1}) and leaving the cluster with an oxygen atom adsorbed in an edge mode, as can be seen in the products **22** and **23**.

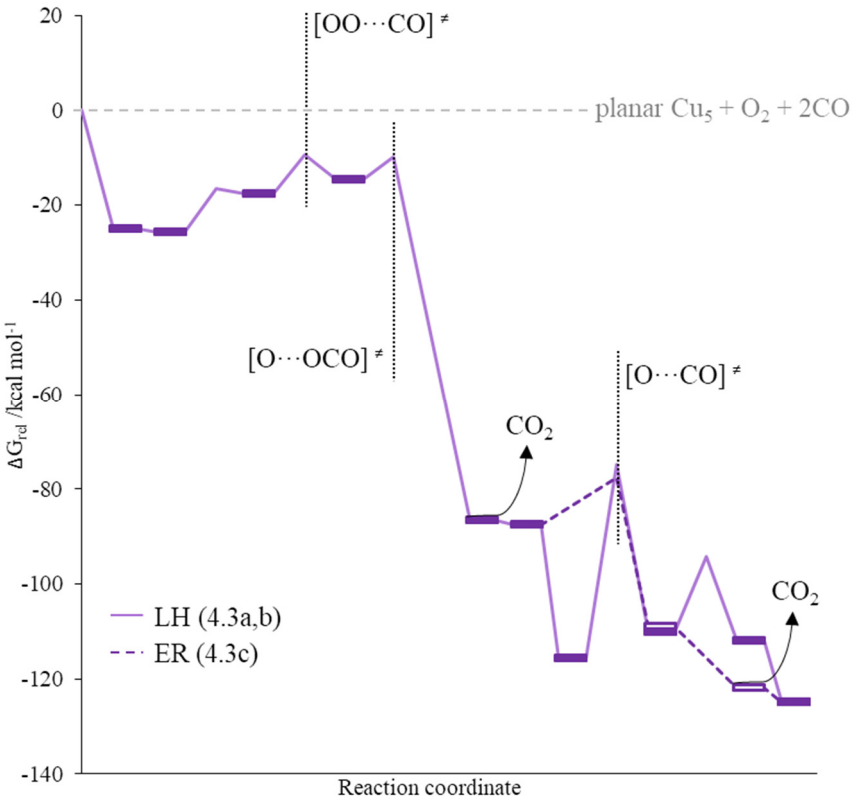

Figure 4.4. Energy profile for the CO oxidation by molecular O_2 in planar Cu_5. a) and b,c) correspond to the first and second part of the catalytic cycle, respectively (see Figure 4.3). Dashed lines correspond to ER paths. Key TSs of the reaction are indicated by vertical point lines.

In order to close the catalytic cycle, the reaction of structure **23** with a second CO molecule was studied (Figure 4.3b). Its adsorption on the site close to the oxygen atom produces structure **24**, with an oxygen atom within the cluster, almost separating one copper atom from the rest. This type of oxidized structures has also been reported for planar Cu_6[212]. From it, the reaction would imply a 40.8 kcal mol^{-1} barrier and a thermodynamically unfavored product where the cluster is broken into planar rhombic Cu_4 + Cu_1, which are bridged by the CO_2 formed. The Cu_5 cluster can be recovered with a barrier of 15.8 kcal mol^{-1} (structure **27**) and produces an unfavorably adsorbed bent CO_2 that readily desorbs (structure **28**). Figure 4.3c shows instead a much more favorable ER mechanism. Indeed, the direct reaction of atomic O with gas-phase CO through TS **29** requires only 9.8 kcal mol^{-1} of energy. The CO_2 produced is adsorbed through one of the oxygen atoms in a bicoordinated mode (structure **30**), but it is more stable monocoordinated (structure **31**) and also desorbs favorably, leaving the planar cluster naked again.

Therefore, catalysis of the CO oxidation by O_2 on planar Cu_5 clusters is possible. It is found that CO, much like water, facilitates the dissociation of O_2, lowering the energy from the high 40.1 kcal mol^{-1} of the monomolecular reaction to the 4.7 kcal mol^{-1} of step **20-[21]-22**. More importantly, although the O_2 molecule readily dissociates producing CO_2, the remaining O atom on an edge reacts easily as well. However, the adsorption of CO in this structure is strong (28.1 kcal mol^{-1}) and leads to a stable oxidized structure (**24**) that can deactivate the catalyst.

3D Cu_5 (Figures 4.5-4.6). The individual steps for the LH path are fairly similar to those of planar Cu_5, first producing an OO-CO intermediate to subsequently break its O-O bond. However, the reactions take place in the *h-111* facet of the 3D cluster as opposed to the edge of the planar Cu_5. Indeed, although we initially started from structure **3-11**, the very first step of the reaction leads us to structure **36**, where the OO-CO intermediate is bent in order to occupy this *h-111* facet (Figure 4.5a). Consequently and in line with the previous O_2 dissociation studied, we also included structure **3-12** in the study, which gave rise to two LH mechanisms (Figure 4.5b,c).

Indeed, the CO molecule can adsorb in structure **3-12** in two different sites near the oxygen with similar adsorption energies, leading to structures **34** and **40**. Then, activation energies of 14.0 and 20.5 kcal mol^{-1}, respectively, are found to produce intermediate OO-CO species **36** and **42**. Finally, the dissociation of the oxygen molecule producing the formation of the CO_2 molecule through the corresponding TSs **37** and **43** involve barriers of 15.3 and 5.5 kcal mol^{-1}, respectively. The CO_2 formed in the second LH case (Figure 4.5c) is first stabilized in a bent geometry, with each oxygen bonded to a Cu atom and the carbon establishing three bonds with the copper atoms nearby (structure **44**). A similar structure involving a CO_2 adsorbed in a bent position has already been reported for copper clusters of size 7 and 13[259] and for nanoparticles in the work of Pascucci et al.[260]. It can evolve to the same more stable mono-

coordinated mode that is directly obtained in the first LH case (Figure 4.5b, structure **38**), and again it desorbs a bit favorably, easily leaving the cluster with an oxygen atom adsorbed in an *hcp* facet mode (structure **39**).

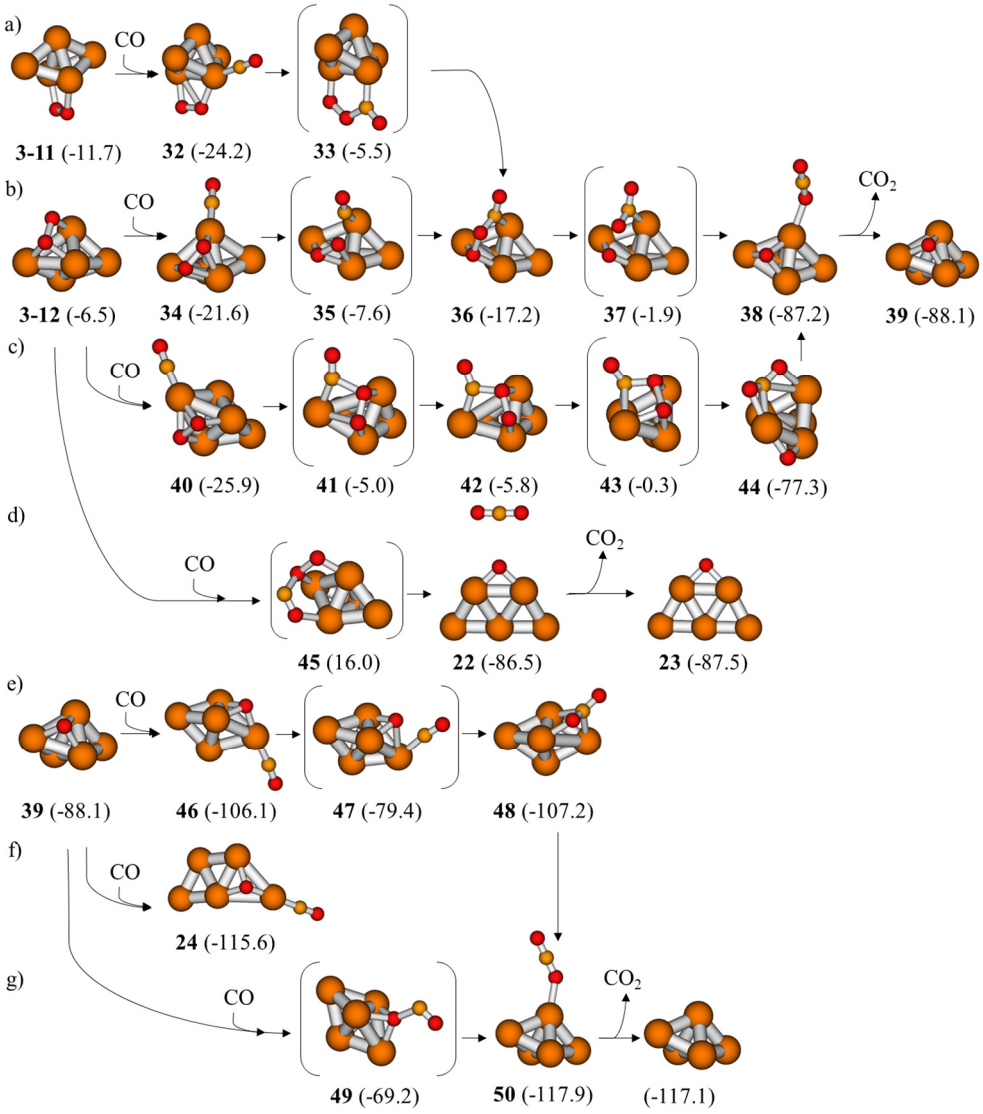

Figure 4.5. Mechanism for the CO oxidation by molecular O_2 in 3D Cu_5. a-d) and e-f) correspond to the first and second part of the catalytic cycle, respectively. Relative Gibbs free energies with respect to separate planar $Cu_5 + O_2 + 2CO$ in kcal mol^{-1} are given in parenthesis. Cu in orange, C in amber, O in red.

Again, no ER mechanism was found for O_2 adsorbed in a *bridge* mode of structure **3-11**, whereas from structure **3-12** a direct mechanism involving a somewhat higher barrier (22.5 kcal mol^{-1}) is found (Figure 4.5d). Through TS **45**, where the CO molecule coordinates through its oxygen atom to the cluster, the formation of CO_2 is produced, but also the deformation of the cluster again into its planar isomer, with an oxygen atom adsorbed in an edge mode, i.e. the same structure **23** that was found in the LH case for planar Cu_5. As a result, in this case the cycle can be closed through the path shown in Figure 4.3c, with a 9.8 kcal mol^{-1} barrier only.

For the other two paths, though, the possible LH and ER mechanisms from structure **39** must be considered. Adsorption of the CO molecule on the site with the highest coordination produces structure **24** again, from which reaction is unlikely (Figures 4.5f and 4.6). The adsorption on the less coordinated Cu produces structure **46**, 9.5 kcal mol^{-1} higher in energy than **24**, that requires 26.7 kcal mol^{-1} of energy to produce

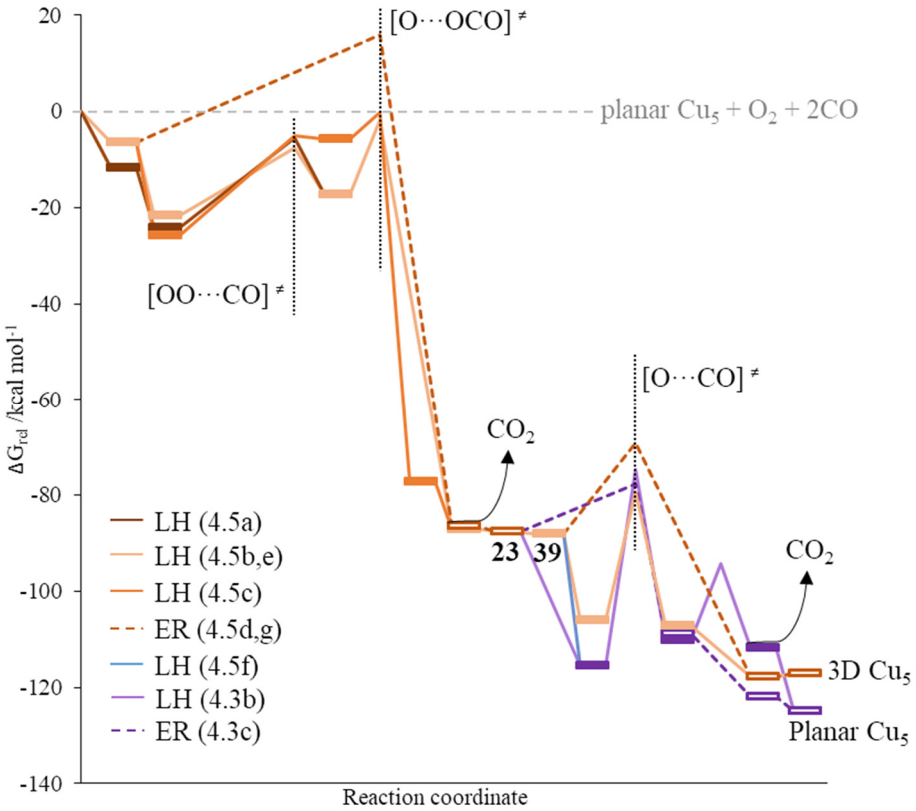

Figure 4.6. Energy profile for the CO oxidation by molecular O_2 in 3D Cu_5. a-d) and e-f) correspond to the first and second part of the catalytic cycle, respectively (see Figure 4.5). Dashed lines correspond to ER paths. Key TSs of the reaction are indicated by vertical point lines. The paths from Figure 4.3b,c are also shown.

a bent CO_2 (Figure 4.5e). As in the other cases where a bent CO_2 was obtained, it can evolve to a more stable monocoordinated mode (structure **50**), and in this case desorbs with a very small energy cost of 0.8 kcal mol^{-1}. In contrast, the direct ER pathway requires 18.9 kcal mol^{-1} of energy to produce the same structure **50** with CO_2 in a *mono* mode through TS **49** (Figure 4.5g).

To sum up, for 3D Cu_5 it is found that the CO + O_2 (LH) reaction competes with the O_2 dissociation, with individual steps in the 14-20 kcal mol^{-1} range (vs 15.8 kcal mol^{-1} for monomolecular O_2 dissociation). The ER mechanism is also possible with a bit higher activation energy than the previous two (22.5 kcal mol^{-1}), and it produces again the planar cluster whose bicoordinated O atom easily reacts (9.8 kcal mol^{-1}), but on which the adsorption of CO may deactivate the catalyst. The easier LH paths mentioned leave the cluster with a tricoordinated O atom that requires almost twice as much energy to react with CO (18.9 kcal mol^{-1}), and it does so also through an ER mechanism.

The possible deactivation in the second part of the cycle for both isomers seems to be caused by the increased adsorption energy of CO at the more oxidized clusters and the stability of the resulting structures **24** and **46**. In this situation more CO molecules may adsorb on the cluster, and such adsorption may draw the O atom closer to one of them, decreasing the energy barrier required for them to react. Indeed, it was found that the addition of more CO molecules is thermodynamically favored and decreases the activation energy for both isomers, from 40.8 to 21.7 kcal mol^{-1} in planar Cu_5 and from 26.7 to 9.7 kcal mol^{-1} in 3D Cu_5 (Figure 4.7). Consequently, deactivation of the catalyst from structures such as **24** and **46** is not definitive and it may not be an issue. Notice, however, that structure **55** recovers a 3D Cu_5 geometry instead of a planar one, driven by the CO molecule remaining. Thus, as observed in the adsorption section, the presence of a higher concentration of CO may favor the 3D isomer over the planar one.

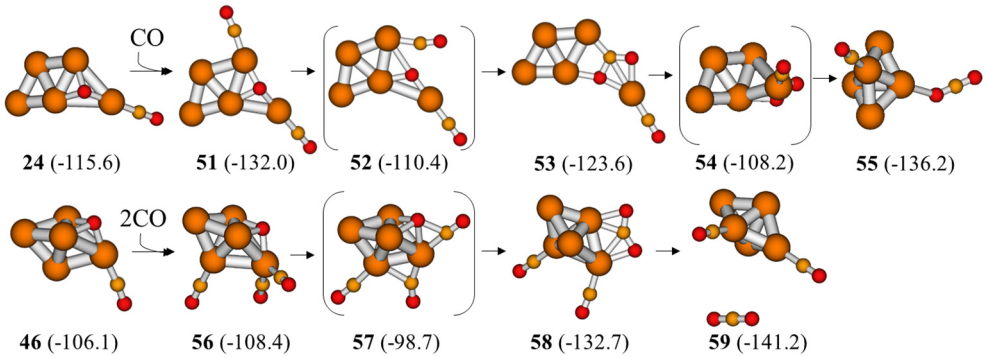

Figure 4.7. Mechanism for the second part of the 2CO + O_2 catalytic cycle (CO oxidation by atomic O), from structures **24** and **46** when more CO molecules are adsorbed. Relative Gibbs free energies with respect to separate planar Cu_5 + O_2 + 3/4CO in kcal mol^{-1} are given in parenthesis. Cu in orange, C in amber, O in red.

Cu_8 (Figures 4.8-4.9). Again, the reaction mechanisms found are similar to those obtained for the Cu_5 clusters, with a few exceptions. Firstly, in the path on Figure 4.8b the OO-CO intermediate is stabilized in a (100) facet (structure **67**) that is not possible in Cu_5. We find again a somewhat higher activation on this mode with respect to that on a (111) facet (the O-O bond distance increases from 1.44 Å in structure **62** to 1.46 Å in **67**) and a lower activation energy for the O-O bond breaking

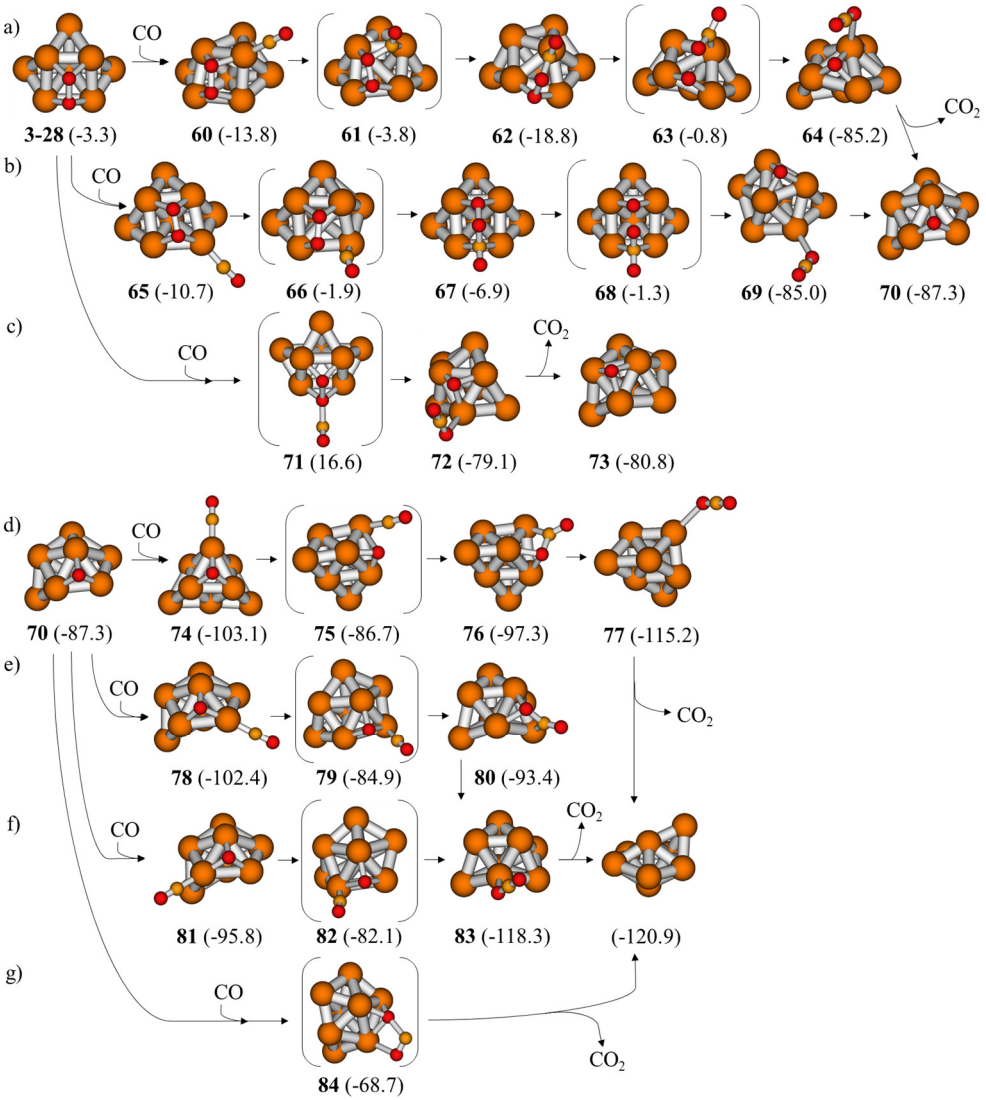

Figure 4.8. Mechanism for the CO oxidation by molecular O_2 in Cu_8. a-c) and d-g) correspond to the first and second part of the catalytic cycle, respectively. Relative Gibbs free energies with respect to separate Cu_8-T_d + O_2 + 2CO in kcal mol^{-1} are given in parenthesis. Cu in orange, C in amber, O in red.

steps (5.6 vs 18.0 kcal mol^{-1}). However, in those minima the O_2 is equally tricoordinated, and such difference in the activation energies seems to be rather caused by the increased stabilization of the OO-CO intermediate in the (111) facet, structure **62**, with respect to structure **67**, probably because the C atom is tricoordinated instead to tetracoordinated and can preserve a double-bond nature in the C-O interaction with the uncoordinated O atom. Regarding the ER path, we find it is again a bit higher in energy with respect to LH mechanisms (19.9 vs 18.0/8.8 kcal mol^{-1}), although it is a bit lower compared to the ER pathway of 3D Cu_5, consistent with the more activated oxygen molecule in structure **3-28**.

To close the cycle, the ER path is very similar to the one of 3D Cu_5 but with the CO coordinating with its O, and the activation energy is also similar, of 18.6 kcal mol^{-1} (Figure 4.5g), showing that the tricoordinated O atom is equally stable on 3D Cu_5 and Cu_8. However, the barriers for the LH paths for Cu_8 are lower than for the ER

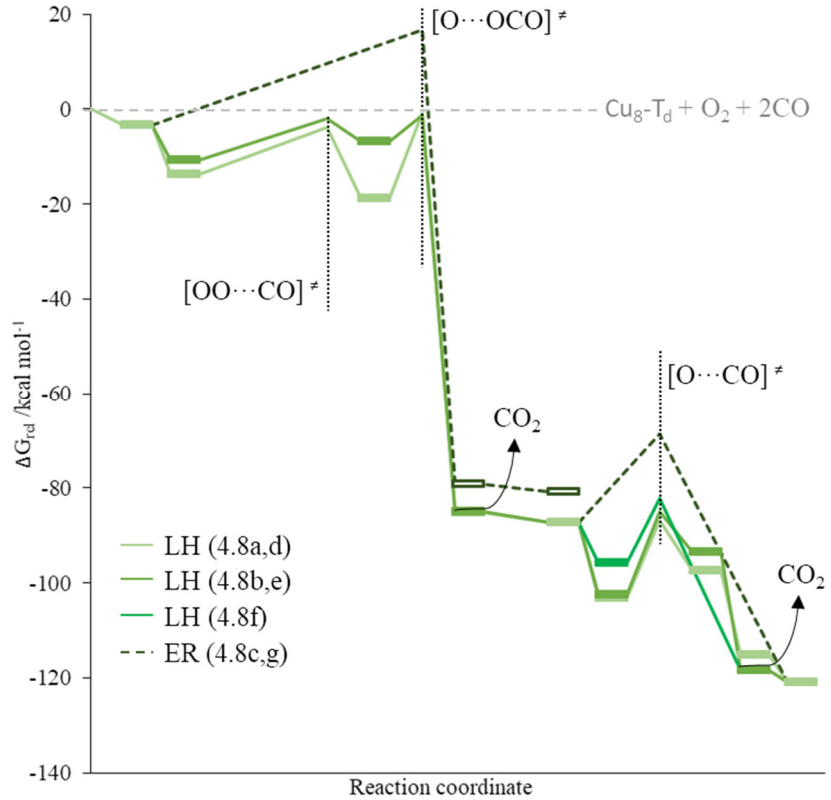

Figure 4.9. Energy profile for the CO oxidation by molecular O_2 in Cu_8-T_d. a-c) and d-g) correspond to the first and second part of the catalytic cycle, respectively (see Figure 4.8). Dashed lines correspond to ER paths. Key TSs of the reaction are indicated by vertical point lines.

mechanism and consequently lower than the LH paths of 3D Cu_5 (16.4/17.5 vs 26.7 kcal mol^{-1}). The latter is likely due to the fact that 3D Cu_5 stabilizes CO in a position at which it is much more separated from the O atom. As seen before, adding two more CO molecules to structure **46**, thus forcing the former CO to move closer, decreases the energy barrier to 9.6 kcal mol^{-1} (Figure 4.7).

All in all we find that for the three clusters the bimolecular reaction of adsorbed O_2 and CO is possible. For planar Cu_5 the ER mechanism was not found, possibly because the lower activation of the O_2 molecule renders it costly. In contrast, barriers within the LH and ER pathways are comparable for 3D Cu_5 and Cu_8, still being slightly lower for LH mechanisms. Also, the activation energy for the ER reaction is a bit lower for Cu_8, consistent with the O_2 molecule being more activated at it. Then, removing the O atom from the clusters to close the cycle is easiest for the edge-stabilized O atoms on planar Cu_5, whereas on Cu_8 and 3D Cu_5 it requires twice as much energy. For both Cu_5 isomers the ER pathway is preferred for this last step, whereas for Cu_8 the LH path is slightly lower. The rate-determining step for planar Cu_5 is still in the formation of the first CO_2, more specifically in the formation the OOCO intermediate, whereas for 3D Cu_5 and Cu_8 the two parts of the cycle have comparable barriers.

4.3.1.2. CO oxidation by previously dissociated O_2 (Cu_n(2O)).

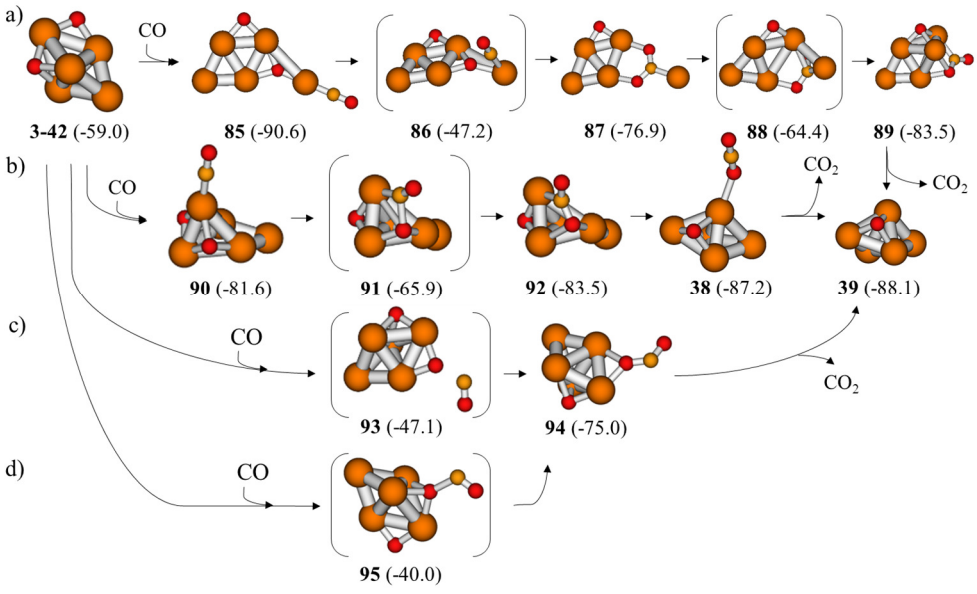

Figure 4.10. Mechanism for the CO oxidation by previously dissociated O_2 in Cu_5. Relative Gibbs free energies with respect to separate planar $Cu_5 + O_2 + 2CO$ in kcal mol^{-1} are given in parenthesis. Cu in orange, C in amber, O in red.

3D Cu_5 (Figures 4.10-4.11). Adsorption of the CO molecule at two of the three inequivalent sites close to the O atoms of structure **3-42**, which comes from the dissociation of O_2 on 3D Cu_5, deforms the cluster into a structure similar to **24** with an additional O atom adsorbed on an edge (structure **85**), from which the reaction follows a similarly costly path towards CO_2 formation (Figure 4.10a). For the third one, at the Cu atom coordinated to both O atoms, the cluster deforms again, but to adopt the more stable geometry already seen after the dissociation of O_2 in the planar cluster (structure **90**). From here, the formation of CO_2 requires 15.7 kcal mol^{-1} of energy and produces through TS **91** the molecule in a bent geometry on a (111) facet again (structure **92**). As before, the molecule is more stable monocoordinated and deforms back to 3D Cu_5 (structure **36**) hence desorbing a bit favourably (-0.9 kcal mol^{-1}).

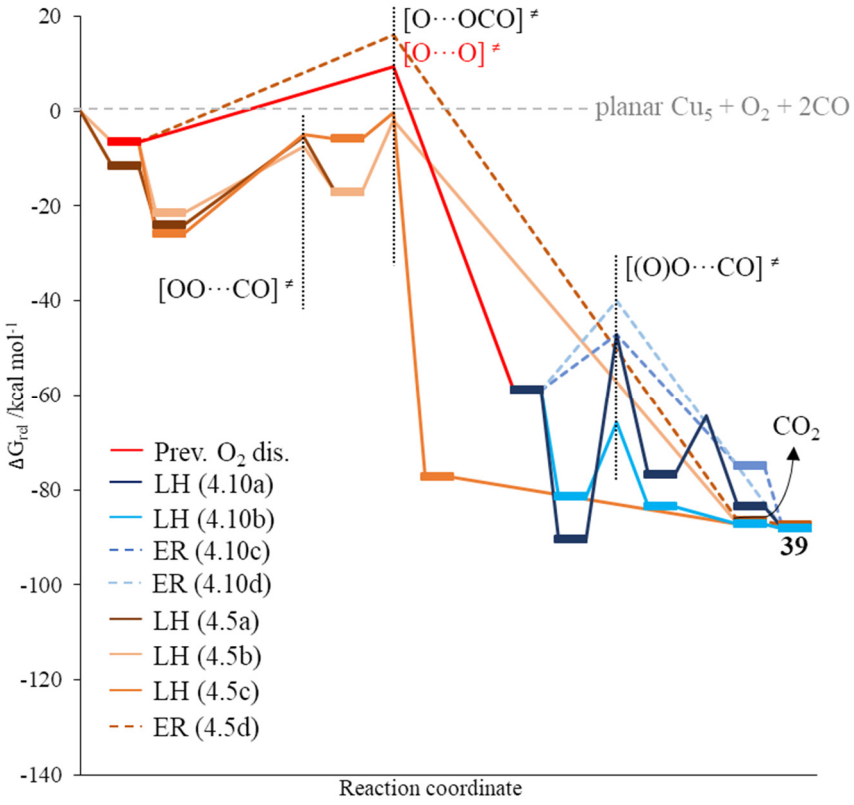

Figure 4.11. Energy profile of the first part of the catalytic cycle for CO oxidation by previously dissociated O_2 on Cu_5 (Figure 4.10). The second part of the cycle follows the paths shown for structure **39** (Figure 4.5e-g and 4.6). The energy profile for the reaction with molecular O_2 (Figure 4.6) is kept for comparison. Dashed lines correspond to ER paths. Key TSs are indicated by vertical point lines.

Regarding ER pathways, regardless of whether the CO reacts with the O in edge position (TS **93**) or with the tricoordinated one (TS **95**), the cluster ended accommodating the resulting CO_2 in a bicoordinated adsorption mode on an edge (structure **94**). However, the difference in the two oxygen atoms is observed in the TS structures **93** and **95** and in their corresponding activation energies, 7.1 kcal mol^{-1} lower for the one with the less stable O atom adsorbed on the edge (Figures 4.10c and d).

The desorption of CO_2 produces in all cases the 3D Cu_5 cluster with a tricoordinated O atom seen before (structure **39**), and therefore closing the cycle would be accomplished via the path shown in Figure 4.5e-g.

To summarize, there is not a big difference for LH and ER barriers for the reaction of CO with atomic oxygen when there is one or two O atoms, although the barrier for the **90-[91]-92** LH path is noticeable lower (vs the **46-[47]-48** path of Figure 4.5), probably due to the reactants being closer. Besides, these $[(O)O\cdots CO]^{\neq}$ ER barriers suggest that removing the first O atom from Cu_5 is somewhat easier than removing the second one ($[O\cdots CO]^{\neq}$) due to one of them being only bicoordinated. However, since structure **3-42** easily evolves to a cluster with tricoordinated O atoms and the latter react more difficultly, this difference may not be observable. Finally, the cluster may suffer deactivation due to the formation of structure **85** but, again, it was found that barriers decrease if a second CO molecule is adsorbed (Figure 4.12).

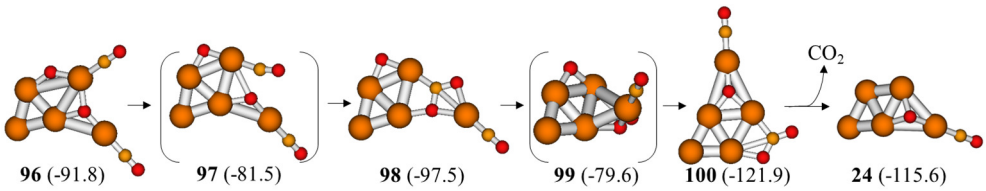

Figure 4.12. Mechanism for CO oxidation from structure **85** when another CO is adsorbed. Relative Gibbs free energies with respect to separate planar $Cu_5 + O_2 +$ 3CO in kcal mol^{-1} are given in parenthesis. Cu in orange, C in amber, O in red.

Cu_8 (Figures 4.13-4.14). From structure **3-48** there are two inequivalent adsorption sites close to the O atoms that lead to structures **101** and **105** and their respective LH paths, which involve similar barriers of 4.7 and 3.9 kcal mol^{-1} to produce the first CO_2. The latter is in a bent position over a (111) facet (structures **103** and **107**) prior to its favorable desorption. These barriers are significantly lower than the ones found in the previous section, even for the second part of the cycle with atomic O. The ER path involves a much higher barrier of 21.5 kcal mol^{-1}, again showing that the tricoordinated O atoms are as stable as those on Cu_5 3D (Figure 4.10d), with the 2.5 kcal mol^{-1} activation energy increase being likely due to the more linear O-Cu-O stable bond formed in structure **3-48**, which is not as good in structure **3-42**.

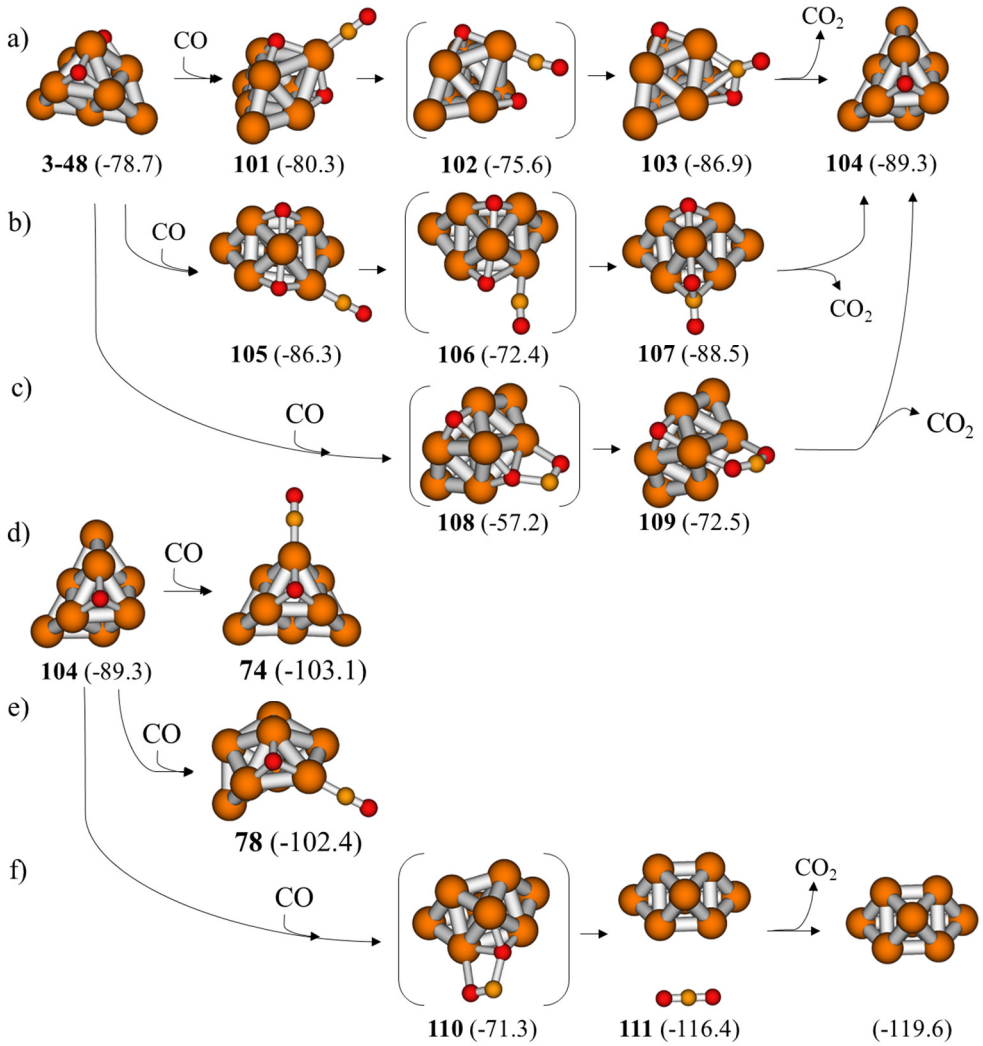

Figure 4.13. Mechanism for the CO oxidation by previously dissociated O_2 in Cu_5. Relative Gibbs free energies with respect to separate planar $Cu_5 + O_2 + 2CO$ in kcal mol^{-1} are given in parenthesis. Cu in orange, C in amber, O in red.

After desorption, the cluster remains in the geometry observed in **3-48** instead of recovering structure **70** (structure **108**), and therefore the closing of the cycle was also studied from structure **108**. However, the adsorption of a CO molecule close to the O atom leads to the structures **74** and **78** found previously (Figure 4.8d-e), and the ER path found has a 18.0 kcal mol^{-1} activation energy (Figure 4.13f), very similar to what is obtained from structure **70** (19.9 kcal mol^{-1}, Figure 4.8g).

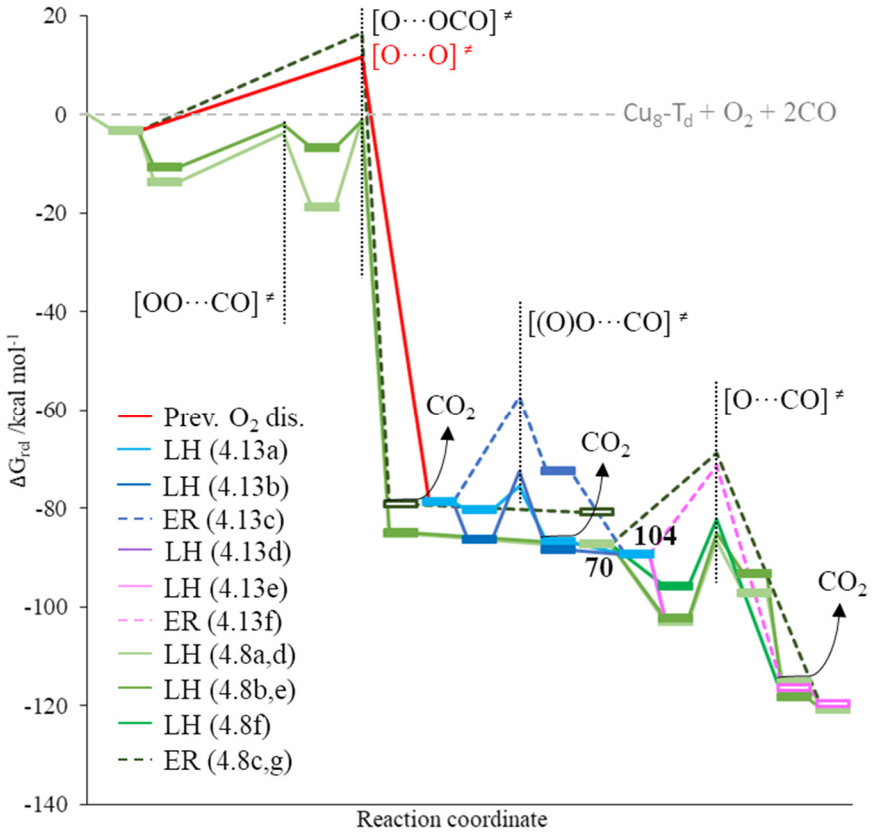

Figure 4.14. Energy profile of the catalytic cycle for CO oxidation by previously dissociated O_2 on Cu_8 (Figure 4.13). The energy profile for the reaction with molecular O_2 (Figure 4.9) is kept for comparison. Dashed lines correspond to ER paths. Key TSs are indicated by vertical point lines.

For 3D Cu_5 and Cu_8 we had found that the bimolecular reaction with CO competes with the monomolecular O_2 dissociation. The differences are not large and thus may be equilibrated by the adsorption of CO, which is larger for 3D Cu_5 and may induce the bimolecular reaction. However, calculating the dissociation of O_2 in the presence of one co-adsorbed CO molecule produces barriers that are somewhat lower than the lone monomolecular dissociation for the most stable adsorptions (Figure 4.15), thus supporting the monomolecular O_2 dissociation as the first step of the mechanism. The results are thus consistent with the work of Wang et al. on Cu_6 and Cu_7 clusters, where the best paths show TSs where the CO molecule stays far and practically does not participate while the O_2 molecule is breaking[212].

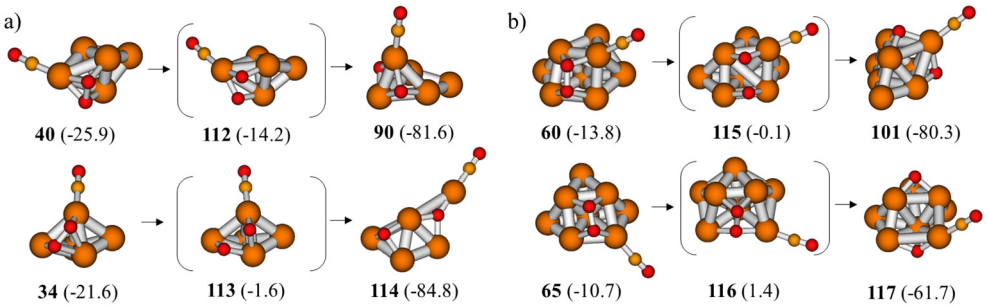

Figure 4.15. Optimized structures for the monomolecular dissociation of O_2 with co-adsorbed CO in a) 3D Cu_5 and b) Cu_8. Relative Gibbs free energies with respect to separate planar $Cu_5 + O_2 + 2CO$ and $Cu_8 + O_2 + 2CO$, respectively, are given in parenthesis in kcal mol^{-1}. Cu in orange, C in amber, O in red. The cluster was fixed during optimization of structure **113**, as it otherwise evolved to **114**.

Thus, for both 3D Cu_5 and Cu_8 clusters the predominant mechanism starts with the monomolecular dissociation of O_2 (11.7 and 13.7 kcal mol^{-1} of activation energy, respectively) followed by the LH step of the formation of the first CO_2 molecule (15.7 and 4.7 kcal mol^{-1}), and finally by the formation of the second CO_2 molecule (18.9 and 16.4 kcal mol^{-1}), with the difference that the latter is an LH step for Cu_8, because, as mentioned, the CO is closer to the O atom than for 3D Cu_5, for which the ER step has a lower barrier (Figure 4.16).

Note that the data presented suggest that planar clusters may only keep their geometry if the concentration or partial pressure of CO is low during reaction. Otherwise, they are likely to deform into 3D Cu_5. However, the results also indicate that the latter will only be slightly worse for the catalysis of CO oxidation: for planar clusters the formation of the OOCO intermediate will be the rds of the reaction (16.5 kcal mol^{-1}), whereas for 3D clusters the predominant mechanism just mentioned has an activation energy for the rds of 18.9 kcal mol^{-1}. Furthermore, the presence of a higher concentration of CO may avoid the deactivation of Cu_5 clusters due to structures with the O atoms between copper atoms, because the CO molecules get closer to the latter facilitating their reaction. Besides, according to the predominant mechanism, Cu_8 would represent a similar or even slightly better candidate (rds of 16.4 kcal mol^{-1}), but the predominance of the path is lower (the highest activation energy of other paths that contribute is of 18.0 kcal mol^{-1}). More importantly, according to the easier oxidation and larger resistance to reduction observed for the Cu_8 sample in Chapter 3, it is likely to oxidize to a larger extent than considered in these calculations due, for instance, to subsequent oxidation reactions at other available facets of the Cu_8 cluster.

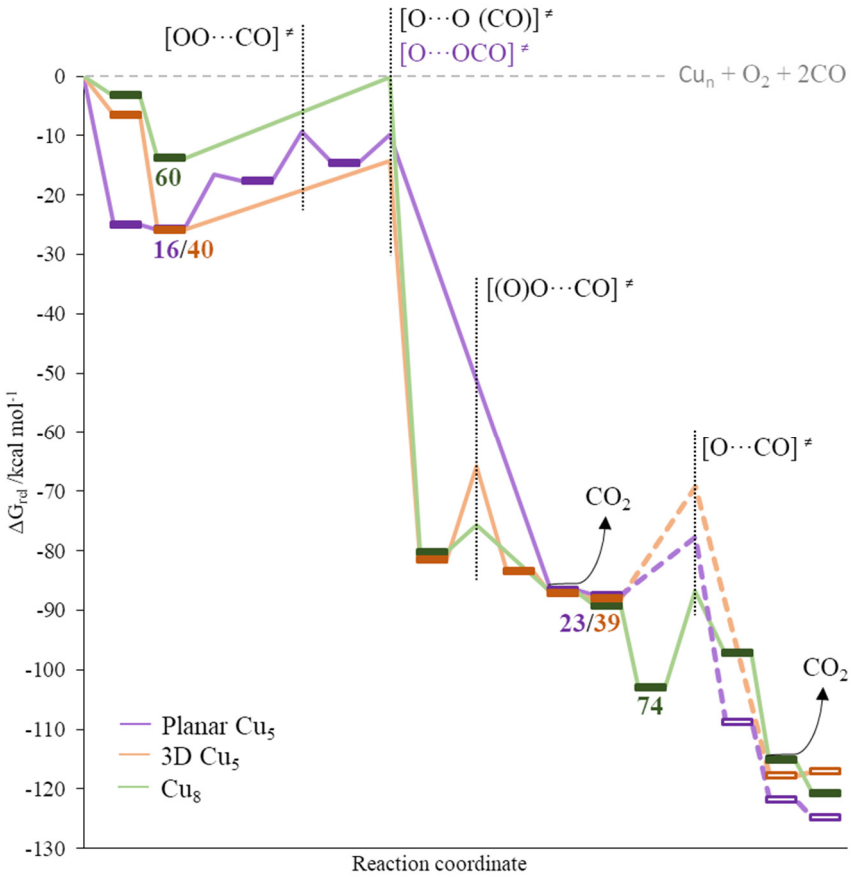

Figure 4.16. Energy profile of the best mechanisms found for the catalytic CO oxidation by planar Cu_5, 3D Cu_5 and Cu_8 clusters. Dashed lines correspond to ER paths. Key TSs are indicated by vertical point lines.

4.3.2. Propene epoxidation on Cu_5 clusters.

In this reaction the desired propene epoxide (PO) is obtained through the reaction of propene with an oxygen atom. An oxametallacycle (OMC) intermediate precursor is first obtained, which then reorganizes to produce PO (Scheme 4.1a). However, when the O atom is to react with propene, it can also capture one hydrogen atom of the methyl group instead. This produces an allyl species that is a precursor to combustion. Moreover, even if the OMC is successfully reached, its rearrangement can also lead to propanal (PA) or propenone (acetone, AC) species (or their enol forms), lowering the selectivity. For Cu(111) it was theoretically found that the path towards PO

from the OMC has a 99% predominance with respect to the other secondary reactions, and the problem lied in the step towards OMC or allyl formation, where the former only achieved a 60%[41]. In principle, more basic O atoms should enhance the reaction towards allyl, and it is possible that O atoms adsorbed on copper clusters are already too basic, as in Cu(111). Another possibility is the direct reaction of propene with molecular O_2. For this to work, the dissociation of O_2 needs to be difficult enough to avoid its monomolecular dissociation but possible enough to dissociate aided by a propene molecule (Scheme 4.1b). With this in mind, planar Cu_5, which preferentially adsorbs O_2 in a *bridge* mode not sufficiently activated to dissociate alone but which readily reacts with CO, seems a good candidate.

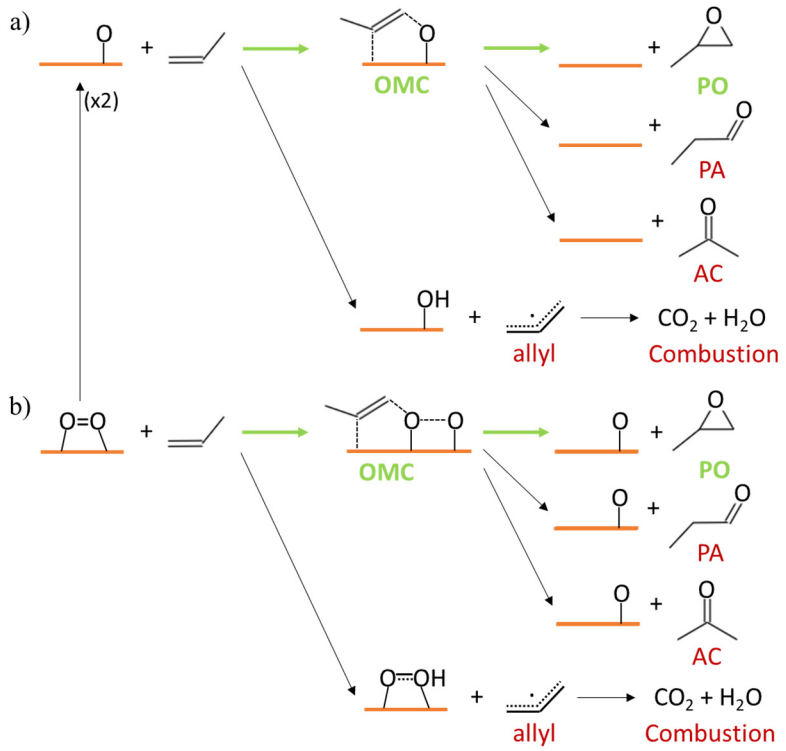

Scheme 4.1. Propene epoxidation mechanism by adsorbed a) atomic oxygen or b) molecular oxygen. An orange line is used to indicate the copper system.

4.3.2.1. Adsorption of C_3H_6 on planar and 3D Cu_5 clusters.

The adsorption of one molecule of propene was studied on the two lowest energy isomers of Cu_5 for the known more reactive sites of the latter, namely, on the two-atoms edge for planar Cu_5 and on top of one central Cu atom for 3D Cu_5 (Figure 4.18).

The interaction between the metal cluster and the molecule is preferentially established through one copper atom only (Figure 4.18). Propene, as an alkene, is a σ-donor π-acceptor species, and thus the interaction with the cluster involves a charge transfer from the π orbital of the molecule to empty *3d* orbitals of the cluster, and some back-bonding from a different *3d* orbital of the copper cluster to the π* antibonding orbital of the molecule. As a result, the double bond of propene gets elongated. The cluster gets oxidized, but the interaction is weak, especially for planar clusters, and the net charge transferred is of 0.07e and 0.03e for structures **122** and **124**, respectively, on which the C=C bond is elongated by 0.043 and 0.047 Å. The slightly larger elongation of the C=C bond in structure **124** correctly correlates with the larger adsorption energy, and the lower net charge implies a larger contribution from back-bonding. Again, all of it correlates with the HOMO-LUMO of the clusters and the lower energy gap of 3D Cu_5 (recall Figure 4.2).

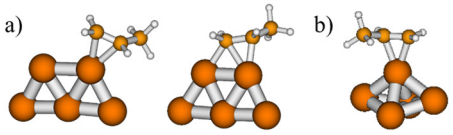

122 (-1.6) **123** (0.7) **124** (-5.5)

Figure 4.18. Optimized structures for the adsorption of a propene molecule on a) planar and b) 3D Cu_5 clusters. Adsorption free energies with respect to the planar isomer are indicated in parenthesis, in kcal mol^{-1}. Cu in orange, C in amber, H in white.

The adsorption of propene is thus clearly weaker than that of O_2, and consequently the co-adsorption of the species will be considered through the adsorption of propene in structures where O_2 was previously absorbed, namely, **3-7, 3-11** and **3-12**. Then, since the dissociation of O_2 before propene adsorbs is possible for 3D Cu_5, the reaction is also studied from structure **3-42**.

4.3.2.2. OMC vs allyl formation by planar Cu_5, 3D Cu_5 and $Cu_5(2O)$ clusters.

Planar Cu_5. The adsorption of propene on the copper atom next to the O_2 molecule requires about 4-5 kcal mol^{-1} (structures **125**, **132** and **135** in Figure 4.19). Once it is achieved, paths divert into those leading to the undesired allyl or to the OMC pursued, as explained before. However, if the molecule adsorbs in such a way that the non-methylated carbon faces the oxygen molecule, as in structure **135**, then the path towards the allyl is impeded because the methyl group is inevitably too far to react. The calculated activation energy for the production of the OMC in this case is of 16.7 kcal mol^{-1} only (**135-[136]-137** path). For the other structures (**125** and **132**), affordable paths towards the allyl can be found, but with barriers 3.6 or 8.0 kcal mol^{-1} higher (TS structures **133** and **130**, respectively). Indeed, regardless of the side the methyl group is at, when propene adsorbs with the methylated carbon facing the O_2 molecule the system evolves to TS **126**, where the O_2 is tilted over the cluster's edge and about to bond with the methylated carbon atom. With 19.1 and 19.6 kcal mol^{-1} barriers from structures **125** and **132**, respectively, this leads to the four-member

cycle of structure **127**. The latter can easily evolve (with a 0.8 kcal mol^{-1} barrier) to a five-member cycle where the two oxygen atoms participate (structure **129**), similar to the structure **137** previously described). In contrast, reaching the hydrogen atoms of the methyl group needs 27.1 kcal mol^{-1} of energy from structure **125** (TS **130**), and 26.6 or 22.2 $kcalmol^{-1}$ from the close in energy structure **132**, depending on which oxygen atom participates (TSs **130** and **133**, respectively). As seen in Scheme 4.1, allyl paths produce adsorbed hydroperoxide species (structures **131** and **134**).

3D Cu_5. From the 3D cluster with O_2 adsorbed in a *bridge* mode (the most stable structure, **3-11**) we obtain again that the adsorption of propene with the unmethylated carbon facing an O atom is slightly worse, although in this case both adsorptions are thermodynamically favored by 5.9 and 4.8 kcal mol^{-1} (structures **138** and **143** in Figure 4.20, respectively). Also, it is similarly found that the path towards the allyl species requires higher energy (TS structure **141**, barrier of 27.3 kcal mol^{-1}) than the paths towards oxometallacycles. Indeed, from structure **143** the cluster deforms into the planar geometry of TSs structure **136** previously found when the formation of an

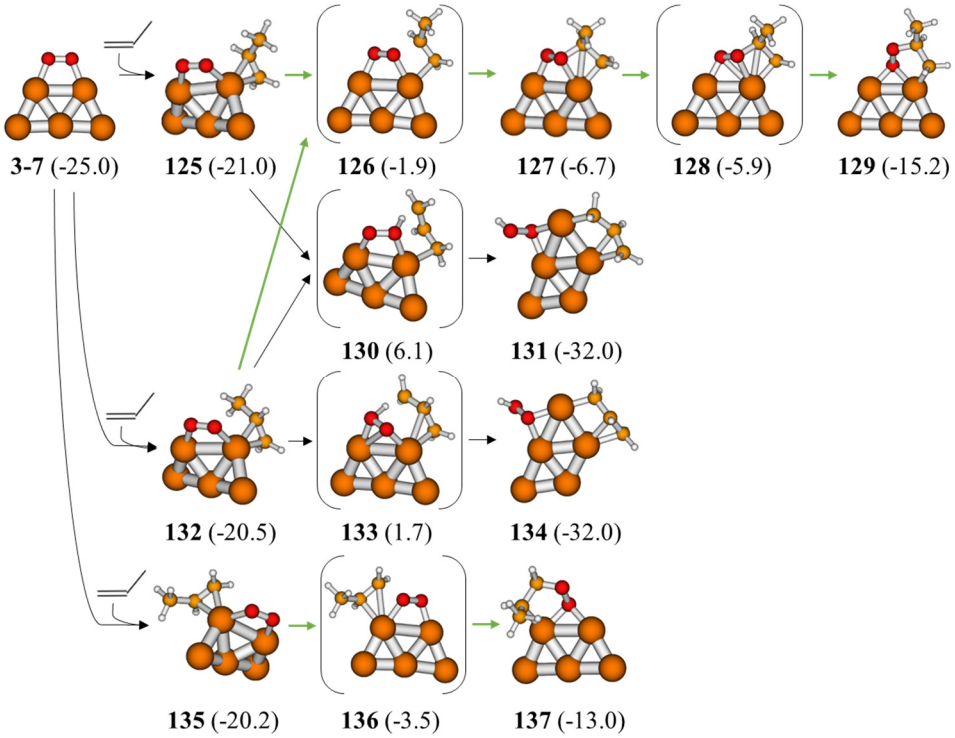

Figure 4.19. Optimized structures for the OMC or allyl formation by planar Cu_5. Relative Gibbs free energies with respect to separate planar $Cu_5 + O_2 + 2C_3H_6$ are given in parenthesis in kcal mol^{-1}. Cu in orange, C in amber, O in red, H in white.

OMC is explored, thus involving a barrier of 13 kcal mol^{-1}. From **138**, the cluster retains its 3D shape and the OMC, produced after surpassing a barrier of 13.0 kcal mol^{-1} (structure **139**), has more interacting points with the cluster, at the unmethylated carbon and at both O atoms (structure **140**).

From the 3D cluster with an O_2 adsorbed in a *h-111* mode (**3-12,** 5.2 kcal mol^{-1} higher in energy than the most stable structure), many structures similar in energy can be obtained, and we chose four representative ones to follow (Figure 4.21). Again, those with the non-methylated carbon closer to the O_2 (structure **163** of Figure 4.21d) are a bit less stable than the others, except for structure **144** (Figure 4.21a), that constitutes one of the most stable structures (together with **151**) and where the two molecules are bridged by an almost detached Cu atom that lies at almost the same distance from the two doubly bonded carbon atoms. Also in this case the attack of O to the methylated C atom of propene to produce OMC is preferred both kinetically (TSs **145** vs **147**), and thermodynamically (structures **146** vs **148**). In spite of the further detachment of the Cu atom in the corresponding TSs **149**, the reaction towards the allyl is affordable (23.5 kcal mol^{-1}) and at least 2.6 kcal mol^{-1} easier than the easiest OMC path from structure **144**. For the remaining two structures, **151** and **159**, the differences between the TSs leading to an OMC and those leading to allyl are also small, of 1.6-3.9 kcal mol^{-1}, and also slightly favoring the production of the undesired allyl species (Figure 4.21b,c).

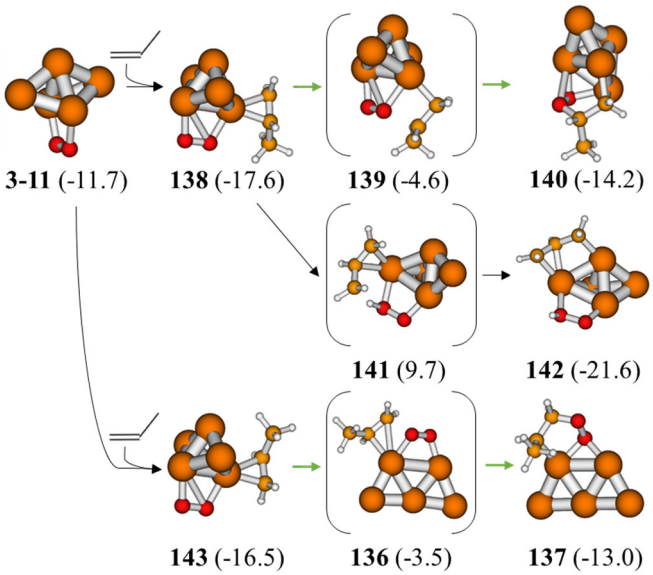

Figure 4.20. Optimized structures for the OMC or allyl formation by 3D Cu_5 (from structure **3-11**). Relative Gibbs free energies with respect to separate planar $Cu_5 + O_2 + 2C_3H_6$ are given in parenthesis in kcal mol^{-1}. Cu in orange, C in amber, O in red, H in white.

Thus, when O_2 is adsorbed in an *h-111* mode on Cu_5 its larger activation confers it a more basic character (consistent with a superoxo species) that is already enough to produce a slight preference towards the allyl in the propene epoxidation reaction.

Cu_5(2O). If O_2 dissociates prior to the adsorption of propene, which may occur on 3D Cu_5, the molecule may adsorb close to an O atom and react as before but also may directly react with an adsorbed O atom via an ER mechanism (Figure 4.22). Searching for these ER TSs at the edge and facet-adsorbed O atoms of structure **3-42** yields structures **166** and **168**, respectively, and thus the edge O atom moves towards a facet adsorption site if it does not react. The corresponding activation energies are 24.5 and 23.2 kcal mol^{-1}, respectively, and directly produce the epoxide

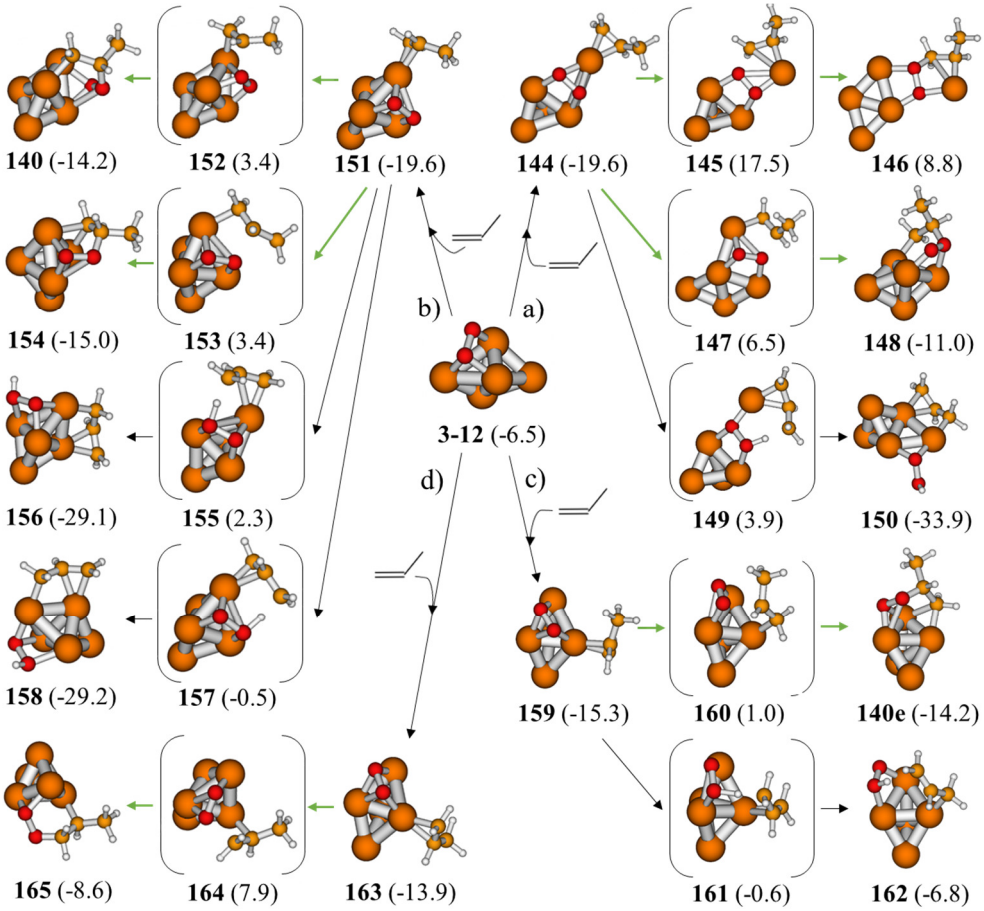

Figure 4.21. Optimized structures for the OMC or allyl formation by 3D Cu_5 (from structure **3-12**). Relative Gibbs free energies with respect to separate planar $Cu_5 + O_2 + 2C_3H_6$ are given in parenthesis in kcal mol^{-1}. Cu in orange, C in amber, O in red, H in white.

adsorbed on the cluster (structures **167** and **169**), that desorb unfavorably by 3.4 and 13.0 kcal mol^{-1}. If the molecule is adsorbed on the cluster instead, either structures similar to **178** or structure **171** are obtained. From structure **178** reaction may be possible but, as observed in the previous section on CO oxidation, barriers are likely to be higher in energy than from structure **171** and were not studied. From this latter structure the molecule can be tilted towards one oxygen or the other to react. In TSs **172** the non-methylated carbon reacts to produce the OMC structure **173** with an activation energy of 28.2 kcal mol^{-1}, whereas in TS **174** the OMC **175** is produced by reaction with the methylated one with a lower barrier of 21.0 kcal mol^{-1}. However, the allyl TS **176** lies 9.8 kcal mol^{-1} even lower in energy, requiring only 11.2 kcal mol^{-1} of activation energy.

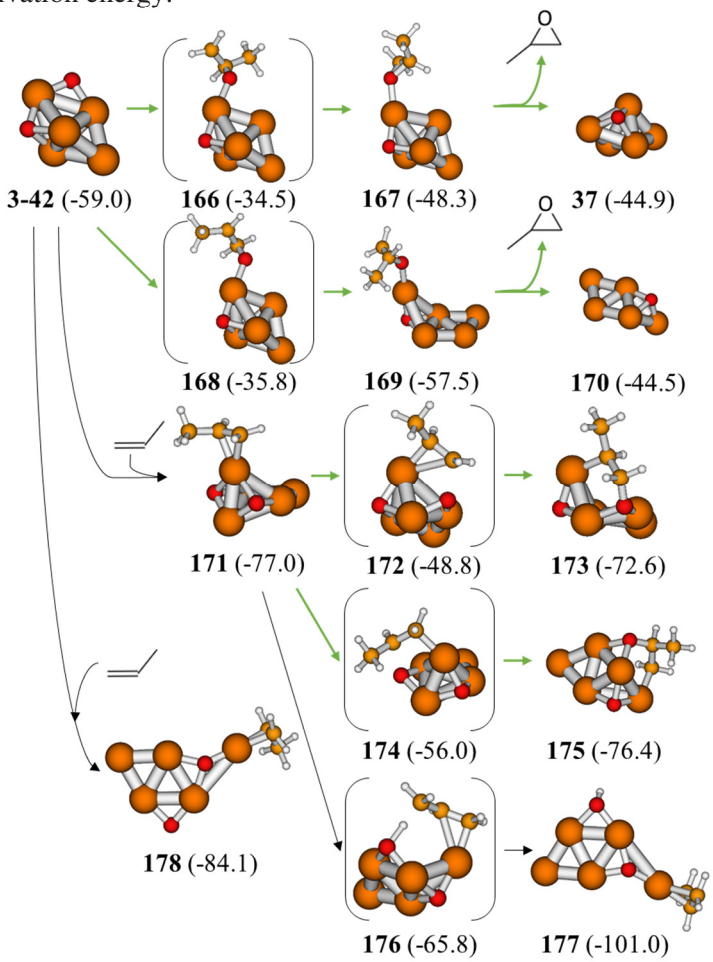

Figure 4.22. Optimized structures for the OMC or allyl formation by previously dissociated O_2 (Cu_5(2O), from structure **3-42**). Relative Gibbs free energies with respect to separate planar Cu_5 + O_2 + $2C_3H_6$ are given in parenthesis in kcal mol^{-1}. Cu in orange, C in amber, O in red, H in white.

The lowest energy paths leading to an OMC and to the allyl for each previous case are plotted in Figure 4.23, where it is all the more clear that when O_2 is dissociated the allyl becomes much more favored than in any of the previous cases. Similarly, it is also noticeable that the energy required for O_2 dissociation is larger than that required for production of the OMC in 3D Cu_5 with O_2 in a *bridge* mode, but smaller if O_2 adsorbs in an *h111* mode, even when the $[O\cdots O]^{\neq}$ TS is higher in energy.

Therefore, all in all it is found that Cu_5 clusters in their reduced metallic state favor the production of an OMC (and thus of PO) by reaction with O_2 due to their preferential adsorption of the latter in the not so activated *bridge* mode. 3D Cu_5 are likely to perform worse because they are also able to adsorb O_2 in a more activated *h111* mode that already slightly favors allyl production, and because such mode is more likely to dissociate the oxygen molecule. Once the molecule is dissociated, the two adsorbed O atoms are too basic and the reaction towards the allyl is greatly enhanced.

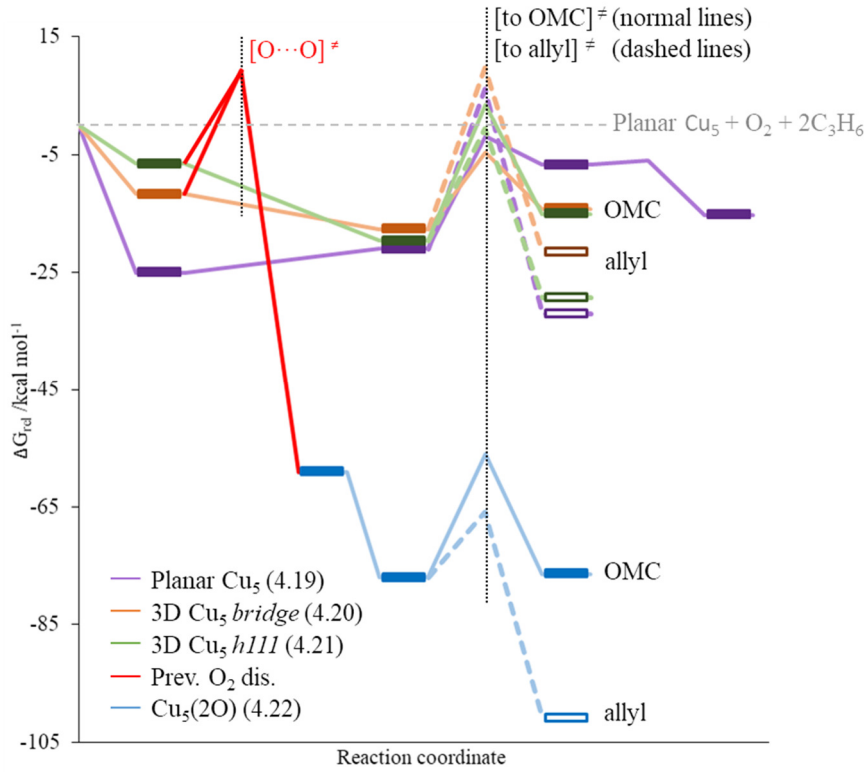

Figure 4.23. Energy profile of the OMC vs allyl formation by planar Cu_5 (purple), 3D Cu_5 with O_2 adsorbed in the most stable *bridge* mode (orange), 3D Cu_5 with O_2 adsorbed in an *h111* mode (green) and by previously dissociated O_2 on Cu_5 (red followed by blue). Dash lines correspond to allyl paths. Key TSs and some OMC/allyl products are indicated.

4.3.2.3. PO formation vs competing reactions from the OMC by planar Cu_5.

Since planar Cu_5 clusters favor the OMC production to a greater extent, and although it is believed that this is the key step towards PO production in the epoxidation of propene, we study now whether the cycle can indeed be closed from the OMC and if competitive reactions towards propanal (PA) or acetone (AC) can be dismissed.

From the OMC cycle of structure **129,** the direct breaking of the O-O bond and formation of PO is not produced (Figure 4.24). Instead, the mechanisms found towards PO either dissociate first the O-O bond (TS **179**), reorganize (**180-[181]-182** step to produce a four-centered cycle) and then produce PO (TS **183**) or lose the Cu-C interaction of the molecule and produce an intermediate where the molecule is bonded to the cluster through the O_2 only (structure **186**), which is the one that reacts break-

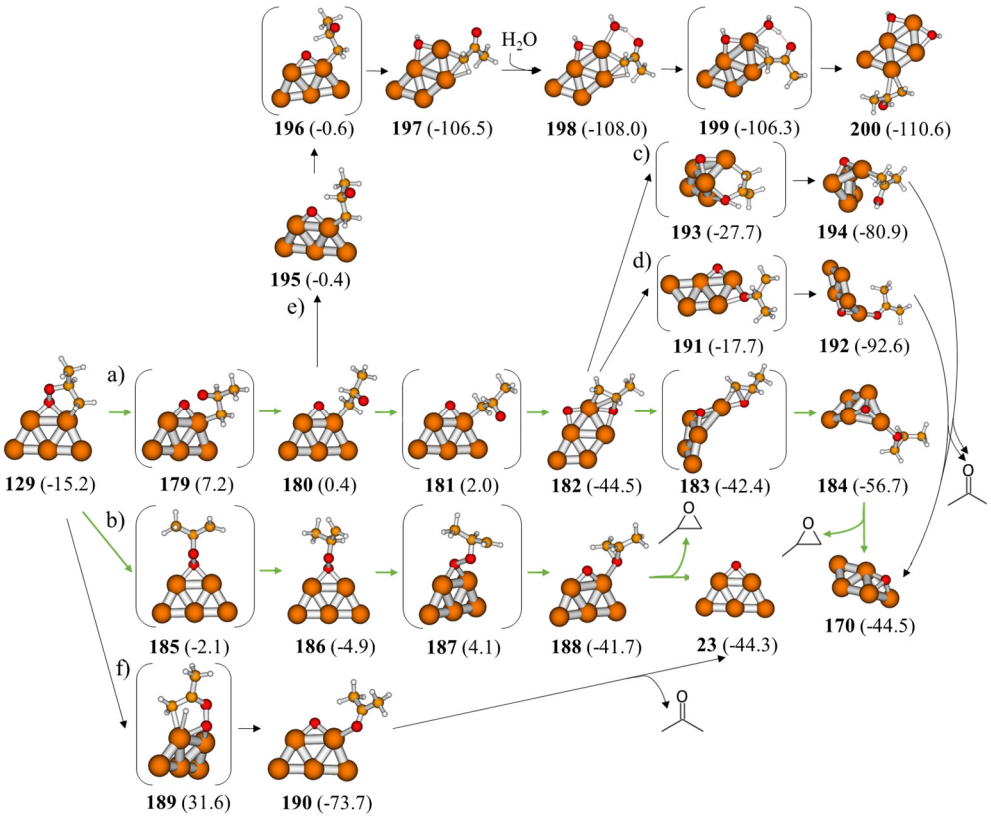

Figure 4.24. Optimized structures for possible reaction mechanisms from the OMC produced on planar Cu_5 (structure **129**). Relative Gibbs free energies with respect to separate planar $Cu_5 + O_2 + 2C_3H_6$ are given in parenthesis in kcal mol^{-1}. Cu in orange, C in amber, O in red, H in white.

ing the O-O bond and creating the PO at the same time (TS **187**). In both paths the highest energy TS involves the dissociation of the O-O bond i.e. TSs **179** and **187**. Given that the latter is lower in energy and that the **129-[185]-186** step has also a 9.3 kcal mol^{-1} lower activation energy than the **125-[179]-180** step, the former more direct path will predominate.

From structures where the O-O bond is still not dissociated the competitive reaction leading to acetone seems unlikely given that it requires the transference of the central hydrogen atom and the dissociation of the O-O bond at the same time. Indeed, trying such step from structure **129** leads to a 46.8 kcal mol^{-1} activation energy (TS **189**) to produce AC (structure **190**). As a consequence, the more predominant direct path (started at structure **185**) is expected to enhance the selectivity towards PO.

Since the other path is nevertheless energetically affordable, we tested the possible reactions to AC from structure **182**. TS **191** implies a barrier of 26.8 kcal mol^{-1} and produces AC directly (structure **192**), whereas in TS **193** the cluster deforms and produces the corresponding enol (2-propenol or isopropenol, structure **194**) with a smaller barrier of 16.8 kcal mol^{-1}. In contrast, the barrier towards PO is of 2.1 kcal mol^{-1} only, which indicates that reaction towards AC will not be a problem either for this mechanism.

In spite of this, we noticed that the hydrogen atom next to CO in structure **180** can be favorably oriented towards the remaining O atom due to the partial positive and negative charges that they respectively present (structure **195**). From here, the transfer of the hydrogen atom to the oxygen atom is extremely easy (barrierless in fact, as a -0.2 free energy barrier is obtained, 0.7 in electronic energy) and the product is much more stable than any of the others shown because a stable hydroxyl and enolate species are formed (structure **197**). The latter can be removed as AC if it retrieves a hydrogen atom (at the O atom as 2-propenol or at the alkyl radical C atom as AC), for instance through an easy reaction with water (**192-[193]-194** step).

From the OMC cycle formed in structure **137**, i.e. when the C atom bonded to an oxygen atom is the unmethylated one, similar results are obtained (Figure 4.25). Thus, we find again a path starting with the dissociation of the O-O bond, TS **201** (although it has one more rearrangement step than the equivalent path from structure **129**) and a more direct one that starts from structure **208**, and again the higher energy TSs of each path are those that involve the breaking of the O-O bond (TSs **201** and **211**, respectively). Besides, again, competitive reactions from structures where the O-O bond is still not dissociated are equally unlikely and, indeed, the reaction towards 1-propenol from structure **137** yields a 32.4 kcal mol^{-1} barrier, whereas the attempts towards propanal always led to the dissociation of the O-O bond first. Competitive reactions towards PA in the indirect path are again found less favorable than the corresponding steps leading to PO, by 14.9, 7.3 and 4.8 kcal mol^{-1} (steps **204-**

[205]-206 vs **204-[217]-218**, **206-[207]-184** vs **206-[215]-216**, and **202-[205]-206** vs **204-[217]-218**, respectively), although PA production from structure **202** is more affordable (TS **219**, 4.5 kcal mol^{-1}; note that TS **203** is 0.3 kcal mol^{-1} lower in energy than the minima, which can be a result of the error limit of the calculation or be caused by the existence of other minima close in energy to **202**, as **203** is a TS of rotation).

In spite of these similarities, in this case the difference between the two paths towards PO is 4.9 kcal mol^{-1} larger, favoring the direct one even more, which results in an even higher selectivity to propene epoxide. All of these conclusions are all the more evident in the energy profile comparison shown in Figure 4.26.

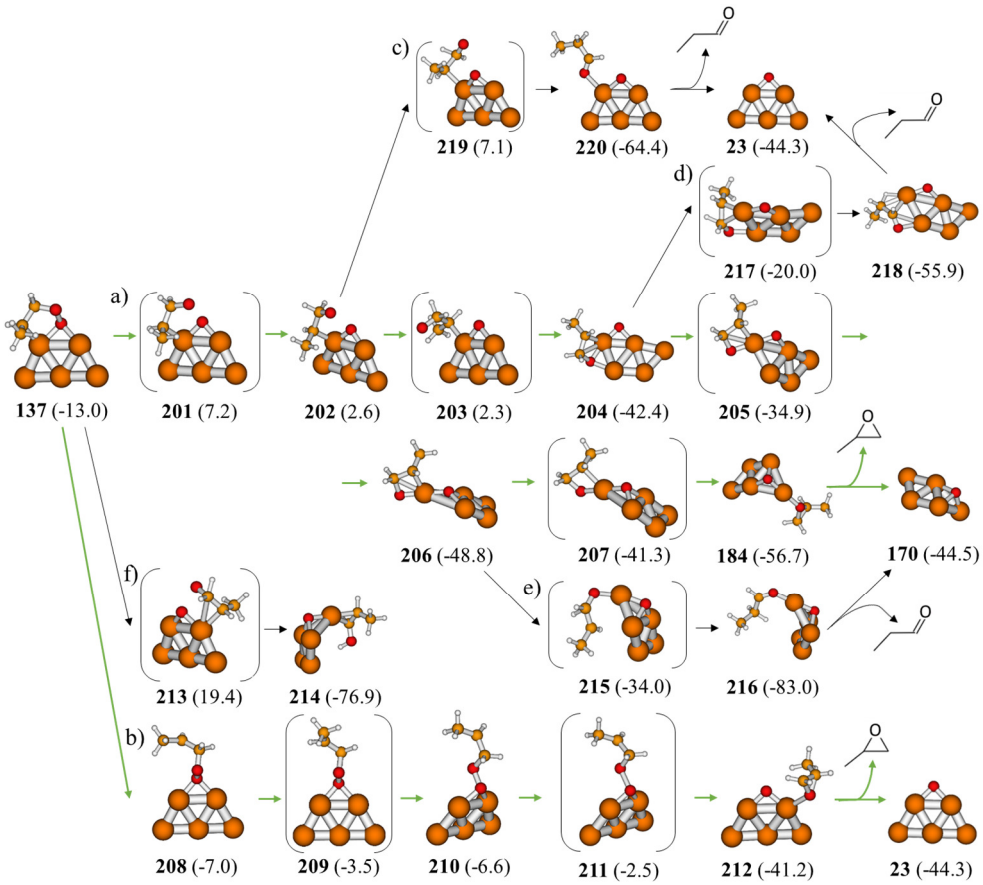

Figure 4.25. Optimized structures for possible reaction mechanisms from the OMC produced on planar Cu_5 (structure **137**). Relative Gibbs free energies with respect to separate planar $Cu_5 + O_2 + 2C_3H_6$ are given in kcal mol^{-1} in parenthesis. Cu in orange, C in amber, O in red, H in white.

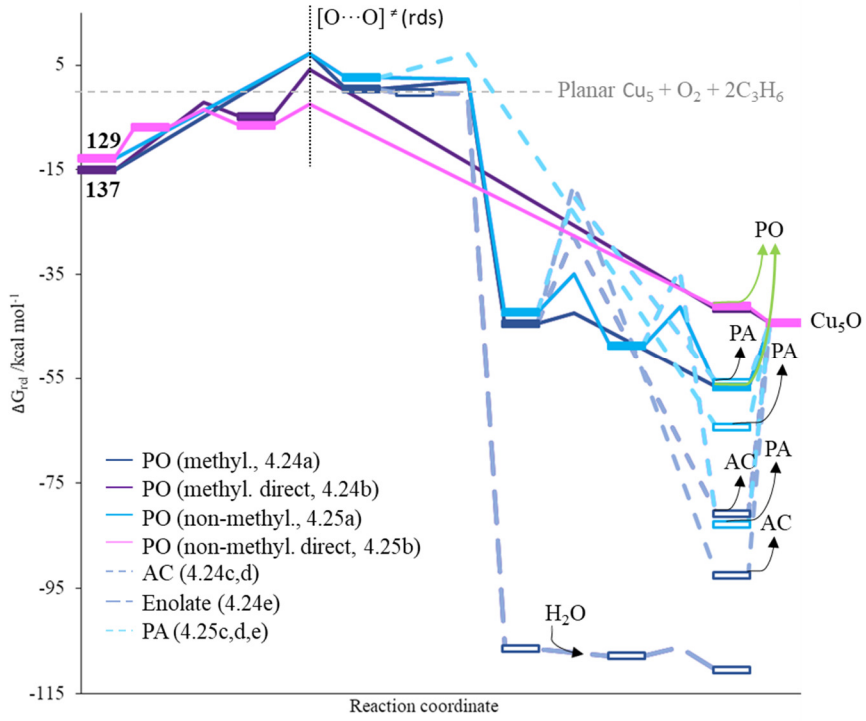

Figure 4.26. Energy profile of paths towards PO (normal lines) or secondary products (dashed lines) on planar Cu_5 from the OMC intermediate with the O bonded to the methylated (structure **129**) or to the non-methylated (structure **137**) C atom of the propene C=C bond. Key TSs and products are indicated.

To sum up, it is then found that the rest of the mechanism towards PO production is affordable and competitive reactions to PA or AC do not predominate over PO. In addition, the rds of the reaction is the dissociation of the O-O bond once the OMC is formed, although the OMC formation step has a similar, only slightly lower, barrier.

4.3.2.4. Closing the cycle: OMC vs allyl formation by Cu_5O.

Given that in section 4.3.2.2 it was found that the $Cu_5(2O)$ system greatly enhances allyl production, reaction of Cu_5O with a second propene molecule in what would be the second part of the cycle may not be so favorable towards PO. To find this out, we studied the paths towards OMC and allyl for the Cu_5O structures obtained in the first part of the cycle for planar Cu_5, namely, structures **23** and **170** (Figures 4.27 and 4.28, respectively).

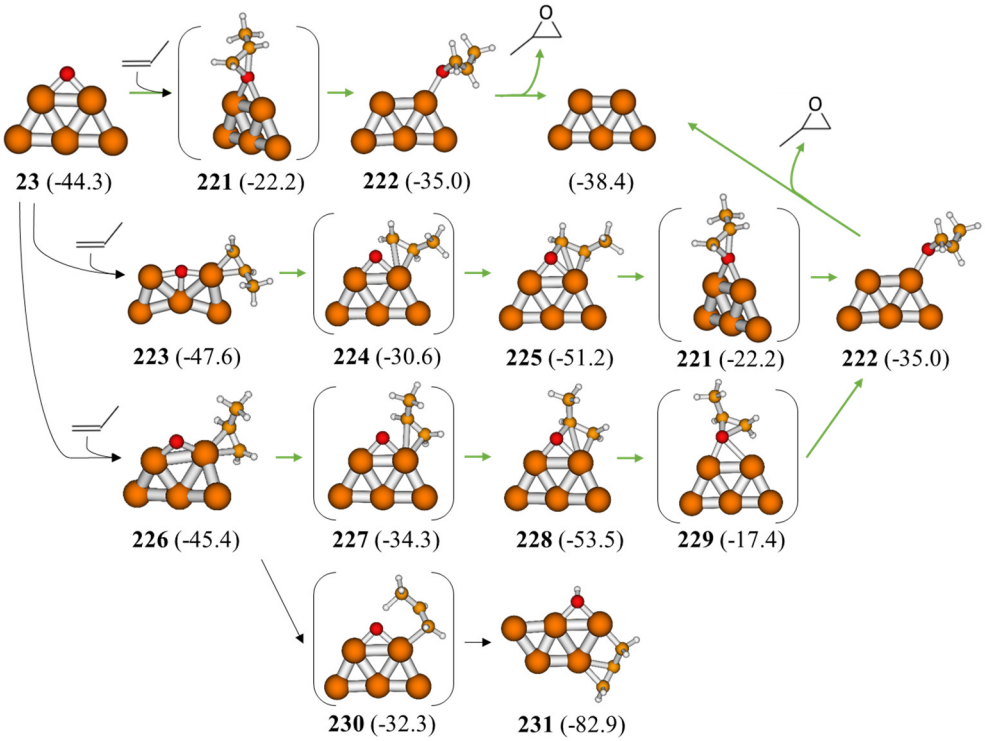

Figure 4.27. Optimized structures for the OMC or allyl formation by Cu_5O (from structure **23**). Relative Gibbs free energies with respect to separate planar Cu_5 + O_2 + $2C_3H_6$ are given in kcal mol^{-1} in parenthesis. Cu in orange, C in amber, O in red, H in white.

Remarkably, from both structures a direct ER TS leading to PO can be found (**221**, after deformation for structure **170**), that only requires 22.1 (22.3 for structure **170**) kcal mol^{-1} of energy and retrieves planar Cu_5 after PO desorption. LH mechanisms from structure **23** present 5.1 and 11.0 kcal mol^{-1} smaller activation energies (TSs **227** and **224**), although adsorption energies of propene are very small, of 1-3 kcal mol^{-1} (structures **226** and **223**, respectively). We find again that reaction with the non-methylated carbon atom is somewhat worse (17.0 vs 11.1 kcal mol^{-1}). However, the adsorption with this carbon atom facing the O atom is now 2.2 kcal mol^{-1} favored compared to the methylated one. Moreover, allyl formation from the latter structure (**226**) requires 2.0 kcal mol^{-1} more energy than OMC formation. In contrast, although from structure **170** adsorption of propene is strong (structures **232** and **235**) and the OMC formation is also somewhat better at the methylated carbon, both of them require much larger activation energies (46.6 and 40.6 kcal mol^{-1} for TSs **233** and **236**, respectively) because in structures **232** and **235** propene is far from the tricoordinated O atom and the reaction requires the detachment of the copper atom the propene is at, destabilizing TSs **233** and **236**.

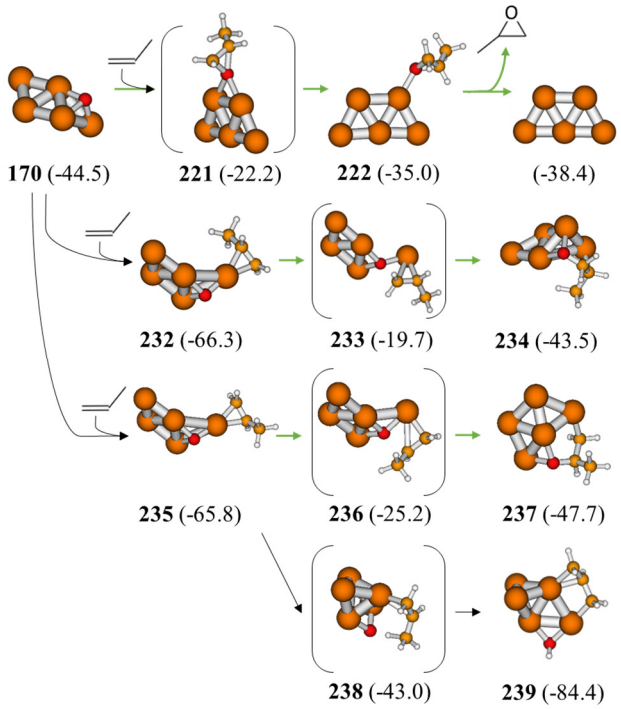

Figure 4.28. Optimized structures for the OMC or allyl formation by Cu_5O (from structure **170**). Relative Gibbs free energies with respect to separate planar $Cu_5 + O_2 + 2C_3H_6$ are given in kcal mol^{-1} in parenthesis. Cu in orange, C in amber, O in red, H in white.

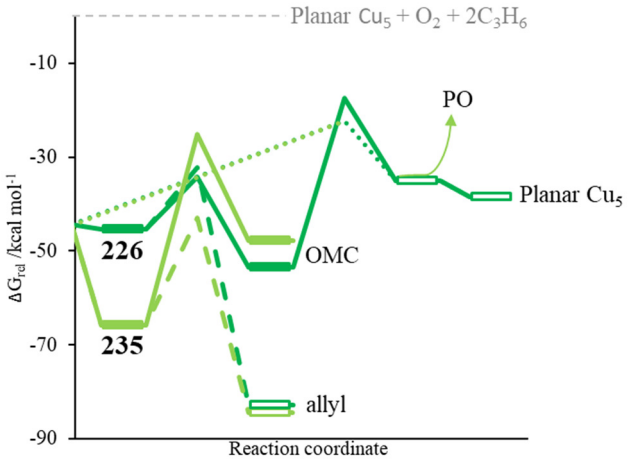

Figure 4.29. Energy profile of the OMC vs allyl formation by Cu_5O from structure **23** (green) or **170** (light green). Dashed and point lines correspond to allyl and PO (ER) paths, respectively.

Reaction towards allyl is not that impeded sterically because the methyl group reaches farther from the adsorption site of the molecule, and thus an activation energy of 22.9 kcal mol^{-1} is obtained (TS **238**). Nevertheless, since the ER path from **170** requires 22.3 kcal mol^{-1}, it will remain slightly predominant, provided the deformation observed is allowed (Figure 4.29).

Once the OMCs of structures **225** and **228** are formed, PO can be obtained directly in a single step with barriers of 29.0 and 36.1 kcal mol^{-1}, respectively (TSs **221** and **229**), obtaining again structure **222** from which the molecule desorbs favorably. While these barriers are rather high, the ER path leading to PO is predominant from structure **23** as well.

It can therefore be concluded that planar Cu_5 clusters favor PO production in the propene oxidation by molecular O_2 for both the first and the second parts of the catalytic cycle over competitive reactions. Although the paths towards allyl formation present affordable activation energies (in the 13-23 kcal mol^{-1} range), they are 3-8 kcal mol^{-1} higher than those of OMC for the first part of the cycle and up to 2 kcal mol^{-1} for the second part, for which the allyl reaction can be directly avoided following an affordable ER step towards PO. Regarding competitive reactions once the OMC is produced, a direct pathway that avoids them is found energetically preferable, but even in the other indirect pathway the production of enolate and some PA may affect selectivity only slightly, for reactions towards PA or AC (or the equivalent enols) are generally more than 7 kcal mol^{-1} higher in energy than following the complete path to PO. In addition, note that the production of PO through the direct pathways ultimately produces structure **23**, as opposed to structure **170**, thus avoiding a possible decrease of selectivity should propene adsorb on it before reacting through the more favorable ER mechanism (Figure 4.30).

Finally, an important result is that, in spite of some minor deformations through the cycle, planar Cu_5 clusters are finally recovered with a planar geometry again, and therefore can immediately undergo the same cycle that favors PO. This is important because, as seen in section 4.3.2.2, Cu_5 clusters are likely to deactivate if they lose their planar geometry.

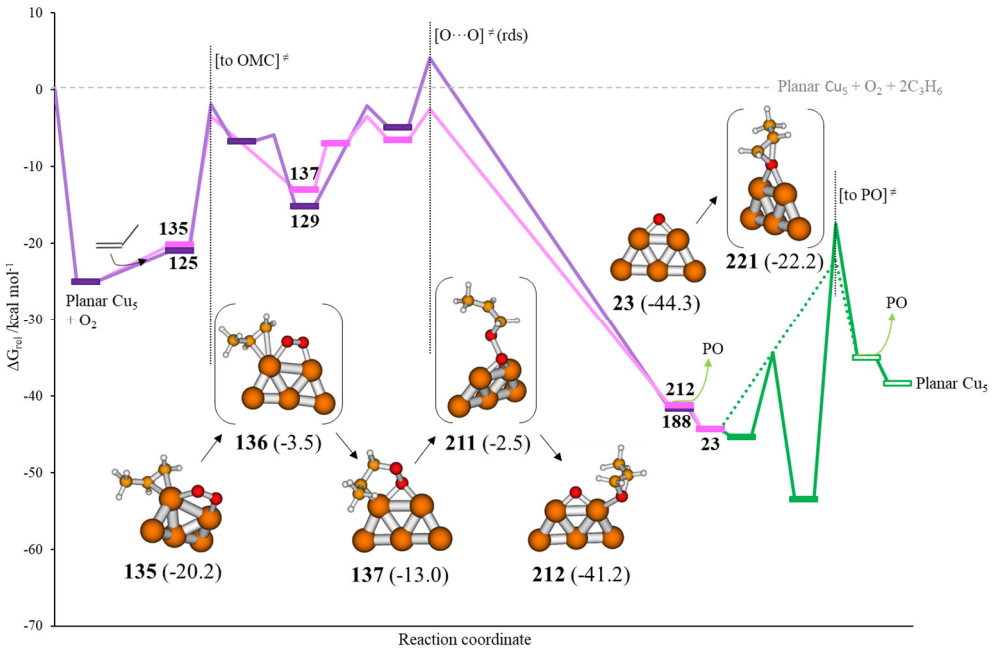

Figure 4.30. Energy profile of the lowest energy paths found for the propene epoxidation by planar Cu_5. The path corresponding to the OMC formed with the non-methylated C atom of the double bond (from structure **135**) is shown in pink, whereas that with the methylated one (structure **125**) is in purple. Green lines correspond to the formation of the second PO molecule (with the ER path in a dashed line). Key TSs and structures are indicated and shown, respectively.

4.4. Conclusions.

Firstly, it is concluded that all clusters studied, namely, planar Cu_5, 3D Cu_5 and Cu_8, are able to catalyze the CO oxidation reaction. The highest activation energy among the steps of the lowest energy pathway is similar for the three of them, and of about 16-18 kcal mol^{-1}. Thus, although planar Cu_5 presents the lowest barrier, it will not represent a great difference in terms of efficiency. There are, however, differences regarding the reaction mechanism.

Indeed, the mechanisms of 3D Cu_5 and Cu_8 are more similar between them than to that of planar Cu_5. For the former two, the O_2 molecule is dissociated first, even in the presence of adsorbed CO, and then two CO molecules react with the resulting O atoms. They differ in the way the latter occur: for Cu_8, LH mechanisms are favoured for both O + CO steps, with the first being significantly easier; for 3D Cu_5, an LH mechanism is still preferential for the first O + CO step, although with a higher activation energy due to the molecule being far from the O atom, but for the second the

ER mechanism is a bit easier. In both of them the second O + CO step is the rds. In contrast, planar Cu_5 did not catalyze O_2 dissociation well, and thus the reaction proceeds forming a OOCO intermediate first, whose O-O bond is broken in a second step, releasing the first CO_2 and leaving one adsorbed O atom. The latter is bicoordinately adsorbed, which lowers the activation energy needed for the final O + CO ER step. As a result, the rds of the reaction is the formation of the OOCO intermediate.

Planar Cu_5 seems prone to deformation towards 3D Cu_5 with a high pressure of CO, but such effect would not diminish the catalytic activity of Cu_5 clusters. In some cases, however, structures where an O atom gets within the Cu_5 cluster have been obtained, for which further reaction gets complicated, increasing the activation energy of some steps. Nevertheless, the presence of other CO molecules has proven to be enough to put the O atom nearer to a CO and recover low barriers. Thus, we do not believe such will be much of a problem on Cu_5, but the higher oxidation of Cu_8 may be. Indeed, subsequent oxidation reactions at other available facets of the Cu_8 cluster are likely to oxidize Cu_8 to a larger extent diminishing its catalytic activity.

Regarding the epoxidation of propene, it is found that the first step leading to the OMC, which is determinant for the selectivity of the reaction, is indeed somewhat favoured with respect to the undesired allyl for planar Cu_5 clusters. 3D Cu_5 would perform worse because the very adsorption of O_2 in an *h111* mode, i.e. as a superoxo species, is enough to favour the reaction with the hydrogens of the methyl group leading to allyl. Once O_2 is dissociated, the preference for allyl formation is clear. However, it is also found that once the first molecule of PO is produced on planar clusters, the O atom again bicoordinately adsorbed still somewhat favours the OMC reaction, with the direct ER reaction being also energetically possible. In addition to this, the complete reaction paths towards PO from the OMCs were studied, and secondary reactions towards PA or AC always presented higher barriers.

Due to all this, planar Cu_5 clusters are promising candidates to catalyze the propene epoxidation reaction with good selectivity to PO.

Chapter 5
Supported Cu clusters

This chapter constitutes a direct continuation on the research line of Chapter 3, with the objective of determining how the properties of copper clusters change when they are no longer in gas phase but deposited on a certain support.

As shown in the Introduction, the selection of a support is not a trivial matter, for it can alter the cluster geometry and oxidation state, among other properties, and is therefore undoubtedly linked to the catalytic activity of the final material[261,262]. In principle, a material that interacts weakly with the cluster is more likely to preserve its metallic state. This seems to be key regarding copper, as the catalytic activity is usually assigned to either Cu^{+} or Cu^{0}, but almost never to Cu^{2+}. However, copper clusters easily aggregate into larger particles and in fact their synthesis without stabilizing ligands that prevent their growth is complicated[96,106,107]. Since larger particles immediately oxidize to CuO, cluster sintering leads to deactivation. Consequently, the interaction with the support needs to be strong enough in order to grant the stability of the clusters.

In the present chapter we study copper clusters of different sizes supported on both pristine and defective graphene and N-doped graphene sheets, and on the $CeO_2(111)$ surface, and also test the dissociation of O_2 on selected Cu_5–supported systems.

5.1. Introduction.

Graphene is a two-dimensional allotrope of carbon that constitutes a quite recent discovery[263]. It has been -and still is- an intensive subject of research due to its properties, such as high mechanical resistance and good thermal and electrical conductivity, among others[264-266]. In addition, although graphene is a conductor (it has a zero band gap), its conduction band is not partially filled (as in metals) but empty. Its band structure can be modified leading to materials of semiconductor behavior and to interesting optical properties. Such modifications are produced when the monolayer is forced to adopt other forms, such as nanoribbons or graphene quantum dots, but also if graphene is chemically doped, either by adsorption or substitution[267,268]. All of it has made graphene a very promising material for applications related to electronics, electrocatalysis, electrochemical or optical sensors, and to energy conversion or storage[265,267-275].

Thus, while the N-doping of graphene was in our case pursued to anchor the copper clusters to the graphene sheet and avoid their sintering without modifying their properties, as also pointed out by others[276], it unavoidably changes, at least, the properties of clean graphene[268-272,277]. For instance, although it is clear that N-doped graphene (or N-graphene) has a good electrocatalytic activity for the Oxygen Reduction Reaction (ORR) and the Oxygen Evolution Reaction (OER), there is no consensus regarding which nitrogen species is the active site or rather which is the most active, with the most recent report pointing to the so-called graphitic N as the determinant species[271,278,279]. Indeed, when nitrogen is introduced in graphene, a number of species can be formed, among which those known as graphitic (or quaternary) N and pyridinic N are common[268,270]. Nevertheless, regarding O_2 dissociation, a DFT study showed that while N-doping decreases the energy barrier with respect to pristine graphene, they remain high at these most common graphitic and pyridinic N sites[277], consistent with the surface being inert in the experiments shown in Chapter 3.

To compare with graphene, which is in principle a more inert support on which clusters are difficultly anchored, we added CeO_2 to our study, a reducible oxide hence more reactive, but on which the metal-support interaction is strong, granting a certain sintering resistance[280].

CeO_2 constitutes a widely used support material in catalysis due to its oxygen storage capacity, because the formation and reparation of oxygen vacancies on its surface is easy due to the similarly easy valence change of its cerium ions between Ce^{4+} and Ce^{3+}[281,282]. Ceria-based materials catalyze the WGS reaction and the selective catalytic reduction of NO_x by NH_3 in automobiles, among other important processes[283-288]. Examples of its beneficial interaction with copper clusters can already be found in the literature: Wang et al. reported the enhanced H_2 oxidation

ability of a Cu/CeO_2 electrode in solid oxide fuel cells[289], and Yang et al. found that a lower barrier for the H_2O dissociation was obtained at the interface of a Cu_4/CeO_2 system hence explaining its catalysis of the WGS reaction[290]. In addition, small copper oxide clusters (Cu^+), have been reported to increase the catalytic activity for CO oxidation in different CeO_2 materials[291,292].

In spite of all of these potential applications, there are but a few theoretical studies on copper clusters supported on CeO_2[289,290,293-296] or graphene[275,297-306], and most of the latter are of the Cu atom[275,297-301].

In the present work we study copper clusters of size n=5, 8, 13 supported on different representative sheets of graphene and N-graphene and on the CeO_2(111) surface, which is is the predominant facet of ceria[307]). Then, the stability, geometry and electronic properties of the species are discussed, and the dissociation of O_2 is tested on selected Cu_5–supported systems.

5.2. Computational details.

5.2.1. Models.

All graphene sheets were modelled by 1x8 supercells built from a graphene unit cell of a = b = 2.468, $\alpha = \beta = 90°$ and $\gamma = 120°$ used previously in the group[308], reoptimized at the PBE level. C and N atoms were removed and substituted, respectively, to create the corresponding defective and N-doped sheets, which were later reoptimized (allowing no changes to the cell).

For the CeO_2(111) surface, a 3x3 supercell slab model was employed to support Cu_5 and a larger 4x4 supercell was used for Cu_8 and Cu_{13}, both generated from a bulk model of a = b = c = 5.490 and $\alpha = \beta = \gamma = 90°$. The slabs contained 9 atomic layers (three O-Ce-O stacks), of which the top 6 were allowed to relax during optimizations.

In all slabs periodic images were separated by a vacuum layer sufficiently large (20 Å for graphene sheets and about 14 Å for ceria). Isolated clusters and the O_2 molecule were optimized in a 15x15x15 $Å^3$ cubic box.

5.2.2. Methods.

Structure optimizations were carried out at the Density Functional Theory (DFT) level with the VASP code[22,231], spin-polarized and using the PBE functional of Perdew, Burke and Ernzerhof (PBE)[158]. To partially remedy the self-interaction error (SIE) of the functional, which prevents electrons to correctly localize in Ce atoms when Ce^{3+} cations are formed, the *4f* orbitals of the Ce atoms are treated using the rotationally invariant approach to the DFT+U method, introduced by Dudarev et al.[164], with a Hubbard-type parameter of U*eff*=4.5[165,166].

The valence density was expanded in a plane wave basis set with a kinetic energy cutoff of 600 eV, and the effect of the core electrons in the valence density was taken into account by means of the projected augmented wave (PAW) formalism[178]. In the reciprocal space, the integration was done at the Γ k-point of the Brillouin zone for graphene and 4x4 ceria slabs, whereas a 2x2x1 k-points mesh generated with the Γ–centered Monkhorst-Pack algorithm[177] was used for $Cu_5/CeO_2(111)$ systems (i.e. 3x3 slabs). The convergence criteria were 10^{-5} eV for the SCF energy and 0.02 eV/Å in the maximal forces per atom. The Gaussian smearing method was employed to determine electron occupancies with a smearing parameter of $\sigma = 0.02$ eV, which was increased to 0.05 eV to evaluate the band structure of graphene sheets, together with an increased 12x12x1 k-points mesh.

Transition states were located using the Improved DIMER[185,186] or CI-NEB[187] algorithms. Stationary points were characterized by partial hessian frequency calculations with the atoms of the surfaces fixed.

Dispersion interactions were taken into account by adding atom pair 1/R6 terms as parameterized by Grimme ("D2")[161] throughout the optimization for grapheme systems, whereas only single-point calculations were done at the PBE(+U) structures on ceria. C and R0 parameters values of 20.00 and 1.860 were chosen for Ce, which were previously calculated and tested[162], and default parameters were adopted for the other atoms (10.80 and 1.562 for Cu and 0.70 and 1.342 for O). Atomic charges were obtained through the Bader analysis[191].

In addition, the Jmol[257], MOLDEN[256] and p4vasp[309] programs were used to build and visualize the systems and their frequencies throughout the work, whereas VESTA[310] and XmGrace/QtGrace were employed to obtain the images of structures and DOS, respectively.

5.3. Results.

5.3.1. Graphene-supported copper clusters.

5.3.1.1. Cu_5, Cu_8 and Cu_{13} on pristine and defective graphene and N-graphene.

The planar and 3D isomers of Cu_5 and the most stable structures for gas phase Cu_8 and Cu_{13} from Chapter 3 (Figure 5.1f) were placed on four different graphene sheets. Both pristine and defective (with one C vacancy) graphene sheets were considered (C128, G and C127, G_V) and, to compare with the experimental results from Chapter 3, a 10% amount of nitrogen was targeted for N-doped models, therefore creating N12C116, NG (clean, with graphitic N atoms only) and N12C115, NG_V (defective, with three pyridinic N atoms at one C vacancy) structures (Figure 5.1a-d). For the NG sheet another distribution of the graphitic N atoms, more separated from each

other, was also considered, but it was 6.5 kcal mol^{-1} higher in energy (Figure 5.1e). The pyridinic NG_V model was nonetheless created from the latter to account for any possible effect missed.

In pristine graphene, carbon atoms arrange in a plane with a hexagonal (honeycomb) lattice structure and are sp^2-hybridized, so that each of them has three sp^2 orbitals and a remaining p_z, each occupied by one electron. The former produce σ bonds that form deep valence bands, whereas the p_z orbitals of all carbon atoms overlap forming a π filled valence band and a π* empty conduction band (Figure 5.2a).

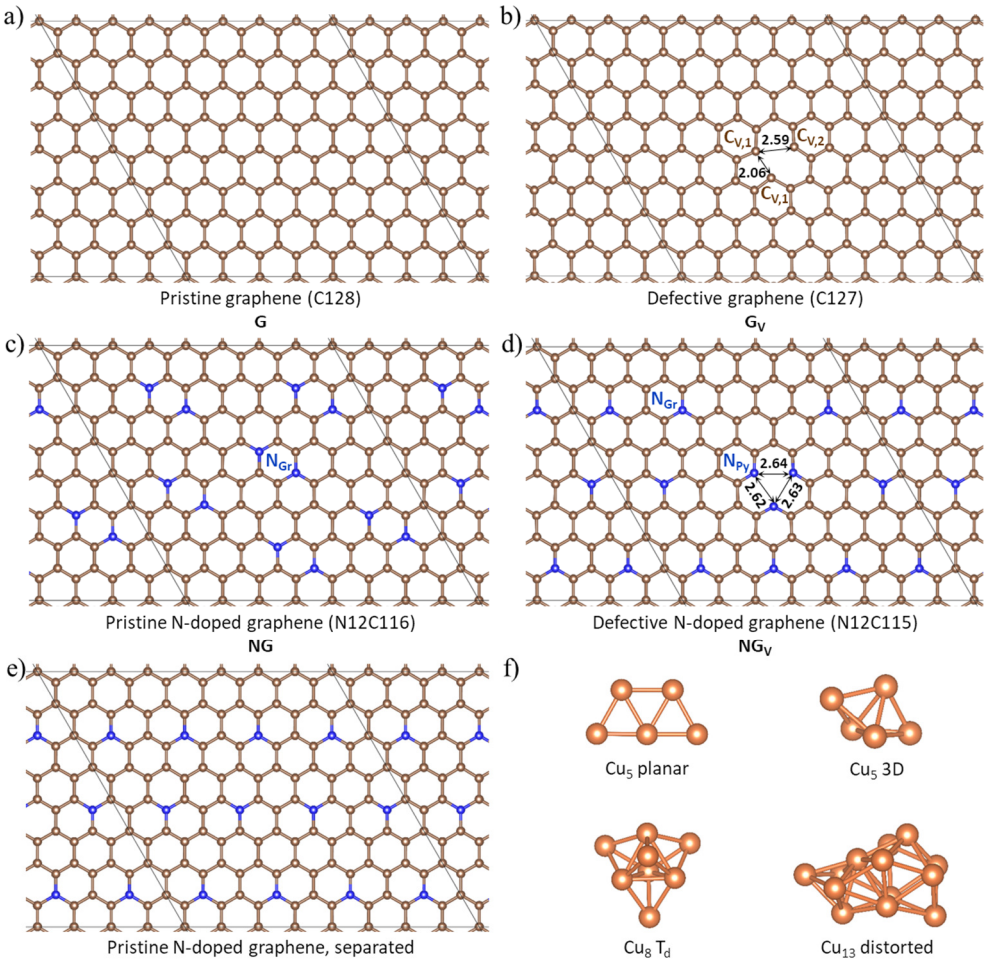

Figure 5.1. a-e) Graphene models employed and f) copper clusters considered. Periodic cells are indicated by black lines. Interatomic distances at C vacancies are indicated in Å. C atoms in brown, N in blue, Cu in orange.

When nitrogen is introduced, both graphitic and pyridinic N are sp^2-hybridized, but since the latter has one lone pair filling its uncoordinated sp^2 orbital, it contributes to the π band with a half-filled p_z orbital, as C atoms do, whereas graphitic N contributes with an additional electron that goes to the π* antibonding orbital[277]. In addition, the C vacancy between the three pyridinic N atoms produces one electron less in the π band. Thus, n-type doping is produced in NG whereas the three pyridinic N atoms-sites in NG_V cause p-type doping[277]. As a consequence, the so-called Dirac point of graphene[264], at which the DOS is zero (there are no states) and which lies at the Fermi level on pristine graphene, is displaced towards lower values for NG and towards larger values for each three pyridinic N atoms-site.

In our case, the contribution of p_z electrons from graphitic N atoms (N_{Gr}) to the π* band that starts from the Dirac point is clearly observed (Figure 5.2b) and, given that the NG_V sheet also has nine N_{Gr} atoms, the n-type doping also predominates (Figure 5.2d). In the case of G_V, with no N atoms, the p-type doping is visible, as the Dirac point lies higher than the Fermi level and a small peak from the π band is empty (Figure 5.2c). Notice that the p_z orbitals of the three C atoms at the vacancy (C_V) do contribute to these peaks at the Fermi level. Moreover, defects corresponding to the sp^2 orbitals of the less-coordinated C_V atoms arise. For the non-equivalent C_V atom at the vacancy ($C_{V,2}$), contributions to deeper σ bands are indeed observed, but the half-filled uncoordinated sp^2 orbital is also observed as an intense localized peak below the Fermi level, whereas its spin-down contribution appears as an empty peak higher in energy, consistent with the fact that a lone two-electron pair on a C atom would be very unstable. In contrast, for the two equivalent C_V atoms that become closer at the C vacancy ($C_{V,1}$), although the three s, p_x and p_y orbitals also contribute to the same defects, their density is more spread: a small contribution is also found in the same peak of $C_{V,1}$ below the Fermi level, but a larger contribution is obtained for the deeper σ bands and the two localized sp^2 states lie higher than the Fermi level, hence empty. Thus, if the $C_{V,1}$ atoms become closer a higher amount of electron density can be shared with the σ bands and, since they are lower in energy, it is also a more stable solution for the system, which therefore prefers leaving the sp^2 orbitals almost empty. The sp^2 covalent character of the defects is moreover seen by the small s and $p_x + p_y$ contributions of the other C atoms at the same energetic positions. The lone pair on pyridinic N atoms (N_{Py}) is stable and the three of them contribute to four (two of each spin) occupied defects below the π* band (Figure 5d). The smaller contributions of s and $p_x + p_y$ C orbitals indicate that the lone pair is shared to some extent, like for C_V atoms in G_V. Indeed, the separation of these defects from the σ bands indicates in both cases a somewhat worse but more localized interaction with respect to C-C bonds. Besides, much like in G_V, the p_z of N_{Py} atoms at the C vacancy contributes to a localized defect from the π band, which now is completely filled due to the n-doping of N_{Gr}.

Due to all of this, N-graphene should have a metallic character. While the orbitals of all N_{Gr} atoms are filled and they are unable to establish covalent bonds, C and N_{Py}

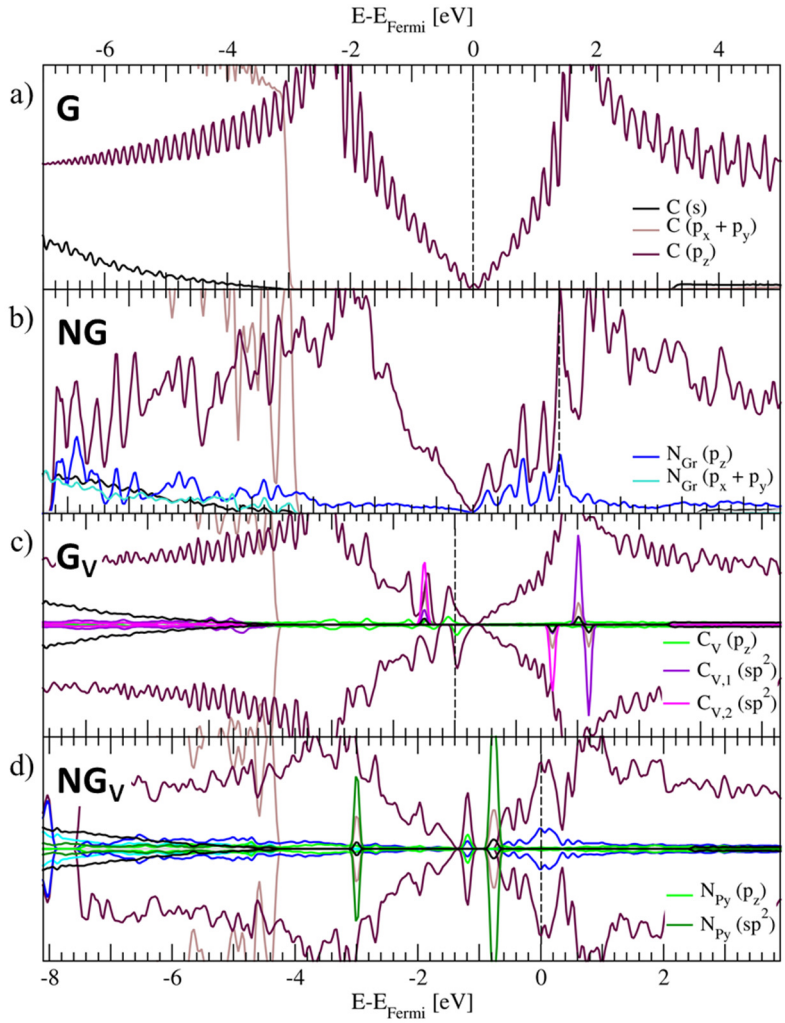

Figure 5.2. Projected density of states (PDOS) of the graphene sheets. For C atoms p_z and p_x+p_y orbitals are projected in dark and light brown, respectively, while the same orbitals of graphitic N (N_{Gr}) are in dark and light blue. *s* orbitals of C atoms are in black, those of N_{Gr} contribute to deeper valence bands and are not shown, and those of pyridinic N (N_{Py}) and C atoms at a C vacancy ($C_{V,1}$ for the two equivalent and closer C atoms and $C_{V,2}$ for the remaining one) contribute to the same defects as the p_x and p_y orbitals and are projected together, indicated as sp^2 in dark green, purple and pink, respectively. Their p_z contributions to the π and π* bands are projected in light green. PDOS are aligned w.r.t. the Dirac point. Dashed lines mark the highest occupied energy level.

atoms can if they break the aromaticity of their shared p_z and undergo a sp^3 hybridization. The latter implies a tetrahedral coordination sphere, and thus only N_{Py} atoms have no steric impediment for it (and C_v ones on G_V).

The introduction of nitrogen additionally causes positively charged C atoms on the surface, due to the difference in electronegativity between N and C (Figure 5.3 and Table 5.1). The Bader charge analysis indicates that carbon atoms directly bonded to graphitic N atoms are positively charged by 0.33e and, correspondingly, the latter show negative charges close to -1e. We found no significant difference between C atoms bonded to one graphitic N ($C_{GrN,1}$) and those that, in addition, have a neighbor C atom also bonded to graphitic N ($C_{GrN,2}$). Pyridinic N atoms present practically the same charge than graphitic N (1.03e), but C atoms bonded to the former have larger positive charges ($C_{PyN,1}$, 0.55e) that are compensated by C neighboring atoms that receive some charge ($C_{PyN,2}$, -0.07e).

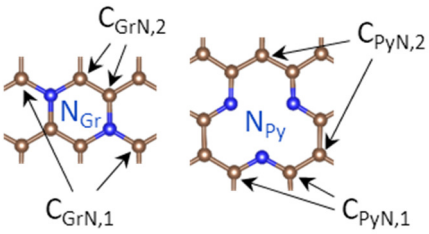

Figure 5.3. Labels used for C atoms in the charge analysis of N-doped graphene sheets (Table 5.1). C in brown, N in blue.

Table 5.1. Average Bader charges over C and N atoms on N-doped graphene sheets. C atom types are labelled as in Figure 5.3.

N-doped sheet	Atom type	Charge (e^-)
Pristine (NG)	N_{Gr}	-0.96
	$C_{GrN,1}$	0.33
	$C_{GrN,2}$	0.33
	Other C	-0.01
Defective (NG_V)	N_{Py}	-1.03
	N_{Gr}	-0.97
	$C_{PyN,1}$	0.55
	$C_{PyN,2}$	-0.07
	$C_{GrN,1}$	0.32
	Other C	0.00

Consistent with this description of the graphene sheets, copper clusters avoid the graphitic N atoms of N-graphene upon adsorption (Figure 5.5) and adsorb preferentially on the vacancies of defective sheets (Figures 5.6 and 5.7).

Thus, clusters adsorbed in G_V, the most unstable system, present the largest adsorption energies regardless of cluster size (from -96.9 to -127.2 kcal mol^{-1}, Table 5.4) followed by NG_V (from -71.0 to -88.6, Table 5.5). The adsorption energy for structures on G or NG are at least 50 kcal mol^{-1} higher, ranging from -30.2 to -49.7 kcal mol^{-1} and being only somewhat better (4-11 kcal mol^{-1}, Tables 5.2 and 5.3) in the N-doped sheet. Separating the total adsorption energy (ΔE_{ads}+D2) into the electronic (ΔE_{ads}) and dispersive (D2) contributions shows that the latter difference between G and NG is not due to dispersion, for it is similar in both cases. Besides, it confirms that dispersion forces are predominant in the Cu_n-surface interaction on G and NG.

It constitutes about 40-65% of the total adsorption energy for Cu_5, but it increases to 70-80% for Cu_8 and to 90% for Cu_{13}, showing that increasingly larger clusters are not able to interact as efficiently through their frontier orbitals (probably because they lose overlapping capability with size), which is also observed in the remaining

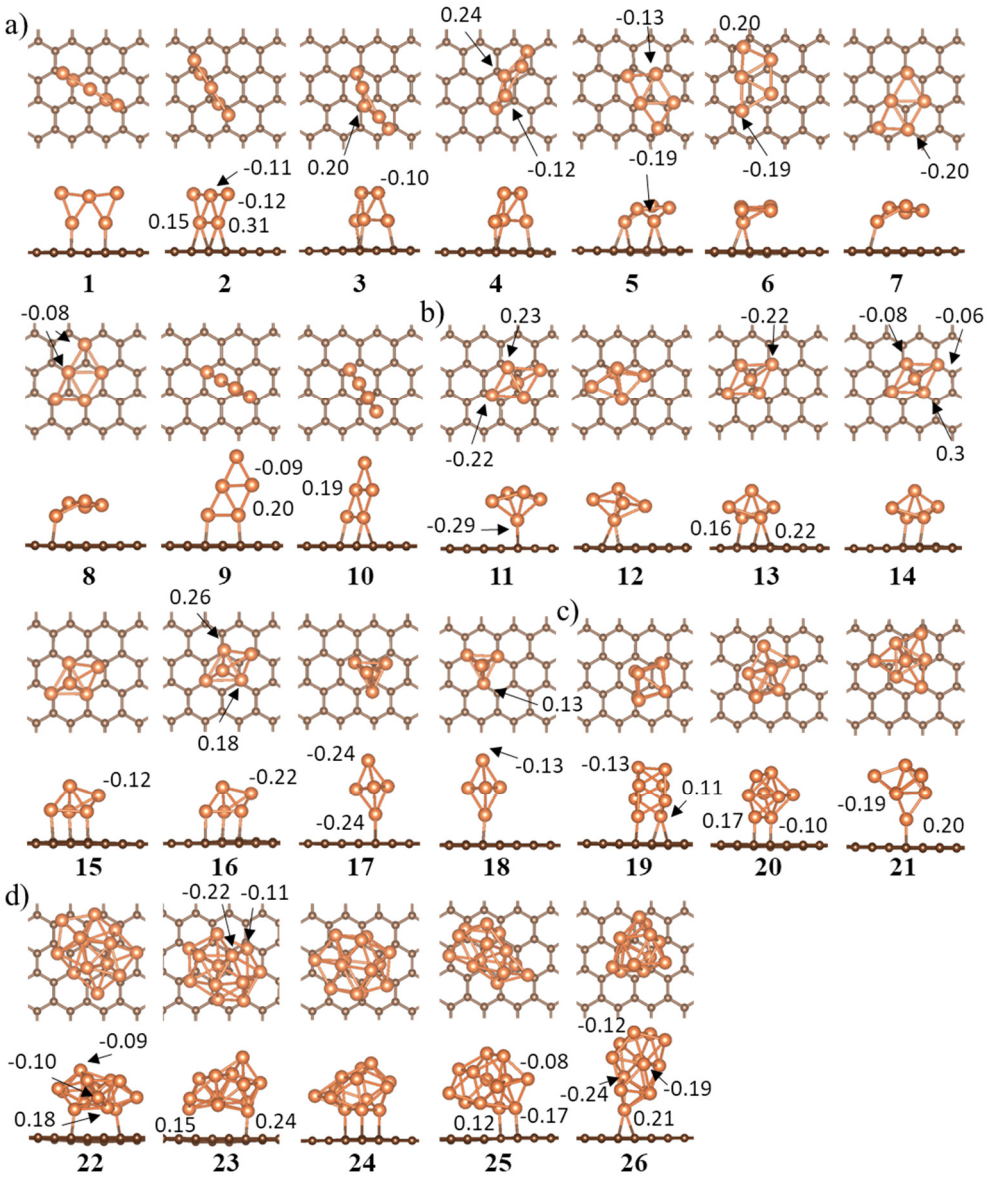

Figure 5.4. Optimized structures of a) planar Cu_5 b) 3D Cu_5 c) Cu_8 and d) Cu_{13} clusters supported on G, in order of decreasing stability. Top and side views are shown. C in brown, Cu in orange. Non-average Bader charges on copper atoms are specified.

adsorption energy (ΔE_{ads}) that follows the order $Cu_5 > Cu_8 > Cu_{13}$. In contrast, the chemical interaction is predominant on G_V and NG_V, and dispersion contributions decrease to 20-40%. In any case, dispersion contributions are rather large (in absolute values) and increase with cluster size due to the higher number of atoms and of C-Cu interactions (about 12-26, 18-31 and 20-47 kcal mol^{-1} for Cu_5, Cu_8 and Cu_{13}, respectively).

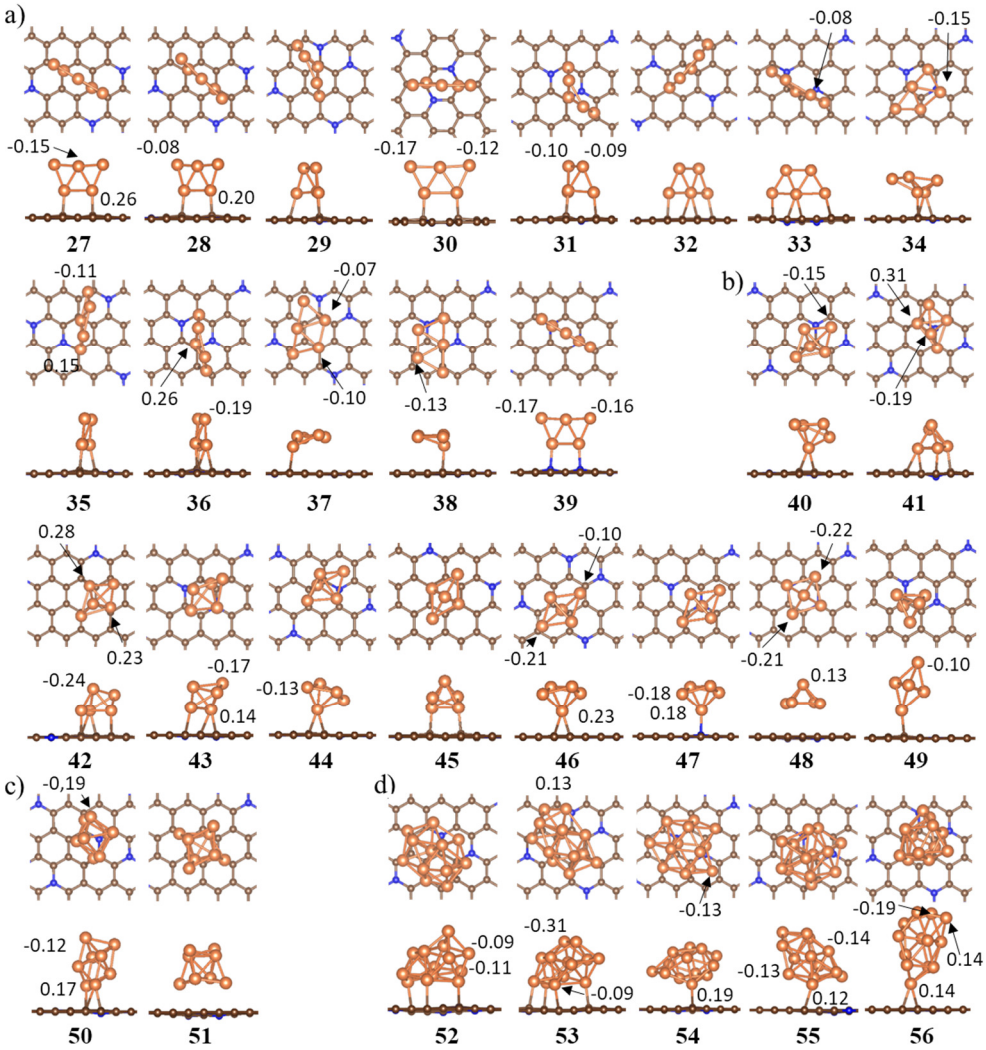

Figure 5.5. Optimized structures of a) planar Cu_5 b) 3D Cu_5 c) Cu_8 and d) Cu_{13} clusters supported on NG, in order of decreasing stability. Top and side views are shown. C atoms are in brown, Cu in orange, N in blue. Non-average Bader charges on copper atoms are specified.

Per atom, total adsorption energies decrease with the increase of atomicity, consistent with the preference of structures where not all the atoms interact with the surface and showing that Cu-Cu interactions are stronger than copper-surface interactions. Thus, while the energetic order of adsorption strength on the different sheets or sites is the same, from the available bibliography adsorption energies of copper clusters are lower than those reported for other transition metals (Ni_5[311], Pt_5[311], Pd_5[311-313], Au_5[308], Ag_8[314], Ag_{13}[315], Pd_{13}[315], Pt_{13}[316], Ni_{13}[317]).

The adsorption is also reflected in the charge transferred between the cluster and the support (Tables 5.2-5.5). In most cases the net effect is for the cluster to give charge

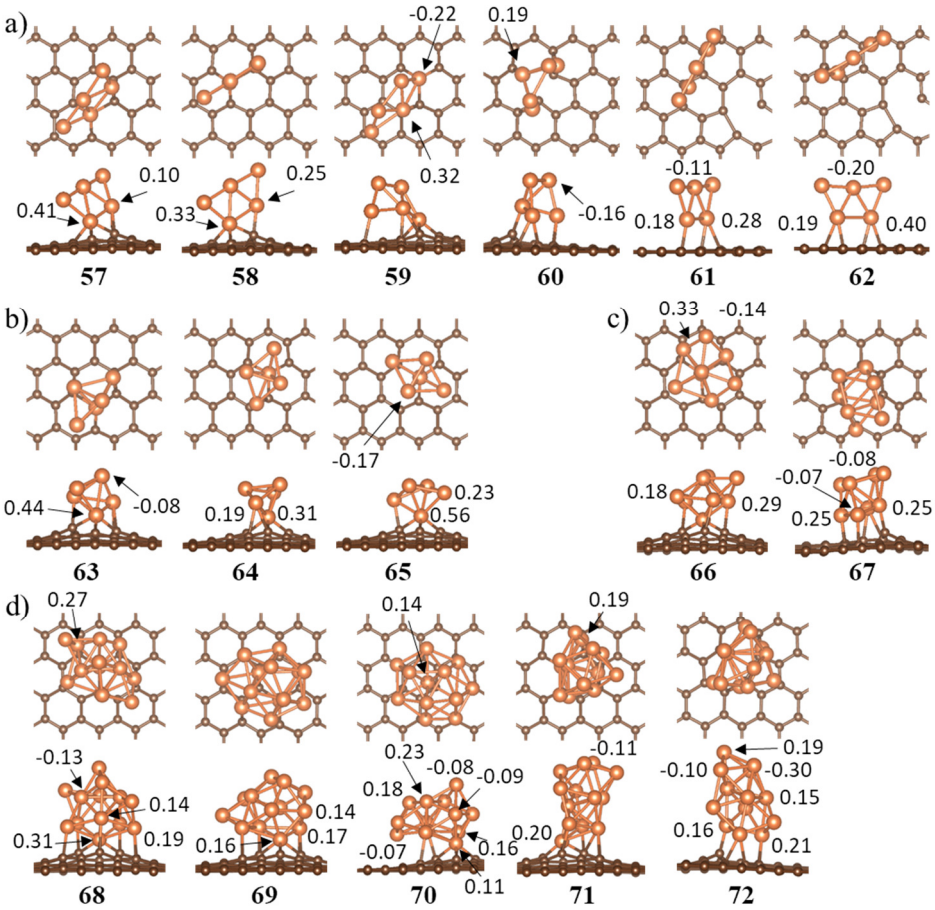

Figure 5.6. Optimized structures of a) planar Cu_5 b) 3D Cu_5 c) Cu_8 and d) Cu_{13} clusters supported on G_V, in order of decreasing stability. Top and side views are shown. C atoms are in brown, Cu in orange. Non-average Bader charges on copper atoms are specified.

to the support, between 0.1 and 0.4e for clean sheets and much larger, between 0.3 and 1.0e, for defective ones. However, in a few isomers and on clean sheets only, small negative charges are found on the clusters, i.e. the support loses charge in favor of the cluster. The most remarkable cases would be those of 3D Cu_5 on G and NG (structures **11** and **40**), which present -0.2 and -0.1e total charge, respectively, and that are, in addition, the most stable structures of that isomer in those supports.

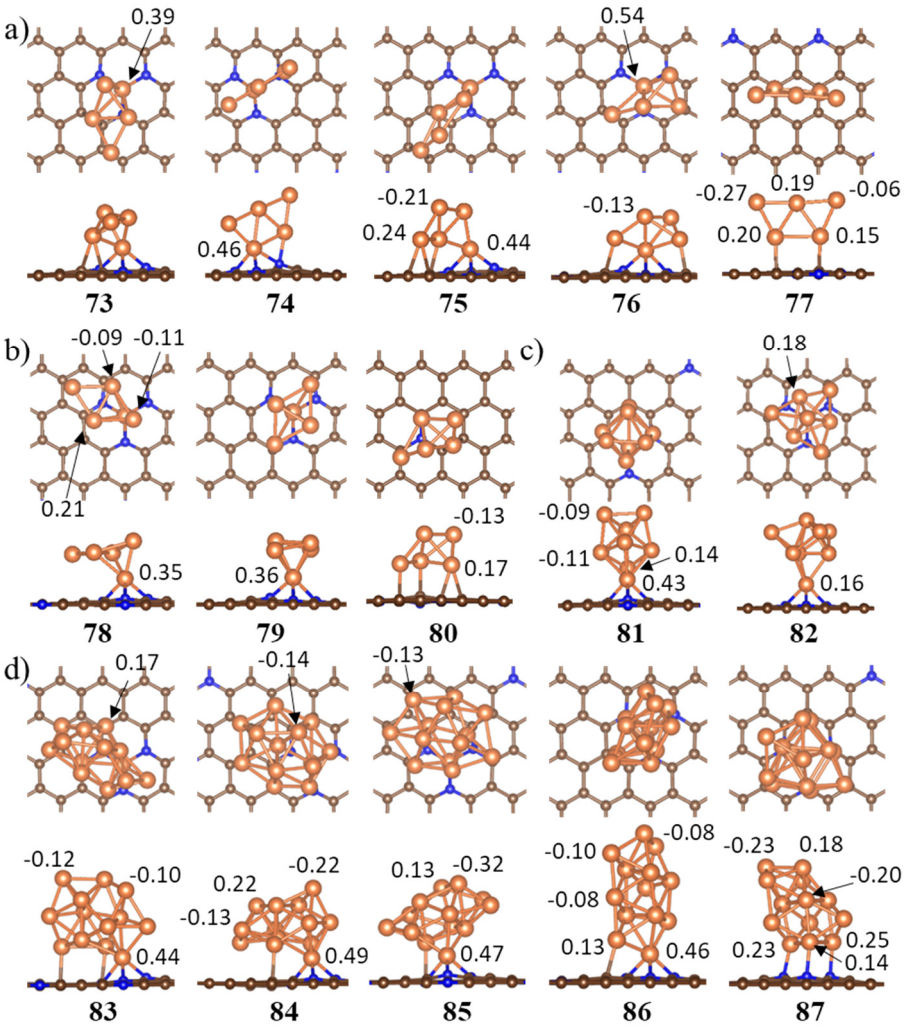

Figure 5.7. Optimized structures of a) planar Cu_5 b) 3D Cu_5 c) Cu_8 and d) Cu_{13} clusters supported on NG_V, in order of decreasing stability. Top and side views are shown. C atoms are in brown, Cu in orange, N in blue. Non-average Bader charges on copper atoms are specified.

Table 5.2. Relative energy w.r.t. the most stable structure per size including dispersion (ΔE_{rel}+D2), adsorption energy w.r.t. each isomer (ΔE_{ads}), dispersion contribution (D2), adsorption energy including dispersion (ΔE_{ads}+D2), adsorption energy per atom including dispersion ((ΔE_{ads}+D2)/n) and charge transferred from the cluster to the support (qCu_n) in the interaction of Cu_n (n = 5, 8 and 13) clusters with G. Energies in kcal mol^{-1}.

Cluster	Structure (Fig. 5.4)	ΔE_{rel}+D2	ΔE_{ads}	D2	ΔE_{ads}+D2	(ΔE_{ads}+D2) /n	qCu_n (e^-)
Cu_5	1	0.0	-9.5	-17.7	-27.2	-5.4	0.11
planar	2	1.3	-8.7	-17.2	-25.9	-5.2	0.26
	3	2.1	-3.2	-21.9	-25.1	-5.0	0.26
	4	2.1	-3.0	-22.1	-25.0	-5.0	0.20
	5	2.3	0.1	-25.0	-24.8	-5.0	-0.08
	6	2.9	1.1	-25.4	-24.2	-4.8	0.12
	7	3.1	1.2	-25.2	-24.0	-4.8	0.08
	8	3.4	1.5	-25.3	-23.7	-4.7	0.05
	9	5.5	-5.5	-16.2	-21.7	-4.3	0.01
	10	5.9	-5.2	-16.1	-21.3	-4.3	-0.02
Cu_5 3D	11	2.9	-14.3	-15.9	-30.2	-6.0	-0.19
	12	3.4	-10.9	-18.9	-29.8	-6.0	0.03
	13	4.4	-4.9	-23.8	-28.8	-5.8	0.22
	14	4.7	-4.6	-23.9	-28.5	-5.7	0.20
	15	5.7	-4.0	-23.5	-27.4	-5.5	0.17
	16	6.2	-3.6	-23.4	-27.0	-5.4	0.28
	17	17.7	-4.2	-11.3	-15.5	-3.1	-0.12
	18	17.9	-4.0	-11.2	-15.2	-3.0	-0.03
Cu_8 T_d	19	0.0	-7.2	-24.5	-31.7	-4.0	0.05
	20	7.7	-0.2	-23.8	-24.0	-3.0	-0.02
	21	11.2	-6.5	-13.9	-20.5	-2.6	0.04
Cu_{13}	22	0.0	-4.5	-40.8	-45.3	-3.5	0.05
distorted	23	4.7	5.0	-45.7	-40.7	-3.1	0.07
	24	9.2	6.1	-42.2	-36.1	-2.8	0.02
	25	10.5	0.7	-35.5	-34.8	-2.7	-0.02
	26	24.6	-0.7	-20.0	-20.7	-1.6	0.05

In many structures the Bader analysis reveals that the copper atoms at the interface are positively charged, whereas atoms in the external surface of the cluster exhibit up to -0.3e negative charge (Figures 5.4-5.7). While this could entail an electrostatic attraction of reagents, the charge among the metal atoms of small clusters is easily redistributable and we expect the total charge on the cluster to be more determinant for chemical processes.

Table 5.3. Relative energy w.r.t. the most stable structure per size including dispersion (ΔE_{rel}+D2), adsorption energy w.r.t. each isomer (ΔE_{ads}), dispersion contribution (D2), adsorption energy including dispersion (ΔE_{ads}+D2), adsorption energy per atom including dispersion ((ΔE_{ads}+D2)/n) and charge transferred from the cluster to the support (qCu_n) in the interaction of Cu_n (n = 5, 8 and 13) clusters with NG. Energies in kcal mol^{-1}.

Cluster	Structure (Fig. 5.5)	ΔE_{rel}+D2	ΔE_{ads}	D2	ΔE_{ads}+D2	(ΔE_{ads}+D2) /n	qCu_n (e^-)
Cu_5	27	0.0	-21.9	-16.6	-38.5	-7.7	0.11
planar	28	0.0	-22.0	-16.5	-38.5	-7.7	0.17
	29	2.2	-14.5	-21.8	-36.3	-7.3	0.10
	30	4.3	-17.4	-16.7	-34.2	-6.8	0.01
	31	5.3	-11.1	-22.1	-33.2	-6.6	-0.08
	32	6.5	-10.5	-21.5	-32.0	-6.4	0.16
	33	8.4	-7.8	-22.4	-30.1	-6.0	0.27
	34	8.5	-5.7	-24.3	-30.0	-6.0	0.02
	35	9.0	-8.2	-21.3	-29.5	-5.9	-0.03
	36	10.5	-6.9	-21.1	-28.0	-5.6	0.16
	37	11.6	-1.6	-25.3	-26.9	-5.4	-0.06
	38	12.6	-0.3	-25.6	-25.9	-5.2	-0.11
	39	25.5	2.9	-15.9	-13.0	-2.6	0.18
Cu_5 3D	40	8.2	-19.4	-16.9	-36.3	-7.3	-0.11
	41	8.6	-11.7	-24.2	-35.9	-7.2	0.15
	42	8.7	-12.1	-23.7	-35.8	-7.2	0.35
	43	9.7	-15.5	-19.3	-34.8	-7.0	-0.04
	44	10.3	-16.2	-18.0	-34.2	-6.8	-0.04
	45	11.6	-10.2	-22.8	-32.9	-6.6	0.02
	46	11.8	-17.0	-15.6	-32.7	-6.5	-0.02
	47	22.7	-7.0	-14.8	-21.8	-4.4	0.00
	48	23.7	2.6	-23.4	-20.8	-4.2	-0.25
	49	24.4	-8.3	-11.9	-20.1	-4.0	-0.14
Cu_8 T_d	50	0.0	-10.9	-24.8	-35.7	-4.5	-0.04
	51	12.2	3.2	-26.6	-23.4	-2.9	0.03
Cu_{13}	52	0.0	-5.3	-44.5	-49.7	-3.8	0.06
distorted	53	0.3	-7.9	-41.5	-49.4	-3.8	0.03
	54	5.1	-4.5	-40.2	-44.7	-3.4	-0.14
	55	9.5	-9.2	-31.1	-40.2	-3.1	-0.02
	56	23.9	-5.5	-20.4	-25.8	-2.0	-0.16

As expected, deformations on the clusters are larger at the defects due to the higher interaction strength, which overcomes the cluster resistance to deformation. This causes, for instance, the deformation of the planar Cu_5 cluster on NG_V into a 3D-like isomer more open, resembling a tetrahedral Cu_4 with an additional atom on one edge (structures **73** and **76** in Figure 5.7), a geometry that is also found as the most stable structure for 3D Cu_5 (structure **78**).

Table 5.4. Relative energy w.r.t. the most stable structure per size including dispersion (ΔE_{rel}+D2), adsorption energy w.r.t. each isomer (ΔE_{ads}), dispersion contribution (D2), adsorption energy including dispersion (ΔE_{ads}+D2), adsorption energy per atom including dispersion ((ΔE_{ads}+D2)/n) and charge transferred from the cluster to the support (qCu_n) in the interaction of Cu_n (n = 5, 8 and 13) clusters with G_V. Energies in kcal mol^{-1}.

Cluster	Structure (Fig. 5.6)	ΔE_{rel}+D2	ΔE_{ads}	D2	ΔE_{ads}+D2	(ΔE_{ads}+D2)/n	qCu_n (e^-)
Cu_5	57	0.0	-87.6	-20.1	-107.7	-21.5	0.51
planar	58	0.1	-88.9	-18.7	-107.6	-21.5	0.50
	59	6.7	-78.7	-22.3	-101.0	-20.2	0.06
	60	25.5	-58.9	-23.3	-82.2	-16.4	0.13
	61	60.5	-29.2	-17.9	-47.2	-9.4	0.44
	62	61.4	-28.3	-18.0	-46.3	-9.3	0.58
Cu_5 3D	63	0.4	-90.9	-22.4	-113.3	-22.7	0.71
	64	3.0	-88.7	-22.0	-110.7	-22.1	0.60
	65	4.0	-88.0	-21.9	-109.9	-22.0	0.56
Cu_8 T_d	66	0.0	-66.1	-30.8	-96.9	-12.1	0.60
	67	15.4	-50.8	-30.7	-81.5	-10.2	0.51
Cu_{13}	68	0.0	-89.6	-37.5	-127.2	-9.8	0.97
distorted	69	4.1	-81.9	-41.1	-123.1	-9.5	0.58
	70	5.3	-71.5	-46.8	-118.4	-9.1	0.65
	71	8.8	-75.6	-28.8	-104.3	-8.0	0.59
	72	22.9	-51.8	-32.1	-83.9	-6.5	0.55

Those examples aside, Cu_5 isomers retain their characteristic planar or 3D geometries. Planar Cu_5 clusters preferentially adsorb by the two atoms edge opposed to the three atoms edge, and 3D Cu_5 clusters do so by one or more of the central atoms of its bipyramidal shape, regardless of the type of graphene sheet. This correlates with the shape of the HOMO and LUMO for planar Cu_5 and 3D Cu_5, which are highly localized in the same areas (Figure 5.8), and also with the charge transfer from the cluster to the support found as the main component of the cluster-graphene interaction. The opposed charge transfer found for 3D Cu_5 (structures **11** and **40**) is also explained by the lower energy of its LUMO, which facilitates the interaction, and its localized shape on top of one central atom, which also correlates with the fact that in those structures the cluster binds to graphene through that copper atom only.

Among the two planar and 3D isomers, planar Cu_5 presents the highest adsorption energy only on the NG sheet, but given that the 3D isomer is 6 kcal mol^{-1} less stable than the planar one, planar Cu_5 is still thermodynamically favored over all but the pyridinic NG_V sheet. Even there it remains close, 2.4 kcal mol^{-1} below. The largest difference lies in the NG sheet, where the most stable planar cluster is 8.2 kcal mol^{-1}

Table 5.5. Relative energy w.r.t. the most stable structure per size including dispersion (ΔE_{rel}+D2), adsorption energy w.r.t. each isomer (ΔE_{ads}), dispersion contribution (D2), adsorption energy including dispersion (ΔE_{ads}+D2), adsorption energy per atom including dispersion ((ΔE_{ads}+D2)/n) and charge transferred from the cluster to the support (qCu_n) in the interaction of Cu_n (n = 5, 8 and 13) clusters with NG_V. Energies in kcal mol^{-1}.

Cluster	Structure (Fig. 5.7)	ΔE_{rel}+D2	ΔE_{ads}	D2	ΔE_{ads}+D2	(ΔE_{ads}+D2) /n	qCu_n (e^-)
Cu_5	73	0.0	-53.6[a]	-22.7[a]	-76.2[a]	-15.2[a]	0.45
planar	74	2.4	-55.3	-18.5	-73.8	-14.8	0.47
	75	2.9	-51.3	-22.0	-73.3	-14.7	0.45
	76	5.0	-48.1	-23.1	-71.3	-14.3	0.48
	77	44.1	-14.9	-17.2	-32.1	-6.4	0.22
Cu_5 3D	78	3.2	-56.0	-23.1	-79.1	-15.8	0.46
	79	8.5	-53.3	-20.5	-73.7	-14.7	0.43
	80	42.3	-15.8	-24.2	-39.9	-8.0	0.20
Cu_8 T_d	81	0.0	-46.1	-24.9	-71.0	-8.9	0.28
	82	9.2	-43.5	-18.2	-61.8	-7.7	0.05
Cu_{13}	83	0.0	-54.2	-34.4	-88.6	-6.8	0.68
distorted	84	1.5	-41.3	-45.8	-87.2	-6.7	0.63
	85	2.9	-47.3	-38.5	-85.7	-6.6	0.45
	86	13.0	-54.0	-21.6	-75.7	-5.8	0.48
	87	26.0	-31.4	-30.7	-62.0	-4.8	0.51

[a]W.r.t. the 3D isomer: ΔE_{ads} = -59.4, D2 = -22.8, ΔE_{ads}+D2 = -82.2, (ΔE_{ads}+D2)/n = -16.4.

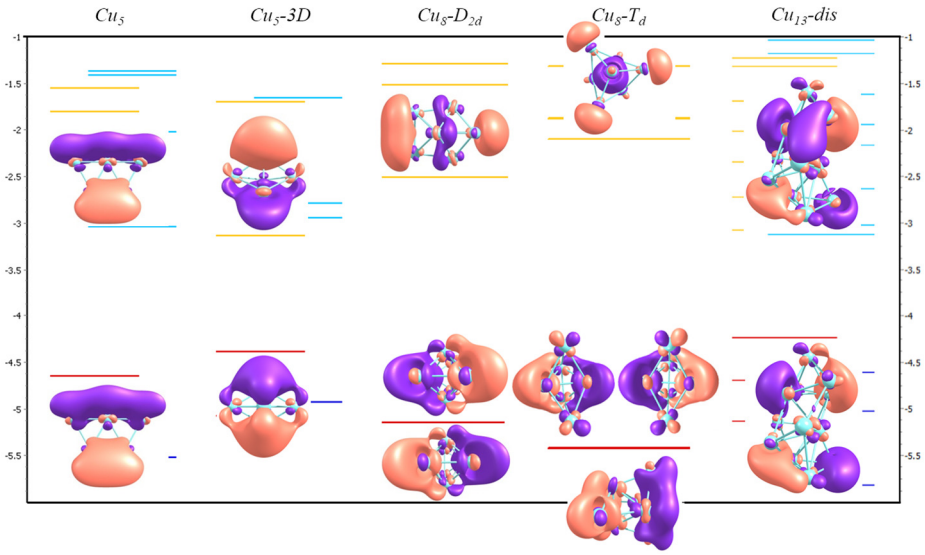

Figure 5.8. Stability and composition of the highest occupied and lowest unoccupied molecular orbitals (HOMOs and LUMOs) of Cu_n clusters (n=5, 8, 13) calculated at the B3PW91/6-311+G(d,p) level (eV).

more stable than the most stable 3D structure. Therefore, while not clearly dominating, planar clusters are favored on NG, whereas pyridinic defects favor 3D clusters and may moreover deform the planar isomer into the 3D one.

Cu_8 clusters are usually transformed into the D_{2d} isomer (structures **19, 50, 67** and **81**), which can be explained by the higher HOMO and lower LUMO of this isomer that enhances the interaction (Figure 5.8), and by the fact that this isomer is also close in energy to the T_d isomer (from Table 3.1 of Chapter 3, only 1.8 kcal mol^{-1} more unstable at the B3PW91/6-311+G(d,p) level and -0.8 kcal mol^{-1} more stable at the periodic PW91 level). Besides, Cu_8 clusters present the lowest adsorption energies and charge transferred of the copper clusters studied (Tables 5.2-5.5), very likely due to the increased stability that their bigger HOMO-LUMO gap confers them (Figure 5.8). In addition, structures adsorbed along the edge of the D_{2d} isomer or at the corner of the T_d isomer (**20, 21, 50, 81, 82**), i.e. those that match the shape of the LUMO, exhibit a net charge closer to zero (even negative in G and NG), pointing again to a back-bonding from the metal to the support, in analogy to what is found for 3D Cu_5.

For Cu_{13} clusters the atomicity increase makes small deformations affordable and a higher number of copper-surface interactions available. As a consequence, Cu_{13} structures present the highest adsorption energies of the copper clusters studied. It is difficult to state how many Cu-C significant interactions are in some structures, given that the calculations include dispersion energies and that some Cu atoms are close to the surface but exceeding common Cu-C distances. However, in the most stable structures Cu_5 and Cu_8 bind to the graphene sheets through a lower number of interactions than Cu_{13}, and therefore the adsorption strength of each Cu-C interaction for Cu_5 is rather comparable to those of Cu_{13} (with those of Cu_8 being weaker).

The deformations of Cu_{13} clusters are also more difficult to track and prevent any comparison with the frontier orbitals of the original isomer. Nevertheless, it can be seen that on pristine surfaces the cluster tends to be shorter and wider, maximizing the number of interactions with the support (structures **22** and **52**), whereas it remains around the defect and it is taller on defective surfaces (structures **68** and **84**). The fact that Cu_{13} clusters present the highest adsorption energy on clean surfaces of the clusters studied contrasts with their smaller charge transferred (Tables 5.2-5.3). This is also explained if back-bonding takes place on clean surfaces whereas it is lost, or at least does not have the same weight, on defective surfaces, consistent with what is found for 3D Cu_5 and Cu_8 clusters. Indeed, the HOMO-LUMO gap of Cu_{13} clusters is smaller than for the other two sizes, and the energy of the HOMO is higher than that of Cu_5, so that both normal and back-bonding interactions are enhanced. At defective surfaces, instead, the copper-surface interaction involves the predominant participation of dangling orbitals of C or N_{Py} atoms as opposed to the π bands.

5.3.1.2. O_2 adsorption on Cu_5/NG and Cu_5/NG_V.

The adsorption of O_2 in the most stable structure for the planar and 3D Cu_5 isomers on the two N-doped sheets, namely, in structures **27, 40, 73** and **74**, was then studied. Note that structure **73** was favored over structure **78** because their geometry is very similar but structure **73** is 3 kcal mol^{-1} more stable (Table 5.5).

Tests on the adsorption of isolated oxygen on the N-doped graphene sheets show very small adsorption energies, ranging from -0.3 to -8.8 kcal mol^{-1} (Figure 5.9 and Table 5.6). While the interaction is reflected in up to 0.3e transferred from the surface to the molecule, it only achieves a minor activation of the latter, elongating the bond in 0.04 Å at the most, and providing vibrational frequencies of around 1330 cm^{-1}.

Note that structures were the O_2 molecule binds to the positively-charged C atoms were tested but, in agreement with previous reports[277], they are more unstable (with positive adsorption energies larger than 5 kcal mol^{-1}) and are not shown.

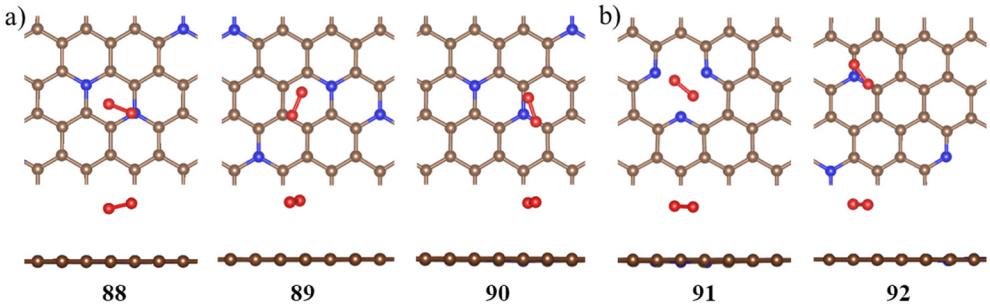

Figure 5.9. Optimized structures of O_2 on a) NG and b) NG_V, in order of decreasing stability. Top and side views are shown. C atoms are in brown, N in blue, O in red.

Table 5.6. Adsorption energy of the O_2 molecule on N-doped graphene surfaces (ΔE_{ads}), closest distance from the molecule to the support ($r_{Sup\text{-}O}$), interatomic O-O distance (r_{OO}), O-O vibrational frequency (ν_{OO}) and charge transferred from the support to the molecule (qO_2).

Surface	Structure (Fig. 5.9)	ΔE_{ads} (kcal mol^{-1})	$r_{Sup\text{-}O}$ (Å)	$r_{OO}{}^a$ (Å)	$\nu_{OO}{}^a$ (cm^{-1})	qO_2 (e^-)
NG	88	-8.8	2.731	1.268	1320	-0.30
	89	-8.4	2.843	1.266	1333	-0.29
	90	-7.8	2.913	1.265	1331	-0.28
NG_V	91	-3.3	2.817	1.240	1463	-0.09
	92	-0.3	2.815	1.270	1318	-0.31

[a]For the gas phase O_2 molecule: r_{OO} = 1.233 Å, ν_{OO} = 1566 cm^{-1}.

Consistent with this weak interaction, the O_2 molecule preferentially adsorbs on the copper cluster in Cu_5/N-graphene structures (Figures 5.10-5.11), and those built with O_2 at the interface either evolve to other structures or are unstable (structure **123**).

Adsorption modes studied in gas phase or isolated copper clusters are found again here (Figures 5.10-5.11 and Tables 5.7-5.8), and thus we have *mono* modes when only one bond is formed between one of the O atoms and a Cu atom (structure **100**, for instance); *top*, when the two O atoms of O_2 are directly attached to the same low coordinated Cu atom (as in structure **99**); *bridge*, when each of the two O atoms in the molecule is directly attached to one Cu atom in the cluster (structure **94**) and *h-111* when the O_2 occupies the hollow position on a (111) facet (structure **93**). Besides these, an additional mode was obtained, which we labelled *mono-bridge* because the O atom bonded to copper in what would be a *mono* structure bridges two Cu atoms instead (structure **98**).

Also consistent with our previous results, we find again that the planar cluster preferentially adsorbs O_2 at its edges and corners, whereas the 3D cluster allows *h-111* adsorption modes. However, the presence of the support facilitates the deformation of the cluster to enhance its interaction with oxygen, so that now *h-111* structures can be found from planar clusters after deformation, as in structure **93** or **115**. Indeed, while bridge modes are very stable for 3D Cu_5, much like in gas phase, *h-111* adsorption modes are now the most stable (structures **93** and **126**).

Other cases where the adsorption of O_2 on the supported cluster causes the deformation of one isomer into the other includes structure **103** and, therefore, the most stable structure obtained on NG starting from the adsorbed planar cluster is a 3D cluster (square-pyramid-like deformed, structure **93**), whereas starting from an adsorbed 3D cluster we obtain a planar one (structure **103**). In addition, the geometry of the isomer opened into a tetrahedral Cu_4 plus one Cu atom that we start with on NG_V (structure **73**) is also obtained from other isomers: once for the NG sheet that started with our known 3D isomer (structure **105**) and another time for NG_V with a planar cluster (structure **113**). The geometry of this isomer facilitates the adsorption of O_2 in an open *h111*-like mode (structure **125**). However, the most stable structure on NG_V almost detaches the Cu atom from the tetrahedral part completely, creating a structure that is reminiscent of the mechanism found for the dissociation of O_2 on the face of a planar Cu_4 cluster in Chapter 3 (structure **50** in Figure 3.11, page 93), and which equally results in a higher activation of the O_2 molecule (Table 5.8).

In Table 5.7 and 5.8 adsorption energies with and without dispersion are indicated (ΔE_{ads}+D2 and ΔE_{ads}, respectively). These are calculated as the difference between the energy of each structure and the sum of the energies of the O_2 molecule plus that of structure **27/74** or **40/73**, depending on whether the geometry of the cluster is planar or 3D on NG/NG_V, respectively. Note that this energy thus includes the de-

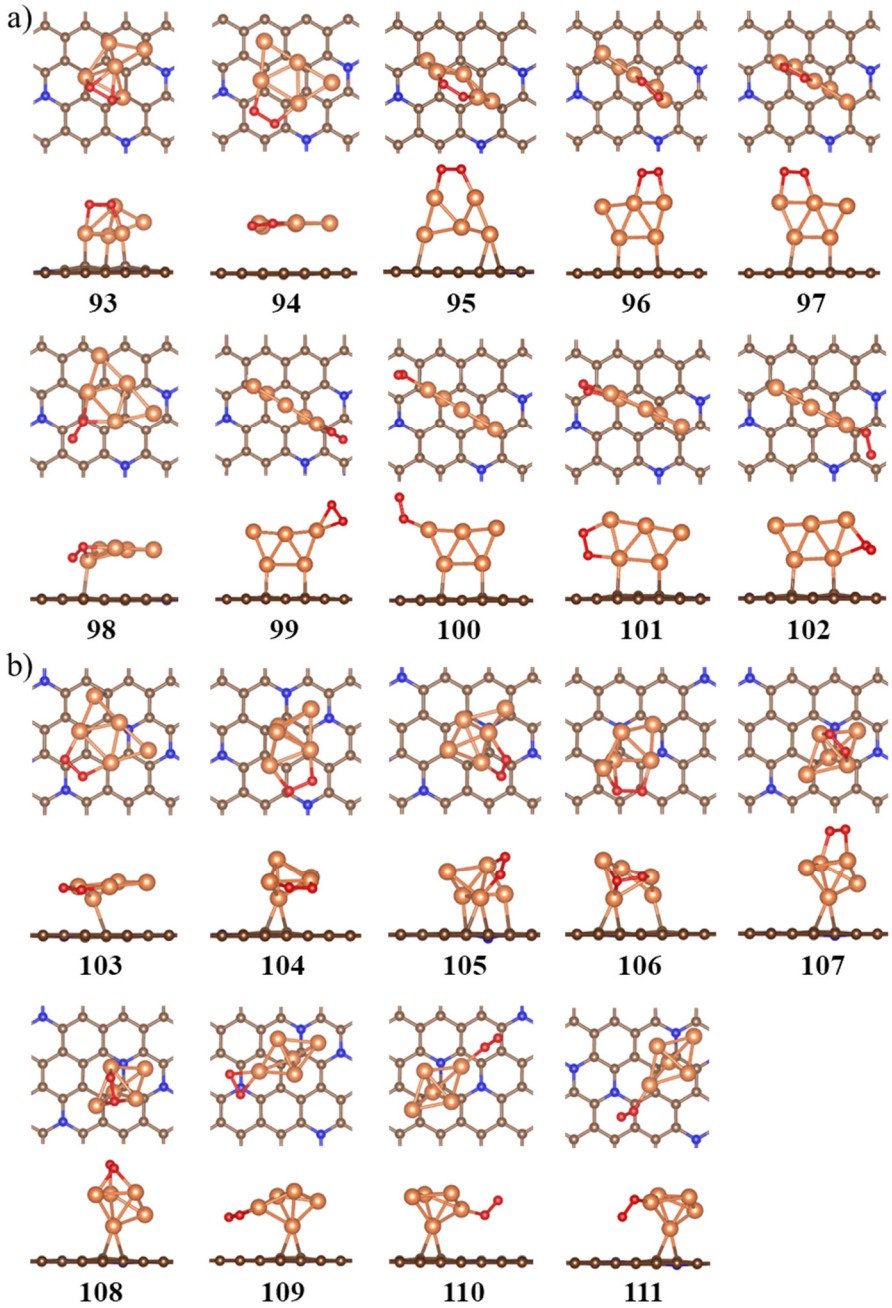

Figure 5.10. Optimized structures, in order of decreasing stability, of the O_2 molecule adsorbed on a) planar Cu_5 (structure 27) and b) 3D Cu_5 clusters (structure 40) on NG. Top and side views are shown. C atoms in brown, Cu in orange, N in blue, O in red.

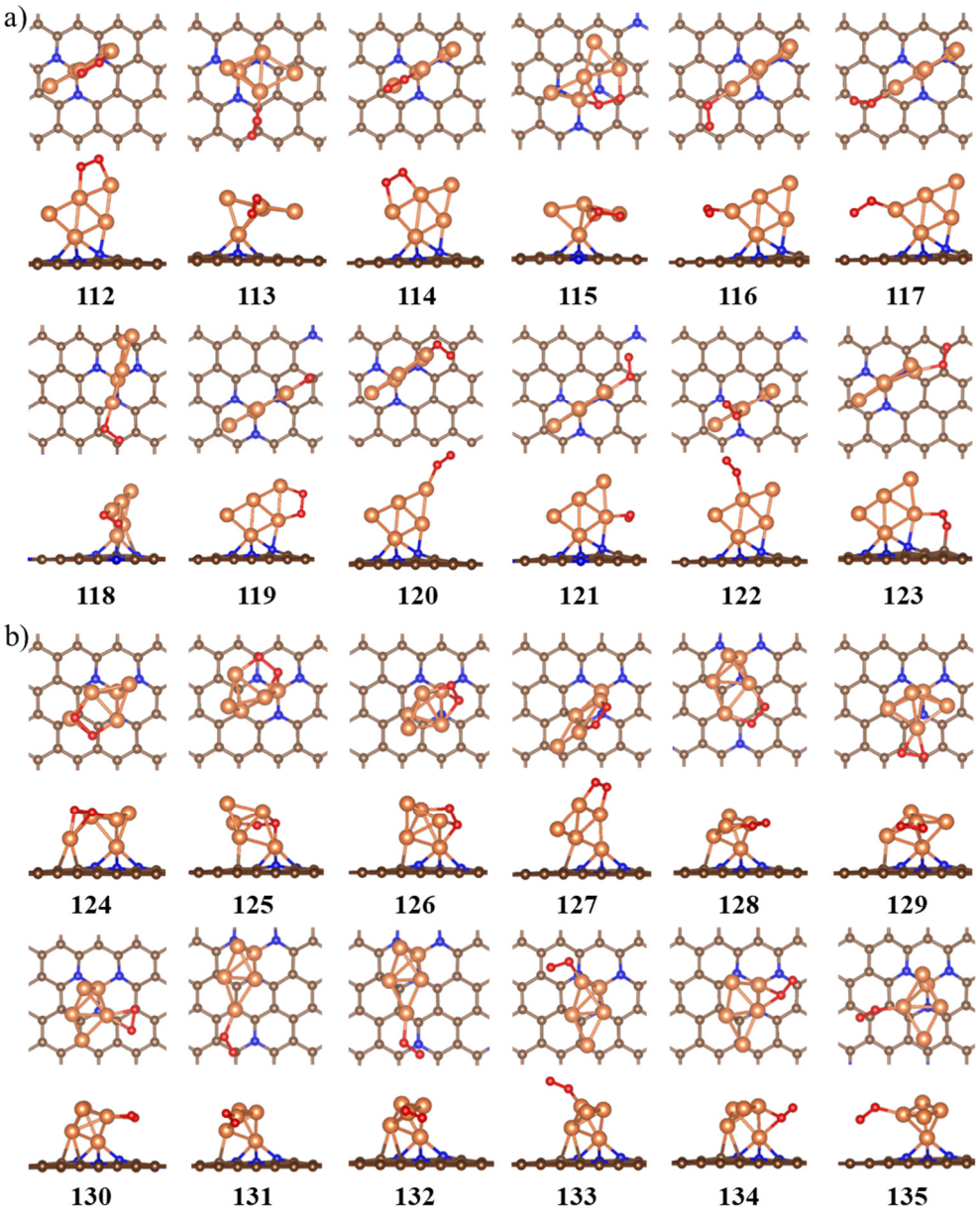

Figure 5.11. Optimized structures, in order of decreasing stability, of the O_2 molecule adsorbed on a) planar Cu_5 (structure **27**) and b) 3D Cu_5 clusters (structure **40**) on NG_V. Top and side views are shown. C atoms are in brown, Cu in orange, N in blue, O in red.

Table 5.7. Adsorption energy of the O_2 molecule on NG-supported clusters (ΔE_{ads}), dispersion contribution (D2), adsorption energy including dispersion (ΔE_{ads}+D2), relative energies including dispersion (ΔE_{rel}+D2), O-O distance (r_{OO}), O-O vibrational frequency (ν_{OO}) and Bader charge on the molecule (qO_2) and change in the Bader charge of the cluster w.r.t. structures (ΔqCu_5). Energies in kcal mol^{-1}.

Structure (Fig. 5.10)	Adsorption mode	ΔE_{rel} +D2	ΔE_{ads} +D2	ΔE_{ads}	D2	r_{OO}[a] (Å)	ν_{OO}[a] (cm^{-1})	qO_2 (e$^-$)	ΔqCu_5 (e$^-$)
93	*h111*	0.0	-53.3[b]	-32.5[b]	-12.6[b]	1.559	654	-0.94	0.92
94	*bridge*	5.2	-39.9	-26.2	-13.6	1.437	768	-0.95	0.53
95	*bridge*	5.7	-39.4	-33.7	-5.7	1.389	942	-0.67	0.46
96	*bridge*	14.2	-30.9	-29.2	-1.7	1.382	957	-0.61	0.37
97	*bridge*	14.8	-30.3	-28.6	-1.7	1.381	955	-0.67	0.43
98	*mono-bridge*	18.4	-26.7	-12.5	-14.2	1.385	920	-0.86	0.51
99	*top*	18.7	-26.4	-25.0	-1.4	1.350	1090	-0.50	0.18
100	*mono*	19.0	-26.1	-24.7	-1.3	1.313	1153	-0.38	0.11
101	*bridge*	20.0	-25.1	-21.9	-3.2	1.413	845	-0.78	0.36
102	*mono-bridge*	26.8	-18.3	-14.2	-4.2	1.347	998	-0.65	0.32
103	*bridge*	2.0	-43.1[c]	-38.6[c]	-12.7[c]	1.444	764	-0.92	0.70
104	*bridge*	8.6	-44.7	-36.7	-8.1	1.459	733	-0.73	0.43
105	*bridge*	11.9	-41.5	-30.3	-11.2	1.400	857	-0.81	0.82
106	*h111*	14.1	-39.2	-31.4	-7.9	1.499	679	-0.89	0.75
107	*bridge*	20.4	-32.9	-31.0	-1.9	1.353	981	-0.61	0.68
108	*h111*	21.8	-31.5	-30.0	-1.5	1.489	701	-0.81	0.78
109	*top*	21.8	-31.5	-27.5	-4.0	1.410	921	-0.81	0.47
110	*mono*	29.5	-23.8	-21.3	-2.5	1.315	1128	-0.56	0.39
111	*mono*	30.3	-23.0	-20.4	-2.7	1.328	1115	-0.60	0.38

[a]For the gas phase O_2 molecule: r_{OO} = 1.233 Å, ν_{OO} = 1566 cm^{-1}.
[b]Calculated vs. structure **40**, as the cluster is more like Cu_5 3D.
[c]Calculated vs. structure **27**, as the cluster is more like Cu_5 planar.

formation energy in case clusters deform to intermediate not traced geometries. Due to this, another clarifying column indicating the relative energies among all clusters, planar or 3D, was added to Table 5.7 (ΔE_{rel}+D2). It is thus found that in the planar cluster the preference for the two-atoms edge *bridge* over other *bridge* or *mono* structures from gas phase is maintained (structure **94**), although the energetical differences again decrease: the three-atoms edge one was almost 15 kcal mol^{-1} higher in energy (p-PW91 values) and here it is 8.5 (structure **95** vs **96**, Table 5.7), while the *mono* structure was 25 kcal mol^{-1} more unstable and here it is 19 kcal mol^{-1} over the groundstate (structure **100**). Dispersion energies are commonly low, but they reach up to -14 kcal mol^{-1} for some structures on NG (**93**, **94**, **98** and **103-106**) and -11.5 for structure **115** on NG_V. However, this is but the result of an artificial contribution due to the stretched out relative position of the cluster with respect to the surface (obtained in the optimizations upon O_2 adsorption), that is not as the upright position from structures **27** or **40**. Thus, the calculated adsorption energies of oxygen are more

Table 5.8. Adsorption energy of the O_2 molecule on NG-supported clusters (ΔE_{ads}), dispersion contribution (D2), adsorption energy including dispersion (ΔE_{ads}+D2), relative energies including dispersion (ΔE_{rel}+D2), O-O distance (r_{OO}), O-O vibrational frequency (ν_{OO}) and Bader charge on the molecule (qO_2) and change in the Bader charge of the cluster w.r.t. structures (ΔqCu_5). Energies in kcal mol^{-1}.

Structure (Fig. 5.11)	Adsorption mode	ΔE_{rel} +D2	ΔE_{ads} +D2	ΔE_{ads}	D2	r_{OO}[a] (Å)	ν_{OO}[a] (cm^{-1})	qO_2 (e$^-$)	ΔqCu_5 (e$^-$)
112	*bridge*	24.4	-25.3	-23.8	-1.5	1.361	971	-0.63	0.45
113	*mono*	24.6	-22.6[b]	-19.9[b]	-2.7[b]	1.312	1146	-0.57	0.25
114	*bridge*	24.6	-25.0	-24.1	-0.9	1.367	938	-0.54	0.31
115	*h111*	24.9	-24.8	-13.3	-11.5	1.453	742	-0.91	0.67
116	*mono*	25.4	-24.3	-21.2	-3.1	1.310	1147	-0.43	0.13
117	*mono*	25.5	-24.2	-21.2	-3.0	1.311	1151	-0.46	0.17
118	*mono*	26.9	-22.8	-18.0	-4.8	1.340	1034	-0.58	0.02
119	*bridge*	28.2	-21.5	-18.9	-2.6	1.383	941	-0.62	0.40
120	*mono*	28.8	-20.9	-20.1	-0.8	1.301	1189	-0.44	0.25
121	*mono*	32.3	-17.4	-12.7	-4.7	1.313	1136	-0.52	0.13
122	*mono*	34.6	-15.1	-13.0	-2.1	1.292	1217	-0.46	0.35
123	*bridge*	40.0	-9.7	-4.5	-5.2	1.410	849	-0.82	0.41
124	*h111*	0.0	-47.2	-44.6	-2.6	1.578	589	-1.03	1.05
125	*h111*	6.6	-40.7	-38.6	-2.1	1.527	618	-0.94	0.72
126	*h111*	12.1	-35.2	-35.7	0.5	1.533	652	-1.04	0.97
127	*bridge*	12.7	-37.0[c]	-33.7[c]	-3.3[c]	1.377	935	-0.70	0.45
128	*bridge*	14.8	-32.5	-28.6	-3.9	1.415	784	-0.69	0.31
129	*top*	17.1	-30.2	-25.1	-5.1	1.430	895	-0.87	0.65
130	*top*	22.1	-25.2	-22.5	-2.7	1.404	944	-0.73	0.48
131	*mono*	25.0	-22.3	-19.8	-2.4	1.312	1143	-0.48	0.34
132	*mono*	25.2	-22.1	-18.9	-3.2	1.311	1149	-0.49	0.34
133	*mono*	25.4	-21.9	-21.6	-0.3	1.306	1175	-0.45	0.22
134	*mono-bridge*	27.3	-21.1	-17.8	-3.3	1.356	1001	-0.70	0.55
135	*mono*	27.4	-19.8	-16.2	-3.7	1.313	1138	-0.50	0.12

[a]For the gas phase O_2 molecule: r_{OO} = 1.233 Å, ν_{OO} = 1566 cm^{-1}.
[b]Calculated vs. structure **73**, as the cluster is in the same geometry.
[c]Calculated vs. structure **74**, as the cluster is more like Cu_5 planar.

accurate for these structures without including dispersion, although even then the contribution from deformation is likely higher than for the rest. Therefore, lacking calculations of such deformation energies, so far we can only compare reliably adsorption energies on NG_V with those of gas phase, and they turn out to be similar in value but opposed in trend: in gas phase they were larger for planar Cu_5 (-49.4 vs -39.5 kcal mol^{-1}) whereas on NG_V it is higher for 3D Cu_5 (-44.6 vs -33.7, from structures **124** and **127**).

In any case, the relationship between charge transferred to the oxygen molecule and its O-O distance and frequency vibration follow the expected trends that were shown in Chapter 3 (Figure 3.6, page 83), with a somewhat larger dispersion due to the lower level of theory (GGA), as also shown in the mentioned chapter (Figure 5.12). Thus, *h111* modes present again the highest activation of the O_2 molecule, with bond distances in the 1.45-1.58 Å range and corresponding vibrational frequencies from 590 to 740 cm^{-1}, followed by *bridge* modes (1.35-1.46 Å and 730-980 cm^{-1} bond distance and vibrational frequency ranges, respectively), and then by *mono* modes (1.29-1.33 Å and 1115-1189 cm^{-1} bond distance and vibrational frequency ranges, respectively). The few new *mono-bridge* structures lie precisely between the *bridge* and *mono* modes, with 1.34-1.39 Å bond distances and 920-1000 cm^{-1} vibrational frequencies. Finally, among the structures corresponding to *top* modes, the one on the planar cluster, structure **99**, presents a lower activation, whereas the other three, on the 3D isomer, exhibit an activation slightly higher than that of the *mono-bridge* mode, comparable to some *bridge* structures (1.40-1.43 Å and 890-940 cm^{-1} bond distance and vibrational frequency ranges, respectively).

The charge transferred to molecular oxygen consistently follows this trend, but with a wider overlap of ranges: for the *h111*, *bridge*, *top*, *mono-bridge* and *mono* modes the ranges are (-1.04, -0.81e), (-0.54, -0.95e), (-0.50, -0.87e), (-0.65, -0.86e) and (-0.43, -0.57e), respectively.

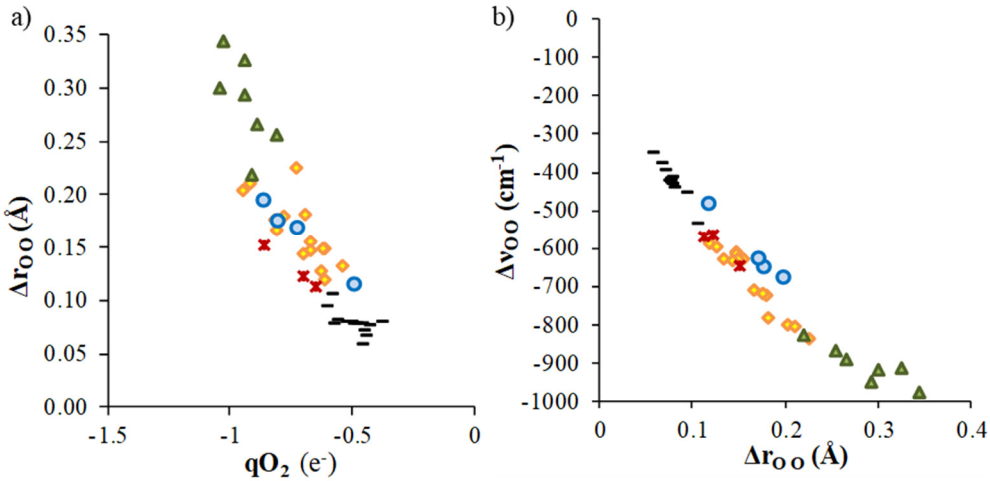

Figure 5.12. Relationship a) between the bond length variation, Δr_{OO}, and the charge transferred, qO_2, and b) between the shift in the ν_{OO} vibrational frequency and the bond length variation, Δr_{OO}, per adsorption mode: *mono* (black lines) *top* (blue circles) *bridge* (yellow diamonds) *h-111* (green triangles) and *mono-bridge* (red crosses).

In most cases, however, the charge gained by the molecule does not match the charge lost by the cluster, i.e. the support participates. With very few exceptions, upon the adsorption of O_2 both the cluster and the support lose charge. There is not a big difference between the amounts of charge given by the two graphene sheets per adsorption mode, but the contribution from the support seems to be slightly smaller on the *h111* mode (Figure 5.13a). However, given the much greater amount of charge transferred from the cluster to the NG_V sheet upon deposition, the net result even after O_2 adsorption is for the support to keep a significant amount of (negative) charge in these structures (Figure 5.13b). The degree of activation of the oxygen molecule still responds to the adsorption mode it is in regardless of the type of support, as just shown, but to achieve it the cluster gets considerably more oxidized on the NG_V sheet for the same adsorption modes (Figure 5.13b).

Making the same analysis but differentiating structures of planar and 3D cluster isomers cannot be made, or not consistently, on *h111*, *mono-bridge* and *top* modes due to the lack of or very low amount of structures with one isomer or the other. However, there is no big difference in the Bader charges in the *bridge* and *mono* comparable modes, with the latter being a bit less activated on planar clusters (Figure 5.14).

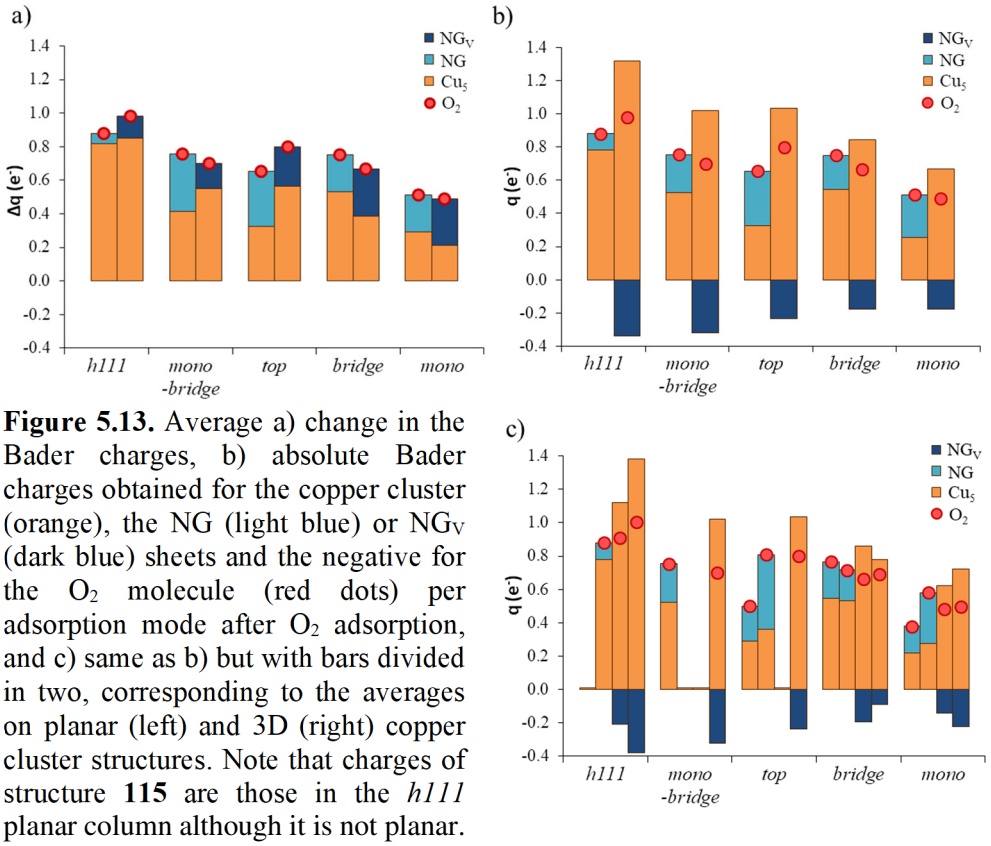

Figure 5.13. Average a) change in the Bader charges, b) absolute Bader charges obtained for the copper cluster (orange), the NG (light blue) or NG_V (dark blue) sheets and the negative for the O_2 molecule (red dots) per adsorption mode after O_2 adsorption, and c) same as b) but with bars divided in two, corresponding to the averages on planar (left) and 3D (right) copper cluster structures. Note that charges of structure **115** are those in the *h111* planar column although it is not planar.

The small negative charge exhibited by the 3D isomer upon deposition over NG (structure **40**) does not seem to be enough to affect the adsorption of O_2. The difference between planar and 3D clusters in both supports comes rather from the absence of stable *h111* modes, which is also clear on Figure 5.14. As a result, much as it was discussed on gas phase clusters, they should be more resistant to oxidation.

The fact that some planar structures evolved upon optimization into 3D isomers and vice versa indicates that such conversions may be affordable for the system, but it cannot be stated without a proper study of the energetic cost, i.e. without studying the transition states. Thermodinamically, on the one hand the adsorption of O_2 is stronger in the 3D clusters on the pyridinic defects, and ultimately produces lower relative energy values, favouring this isomer over the planar cluster (Tables 5.7 and 5.8). On the other hand, the most stable planar structure over NG was 8.2 kcal mol^{-1} more stable than the 3D groundstate (and after O_2 adsorption the groundstates differ by 2 kcal mol^{-1} only). Moreover, on NG_V the adsorption of O_2 in the two-atoms edge of the planar Cu_5, which was the most stable structure in gas phase, is precisely recovered from a 3D isomer, producing structure **127** which, in addition, is almost 12 kcal mol^{-1} more stable than the next more stable planar structure.

All in all, we can point out that: i) the isolated 3D isomer is 6 kcal mol^{-1} higher in energy than the planar one, ii) the planar isomer is more favoured (thermodynamically) than the 3D one on all supports but the NG_V sheet, and the difference is largest on NG, iii) upon O_2 adsorption, 3D structures become more favoured thermodynamically, especially at the defective pyridinic sites and iv) interconversion of isomers seems to be affordable in both directions.

As a result of this, it is not expected to obtain a very high predominance of one isomer over the other, but the data suggests that NG is the surface of choice in order to favour the planar isomer as much as possible. However, given the low adsorption energies of all copper clusters on NG very low loadings would still be needed to favour dispersion and avoid the sintering, much as it was done for the samples we compared our results with in Chapter 3. Since the planar isomer does not adsorb molecular oxygen in the more activated *h111* mode, the Cu_5/N-graphene system should be more resistant to oxidation.

5.3.1.3. O_2 dissociation on Cu_5/NG and Cu_5/NG_V clusters.

The most stable structures of both planar and 3D Cu_5 with O_2 adsorbed in different modes on the two graphene sheets were then tested for O_2 dissociation (Figure 5.15).

Structures **94** and **95** were initially selected for the planar isomer in the clean N-doped sheet. Although both present O_2 adsorbed in a bridge mode, it is interesting to see the difference between them, because they are very close in energy but the former

seems to activate O_2 a bit more, whereas the latter has less contact with the surface and its results should be more similar to those obtained in gas phase.

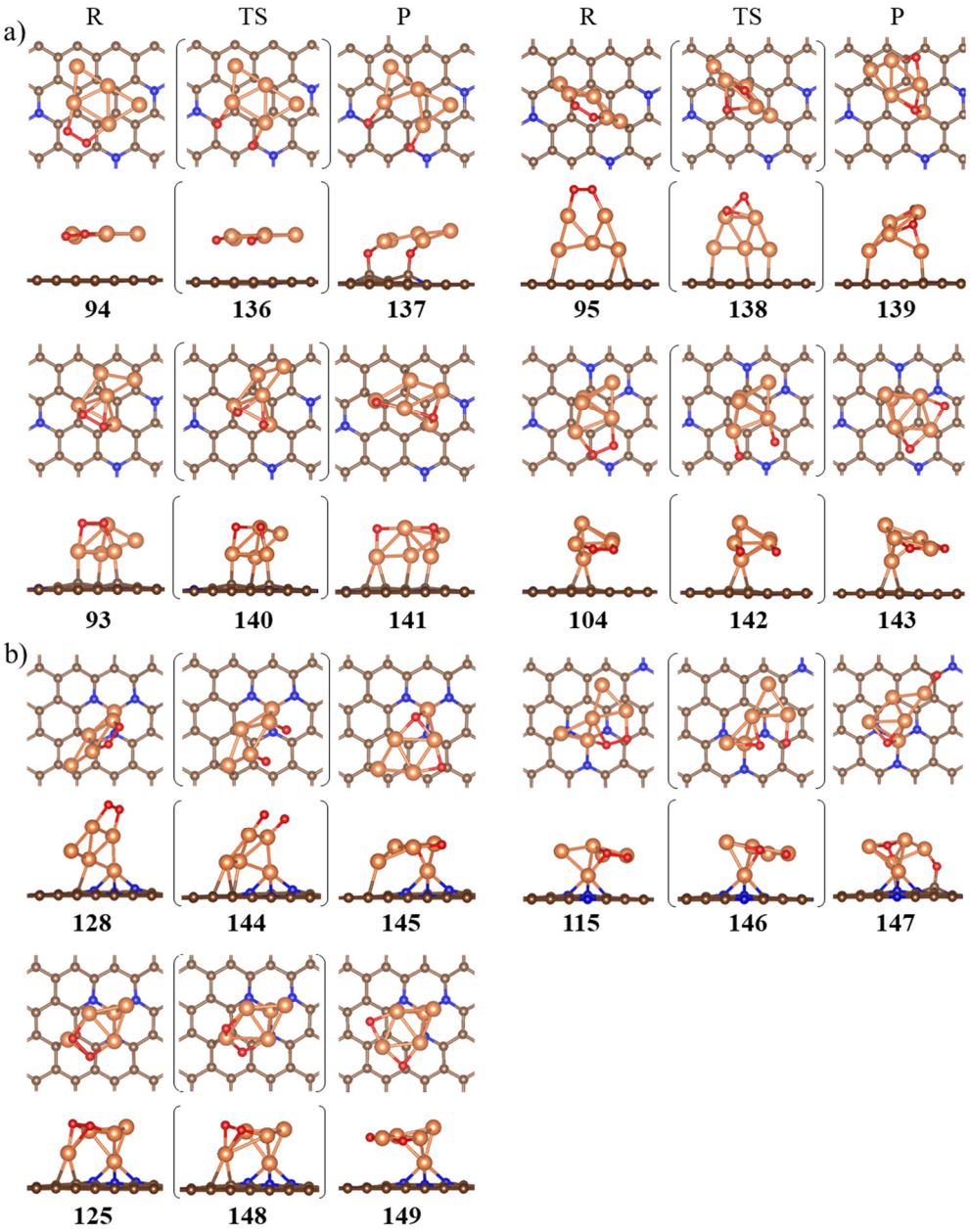

Figure 5.15. Optimized structures for the O_2 dissociation by the planar (up) and 3D (down) isomers of Cu_5 on a) NG and b) NG_V. Top and side views are shown. C atoms are in brown, Cu in orange, N in blue, O in red.

In energy structure **94**, a TS with the two oxygen atoms separated and stabilized by the support was readily found (**136**) leading to a product where such stabilization produces actual bonds between the oxygen atoms and the carbon atoms of the surface (**137**), which clearly become sp^3 hybridized and move upwards with respect to the plane of the sheet.

The activation energy from structure **94** is moderately high, consistent with the lower activation of the *bridge* mode (Table 5.9). The fact that the cluster lies down on its face in principle maximizing the copper-surface interactions and yet standing a bit apart (resembling to float), raised the question of whether the addition of Grimme's D2 dispersion forces in the optimization was key to stabilize the structure. However, the reoptimization of the structures without dispersion forces was achievable and lead to a very similar activation energy (25.6 vs 23.7 kcal mol^{-1}), although the separation of the cluster from the surface is immediately visible by how it becomes tilted, with the O_2 still facing the surface but at a 0.25 Å larger separation (Figure 5.16b).

From structure **95**, we did not succeed in converging a structure with the two oxygen atoms separated as before, but a TS with them moved towards more stable bridge positions, much like for gas phase clusters, was achieved (**138**). The activation energy is similar but slightly higher (28.3 kcal mol^{-1}), consistent with the stabilization from the interaction of the O with the support mentioned for the **94-[136]-137** path.

Regarding the 3D isomer on graphitic N-doped graphene, structures **93** and **104** were selected, as they are the most stable *h111* and *bridge* modes, with the former being 8.6 kcal mol^{-1} more stable. Although in structure **93** the O_2 molecule is adsorbed in the (111) facet of the cluster, it is easy to see that it is oriented so that it creates four

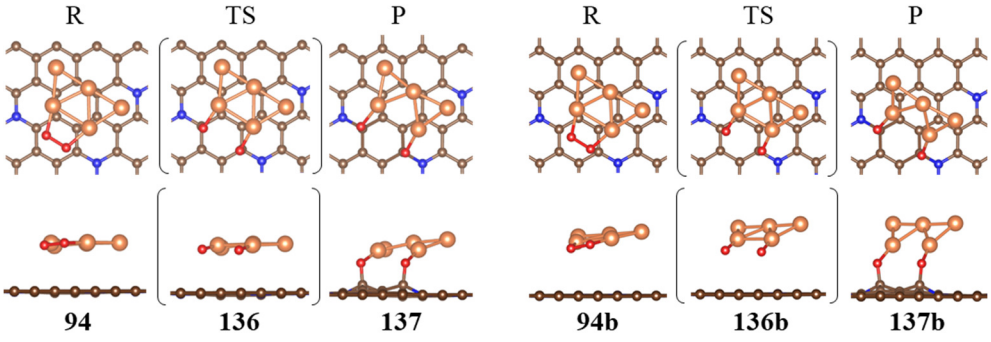

Figure 5.16. Optimized structures for O_2 dissociation from structure **94** in the presence (left) and absence (right) of dispersion energies in the calculations (ΔE_{act} = 23.7 kcal mol^{-1}, r_{OO}(TS) = 2.635 Å and ΔE_{reac} = -50.4 kcal mol^{-1} for the latter "b" structures). Top and side views are shown. C atoms are in brown, Cu in orange, N in blue, O in red.

Table 5.9. Adsorption energy of O_2 on N-graphene-supported clusters (ΔE_{ads}), activation energy for O_2 dissociation (ΔE_{act}), O-O distance in the TS (r_{OO}(TS), in Å), reaction energy (ΔE_{reac}) and recombination energy (ΔE_{reco}). Energies include dispersion and are in kcal mol^{-1}.

Surface	Cu_5 isomer	Path (Fig. 5.15)	ΔE_{ads}	ΔE_{act}	r_{OO}(TS)	ΔE_{reac}	ΔE_{reco}
NG	Planar	94-[136]-137	-39.9	25.9	2.643	-47.2	73.1
		95-[138]-139	-39.4	28.3	1.913	-59.2	87.5
	3D	93-[140]-141	-53.3	1.9	1.827	-58.0	59.9
		104-[142]-143	-44.7	18.7	2.471	-58.1	76.8
NG_V	Planar	127-[144]-145	-37.0	28.3	2.394	-63.4	91.4
		115-[146]-147	-24.8	8.1	1.724	-58.6	66.7
	3D	124-[148]-149	-47.2	2.0	1.817	-45.7	47.7

O-Cu interactions. As a result, the activation of the molecule is a bit higher than in other *h111* modes, becoming closer to what would be obtained in a proper *h100* mode (Table 5.7). Consistent with this, the activation energy from this structure is much lower than from the *bridge* mode of structure **104** (Table 5.9). Notice that the order according to the activation of O_2 is also maintained here, where the more activated structure **104** leads to a lower activation energy than structure **94**.

In the case of defective pyridinic graphene, we studied structures **127** and **124** for the planar and 3D isomers, respectively, but also structure **115** due to its singularity.

In TS **144** the planar cluster slightly deforms to produce more Cu-C interactions and the oxygen atoms are monocoordinated to one Cu atom each, like in TSs **136** and **138**. The activation energy is consistently similar to that of those cases. From **124**, as expected, the barrier is much lower (Table 5.9). The detachment of the Cu atom from the cluster produces four total O-Cu interactions in the minimum and two per O atom in the TS **148**, and therefore the activation of the O_2 is higher and the activation energy of the step lower, again both much more similar to those of an *h100* mode. Finally, from structure **115**, although the geometry of the cluster is strange (note that it is much more unstable than other structures), the molecule has the three Cu-O interactions characteristic of an *h111* mode and the activation energy is thus in the range of this adsorption mode, i.e. lower than what is found for *bridge* modes but a bit larger than for the close to *h100* modes.

Regarding the product structures, the oxygen atoms generally prefer to adsorb bicoordinately to the copper atoms occupying bridge sites, although in a few cases graphene participates (structures **137** and **147**) or a tricoordination with the O atom on a 111 facet is possible (structures **145** and **147**). In gas phase such bridge sites were only possible in planar structures, whereas we observe here that the support allows the opening of the Cu_5 3D cluster and prevents to a certain extent the occupation of facet sites by O atoms. In spite of this, the reaction energies are similarly

clearly negative, showing the exothermicity of the process. Furthermore, we observe again that the recombination of O_2 from two O atoms, that is, the reduction of the cluster, is easier in the 3D cluster (Table 5.9 and Figure 5.17). Given the deformations shown throughout this work, the one that structure **145** already shows, and the energetic proximity of the minima for a given surface (Figure 5.17), it is clear that the result obtained in gas phase regarding the interconversion of 2O-Cu_5 structures is similarly achievable, and therefore both planar and 3D clusters are reducible through the 3D isomer along the same lowest energy path. Interestingly, the activation energies for the recombination on NG provide values very similar to what was obtained in gas phase at the PW91 level (73.1 and 61.8 kcal mol^{-1} for planar and 3D Cu_5, respectively), whereas for NG_V recombination from planar and 3D clusters increase and decrease, respectively, by around 20 kcal mol^{-1}. The NG_V surface thus favours again 3D structures more easily oxidizable, but it is remarkable that even when it does, the 3D isomers are also at least more easily reducible.

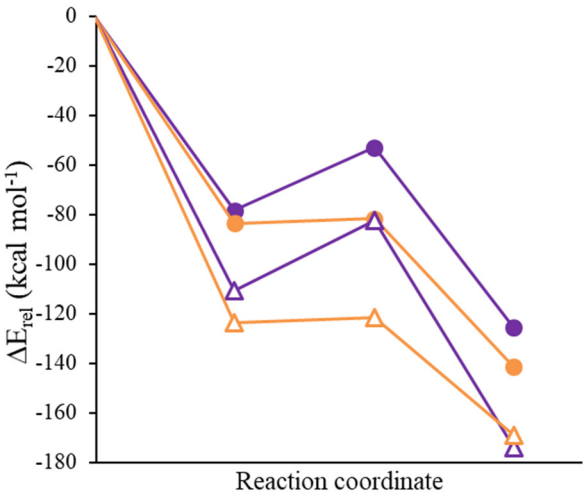

Figure 5.17. Energy profiles for the O_2 dissociation over planar (purple) or 3D (orange) Cu_5 clusters deposited on NG (full dots) or NG_V (empty triangles). The zero of energy is chosen for each surface as: E(planar Cu_5) + E(N-graphene sheet) + E(O_2).

5.3.2. Ceria-supported copper clusters.

5.3.2.1. Cu_5, Cu_8 and Cu_{13} on the CeO_2(111) surface.

As for graphene, the planar and 3D isomers of Cu_5 and the most stable structures for gas phase Cu_8 and Cu_{13} from Chapter 3 (Figure 5.18b) were placed on the CeO_2(111) surface. Cu_5 was placed in a 3x3 slab whereas a 4x4 slab was used for the larger Cu_8 and Cu_{13} (Figure 5.18a).

The strength of the metal-support interaction in this case induces structures where the copper clusters match the high symmetry of the $CeO_2(111)$ surface, and we found very few isomers close in energy to the lowest energy structures (Figure 5.19).

For Cu_5, the structures **150** and **156** obtained from the planar and 3D isomer, respectively, are energetically very close, within 1-2 kcal mol^{-1}, and the groundstate changes from the 3D to the planar isomer when dispersion is included (Table 5.10). The geometry of the cluster in structure **150** is very similar to that of the most stable planar structure for Cu_5 found in gas phase, with one of the terminal less-coordinated copper atoms slightly bent towards the surface, from where an oxygen atom also moves to provide a better Cu-O interaction. In structure **156** the geometry is that of the open 3D Cu_5 already seen on graphene, with one of the Cu-Cu bonds broken.

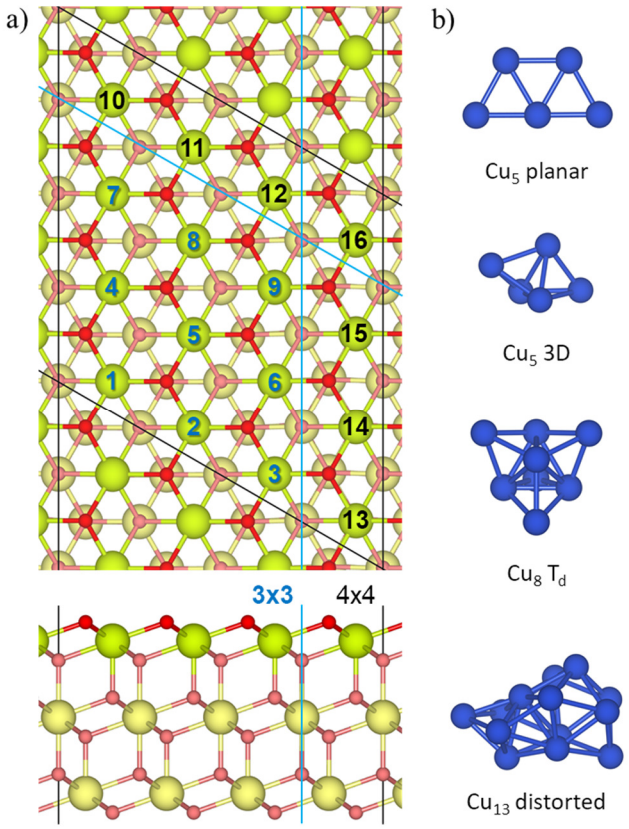

Figure 5.18. a) $CeO_2(111)$ surface slabs employed and b) copper clusters considered. Periodic cells are indicated by black and blue lines for the (4x4) and (3x3) slabs, respectively. Cu atoms in dark blue, O atoms in red (subsurface O atoms in pink), Ce atoms in green (subsurface Ce atoms in yellow). Surface Ce atoms are numbered for reference.

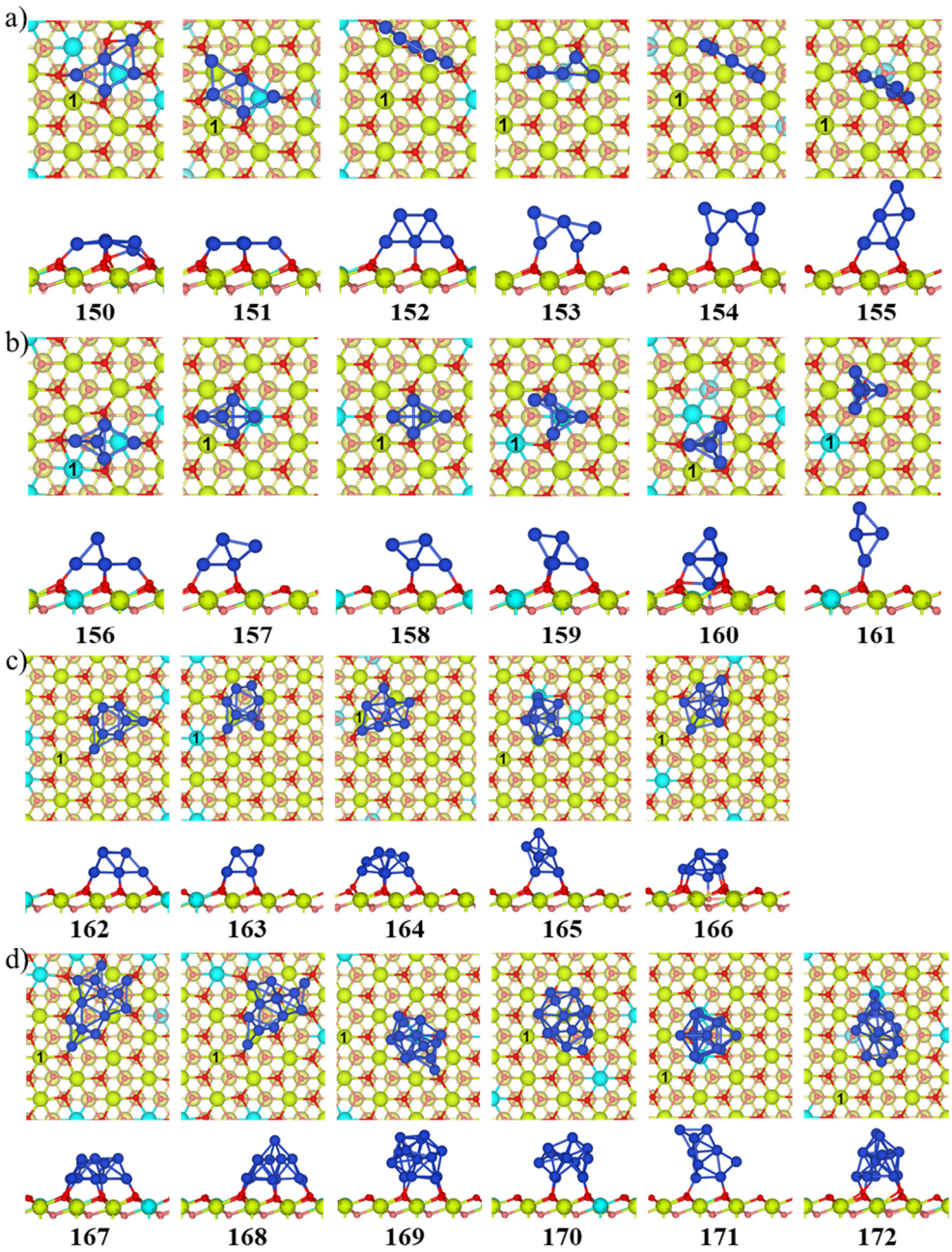

Figure 5.19. Optimized structures of a) planar Cu_5 b) 3D Cu_5 c) Cu_8 and d) Cu_{13} clusters supported on $CeO_2(111)$, in order of decreasing stability. Top and side views are shown. Ce atoms are in green (subsurface atoms in yellow), O in red (subsurface atoms in pink), Cu in blue, Ce^{3+} atoms in light blue.

Table 5.10. Relative energy w.r.t. the most stable structure per size including dispersion (ΔE_{rel}+D2), adsorption energy wr.t. each isomer (ΔE_{ads}), adsorption energy with dispersion included (ΔE_{ads}+D2), adsorption energy with dispersion per atom ((ΔE_{ads}+D2)/n), charge transferred from the cluster to the support (qCu_n), positions of the Ce^{3+} produced (Ce^{3+} pos.) and total magnetic moment (mag) in the interaction of Cu_n (n = 5, 8 and 13) clusters with CeO_2(111).

Cluster	Structure (Fig. 5.19)	ΔE_{rel}+D2	ΔE_{ads}	ΔE_{ads}+D2	(ΔE_{ads}+D2) /n	qCu_n (e^-)	Ce^{3+} pos.	mag
Cu_5	150	0.0	-122.2	-142.6	-28.5	1.53	4, 5, 6	-1
planar	151	23.8	-98.6	-118.8	-23.5	1.16	5, 16	1
	152	33.7	-93.3	-108.9	-21.8	0.60	6	-1
	153	57.6	-71.7	-85.0	-17.0	0.58	18	-1
	154	59.1	-71.4	-83.5	-16.7	0.57	13	-1
	155	68.4	-63.4	-74.2	-14.8	0.58	18	-1
Cu_5 3D	156	1.4	-128.9	-147.2	-29.4	1.38	1, 5, 9	-1
	157	21.8	-110.7	-126.8	-25.4	0.63	5	1
	158	26.9	-105.4	-121.7	-24.3	0.67	3	1
	159	28.6	-105.1	-120.0	-24.0	0.95	1, 5	-1
	160	42.1	-92.0	-106.5	-21.3	1.49	4, 9, 17	1
	161	107.2	-33.7	-41.4	-8.3	0.61	1	1
Cu_8 T_d	162	0.0	-121.4	-146.6	-18.3	1.19	13, 16	0
	163	19.1	-105.0	-127.5	-15.9	1.11	1, 7	0
	164	28.7	-95.8	-117.9	-14.7	1.14	17, 24	0
	165	30.6	-90.4	-116.0	-14.5	1.19	10, 12	0
	166	38.5	-90.3	-108.1	-13.5	1.03	8, 9	0
Cu_{13}	167	0.0	-172.4	-210.6	-16.2	2.13	7,11,13,26	-1
	168	8.9	-165.7	-201.7	-15.5	1.73	7, 11, 15	-3
distorted	169	66.0	-121.3	-144.6	-11.1	1.12	6, 7	1
	170	71.3	-110.9	-139.3	-10.7	1.15	3, 15	-1
	171	95.6	-92.2	-115.0	-8.8	1.04	5, 8	1
	172	94.5	-88.7	-116.1	-8.9	1.52	11, 16, 24	1

The latter is also obtained in structure **159**, absorbed through a (111) facet and with the less coordinated Cu atom up on an edge, not interacting with the surface. These two structures present the largest deformations found in the study for Cu_5.

For Cu_8, the geometry of the T_d isomer used as input is clearly deformed in all cases. Among the two lowest energy structures, in the second one (**163**) it adopts the D_{2d} structure also seen to enhance the interaction in graphene, but the groundstate (structure **162**) is constituted by a bilayered structure where the layer in contact with the surface matches the hexagonal surface of ceria much like planar Cu_5 and the next layer is composed of the remaining three Cu atoms following what would be an hexagonal packing. Note, nevertheless, that the D_{2d} isomer of structure **163** interacts

matching the hexagonal symmetry as well, through three Cu atoms in a triangular geometry and a fourth atom forming an elongated planar Cu_4.

For Cu_{13}, similarly, although we are able to optimize less deformed structures, more open structures that follow the surface symmetry are much more stable (**167** and **168**). Starting with the distorted Cu_{13} isomer from gas phase, optimization algorithms led to structure **168**, and structure **167** was manually created from the former to determine whether the bilayered structure was thermodynamically preferred. However, it is also evident from structure **167** that the matching between one layer of copper and ceria would not be perfect, consistent with the results of Yang et al.[290]. This was already suggested by the slightly larger adsorption energy of 3D Cu_5 (Table 5.10) and by the displacement of one O atom of ceria towards the planar Cu_5 cluster in structures **156** and **150**, respectively, but it is all the more evident here because atoms in the contact layer separate to establish more stable Cu_3 (or open Cu_5) clusters as islands, and the atoms of the second layer are the ones that maintain the cluster together. Indeed, these atoms provide a stabilization of the atoms in the contact layer that lone Cu_3 (and planar Cu_5) clusters lack, thus allowing the lengthening of Cu-Cu bonds needed for a better match: an average of 2.348 Å is obtained for the ground-state of Cu_3 in a 3x3 CeO_2(111), consistent with previous results[290,296], whereas the three Cu_3 islands in structure **167** present an average Cu-Cu distance of 2.583 Å. On Cu_8 the effect may not be that evident visually, but it is also observed in the lengthening of the Cu-Cu bonds of the Cu_5-like contact layer: an average of 2.673 Å is obtained for the planar Cu_5 layer of structure **162** vs the 2.461 Å of structure **150**).

The strong metal-support interaction is reflected in high adsorption energies, 34-83 kcal mol^{-1} higher than those on G_V (Table 5.10). The 6-7 kcal mol^{-1} larger adsorption energy of 3D Cu_5 with respect to planar Cu_5 is remarkable considering it has one less Cu-O bond, but the two groundstates are still equally stable thermodynamically (recall isolated 3D Cu_5 is 6 kcal mol^{-1} higher in energy). The adsorption energy of planar Cu_5 and Cu_8 is very similar, showing that the three additional Cu atoms of structure **162** are not able to affect much the Cu_5-like interaction of the contact layer, consistent with its strength. In contrast, Cu_{13} interacts with 8 Cu atoms and shows a significantly higher adsorption energy. Nevertheless, since not all the atoms are in contact with the surface as the atomicity increases, the adsorption energy per atom decreases with increasing cluster size, also showing the probable instability of a monolayer and the growth towards non-planar structures.

In addition, as already mentioned in the introduction, when copper clusters are adsorbed on this surface a reduction of one or more Ce^{4+} to Ce^{3+} is expected as a result from the oxidation of the cluster. Odd-numbered clusters should easily give up their unpaired electron, whereas even clusters have a closed shell electronic structure that grants them an enhanced stability and resistance to oxidation. We find that the interaction of ceria with the copper clusters is strong enough to overcome the latter effect,

breaking their electronic structure and producing another unpaired electron that the surface is also able to accommodate. This way, for Cu_8 clusters on $CeO_2(111)$ two electrons are transferred, allowing the cluster to retrieve a cationic closed shell structure, and two reduced Ce^{3+} are formed in the surface. Moreover, this happens also to Cu_5 and Cu_{13}, which lose up to three and four electrons, respectively, producing three or four Ce^{3+} ions. Correspondingly, the charge transferred from the copper cluster to the surface in the groundstate structures is around 1.2e, 1.5e and 2.1e for Cu_8, Cu_5 and Cu_{13}, respectively (Table 5.10). Only one Ce^{3+} is reported for the groundstate of Cu_3 and Cu_1 on ceria[290,295], probably because their electronic structure is less dense and losing two additional electrons is too unstable for clusters of small atomicity.

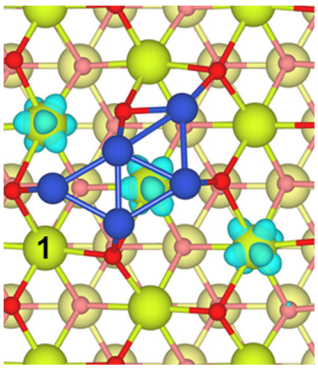

Figure 5.20. Top view of the partial charge density plot for the energetic range that comprises the states of the three Ce^{3+} found in structure **150**. The *f*-shaped density is shown in light blue (0.006 eV/Å^3), Ce atoms in green (subsurface atoms in yellow), O in red (subsurface atoms in pink), Cu in blue.

Regarding charge distribution within the clusters, atoms in contact with the surface are in general more positively charged, whereas the external ones tend to preserve their neutral metallic character or even become slightly negatively charged (<0.1e). This is especially evident in the bilayered structures that constitute the groundstates of Cu_5-3D, Cu_8 and Cu_{13}, where the first layer of atoms are averagely charged by 0.34e, 0.27e and 0.29e, respectively, while those on top present an average Bader charge of 0.03e, -0.06e and -0.04e, respectively.

The specific position of the reduced cerium atoms can be detected by inspection of the spin density, looking for the singly occupied *4f* states. They are indicated in light blue in Figure 5.19, and the spin-density of structure **150** is shown in Figure 5.20 as an example to further show the *f*-shaped density around Ce^{3+} atoms. It was found that care must be taken in the determination of the groundstate of copper-ceria structures, for the specific position of a Ce^{3+} for a given structure can change the energy of the system by as much as 0.25 eV. This becomes important when more than one atom is reduced and, furthermore, the optimization did not always arrive to the most stable configuration on the first attempt.

For Cu_5, different Ce^{3+} positions were explored for structures **150** and **156**, but all our efforts evolved back to those structures or to **150-Ce4,5,12** and **156-Ce5,6,9**, which lie between 7-12 kcal mol^{-1} higher in energy (Figure 5.21a). Thus, in these calculations the difference in energy (including dispersion) between the two most

stable isomers is of 1.4 kcal mol^{-1} favoring the planar one. However, a similar exploration of the Ce^{3+} positions in the 4x4 slab seems to favor the planar one by 6.9 kcal mol^{-1} (structures **150-p(4x4)** and **156-p(4x4)** in Figure 5.21b). It is important to note then that the 3x3 slab may be too small to study this effect appropriately, as the result of the three Ce^{3+} produced being on a continuous line may be affecting the stability of structures **150** and **156**. In a 4x4 slab such periodic lines of Ce^{3+} are not possible and are altogether lost, with at least one of the Ce^{3+} moving away from the other two. In this regard, the 3x3 results would represent a sample with higher Cu loading (or coverage). Indeed, the two Ce^{3+} produced for tetrahedral Cu_4 on CeO_2(111) similarly arrange in a surface line in a report on a 2x2 slab, although the number of different distributions are much lower in such a small model[290]. Even in a 4x4 slab, however, more calculations would be needed in order to unambiguously determine the most stable position of the Ce^{3+} produced and properly compare the two structures. Nevertheless, both models show that the planar and 3D isomers of Cu_5 are close in energy and a more or less even distribution of them should be expected. The same can be said about the two lowest energy structures for Cu_8 and Cu_{13}, which are clearly energetically apart from the rest of the structures obtained, but for which other Ce^{3+} distributions should be explored.

Figure 5.22 shows the Projected Density of States (PDOS) of the lowest energy structures from Figure 5.19. The defined peaks or defects denote the marked ionic

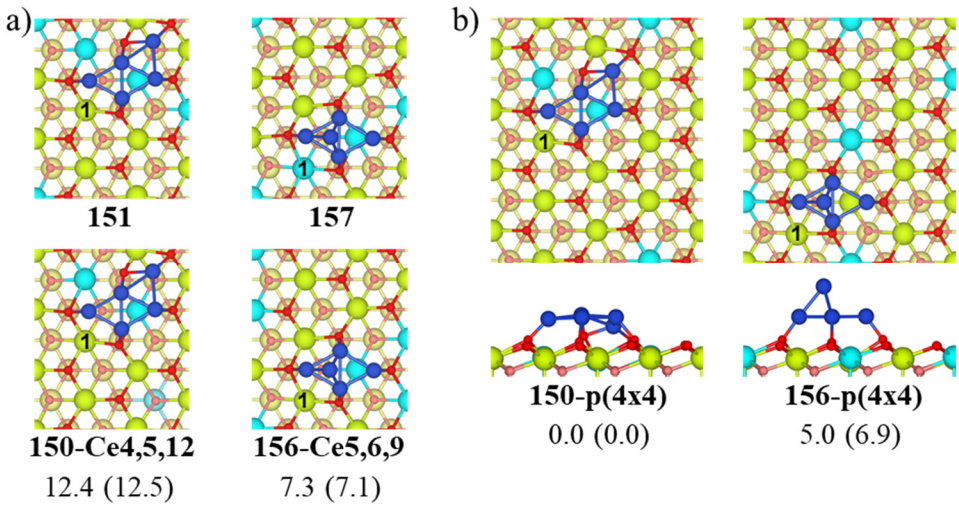

Figure 5.21. Optimized structures of a) groundstates (up) and another distribution of Ce^{3+} atoms for the same structures (down) for planar (**150**) and 3D Cu_5 (**156**) on a CeO_2 (111) p(3x3) slab (top views), and b) the same structures on a p(4x4) slab (top and side views). Relative energies are shown, in parenthesis including dispersion. Ce atoms are in green (subsurface atoms in yellow), O in red (subsurface atoms in pink), Cu in blue, Ce^{3+} atoms in light blue.

character of the bonds in these systems. In all cases some copper *3d* states appear in the former surface gap (Cu(*3d*), in orange) coinciding in energy with smaller contributions from *2p* states of the oxygen atoms that they most interact with (O(*2p*), in red), and with negligible contributions from cerium atoms (Ce(*4f*), in blue). This spatial coincidence indicates the covalent character of the interaction between Cu and O atoms. In all cases as well, the same number of defects from the reduced Ce^{3+} found in each structure appears in the gap. For both isomers of Cu_5, one of these Ce^{3+} *4f* states constitutes now the highest occupied state of each system, whereas for Cu_8 the latter lie deeper and two equivalent *3d* states of copper are the highest occupied instead. In the case of Cu_{13}, *4f* states corresponding to the three surface Ce^{3+} are further stabilized toward lower energy values, whereas the fourth one at the sub-surface lies at the Fermi level hence constituting a partially filled band of metallic character. However, the defect corresponds mainly to a band below the Fermi level and very slightly delocalizes into a band close above with an occupation of 0.0023. Two 4f states of Ce^{3+} contribute mainly to the two bands, and this makes us think that this may rather be an artifact of the SIE delocalization problem and one can assume that the defect lies localized below the Fermi level. In such case, according to the calculated energy of the bands, there would be practically no band gap, as the filled and empty implicated bands are 0.08 eV separated in energy. However, in the next stable structure **168** that was not altered by hand before optimization, the cluster is less oxidized, this fourth Ce^{3+} is not produced and a larger band gap for Cu_{13}, of 0.77eV, is obtained, much like for the other cluster sizes. Band gaps of 0.87, 0.28 and 0.77 eV are found for planar Cu_5, 3D Cu_5 and Cu_8, respectively.

In addition, for structures **150, 156** and **167** the deeper oxidation of the cluster produces an empty state of mixed nature below the empty *4f* band of Ce; more than one for structure **156**. That of structure **150** is very close to the empty *4f* band of Ce and has a greater *4f* contribution, but in the case of structure **156** it is much closer to the Fermi energy (as shown by the lower band gap), and has a greater *3d* character (Figure 5.22). As a result, naturally, the structures with the more oxidized Cu_n clusters, **156** and **167**, are also the more easily reducible systems. Indeed, the empty *3d* copper states produced in the latter case constitute additional acceptor bands and Cu_5 is the only system where reduction would not necessarily take place in another cerium atom. The fact that bigger clusters have more electron density shared and therefore are stable losing more charge is again observed here, for structure **168** of Cu_{13}, having lost the same three electrons than both Cu_5 structures, shows occupied *3d* states very close to the Fermi level, just as Cu_8, whereas structure **167** is more oxidized and presents less *3d* peaks below the Fermi level and more above it.

Finally, note that the easier oxidation of planar Cu_5 (**150**) and the higher reducibility of the non-planar Cu_5 isomer (**156**) implies that the interconversion of the isomers can be a very interesting process in a redox cycle, similar to what was observed in Chapter 3, where an easy interconversion of the minima favors the recombination of the O_2 molecule for both isomers in gas phase.

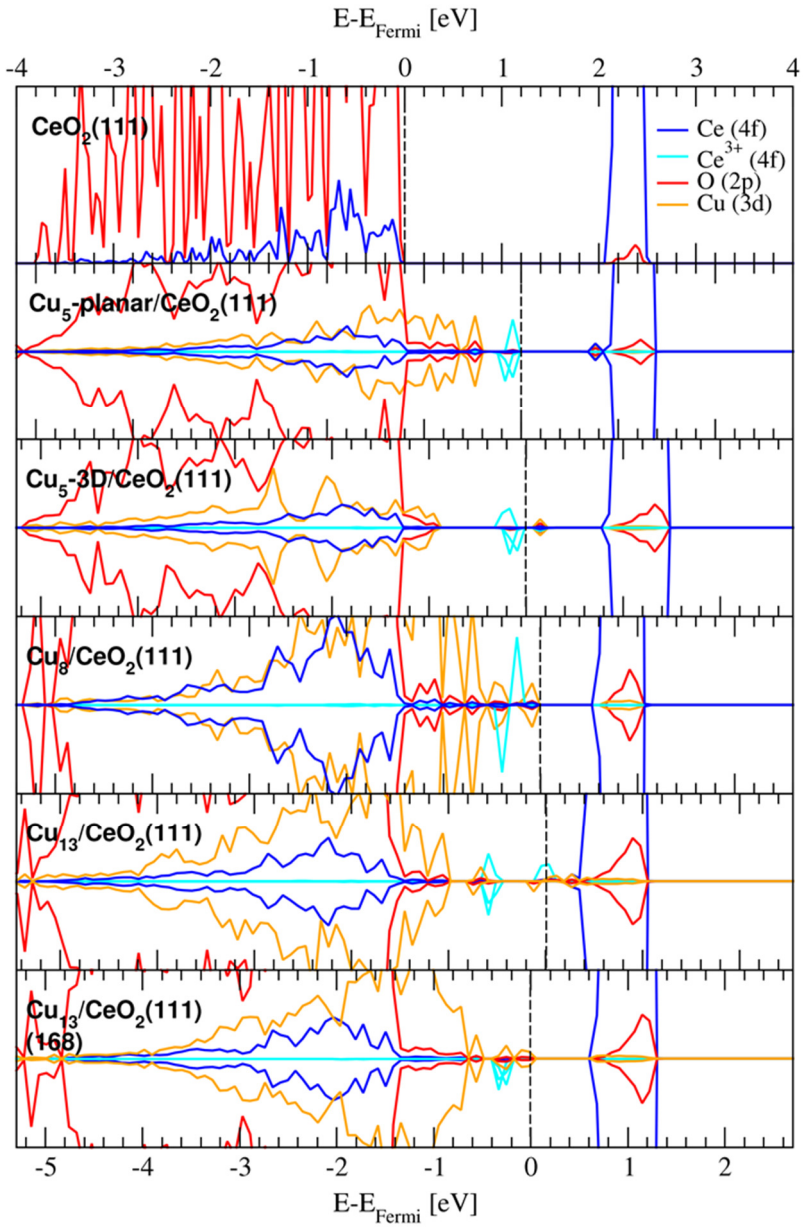

Figure 5.22. Projected density of states (PDOS) of the most stable structures for the Cu_n clusters (n=5, 8, 13) supported on the CeO_2(111) surface compared to the PDOS of the clean surface. *2p* orbitals of O are projected in red, *3d* of Cu in orange and *4f* of Ce in blue, with the defects corresponding to Ce^{3+} in light blue. PDOS are aligned w. r. t. the O (*2p*) valence band maximum of the O-atoms. Dashed lines indicate the highest occupied energy level.

5.3.2.2. O_2 adsorption over $Cu_5/CeO_2(111)$.

The adsorption of O_2 in the most stable structure for the planar and 3D Cu_5 isomers, namely, in structures **150** and **156**, was now studied.

In the tests on the adsorption of isolated oxygen on the $CeO_2(111)$ surface, the molecule always moved away or stayed far, weakly interacting with a Ce atom (Figure 5.23). The resulting adsorption energy (including dispersion) is of -2.0 kcal mol^{-1}. The interaction is therefore worse than with graphene, producing almost no change in the O-O bond or its vibrational frequency (1.233 Å and 1561 cm^{-1}) with only 0.04e charge transferred.

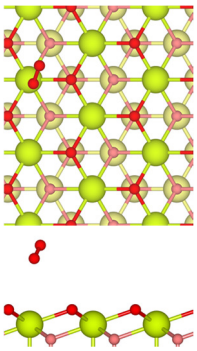

Figure 5.23. Optimized struc. of $O_2/CeO_2(111)$.

Consistent with this weak interaction, the O_2 molecule again prefers to adsorb on the copper cluster (Figures 5.24 – 5.25 and Tables 5.11 - 5.12). Indeed, structures with O_2 on ceria in the neighborhood of Ce^{3+} atoms lead to the molecule adsorbing on top of the cluster for planar Cu_5 (and subsequently dissociating, not shown) and unstably binding to one cerium and one copper atom at the interface for 3D Cu_5 (structure **191**).

The *mono*, *top*, *bridge, h-111* and *mono-bridge* adsorption modes previously seen are found again here. However, the planar cluster is now flat with all its atoms in contact with the surface and the *bridge* modes that constituted the most stable structures are now unstable (as in structure **181**). Instead, the adsorption of the cluster on ceria allows the adsorption of O_2 on its (111) facets, a feature impossible in gas phase planar Cu_5, and with a large adsorption energy (structures **173-177**). Indeed, the highest occupied band corresponding to the highest occupied defect observed in the PDOS of mainly Cu *3d* character spreads out along one of the internal Cu-Cu bonds, which explains the preferred interaction over the face (Figure 5.26). The adsorption of the molecule in these *h111* modes produces, much like additional Cu atoms in a second layer, the lengthening of the Cu-Cu bonds (an average of 2.699 Å Cu-Cu bond distance is obtained for the three Cu atoms below the O_2 in structure **173** as opposed to 2.398 Å for the same atoms in structure **150**), and it establishes O-Cu-O quasilinear bonds that result in an increased positive charge for the Cu atoms involved, which can be considered Cu^+ (0.5-0.6e). In general, the charge transferred to the molecule in these most stable modes comes from the cluster, and the same amount of pre-existing Ce^{3+} are found, although they change their positions (probably partially due to the movement of surface O atoms to enhance the new O-Cu-O interactions). For the other structures, however, the cluster does not lose that much charge and some Ce^{3+} oxidize to Ce^{4+} instead.

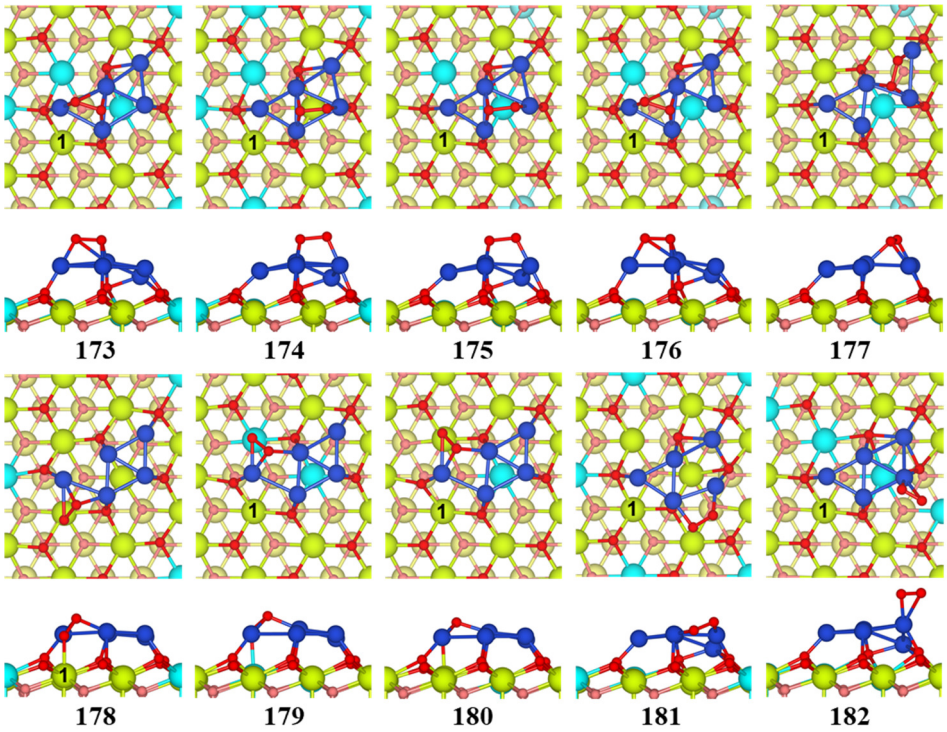

Figure 5.24. Optimized structures of O_2 adsorbed on CeO_2(111)-supported planar Cu_5 in order of decreasing stability. Top and side views are shown. Ce atoms in green (subsurface in yellow), O in red (subsurface in pink), Cu in blue, Ce^{3+} in light blue.

Table 5.11. Adsorption energy of O_2 on CeO_2(111)-supported 3D Cu_5 including dispersion ($\Delta E+D2_{ads}$), dispersion contribution (D2), relative energy w.r.t. the most stable structure with dispersion ($\Delta E+D2_{rel}$), O-O distance (r_{OO}), O-O vibrational frequency (ν_{OO}), Bader charge on the molecule (qO_2), change of the Bader charge on the cluster (ΔqCu_5), positions of the Ce^{3+} produced (Ce^{3+} pos.) and total magnetic moment (mag).

Structure Fig. 5.24	Adsorption Mode	$\Delta E+D2_{rel}$ (kcal mol^{-1})	$\Delta E+D2_{ads}$ (kcal mol^{-1})	D2 (kcal mol^{-1})	r_{OO}[a] (Å)	ν_{OO}[a] (cm^{-1})	qO_2 (e$^-$)	ΔqCu_5 (e$^-$)	Ce^{3+} pos.	Mag
173	*h111*	0.0	-56.8	-3.3	1.540	625	-1.09	1.04	3, 4, 6	1
174	*h111*	4.1	-52.7	-3.4	1.544	629	-1.08	1.06	3, 4, 7	1
175	*h111*	6.3	-50.5	-3.5	1.544	620	-1.08	1.04	4, 5, 12	1
176	*h111*	10.4	-46.4	-3.3	1.536	630	-1.09	1.06	4, 5, 12	1
177	*h111*	12.7	-44.1	-4.8	1.509	655	-1.05	0.62	5, 12	3
178	*h111*	32.5	-24.3	-4.9	1.493	731	-1.11	0.25	3	1
179	*h111*	34.9	-21.9	-4.6	1.464	799	-1.00	0.41	4, 5	1
180	*h111*	38.5	-18.5	-5.3	1.496	722	-1.12	0.20	5	-1
181	*bridge*	40.3	-16.5	-4.1	1.420	856*	-0.92	0.51	3, 7	1
182	*top*	42.7	-14.1	-0.8	1.306	1182	-0.41	0.44	4, 5, 6	1

[a]For the gas phase O_2 molecule: r_{OO} = 1.233 Å, ν_{OO} = 1566 cm^{-1}.
*Had a -49 cm^{-1} imaginary frequency involving the O_2 molecule.

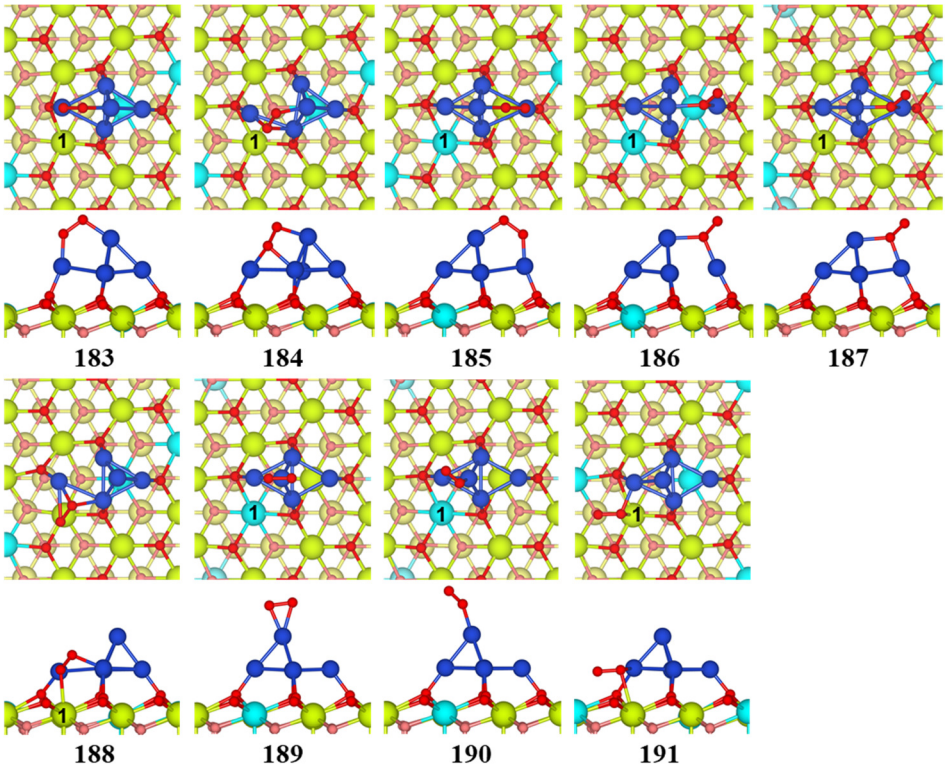

Figure 5.25. Optimized structures of O_2 adsorbed on CeO_2(111)-supported 3D Cu_5 in order of decreasing stability. Top and side views are shown. Ce atoms in green (subsurface in yellow), O in red (subsurface in pink), Cu in blue, Ce^{3+} in light blue.

Table 5.12. Adsorption energy of O_2 on CeO_2(111)-supported 3D Cu_5 including dispersion ($\Delta E+D2_{ads}$), dispersion contribution (D2), relative energy w.r.t. the most stable structure with dispersion ($\Delta E+D2_{rel}$), O-O distance (r_{OO}), O-O vibrational frequency (ν_{OO}), Bader charge on the molecule (qO_2), change of the Bader charge on the cluster (ΔqCu_5), positions of the Ce^{3+} produced (Ce^{3+} pos.) and total magnetic moment (mag).

Structure Fig. 5.25	Adsorption Mode	$\Delta E+D2_{rel}$ (kcal mol^{-1})	$\Delta E+D2_{ads}$ (kcal mol^{-1})	D2 (kcal mol^{-1})	r_{OO}[a] (Å)	ν_{OO}[a] (cm^{-1})	qO_2 (e$^-$)	ΔqCu_5 (e$^-$)	Ce^{3+} pos.	Mag
183	*bridge*	13.4	-44.8	-3.0	1.369	985	-0.73	0.39	5, 9	-1
184	*h111*	13.8	-44.4	-3.3	1.451	785	-0.87	0.36	5, 9	-1
185	*bridge*	26.2	-32.0	-3.2	1.375	947	-0.75	0.36	1, 9	-1
186	*m-bridge*	28.6	-29.7	-3.6	1.357	1025	-0.72	0.34	1, 5	-3
187	*m-bridge*	33.3	-25.0	-2.7	1.355	1029	-0.70	0.36	9, 16	3
188	*h111*	32.9	-25.4	-3.7	1.428	821	-0.92	0.45	5, 9	2.7
189	*top*	38.0	-20.2	-1.1	1.341	1124	-0.52	0.15	1, 16	0.9
190	*mono*	49.2	-9.0	-1.2	1.291	1214	-0.45	0.08	1, 16	1
191	*m-bridge*	55.0	-3.2	-5.3	1.340	1045	-0.71	0.13	3, 5	1

[a]For the gas phase O_2 molecule: r_{OO} = 1.233 Å, ν_{OO} = 1566 cm^{-1}.

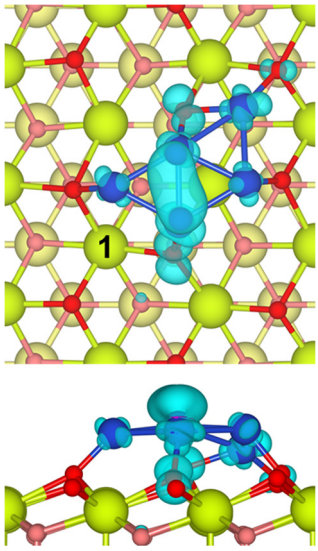

Figure 5.26. Top and side views of the partial charge density plot for the highest band corresponding to filled Cu *3d* states found in structure **150**. Ce atoms in green (subsurface atoms in yellow), O in red (subsurface atoms in pink), Cu in blue, charge density (0.004 eV/Å) in light blue.

For 3D Cu_5 such *h111* modes involving so many O-Cu-O interactions are not possible and its open structure is now the one that preferentially favors a *bridge* mode (structure **183**), closely followed by an open *h111* mode at the same site (structure **184**). As a consequence, the cluster never oxidizes as much as the O_2 reduces and at least one Ce^{3+} is always re-oxidized, and even at the mentioned *h111* mode the molecule is less oxidized than at the same modes on planar Cu_5. Nevertheless, the Cu-Cu distances of the atoms around the molecule lengthen as well, further separating the tetrahedral Cu_4 moiety from the remaining Cu atom (an average of 2.778 Å is obtained for the two Cu-Cu bonds of the latter in structure **183** as opposed to 2.503 Å for the same bonds in structure **156**). Indeed, in these structures one O-Cu-O interaction can be observed for the more separated atom mentioned, and the latter is again more positively charged that the rest (0.5-0.6e).

The previous trends regarding the adsorption modes of O_2 and its activation are again followed here (Figure 5.27 and Tables 5.11-5.12). However, a clear distinction is observed between the adsorption modes when the molecule is adsorbed on the cluster with respect to the same modes when it adsorbs at the interface. Thus, in the latter case a lower activation of the molecule is observed both for *h111* modes (structures **173-176** and **184** as opposed to **178-180** and **188**) and *mono-bridge* modes (structures **186-187** vs **191**), although the charge transferred to the oxygen molecule is practically the same. The weaker interaction and activation therefore must respond to the different nature of the $Cu^{0/+}$-O and $Ce^{4+/3+}$-O interactions, among which the former seems to be preferable for the system.

In any case, the copper-ceria interaction produces the loss of stable less activated adsorption modes for the O_2 molecule on planar Cu_5 and introduces some of them for 3D Cu_5, precisely reversing the results obtained for gas phase and graphene-supported copper clusters. However, the energetic proximity of the activated *h111* mode (structure **184**) for the 3D isomer suggests that both planar Cu_5 and 3D Cu_5 may activate the molecule enough for its dissociation on ceria.

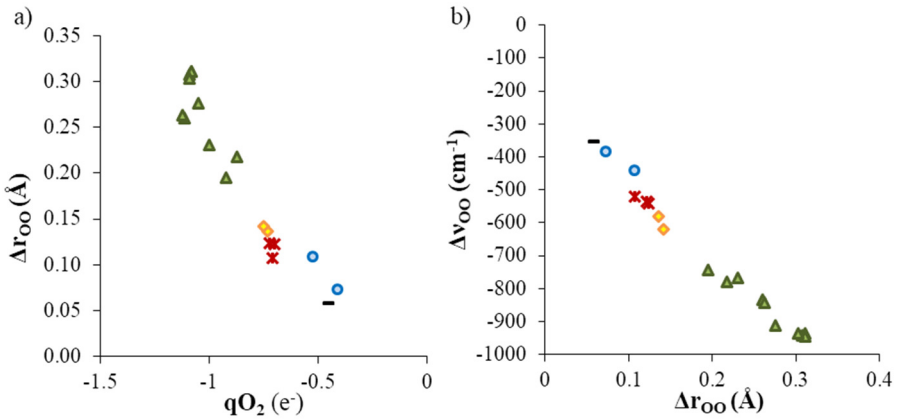

Figure 5.27. Relationship a) between the bond length variation, Δr_{OO}, and the charge transferred, qO_2, and b) between the shift in the ν_{OO} vibrational frequency and the bond length variation, Δr_{OO}, per adsorption mode: *mono* (black lines) *top* (blue circles) *bridge* (yellow diamonds) *h-111* (green triangles) and *mono-bridge* (red crosses).

5.3.2.3. O_2 dissociation over $Cu_5/CeO_2(111)$.

The most stable structures of both planar and 3D Cu_5 with O_2 adsorbed were then tested for dissociation (Figure 5.28 and Table 5.13). For planar Cu_5, all the most stable structures involved similar *h111* modes of the molecule on (111) facets of the cluster, and thus structure **173** was considered as representative enough for the planar isomer. For 3D Cu_5, the close in energy *bridge* and *h111* modes of structures **183** and **184** were both explored.

As expected from the high activation of the O_2 molecule in the *h111* modes on the planar cluster, the activation energy for O_2 dissociation from structure **173** is low, 9.6 kcal mol^{-1}, whereas that from the less activated *bridge* mode of structure **183** is higher, 25.1 kcal mol^{-1}. TSs from both structures **183** and **184** were difficult to find, presumably because the oxygen atoms do not find enough Cu-O interactions to be stable, but also because O_2 and the copper atom on top allow the displacement of the copper atoms below. Eventually, the TS from structure **183** evolved towards an *h111* mode (structure **194**), much like for the *bridge* mode of 3D Cu_5 in gas phase. Thus, it is similar to the TS **196** obtained from structure **184**, and the corresponding barriers are of 25.1 and 20.6 kcal mol^{-1}, respectively (Table 5.13). Indeed, in both TSs one of the O atoms is bridged and stabilized, but the second one does not achieve the same stabilization obtained in other TSs characteristic of *h111* adsorption modes. As a result, the activation energy from structure **184** is still high for an O_2 molecule adsorbed in an *h111* mode, even in spite of the high activation of the O-O bond.

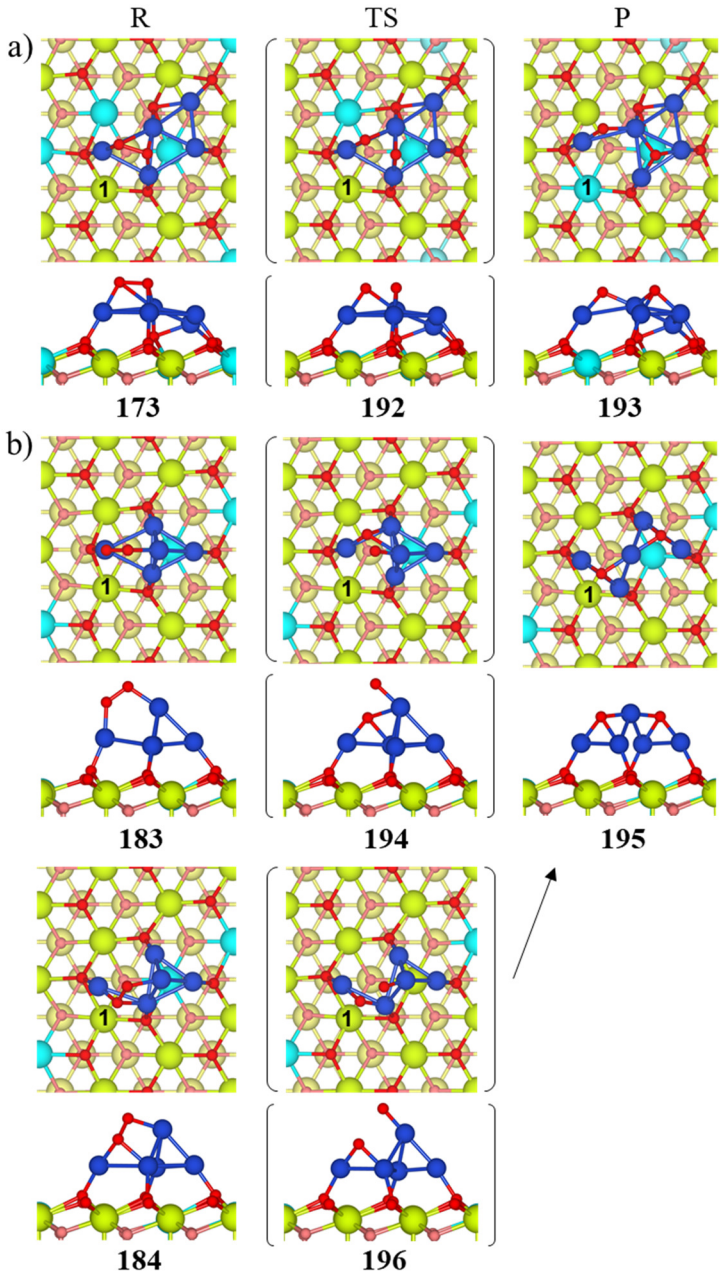

Figure 5.28. Optimized structures for the O_2 dissociation by the planar (a) and 3D (b) isomers of Cu_5 on $CeO_2(111)$. Top and side views are shown. Ce atoms are in green (subsurface atoms in yellow), O in red (subsurface atoms in pink), Cu in blue, Ce^{3+} atoms in light blue.

Table 5.13. Adsorption energy of O_2 on $CeO_2(111)$-supported clusters (ΔE_{ads}), relative energies (ΔE_{rel}), activation energies for O_2 dissociation (ΔE_{act}), O-O distance in the TS ($r_{OO}(TS)$, in Å) and reaction energies (ΔE_{reac}). Energies include dispersion and are in kcal mol^{-1}.

Cu_5 isomer	Path (Fig. 5.28)	ΔE_{rel}	ΔE_{ads}	ΔE_{act}	$r_{OO}(TS)$	ΔE_{reac}	ΔE_{reco}
Planar	173-[192]-193	0.0	-56.8	9.6	1.777	-20.8	30.4
3D	183-[194]-195	13.4	-44.8	25.1	2.000	-77.5	102.6
	184-[196]-195	13.8	-44.4	20.6	2.336	-77.8	98.5

With that exception, the values are in the range found for the same adsorption modes on graphene-supported clusters and further confirm that the activation of the O_2 molecule depends on its adsorption mode, regardless of the copper cluster isomer it is achieved through. However, it also shows that the reactivity of the cluster for a given morphology can be severely changed via the MSI, for in $Cu_5/CeO_2(111)$ systems the planar cluster is more active in the dissociation of O_2 than the 3D isomer; exactly the opposite result to what is found for gas phase and graphene-supported clusters.

Regarding the product structures, the tricoordination of the O atoms on (111) facets is possible and favored (structures **193** and **195**). In graphene, the opening of the Cu_5 3D cluster prevented to a certain extent the occupation of facet sites by O atoms, but here the production of O-Cu-O strong interactions prevails and deforms the clusters further oxidizing them. Indeed, in structures **193** and **195** the O atoms further receive –0.74 and -1.32e charge that comes almost entirely from the clusters (0.58 and -1.32e), and the same amount of Ce^{3+} ions that appeared in the reactants are observed.

Reaction energies are again clearly negative, but now the recombination of O_2 from two O atoms, that is, the reduction of the cluster, is not easier in the 3D cluster (Table 5.13). Besides, since the 3D cluster is severely deformed upon dissociation (Figure 5.29), it is difficult to state whether it would recover the original structure, as from those points the recombination of the molecule may be more easily produced via other geometries for the cluster. Nevertheless, we find again that the isomer that more easily dissociates O_2, planar Cu_5, is also the more easily reducible species. Besides, the recombination energy from structure **193** is of 30.4 kcal mol^{-1} only, as opposed to the 73.1 of isolated planar clusters, although the bicoordinated O atom of said structure may be able to move towards a more stable position, increasing ΔE_{reco}. Therefore, the recombination of 2O atoms back to O_2 may be possible for planar $Cu_5/CeO_2(111)$, but it is highly unlikely on 3D $Cu_5/CeO_2(111)$. As a result, for Cu_5 to preserve its metallic state on ceria, 3D Cu_5 would be the isomer to pursue.

In addition, although barriers are higher for 3D Cu_5, they are not prohibitive, and the oxidation of the cluster may be achievable with higher temperature. Thus, although the $Cu_5/CeO_2(111)$ system is likely to keep the cluster oxidized, only one of the copper atoms loses charge enough to consider it near Cu^{2+} (0.85e in structure **195**),

whereas the others remain closer to a Cu^+ state (0.5-0.6e). Therefore, the system may still be suitable to undergo oxidation reactions that require Cu^+ species, as mentioned in the introduction, and, while the recombination back to O_2 may not be possible, reaction of the O atom with subsequent species may still be.

All in all, we can point out that: i) the isolated 3D isomer is 6 kcal mol^{-1} higher in energy than the planar one, ii) the planar isomer is somewhat more favoured (thermodynamically) than the 3D one (by 1.4 / 6.9 kcal mol^{-1} calculated on 3x3/4x4 slabs) iii) upon O_2 adsorption, planar structures are also more favoured thermodynamically, iv) interconversion of isomers is not observed during optimizations due to the symmetry of the slab and the high interaction strength, v) planar clusters adsorb stretched out over ceria, adsorbing O_2 in highly activated *h111* modes and therefore showing a low activation energy for dissociation and vi) 3D clusters are opened upon adsorption, which favours the adsorption of O_2 in *bridge* modes and even destabilizes the TS from molecules adsorbed in *h111* modes, thus impeding O_2 dissociation.

As a result, planar clusters are somewhat thermodinamically favoured and hence O_2 dissociation is likely to occur on the $Cu_5/CeO_2(111)$ system, although the material may be reducible. In addition, the high adsorption energies of all clusters imply that 3D Cu_5 clusters can be stable on ceria, and a Cu^+ state may also be stabilized by oxidizing them. As opposed to gas phase (and graphene), where planar Cu_5 clusters (and planar Cu_5 clusters on NG sheets) are expected to show the greatest resistance to oxidation, 3D Cu_5 clusters are more resistant on ceria (Figure 5.29).

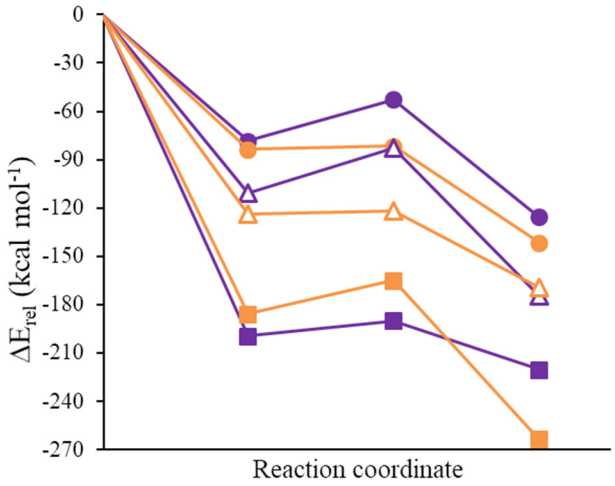

Figure 5.29. Energy profiles for the O_2 dissociation over planar (purple) or 3D (orange) Cu_5 clusters deposited on NG (full dots), NG_V (empty triangles) or $CeO_2(111)$ (full squares). The zero of energy is chosen for each surface as: E(planar Cu_5) + E(surface) + E(O_2).

5.4. Conclusions.

It is found that the interaction between copper clusters (Cu_n, n= 5, 8, 13) and clean graphene and N-graphene is weak, losing Cu-C interactions in favour of Cu-Cu bonds with increasing size. Adding nitrogen to graphene enhances the interaction, but proper chemical adsorption is only achieved at the defects explored, namely, C vacancies and three pyridinic N atoms sites.

The weak physisorption nevertheless grants Cu_5 clusters a certain stabilization that facilitates their deformation upon the adsorption of a molecule such as O_2. Given this and the energetical proximity of their planar and 3D isomers, interconversion of isomers is commonly observed during calculations, reflecting their fluxionality.

In spite of this, the conclusions on N-graphene are very similar to the results obtained in the previous chapter on gas phase clusters, i.e. planar clusters are favoured, adsorb O_2 in *bridge* modes and hence are less active towards its dissociation. The three pyridinic N atoms site somewhat favours the 3D isomers thermodynamically, but interconversion from 3D to planar clusters has also been produced at this site.

Regarding $CeO_2(111)$, it is found that the hexagonal symmetry of the surface more or less matches the geometry of planar Cu_5 or Cu_3, which adds to the strong O-Cu interaction. Thus, larger clusters such as Cu_8 or Cu_{13} are more stable forming a first layer of Cu_5 or Cu_3 islands connected through a second layer of copper atoms. When clusters are adsorbed on ceria, they get oxidized and produce Ce^{3+} atoms on the surface, whose positions can greatly change the energy of the structure.

Nevertheless, the strong interaction and the symmetry matching produces very few geometries close in energy for the Cu_5 clusters, which do not deform into one another in the calculations. Planar clusters adsorb parallel to the surface, interacting with all five atoms, and the 3D cluster breaks one of its Cu-Cu bonds to interact with four atoms in a rhombus shape, leaving the remaining Cu atom on top of one of the facets.

Since planar clusters are not in an upright position anymore, the adsorption of O_2 at its edges is highly impeded. Instead, O_2 is able now to strongly adsorb at the planar Cu_5 *h111* facets, getting highly activated in the process. In contrast, the molecule prefers a *bridge* site on the opened 3D cluster, and even when a *h111* mode is close in energy, the copper atoms are not close enough to stabilize both O atoms at the TS, thus yielding a higher activation energy.

Therefore, while on clean N-graphene the properties of the Cu_5 clusters observed from gas phase are kept, supporting them on ceria produces a totally different material with reversed results as regards the Cu_5 isomers: planar clusters are more resistant to oxidation (and more easily reducible) on N-graphene and gas phase, whereas 3D clusters are more resistant to oxidation on $CeO_2(111)$.

Chapter 6
Heck reaction on Pt_3 and Pd_3 clusters

The formation of new C-C bonds through coupling reactions is a key process in organic synthesis, and consequently has important practical applications in fine chemistry and pharmaceutical industries[318-321].

Among them, cross-coupling reactions such as Heck, Suzuki, Sonogashira or Stille are typically and efficiently catalyzed by palladium salts and complexes in homogeneous phase[141-143], but also by metallic nanoparticles as heterogeneous solid catalysts[133,134,137,144]. However, the key role of clusters composed by three or four palladium atoms in these couplings has been demonstrated very recently by other researchers at the ITQ[42].

In the present chapter we present the joint study that continued this line of research, showing that not only small palladium but also small platinum clusters efficiently catalyze the Heck and other cross-coupling reactions[147].

6.1. Introduction.

The accepted mechanism for Pd-catalyzed C-C bond forming reactions in homogeneous phase involves a Pd^0/Pd^{II} redox cycle (Scheme 6.1). The first step consists of an oxidative addition of the aryl halide reactant to a Pd^0 centre, yielding a Pd^{II} intermediate complex that is subsequently attacked by a nucleophile species.

In the Heck reaction (Scheme 6.1a) the nucleophile is a terminal alkene that is inserted in the Pd-Ar bond. The olefinic product is generated by β-hydride elimination, and the presence of a base is required to regenerate the Pd^0 active site. In other Pd-catalyzed cross-coupling reactions, a transmetalation step connects the main catalytic cycle in which the aryl halide adds to palladium and the new C-C bond is formed with a secondary cycle in which the partner reactant is activated. In the Suzuki reaction, the second reactant is an aryl boronic acid (Scheme 6.1b) and the presence of a base is crucial for the reaction to proceed. In the Sonogashira coupling a terminal alkyne is activated on a co-catalyst, usually copper, in the presence of base, and is subsequently transferred to the palladium centre (Scheme 6.1c). In the transmetalation step the organic group R becomes attached to the Pd^{II} centre substituting the halogen atom and, finally, the new C-C bond is formed and the product desorbs in a reductive elimination step, regenerating the Pd^0 active site[322-324].

The Heck reaction, particularly, is efficiently catalyzed by Pd complexes in homogeneous phase, by ligand-free palladium compounds such as $PdCl_2$ or $Pd(OAc)_2$, by Pd NPs stabilized by polymers and dendrimers, and by Pd NPs supported on carbon, silica or metal oxides. However, it has been demonstrated that under reaction conditions all these catalysts tend to form soluble Pd^0 colloids or small nanoparticles that are stabilized to some extent by the anions present in solution, and that act as reservoir of the active Pd species. Pd^{2+} salts and complexes are reduced to Pd^0 by action of the reactant or solvent (Scheme 6.1d), while in the case of heterogeneous catalysts it has been proposed that the aryl halide reactant attacks the Pd atoms at the NP surface producing leaching and generating monomeric Pd species. At the end of the catalytic cycle these Pd atoms can either enter a new cycle or be redeposited again on the Pd NP, following a dissolution-redeposition equilibrium mechanism (Scheme 6.1e). If leaching is slow the colloidal Pd species can grow into larger particles that precipitate as palladium black, leading to catalyst deactivation[130,132-134,325].

Therefore, the key point to optimize Pd based catalysts for cross-coupling reactions seemed to be to control the rates of release and recapture of the soluble active Pd species. However, it was still more crucial to identify the true nature of this soluble active Pd species.

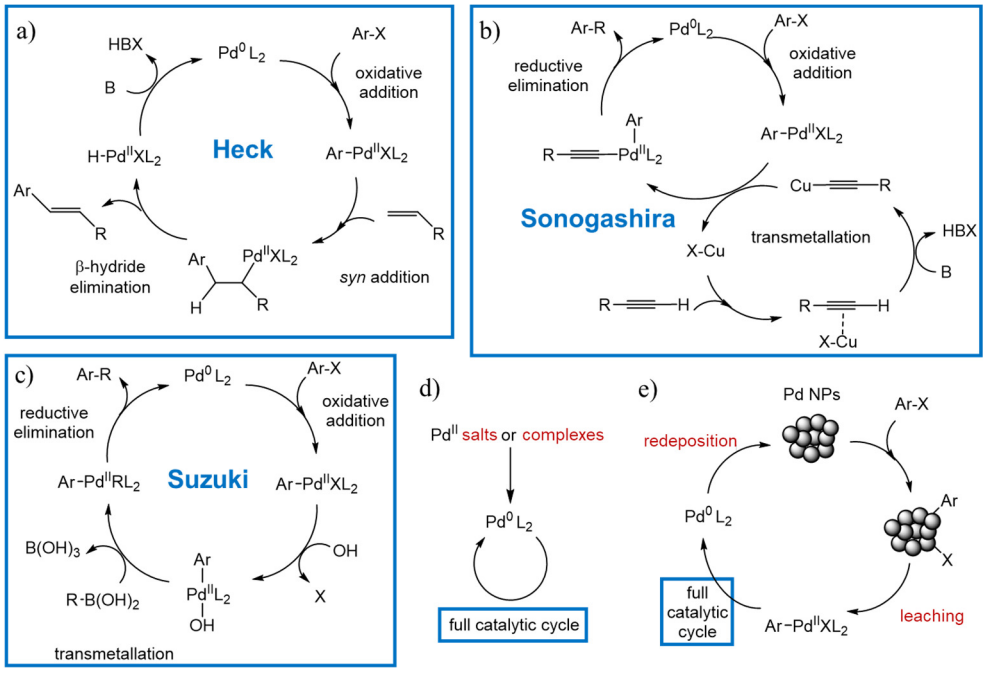

Scheme 6.1. Mechanism for Pd-catalyzed a) Heck, b) Sonogashira and c) Suzuki cross-coupling reactions, d) formation of metallic Pd^0 from Pd^{II} salts or complexes in solution and e) dissolution-redepositon mechanism for Pd nanoparticles.

To this end, Corma et al. studied in detail the kinetics of the Heck, Sonogashira, Suzuki and Stille cross-coupling reactions using different homogeneous and heterogeneous Pd-based pre-catalysts, concluding that reaction starts only when small Pd_3 and Pd_4 clusters appeared in the reaction medium after an induction time, these clusters being responsible for the catalytic activity[42]. This knowledge allowed the ex situ preparation of sub nanometer Pd clusters by adding Pd NPs to an aqueous solution of N-methylpyrrolidone (NMP), the storage of such clusters in aqueous solution for long periods, and their subsequent use in cross-coupling reactions without loss of catalytic properties.

The identification of Pd clusters as the active species pointed out a new possibility: To our knowledge, only some Pt salts and complexes dissolved in boiling amide solvents (dimethylformamide (DMF), NMP) have shown catalytic activity for the Heck coupling[326-328], but since these reaction conditions are exactly those in which very active catalytic subnanometer Pd clusters for cross–coupling reactions are formed[42], it may very well occur that Pt clusters are also active species for the Heck coupling.

Following this idea, Dr. Antonio Leyva-Pérez and Dr. Miguel Ángel Crespo successfully prepared (and tested) Pd and Pt subnanometer species solid-stablized within ethylene vinyl alcohol co–polymer (EVOH) in a very simple one–pot procedure, to give stable and non–toxic (biocompatible) solid materials, storable for at least 1 year. Other researchers also participated in this work, especially regarding the characterization[147]. Testing those samples, it is concluded that not only Pd but also Pt subnanometer species of few atoms catalyze the Heck, Suzuki and Sonogashira reactions of aryl halides. Indeed, Pt@EVOH presents a kinetic profile with no induction time, as opposed to other Pt species tested ($PtCl_4$ (Pt^{4+}), $Pt(acac)_2$ (Pt^{2+}) and Pt nanocubes (Pt^0)). Furthermore, it is found that which base is employed is determinant for the coupling to proceed.

In general, the rate-determining step (rds) of the couplings is the oxidative addition of the aryl halide on the metal, which is reflected in the typical reactivity order I > Br >> Cl. The following steps, i.e. transmetallation or alkene migratory insertion (for the Heck reaction) and reductive elimination, depend on the particular metal–organic reactant interaction arisen from the initial oxidative addition, and consequently, most efforts have focused on the design of organometallic species expected to collapse into the final coupling product. In contrast, the role of the base is usually overlooked, and it is just considered as a secondary player to capture released hydrogen atoms in a general way, despite abstraction of the hydrogen atom out of the catalytic site is a fundamental part of the process. Taking into account that the base is the most reactive of the coupling reagents and is added in excess with respect to any other species, it seems reasonable to think that it could influence not only the overall reaction rate but also the selectivity of the process. However, it has not been possible so far to assess its influence due to its excess in the reaction media and because the clusters were prepared and stabilized by acetate or amine bases *in–situ*, in reducing amide solvents. An independent synthesis of the clusters (*ex–situ*) would overcome this problem, and it is indeed what our colleagues have achieved.

Thus, in order to clarify the previous points, our collaboration in this study was focused in the reaction mechanism of the Heck coupling at small Pd and Pt clusters.

6.2. Computational details.

6.2.1. Models.

Clusters of three atoms were selected as the catalysts to study theoretically because, as shown in the introduction, past results of the group showed catalytic activity from Pd_3 and Pd_4 clusters for the same reactions, and the hypothesis that was being built was that the same clusters sizes of platinum could behave similarly.

Therefore, we employed a periodic model of Pt_3 and Pd_3 clusters, i.e. clusters and molecules were placed in a 20x20x20 $Å^3$ cubic box, large enough to avoid spurious interactions between periodically repeated systems.

Besides, the need to compare with single atoms and complexes presented itself along the study, and they were modelled by equivalent periodic systems.

6.2.2. Methods.

Structure optimizations were carried out at the Density Functional Theory (DFT) level with the VASP code[22,231], spin-polarized and using the PW91 functional of Perdew and Wang[157]. The valence density was expanded in a plane wave basis set with a kinetic energy cutoff of 500 eV, and the effect of the core electrons in the valence density was taken into account by means of the projected augmented wave (PAW) formalism[178]. In the reciprocal space, the integration was at the Γ k-point for the Brillouin zone. The positions of all atoms in the system were fully optimized without any restriction and all stationary points were characterized by partial hessian frequency calculations with the atoms of the cluster fixed. The latter were additionally used to calculate the corresponding free energies through partition functions. Transition states were located using the DIMER[185,186] or CI-NEB[187] algorithms.

The Gaussian 09 program package[19], was employed to obtain the molecular orbital distribution of the clusters using the natural bond order (NBO) approach[188], re-optimizing the structures at the B3LYP[160,329]/LANL2DZ[175,176] level, whereas the ChemCraft[258] program was employed to obtain their graphical representation.

In addition, the Jmol[257] and MOLDEN[256] programs were used to build and visualize the systems and their frequencies throughout the work.

6.3. Results.

6.3.1. Background from experiments.

6.3.1.1. Heck reaction catalyzed by Pd@EVOH and Pt@EVOH clusters.

The Heck reaction of aryl iodides and bromides with acrylates was previously proven to be catalyzed by in–situ formed $Pd_{3–4}$ clusters, after endogenous reduction of Pd salts in aqueous amide solvents (DMF, NMP) at reaction temperatures >130 ºC[42].

These reaction conditions are mandatory for the formation and activity of the tiny clusters, since the amide solvent reduces and aggregates the Pd compounds only at those temperatures[330,331], with water as cluster stabilizer[332]. These restrictions in

the reaction conditions severely limit the application of the catalytic Pd clusters for other substrates and, for instance, styrenes are not reactive. The stabilization of Pd clusters in EVOH copolymers allows not only to use them under demand as catalysts but also to test other reaction conditions for the Heck coupling. Thus, Figure 6.1 shows that styrenes can now be coupled with different aryl iodides and bromides in toluene at 95 ºC, using dicyclohexyl methyl amine as a base, to give the Heck products **A1–A7**, in good to excellent yields and with selectivity to the trans isomer. An acrylate also engages well in the coupling (product **A8**).

Kinetic experiments did not show a visible induction period during the coupling in toluene, which indicates that Pd@EVOH liberates the catalytically active subnanometer Pd clusters at the very beginning of the reaction. Furthermore, a new experiment where Pd@EVOH is pre–dissolved with an isopropanol/water mixture before adding the reactants, which breaks the co–polymer crystallinity[34,333], shows a slightly faster initial rate. ICP-MS analysis of the EVOH polymer after reaction confirms the complete liberation of the Pd cargo into solution.

These results show that Pd@EVOH can be used as a reservoir of subnanometer Pd clusters for the Heck reaction, to be liberated under the desired reaction conditions.

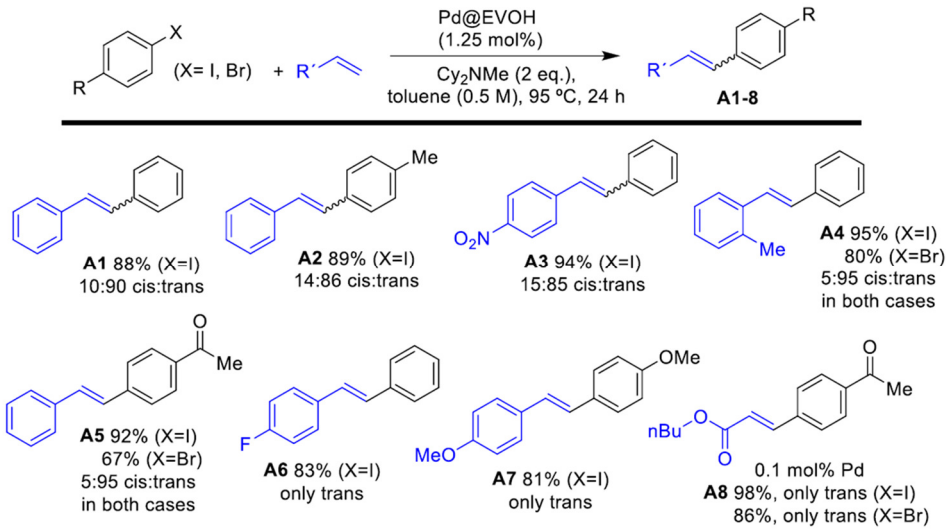

Figure 6.1. Results of the Heck cross–coupling reaction of different iodo and bromoarenes with alkenes using Pd@EVOH as a catalyst, and toluene as a solvent. Full conversion in all cases, mass balance completed with the corresponding biphenyl and benzene derivatives.

Analogously to Pd@EVOH, ICP-MS analysis confirmed the rapid deliverance of Pt clusters into solution from Pt@EVOH, and if the reaction is carried out with Pt@EVOH pre–dissolved in an isopropanol/water mixture a slightly faster initial rate is similarly found. These results indicate that Pt@EVOH acts as well as a reservoir of the catalytically active Pt species for the cross–coupling reaction, which are released under reaction conditions.

The kinetic profile of subnanometer Pt clusters independently prepared in amide solvents[330,331] is very similar to Pt@EVOH, i.e. without any induction time. Indeed, the kinetic curves show higher stability and activity of the Pt clusters if they are released from EVOH than when the clusters are formed in situ from Pt salts. These results support that subnanometer Pt clusters are catalytically active species of the reaction, although it is not possible to discard absolutely the presence of some single atoms or Pt(0) species together with the clusters.

Figure 6.2 shows that, indeed, Pt@EVOH experimentally catalyzes the Heck reaction of not only different aryl iodides but also of aryl bromides with alkenes in the presence of KOAc. Aryl iodides react well with acrylates and also styrene to give the coupled products **A5–A15** in good to excellent yields, including the industrially produced UV–protecting agent cinnamyl **A16**. Aryl bromides are also reactive and give the same products, although in lower yields.

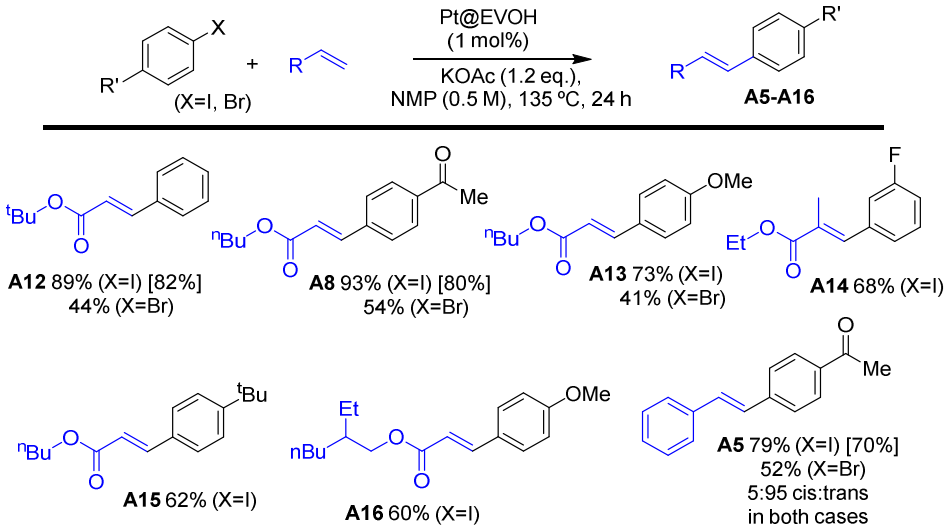

Figure 6.2. Results of the Heck cross–coupling reaction of different iodo and bromoarenes with alkenes using Pt@EVOH as a catalyst. GC yields, between brackets isolated yields. Full conversion for aryl iodides, mass balance completes with biphenyl and benzene derivatives. For aryl bromides, a 20% of biphenyl and benzene derivatives is typically found.

6.3.1.2. Reactivity results on the reaction mechanism.

The accepted steps of the Heck reaction on organometallics include, in this order, oxidative addition, alkene migratory insertion, β–hydride elimination and reductive elimination[332]. In principle, Pt^0 is amenable to do not only the alkene migratory insertion[334], β–hydride elimination[335] and reductive elimination[336,337], but also the oxidative addition of the C_{sp2}–halide bond[338-343]. The latter is generally the rate–determining step (rds) of the reaction, and has been unambiguously snap-shotted with a variety of single atomic heavy–late organometallic complexes of Au and Pt[338-343].

However, kinetics for different subnanometer cluster catalysts and reagent concentrations at initial reaction times show that the rate equation is[147]:

$$v_0 = k_{app1}[Pd][PhBr][KOAc][acrylate]^{-1} \quad | \text{ for Pd clusters}$$
$$v_0 = k_{app2}[Pt][PhI][KOAc][acrylate] \quad | \text{ for Pt clusters}$$

This indicates that all the reagents are implicated in the rds of the reaction, including the base employed. Notice that [base] is irrelevant at high concentrations (>0.5 M), and this rapid saturation of the catalytic site may also explain why the amount and nature of the base has traditionally been obviated from mechanistic studies.

Once found that the base seems to affect the reaction according to this kinetic data, Table 6.1 reveals that the activity of Pt clusters is dramatically lost when employing Bu_3N. Furthermore, KOAc as base is needed to produce good conversion, although all bases provide good selectivity to the Heck product. This effect does not occur for the Pd clusters[42], where amine and other inorganic bases are also active.

Kinetic measurements by changing the cation to increase the basicity of the acetate, from Li^+ to Cs^+, do not show any significant influence in the initial rate of the reaction with Pt clusters. This, together with the fact that carbonates and phosphates of higher pK_a (between 9 and 12) are not effective either[344], indicates that an intermolecular deprotonation based on classical acid–base interactions (in what would be the last reductive elimination of the Heck reaction) is not the main effect in the role of the base and does not explain why only KOAc is effective. The possible dual base/stabilizer role of KOAc was also discarded by kinetic experiments where acetyl acetate, AcOAc, is added to Bu_3N in order to mimic the effect, which provided equally unsuccesful results with Pt clusters. Lastly, the acetate is a prototypical ambiphilic base[345,346], and a chelating effect has been previously observed in C-H activation reactions promoted by bimetallic molecular complexes[347]. Thus, the possible interaction of the acetate with different Pt atoms of the cluster seems reasonable to explain the uniqueness of this base to trigger the Pt–catalyzed Heck reaction.

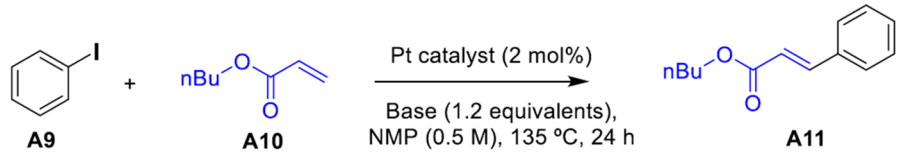

Scheme 6.2. Heck reaction between iodobenzene **A9** and butyl acrylate **A10** with KOAc as a base, in NMP at 135 ºC for 24 h, catalyzed by Pt catalysts.

Table 6.1. Results for the Heck reaction catalyzed by Pt@EVOH, calculated by GC using n–dodecane as an external standard. Conversion refers to iodobenzene **A9**. Between parentheses, isolated yields. Mass balance completed with bi-phenyl and benzene.

Base	**Conversion (%)**	**A11 (%)**
KOAc	100	93(86)
Bu_3N	<5	-
K_2CO_3	15	14
K_3PO_4	30	27
KO^{t}Bu	<5	-
KF	<5	-
Cy_2NMe	25	22

From the results above, it is clear that the reaction mechanism of the Heck coupling on Pd or Pt clusters is not straightforward. To spot the differences between the metals and unravel the mechanism, the four elementary steps of the traditional Heck reaction were studied by means of DFT calculations on Pd_3 and Pt_3 cluster models.

6.3.2. Mechanism of the Heck coupling by Pd and Pt clusters.

6.3.2.1. Reaction steps in the Heck coupling of iodobencene and n-butyl-acrylate.

Oxidative addition of iodobenzene.

Figure 6.3 shows that the most stable structure for the adsorption of the reactant iodobenzene is different in each cluster. For palladium, iodobenzene is preferentially adsorbed through the arene, face to face with the three metallic atoms (structure **8**), whereas for platinum the adsorption is produced in the edge of the cluster, either through the cycle or along the C-I bond (structure **9**). Other minima close in energy to **8** and **9** can be found for both clusters, but while for Pd_3 the same adsorptions along the edge found for Pt_3 are stable (structures **1** and **2**, about 5 kcal/mol higher in energy), the structure analogous to **8** with iodobenzene in the face of a Pt_3 cluster is almost 26 kcal/mol less stable (structure **16**).

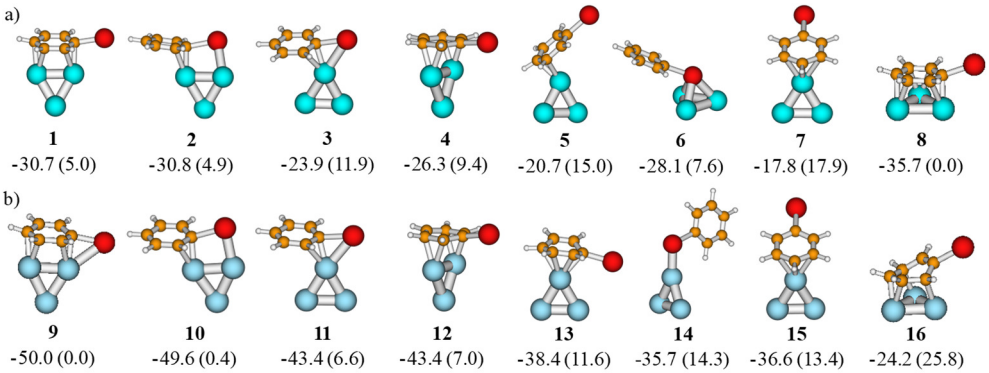

Figure 6.3. DFT optimized structures for the adsorption of iodobencene on Pd_3 (a) and Pt_3 (b) clusters. I atoms in red, C in amber, H in white. Electronic adsorption energies are shown, relative to the most stable structure in parenthesis (in kcal mol^{-1}).

Figure 6.4 shows that this difference in adsorption is readily explained by the shape of the HOMO and LUMO of each cluster. The interaction involves a charge transfer from the HOMO of of the molecule (characterized by a mixture of the p_z orbital of the I atom and π contributions from the ring) to the LUMO of the metal cluster, and also a back-bonding from the HOMO of the cluster to the LUMO of iodobenzene (σ*(C-I), centered along the C-I bond)[230]. The LUMO of Pd_3 lies lower in energy, enhancing the interaction, and it is spread in the face of the cluster hence matching the HOMO of iodobenzene and thus directing the adsorption of the molecule through the cycle towards this face. In spite of this, the adsorption energy is ultimately higher for Pt_3, presumably due to the rupture of the aromaticity in the benzene ring of iodobenzene upon planar adsorption on Pd_3.

Table 6.2 shows, surprisingly, very low activation energies for this elementary step from the most stable structures of adsorbed iodobenzene for both clusters: as low as 0.6 and 2.5 kcal mol^{-1} for Pd_3 and Pt_3, respectively. The imaginary mode of transition state **17** (Figure 6.5) rather involves the displacement of the molecule in the face of the cluster, but as soon as the iodine touches the palladium in this structure the molecule dissociates, and no intermediate could be stabilized prior to **18** nor any other TS more clearly showing the breaking of the C-I bond. Alternative paths from the close in energy minima similarly produce very low barriers (Figure 6.5). The largest barrier obtained, of 9 kcal mol^{-1}, is found for structure **9** of Pt_3, which is practically isoenergetic with structure **10**, but on which the breaking of the C-I bond takes place at the corner of one platinum atom instead of between two of them. In addition, the process is thermodynamically favored for both Pd_3 and Pt_3. Therefore, the oxidative addition proceeds with extreme ease in both clusters, but even more so on Pd_3.

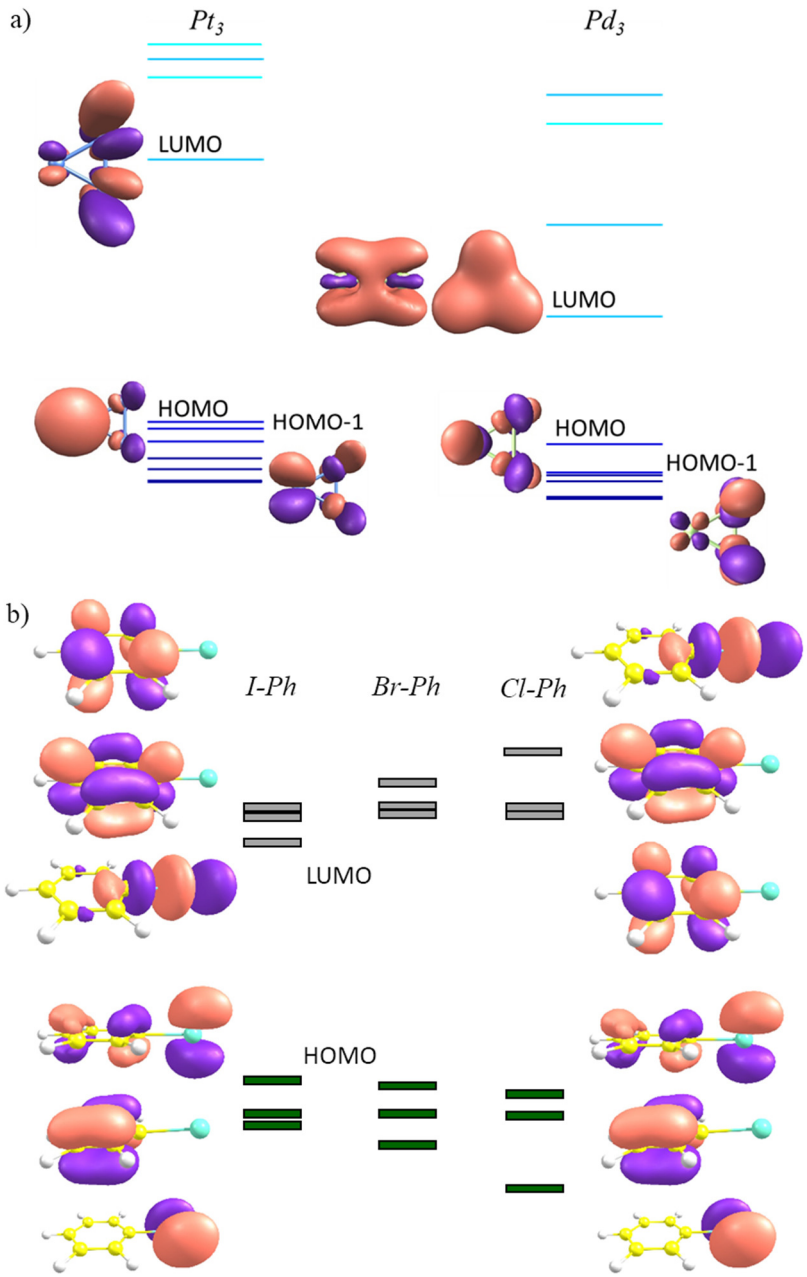

Figure 6.4. Molecular orbital distribution and composition of the highest occupied and lowest unoccupied molecular orbitals of a) Pt_3 and Pd_3 clusters calculated at the B3LYP/LANL2DZ level and b) Iodo-, Bromo- and Chlorobenzene adapted from ref. [230].

Table 6.2. DFT-calculated electronic adsorption energies of the reactants, $\Delta E_{ads}(R)$, activation energies, ΔE_{act}, and electronic reaction energies, ΔE_{reac}, for the elemental steps shown in Figures 6.5-6.7, 6.9 and 6.11 (in kcal mol^{-1}).

Path	Catalyst	$\Delta E_{ads}(R)$	ΔE_{act}	ΔE_{reac}
Oxidative addition				
1-[17]-18	Pd_3	-35.7	0.6 (2.2[a])	-26.1 (-14.2[a])
10-[25]-26	Pt_3	-49.6	2.5 (5.1[a])	-21.3 (-11.1 [a])
9-[27]-28		-50.0	9.1	-5.8
31-[32]-33	$PdCl_2$	-26.5	15.4	4.0
34-[35]-36	$PtCl_2$	-16.8	16.0	-11.7
37-[38]-39	Pd_1	-33.6	3.0	-18.4
40-[41]-42	Pt_1	-50.3	5.2	-34.3
Alkene insertion				
44-[45]-46	Pd_3	-36.3	30.2 (18.8[a])	-3.4 (-11.6[a])
48-[49]-50	Pt_3	-62.7	44.8 (27.2[a])	23.3 (-3.4[a])
β-elimination				
57-[58]-59	Pd_3	-	6.9	-12.7
60-[61]-62	Pt_3	-	3.9	-22.6
Reductive elimination with KOAc				
67-[68]-69	Pd_3	-	29.2	19.9
73-[74]-75	Pt_3	-	27.9	17.2
Reductive elimination with NMe_3				
70-[71]-72	Pd_3	-23.4	28.8	28.4
76-[77]-78	Pt_3	-44.1	40.6	28.7

[a]For the same paths including a co-adsorbed solvent molecule (Figures 6.13-6.14).

The oxidative addition step was also calculated on $PdCl_2$ and $PtCl_2$ to model the reactivity of Pd^{2+} and Pt^{2+} cations, and on reduced Pd_1 and Pt_1 single atoms (Figure 6.6, Table 6.2). The activation barriers on $PdCl_2$ and $PtCl_2$ are > 10 kcal mol^{-1} larger than on the corresponding reduced atoms, which in turn are ~ 3 kcal mol^{-1} higher than on Pd_3 and Pt_3 clusters. These values suggest that despite single atoms cannot be excluded as catalytic species, their reactivity is not higher than that of small clusters, consistent with the experiments with $Pt(acac)_2$[147].

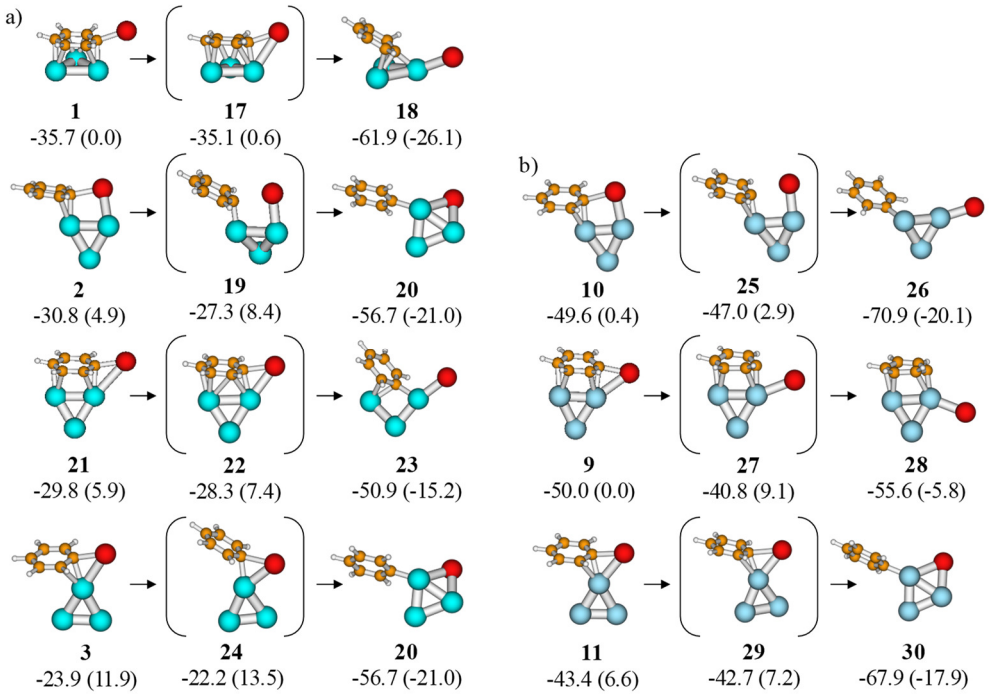

Figure 6.5. DFT optimized structures for the oxidative addition of iodobenzene on Pd_3 (a) and Pt_3 (b) clusters. I atoms in red, C in amber, H in white. Electronic adsorption energies are shown, relative to the most stable structure in parenthesis (in kcal mol^{-1}).

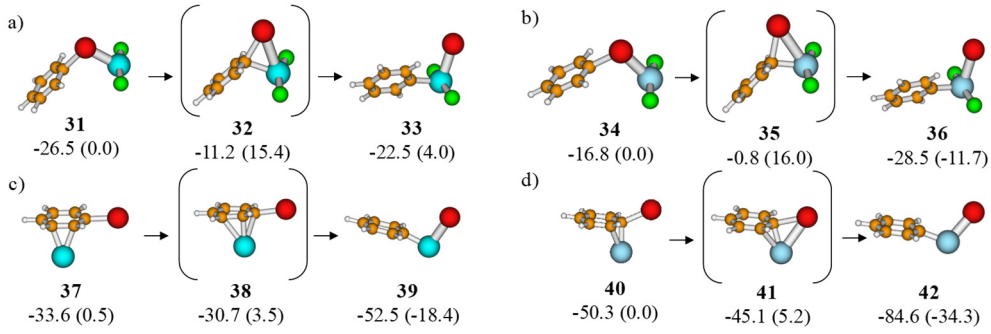

Figure 6.6. DFT optimized structures for the oxidative addition of iodobenzene to $PdCl_2$ (a), $PtCl_2$ (b), Pd_1 (c) and Pt_1 (d) single atoms. I atoms in red, C in amber, H in white, Cl in green. Electronic adsorption energies are shown, relative to the most stable structure in parenthesis (in kcal mol^{-1}).

Alkene migratory insertion and β-elimination.

Figure 6.7 shows the study for the alkene migratory insertion step, by adsorbing n-butyl-acrylate in the most stable product intermediates from the previous step. Adsorption structures where the acrylate only interacts through the double bond are found less stable than those where oxygen atoms also participate (Figure 6.8). Other more stable initial structures, by 9.4 and 7.2 kcal mol^{-1}, were respectively found for Pd_3 and Pt_3 (structures **43** and **47** in Figure 6.7), but the barriers obtained from them were much too high (more than 50 kcal mol^{-1}) and are not shown. Both the minima and the transition states of this step are similar in both metal clusters, and it can be seen that in the TS the acrylate moves towards the adsorbed phenyl and the mentioned interaction of its oxygen atoms is lost. As a result, the alkene insertion turns out to be a difficult process in both systems, and again more difficult on Pt_3 than on Pd_3 (see Table 6.2).

Then, the β-elimination step produces the final product, as shown in Figure 6.9. The abstraction of the hydrogen atom closest to the metal catalyst very clearly leads to the trans product isomer, but this stereospecificity comes from the previous adsorption mode of the n-butyl-acrylate to the metal. Indeed, the fact that minima are more stable when one of the oxygen atoms of the molecule also participates in the adsorption causes a steric impediment for any molecule coming from the cis side.

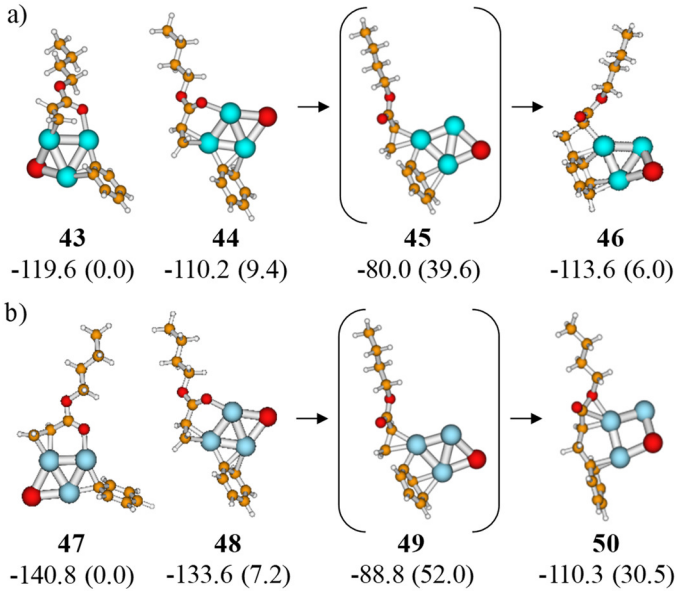

Figure 6.7. DFT optimized structures for the alkene insertion of iodobenzene to Pd_3 (a) and Pt_3 (b) clusters. I and O atoms in red (big and small, respectively), C in amber, H in white. Electronic energies w.r.t. E(cluster) + E(iodobenzene) + E(n-butyl-acrylate) are shown, relative to the most stable structure in parenthesis (in kcal mol^{-1}).

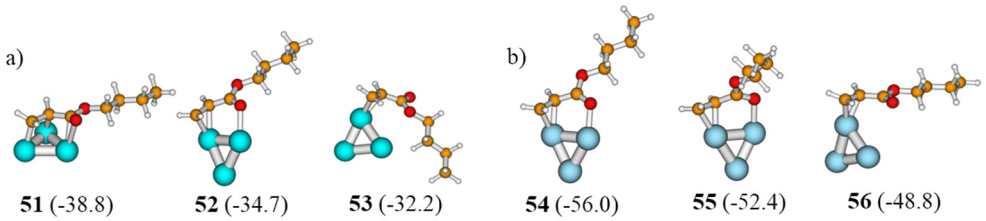

Figure 6.8. DFT optimized structures for the adsorption of n-butyl-acrylate on Pd_3 (a) and Pt_3 (b) clusters. O in red, C in amber, H in white. Electronic adsorption energies are shown (in kcal mol^{-1}).

Adsorption of a styrene molecule on the cluster (Figure 6.10) shows that this must also be the case for styrenes, as the participation of the aromatic cycle in the adsorption also stabilizes the system. As a result, in the coupling step the adsorbed phenyl always prefers the opposite side of the adsorbed double bond, thus leading to the trans product isomer much in agreement with experiment.

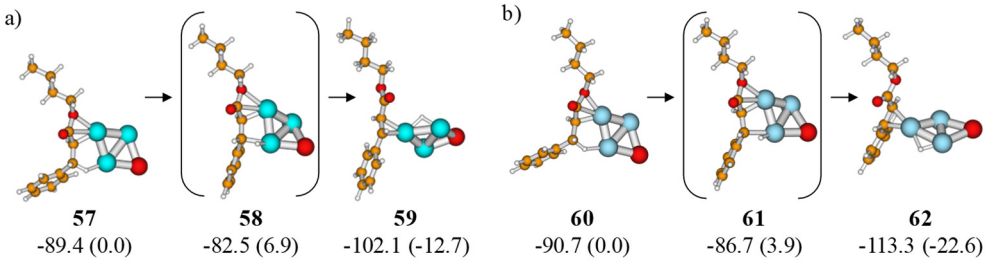

Figure 6.9. DFT optimized structures for the β-elimination step on Pd_3 (a) and Pt_3 (b) clusters. I and O atoms in red (big and small, respectively), C in amber, H in white. Electronic energies w.r.t. E(cluster) + E(iodobenzene) + E(n-butyl-acrylate) are shown, relative to the most stable structure in parenthesis (in kcal mol^{-1}).

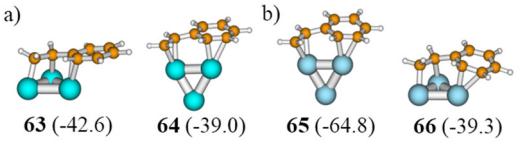

Figure 6.10. DFT optimized structures for the adsorption of styrene on Pd_3 (a) and Pt_3 (b) clusters. C atoms in amber, H in white. Electronic adsorption energies are shown (in kcal mol^{-1}).

Reductive elimination.

Finally, the last step of the coupling would be the recovering of the clean cluster catalyst in order to start a new cycle, which is achieved through a reductive elimination step by reaction with a base. Figure 6.11 models both acetate and trimethylamine (NMe_3, as a simplified model representative of Bu_3N), as the greatest differential behaviour between Pt_3 and Pd_3 lies in the inactivity of the former with Bu_3N. In the case of the acetate the iodine is removed, assuming its reaction with the K^+ cation.

The acetate does indeed adsorb on the metal cluster through the two oxygen atoms, whereas the trimethylamine produces a single interaction through its nitrogen atom. This step constitutes again a difficult process for both bases in both metal clusters, but a 10 kcal mol^{-1} higher barrier is obtained for Pt_3 with NMe_3 (see Table 6.2). The difference in these processes for the two metals lies in the increased adsorption of trimethylamine on the Pt_3HI intermediate as compared to that on Pd_3HI. Indeed, hydrogen and iodine preferentially adsorb in the facets of the palladium cluster, which leaves all metals atoms more coordinated than in platinum. Thus, although adsorption energies of reactants are consistently higher on Pt_3 (see Table 6.2 and Figures 6.5, 6.8 and 6.10), the adsorption energy of NMe_3 further increases by 6 kcal mol^{-1} when going from clean Pt_3 to Pt_3HI, whereas in the case of palladium it additionally decreases when going from the analogous Pd_3 to Pd_3HI, by 2 kcal mol^{-1} (Figure 6.12).

In the case of the acetate, the transition state does not require complete desorption of the base in neither system and similar barriers are produced for the two metals. Note that a higher adsorption energy for the resulting acetic acid on platinum is nevertheless also observed (−33.0 vs −19.9 kcal mol^{-1}).

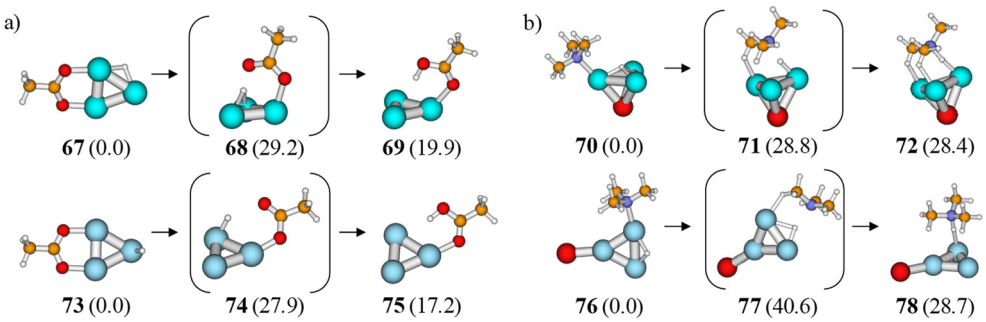

Figure 6.11. DFT optimized structures for the reductive elimination step with acetate (a) and trimethylamine (b) to Pd_3 (up) and Pt_3 (down) clusters. I and O atoms in red (big and small, respectively), N in dark blue, C in amber, H in white. Relative electronic energies are shown (in kcal mol^{-1}).

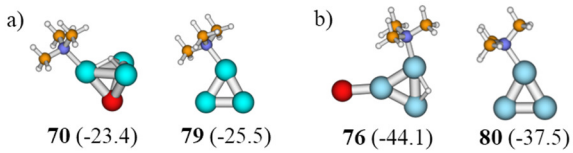

Figure 6.12. DFT optimized structures for the adsorption of NMe_3 on Pd_3 (a) and Pt_3 (b) clusters with HI previously adsorbed (left) or in the clean cluster (right). I and O atoms in red (big and small, respectively), N in dark blue, C in amber, H in white. Electronic adsorption energies are shown (in kcal mol^{-1}).

6.3.2.2. Proposed mechanism.

The surprising differences in the barriers for the first two elementary steps on the small clusters with respect to what is traditionally found for organometallics, with the oxidative addition not being the rds of the reaction, seem to be caused by the metallic nature of the catalytically active species, and by the additional participation of more than one metal atom in the process. Thus, while this produces the desired easier breaking of the C-I bond of iodobenzene, it also allows a higher stabilization of the fragments for the subsequent coupling and, as consequence, larger activation barriers are obtained for the alkene coupling step. However, notice that the inclusion of only one molecule of each pertinent reactant in our model neglects the effect that the co-adsorption of other reactant or solvent molecules might have on the reaction mechanism.

Indeed, it is reasonable to think that additional adsorbed molecules may favor recombination steps and may impede bond-breaking reactions. Furthermore, the relatively large adsorption energies of all reactants in both catalysts (Figures 6.5, 6.8 and 6.10) support the idea of clusters being surrounded by interacting molecules. With this in mind, we simulated as well the oxidative addition and the alkene insertion steps having one solvent molecule of NMP adsorbed on the cluster (Figures 6.13-6.14). The influence of one co-adsorbed solvent molecule on the oxidative addition

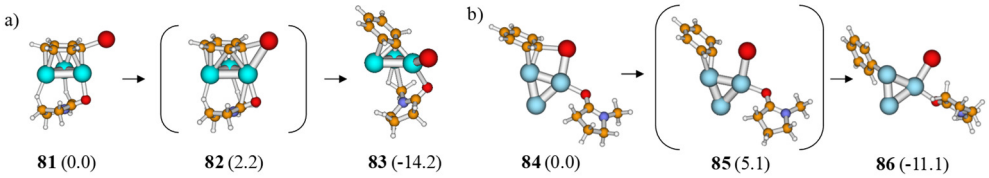

Figure 6.13. DFT optimized structures for the oxidative addition of iodobenzene to Pd_3 (a) and Pt_3 (b) clusters when a molecule of NMP is co-adsorbed. I and O atoms in red (big and small, respectively), N in dark blue, C in amber, H in white. Relative electronic energies are shown (in kcal mol^{-1}).

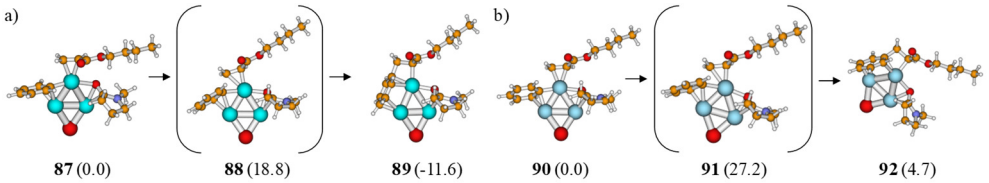

Figure 6.14. DFT optimized structures for the oxidative addition of iodobenzene to Pd_3 (a) and Pt_3 (b) clusters when a molecule of NMP is co-adsorbed (down) compared to in the clean clusters (up). I and O atoms in red (big and small, respectively), N in dark blue, C in amber, H in white. Electronic energies with respect to the reactive minimum (in kcal mol^{-1}) are given in parenthesis.

step is limited, since activation energy barriers only increase from 0.6 to 2.2 kcal mol^{-1} for Pd_3 and from 2.5 to 5.1 kcal mol^{-1} for Pt_3. In contrast, the large barrier corresponding to the alkene coupling decreases by more than 10 kcal mol^{-1} in both catalysts as soon as another molecule impedes the enhanced stabilization of the acrylate through its oxygen atoms.

Consequently, with the data presented here it is possible to conclude that i) the oxidative addition is not the rate-determining step of the reaction, ii) the β-elimination is not a complicated process on neither cluster either and iii) both the alkene insertion and the final reductive elimination step are two difficult processes in both Pt_3 and Pd_3 clusters. It is therefore not surprising that the rate of the reaction depends on what gives rise to the coupling parts of the alkene insertion, namely, [PhI] and [acrylate], and also on the base, [KOAc].

Following on the comparison between platinum and palladium, Figure 6.15 shows that while the mechanism is similar for Pt_3 and Pd_3 clusters, the alkene insertion and the reductive elimination by trimethylamine are particularly problematic for platinum (see Table 6.2). In both cases the key issue seems to be the enhanced adsorption of reactants on Pt_3. If one compares the structures and adsorption energies of all the reactants on clean clusters (Figures 6.5, 6.8 and 6.10), it is easy to see that iodobenzene and n-butyl acrylate generally interact with two atoms of the cluster. Thus, the comparable structures with two molecules of NMe_3 provide larger adsorption energies in the case of Pt_3 by 10 kcal mol^{-1} at the least (Figure 6.16).

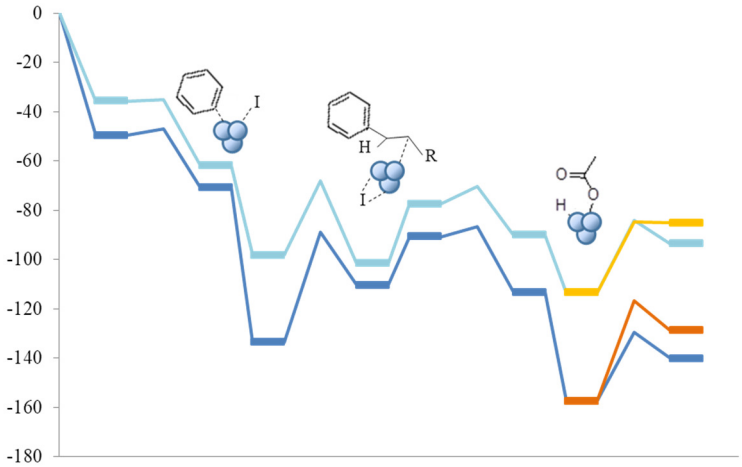

Figure 6.15. Energy profile for the reaction mechanisms explored for Pd_3 (light blue) and Pt_3 (dark blue) using KOAc as base. Yellow and orange lines correspond to the reductive elimination by NMe_3 in Pd_3 and Pt_3, respectively. Minima are indicated with rectangular markers. The adsorption energy of OAc is not known and its reductive elimination step was aligned to that of NMe_3.

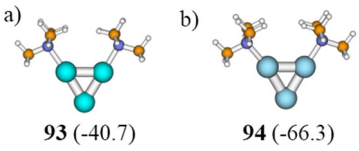

Figure 6.16. DFT optimized structures for the adsorption of two NMe_3 molecules on Pd_3 (a) and Pt_3 (b) clusters. N atoms in dark blue, C in amber, H in white. Electronic adsorption energies are shown (in kcal mol^{-1}).

The values are however much closer for all adsorbates in Pd_3, hence suggesting a poisoning by NMe_3 of the Pt_3 catalyst. This idea would also be in agreement with Cy_2NMe providing some activity, as its cyclohexyl groups would serve both as stabilizing agents of the molecule when desorbing to react and also as steric impediment to adsorb two molecules of base in close Pt atoms. Indeed, since all reagents bind more strongly to Pt_3, the interaction of the cluster with the base needs to be strong enough so as to be able to displace one and be near the adsorbed hydrogen atoms, but it should not be too strong or otherwise it would not be able to desorb and react. In such situation, the possibility of maintaining a certain degree of stabilization of the base upon reaction would greatly facilitate the process, and that is what is observed for the acetate, where one oxygen atom binds the molecule to the cluster while the other interacts with the hydrogen atom. Therefore, although not conclusive, these results point to the idea of a too strong adsorption of the base as the general cause for deactivation in Pt_3, and to the combined effect of adsorption and stabilizing (chelating) interactions of KOAc with the cluster as the key to ultimately catalyze the Heck reaction in this system. Pd_3, on the contrary, would not have any problem with the majority of bases because the adsorption energies of all reagents are similar and lower. This, in addition, would also explain the fact that higher concentrations of the acrylate also decrease the catalytic activity, for they would occupy the active sites impeding the adsorption and reaction of the base. In Pt_3, the bases seem to be the most strongly adsorbed species and a higher concentration of the acrylate only favors the difficult alkene migration step and leads to a higher reaction rate.

Figure 6.17 depicts the proposed mechanism for the Heck reaction catalyzed by subnanometer Pt clusters taking into account all the considerations commented above. The mechanism for Pd clusters would be analogous but extendable to other bases.

6.3.2.3. Oxidative addition of bromobenzene and chlorobenzene.

Given that very low energy barriers are obtained on both clusters for the oxidative addition of iodobenzene, and given the fact that the Heck reaction with bromoarenes also occurs with both palladium and platinum, we proceeded to study the oxidative addition of bromobenzene and clorobenzene to both clusters (Figure 6.18).

Table 6.3 shows that the interaction strength and thus the adsorption energy of the molecules slightly decrease from iodobenzene to bromobenzene and to chlorobenzene (see also Table 6.2). In addition, on Pt_3 the structures analogous to **10** for

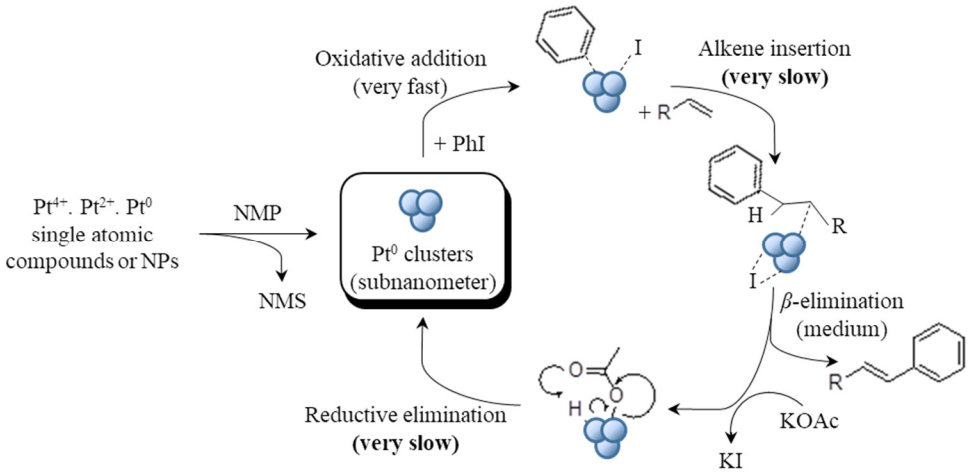

Figure 6.17. Proposed mechanism for the Heck reaction catalyzed by Pt clusters.

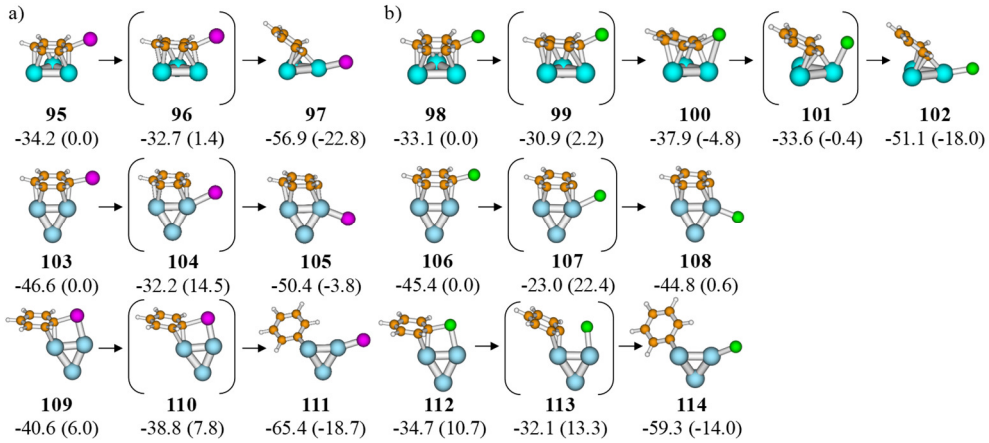

Figure 6.18. DFT optimized structures for the oxidative addition of bromobenzene (a, Br in magenta) and chlorobenzene (b, Cl in green) on Pd_3 (up) and Pt_3 (down).

bromobenzene and chlorobenzene become more unstable, much more for the latter (+6,0 and +10,7 kcal mol^{-1}, respectively). Both facts are again readily explained by looking at the HOMO and LUMO orbitals of each molecule (Figure 6.4). Indeed, while their HOMO levels are similar (characterized by the p_z orbital of the heteroatom and π contributions from the aromatic ring, as mentioned before), the σ*(C-X) LUMO increase in energy, hence weakening the back-bonding interaction with the metal, and also changes in nature. Thus, the σ*(C-X) orbital becomes increasingly destabilized in bromobenzene and more especially in chlorobenzene, for which an aromatic π* orbital becomes the LUMO. As a result, in going from iodobenzene to chlorobenzene the interaction is increasingly stabilized when the molecule adsorbs through the cycle (Figure 6.19).

Table 6.3. DFT-calculated electronic adsorption energies of the reactants, $\Delta E_{act}(R)$, activation energies, ΔE_{act}, and electronic reaction energies, ΔE_{reac}, for the oxidative addition of bromo- and chlorobenzene shown in Figures 6.18 and 6.20 (kcal mol^{-1}).

Path	Catalyst	$\Delta E_{ads}(R)$	ΔE_{act}	ΔE_{reac}
Oxidative addition of PhBr				
95-[96]-97	Pd_3	-34.2	1.4	-22.8
103-[104]-105	Pt_3	-46.6	14.5	-3.8
109-[110]-111		-40.6	1.8 (7.8[a])	-24.7 (-18.7[a])
131-[132]-133	Pd_1	-32.2	2.8	-13.6
134-[135]-136	Pt_1	-49.0	12.1	-28.4
Oxidative addition of PhCl				
98-[99]-100	Pd_3	-33.1	2.2	-4.8
100-[101]-102		-	4.3	-13.2
106-[107]-108	Pt_3	-45.4	22.4	0.6
112-[113]-114		-34.7	2.6 (13.3[a])	-24.6 (-14.0[a])
137-[138]-139	Pd_1	-31.0	7.8	-8.0
140-[141]-142	Pt_1	-47.7	18.2	-23.4

[a]From the most stable minimum.

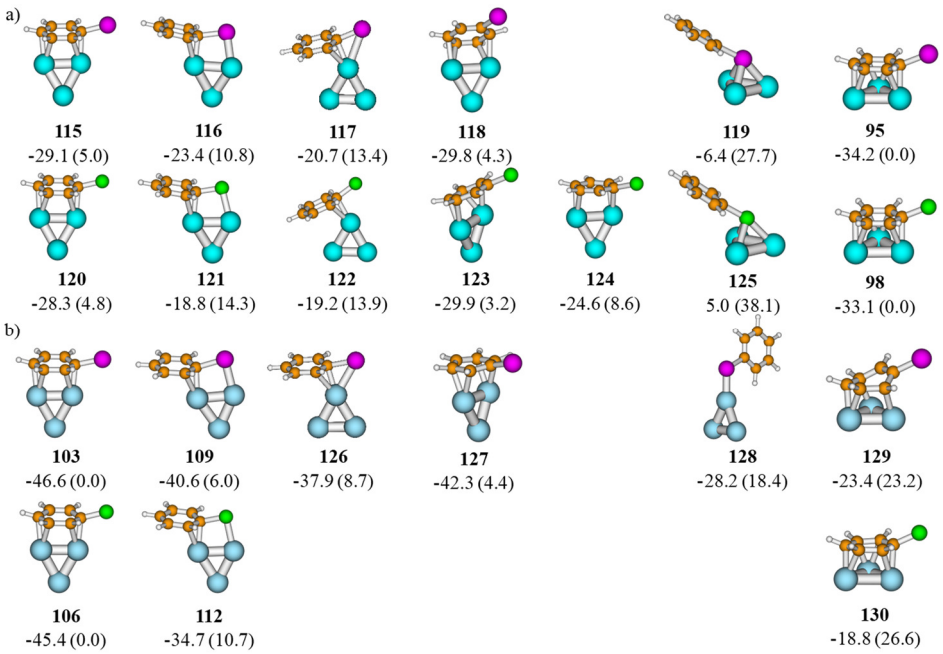

Figure 6.19. DFT optimized structures for the adsorption of iodobencene on Pd_3 (a) and Pt_3 (b) clusters. Br atoms in magenta, Cl atoms in green, C in amber, H in white. Electronic adsorption energies are shown, relative ones in parenthesis (kcal mol^{-1}).

While the activation energies for this elemental step follow the expected order according to the C-X bond strength, i.e. that of iodobenzene is lower than bromobenzene which is at the same time lower than that of chlorobenzene, activation energies are still strickingly low, especially for Pd_3 (Table 6.3, Figure 6.18). In the case of chlorobenzene on Pd_3, the increased strength of the C-X bond allows stabilizing an additional reaction intermediate and a transition state were the breaking of the bond is more clearly seen. Indeed, after a transition state **99** fully analogous to **17** and **96**, an intermediate structure with a bent chlorobenzene is found (**100**), whose C-Cl bond breaks through a transition state, **101**, that provides the highest barrier (4.3 kcal mol^{-1}). The fact that both structures **100** and **102** are more stable than initial reactant **98**, and the reasonable presumption of an analogous but lower barrier in the case of iodobenzene and bromobenzene, explains why the optimization of said structures always led to structures **18** and **97**, respectively.

For Pt_3, transition states **104** and **107** are analogous to **27**, whereas TSs **110** and **113** are analogous to **25**. The oxidative addition of chlorobenzene on Pt_3 is not kinetically nor thermodynamically favored, but in the case of bromobenzene, although structure **109** is 6.0 kcal mol^{-1} higher than structure **103** in energy, it also provides a much lower barrier, of only 1.8 kcal mol^{-1} (7.8 from the most stable mimimum). Therefore, although barriers are larger on Pt_3 with respect to Pd_3, according to these results the oxidative addition could also be possible for bromobenzene on Pt_3, consistent with the experimental results shown in the previous section.

In addition, theoretical calculations on the oxidative addition of bromo- and chlorobenzene to Pd and Pt single atoms show that, again, the latter cannot be excluded as active species but their activity is not greater than that of clusters, with barriers of 2.8 and 7.8 for Pd and of 12.1 and 18.3 for Pt (Figure 6.20, Table 6.3).

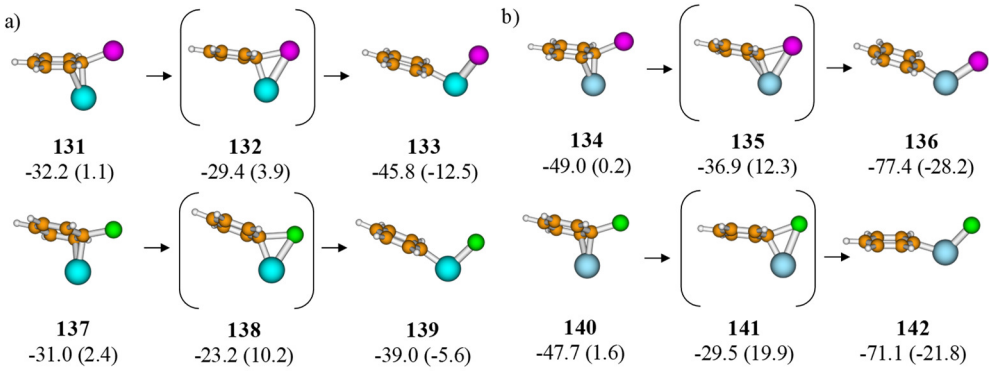

Figure 6.20. DFT optimized structures for the oxidative addition of bromo- and chlorobenzene to Pd_1 (a) and Pt_1 (b) single atoms. Br atoms in magenta, Cl in green, C in amber, H in white. Electronic adsorption energies are shown, relative to the most stable structure in parenthesis (in kcal mol^{-1}).

All in all, our theoretical studies show that the oxidative addition does not limit the Heck reaction on neither cluster nor single atoms, and that the chosen base has a larger impact on reactivity than was traditionally thought.

Consistent with the easy overcoming of the energy barrier computationally found for the oxidative addition of chlorobenzene by the Pd single atoms and clusters, the Suzuki coupling of aryl chlorides with different boronic acids was found to proceed well with Pd@EVOH and K_3PO_4 as a base[147]. These reaction protocols constitute a rare case of ligand-free metal activation of aryl chlorides for Suzuki cross-coupling reactions.

6.4. Conclusions.

DFT calculations show that the difficulty of the oxidative addition of halobenzenes is directly proportional to the strength of their C-X bond, i.e. barriers follow the order PhCl > PhBr > PhI for both palladium and platinum. Palladium species, however, always show smaller barriers than platinum, although those of $PtCl_2$ and $PdCl_2$ are more similar, higher than those of clusters and single atoms. The smaller barriers for Pd_3 can be explained by the lower energy of its LUMO and by its shape, which favors the adsorption of halobenzenes on the face through the aryl and also provides more stable TSs for the oxidative addition. Nevertheless, the barriers are very low for both Pd_3 and Pt_3, indicating that the oxidative addition of halobenzenes does not limit the Heck reaction, especially on Pd_3.

The β-elimination step is not a problem on either cluster, but it is found that both the alkene insertion and the final reductive elimination steps are difficult for Pd_3 and Pt_3. The latter are particularly problematic for Pt_3, and in both cases it seems to be due to the enhanced adsorption of reactants, specially the base. Thus, using acetate as base works because it avoids desorbing the base completely, allowing the elimination step to take place. In contrast, reagents on Pd_3 show lower and more similar adsorption energies, which leads to an efficient catalysis of the coupling with a wider variety of bases.

All in all, the combined experimental and computational study shows that the oxidative addition does not limit the Heck reaction on clusters nor single atoms of neither palladium nor platinum, translating the rds of the coupling to a later step where the base actively participates. Indeed, computational calculations indicate that an adequate balance of the adsorption strength of the base and its facility to undergo the reductive elimination step is key to catalyze the Heck reaction. With a suitable base, the ligand–free Pt–catalyzed Heck coupling of aryl iodides and bromides and the Pd–catalyzed Suzuki coupling of aryl chlorides were successfully carried out.

228

Chapter 7
CO + NO reaction by Pt clusters

The interest of the CO + NO reaction, much like CO oxidation, lies in reducing air pollution eliminating not only CO but also NO, through their oxidation and reduction, respectively. It is one of the reactions that takes place in internal combustion engines, at the so-called Three-Way Catalysts (TWC) that aim to convert CO, NO_x and unburnt hydrocarbons into less harmful CO_2, H_2O and N_2 species[348].

Recently, fellow researchers at the ITQ succeeded in the preparation of Au and Pt clusters of low atomicity stabilized inside a pure-silica zeolite, allowing the exploration of their application as catalysts for potential industrial applications such as the aerobic oxidation of cyclohexane to cyclohexanol and cyclohexanone or the propane dehydrogenation to propylene[349,350].

In the present chapter the joint study that continued this line of research is presented, showing that these Pt clusters stabilized in the pores of a zeolite are able to catalyze the NO reduction by CO at a temperature as low as 140 K[148].

7.1. Introduction.

The high temperature combustion of fuels in internal combustion engines favor the oxidation of N_2 from the air into nitrogen oxides (NO_x). Among them, NO_2 is an important pollutant, component of smog, that produces nitric acid when combined with water (thus being irritating), and NO can be readily oxidized in the atmosphere to NO_2 or disproportionate to NO_2 and N_2O, the latter of which is a greenhouse gas and catalyzes the breakdown of ozone (needed in the atmosphere to absorb UV rays). CO and unburnt hydrocarbons are also present in these engines, and Three-Way Catalysts (TWC) are employed to eliminate CO and NO_x and to oxidize the hydrocarbons at the same time. Since the NO_x need to reduce and the rest to oxidize, such catalysts work best at stoichiometric air/fuel conditions, oscillating between a lean (excess air) condition, when CO and hydrocarbon conversion is preferred, and a rich condition, when there is more fuel and the reduction of NO_x gets favoured[348].

These catalysts are traditionally made of a mixture of metals, most commonly rhodium and platinum or palladium, dispersed by impregnation on metal oxides of high porosity such as alumina to avoid the alloying of the different metals[348,351-355]. The support often participates in the reaction, and ceria and zirconia are in fact known promoters[282,348,355,356].

Searching for cheaper metal alternatives, smaller particles imply less precious metal used and hence more economic catalysts, which adds to the interest of the potential catalytic properties of clusters. The effect of a smaller particle size has already been reported for palladium, for which subnanometric Pd_n clusters with $n < 20$ have shown enhanced catalytic activity in the CO + NO reaction compared to larger particles and single crystals[357,358].

Naturally, the metal oxides used as support are all the more important in these catalysts, as exemplified by the recent work of Koga et al.[356], who found a lower activation energy barrier for NO dissociation (which is usually the rate-determining step of the reaction) on zirconia than on ceria for the three M_4 clusters studied (M= Rh, Pt, Pd). Due to all this, DFT-based studies on the reaction mechanism in metal clusters and single-atoms are increasingly reported[356,359-362].

In the present work, we aim to see whether such effect from small particle size is observed for platinum compared to larger particles. To this end, Dr. Patricia Concepción and Dr. Lichen Liu succeeded in the preparation of Pt clusters of low atomicity stabilized inside a pure-silica zeolite[350] and tested them in the CO + NO reaction. Their results, in combination to our DFT calculations, lead to the conclusion that Pt clusters are able to catalyze the NO reduction by CO at very low temperature[148].

7.2. Computational details.

7.2.1. Models.

Clusters of 4, 10, 13 and 38 atoms were considered, together with a Pt atom placed in the cavity of the MCM-22 zeolite and the Pt(111) surface, used to represent large nanoparticles.

We employed periodic models for all systems. Therefore, clusters (and molecules) were placed in a 20x20x20 $Å^3$ cubic box, large enough to avoid spurious interactions between periodically repeated systems. Then, Pt single atoms in MCM-22 were modeled by placing a Pt atom in the large cage of a pure silica model of the MWW crystalline structure, with lattice parameters a = b = 14.390 and c = 25.198 Å, and containing 216 atoms in the conventional unit cell (72 T and 144 O). Finally, the Pt(111) surface was simulated by means of a 3×3 supercell slab model consisting of 45 Pt atoms arranged in five atomic layers and separated by a vacuum region of 15 Å to avoid interaction between periodically repeated slabs.

7.2.2. Methods.

Structure optimizations were carried out at the Density Functional Theory (DFT) level with the VASP code[22,231], spin-polarized and using the PW91 functional of Perdew and Wang[157]. The valence density was expanded in a plane wave basis set with a kinetic energy cutoff of 500 eV, and the effect of the core electrons in the valence density was taken into account by means of the projected augmented wave (PAW) formalism[178]. In the reciprocal space, the integration was at the Γ k-point for the Brillouin zone for the clusters, the positions of all their atoms were fully optimized without any restriction and all stationary points were characterized by partial hessian frequency calculations with the atoms of the cluster fixed. For the Pt(111) model, integration in the reciprocal space was carried out using a 3×3×1 mesh of Monkhost-Pack[177] *k*-points, and during the geometry optimizations the positions of the adsorbates and of the Pt atoms of the two uppermost layers were allowed to fully relax. Finally, the Pt single atoms in MCM-22 were modeled by placing a Pt atom in the large cage of a pure silica model of the MWW crystalline structure, with lattice parameters a = b = 14.390 and c = 25.198 Å, and containing 216 atoms in the conventional unit cell (72 T and 144 O). Integration in the reciprocal space was carried out at the Γ k-point of the Brillouin zone, and the positions of all atoms in this model were fully optimized without restrictions.

All calculations are spin-polarized, and all stationary points were characterized by partial hessian frequency calculations in which the Pt atoms of the catalyst model were kept fixed. Transition states were located using the DIMER[185,186] or CI-NEB[187] algorithms. The Jmol[257], Avogadro[363,364] and MOLDEN[256] programs were used to build and visualize the systems and their frequencies during the work.

7.3. Results.

7.3.1. Background from experiments.

7.3.1.1. Catalyst preparation and structure characterization.

Subnanometric Pt species, including single Pt atoms (Pt-SA) and Pt clusters (Pt-CL) confined in MCM-22 zeolite, were synthesized following a new strategy[350], where the 12 ring "cups" (~0.7 nm) on the surface and the internal supercages (~0.7×1.8 nm) can stabilize those Pt species[365]. A different material containing larger Pt nanoparticles supported on mesoporous MCM-41 (Pt-NP sample) was synthesized by conventional wetness impregnation.

The three samples were characterized by high-angle annular dark-field high-resolution scanning transmission electron microscopy imaging (HAADF-HRSTEM imaging). Pt-SA sample mostly contains Pt single atoms together with a small fraction of Pt clusters with particle diameter below 0.7 nm. In the Pt-CL sample, subnanometric Pt clusters with diameter between 0.2 and 0.7 nm were mainly observed, as well as a few Pt single atoms. An average atomicity of 13 atoms was determined by extended X-ray absorption fine structure spectroscopy (EXAFS) performed on this sample. Finally, Pt nanoparticles with diameter ranging from 0.7 to 3.0 nm and an average particle size of 2.0 nm, were observed in the Pt-NP sample.

7.3.1.2. Catalytic studies with combined Infrared-Mass spectrometry.

The catalytic performance of the three Pt samples in the CO+NO reaction was followed by mass-spectrometry (MS) using a coupled IR-MS system that allows to obtain information of adsorbed species from the IR spectra acquired under *operando* conditions and, simultaneously, to analyze catalyst reactivity. Isotopically labeled ^{13}CO and ^{15}NO were used as reactants for identification of reaction products based on their mass signals[148].

At 200 K, the Pt-SA sample was initially inactive. $^{13}CO_2$ production started to be observed after 172 s, increasing slowly with reaction time. $^{15}N_2$ formation was only detected in very low amounts at ~623 s. The *ex situ* TEM experiments after the CO + NO reaction on Pt-SA sample show that agglomeration of Pt single atoms occurs, and after 850s of reaction Pt clusters and nanoparticles around 1 nm were formed.

For the Pt-CL sample, $^{13}CO_2$ was formed from the beginning of the reaction and its production remains stable with time, while $^{15}N_2$ evolution appeared delayed (between 313 and 490 s). Gas phase production of $^{15}N_2$ was below the stoichiometric value of 0.5 (i.e. $^{15}N_2/^{13}CO_2 \sim 0.2$).

In contrast, for the Pt-NP sample both $^{13}CO_2$ and $^{15}N_2$ were already detected in the first seconds of the reaction, while in this case the $^{15}N_2/^{13}CO_2$ ratio in the products was ~ 1.5. HAADF-HRSTEM images confirmed that no obvious sintering of Pt species under the present reaction conditions occurred on either Pt-CL or Pt-NP sample.

$^{13}CO_2$ production rates on the three samples at 200K at the initial reaction time (~100s, in red) and after 700s of reaction (in black) are plotted together in Figure 7.1.

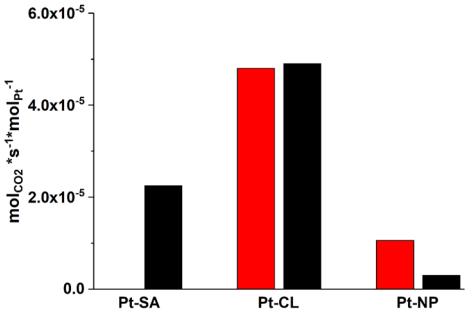

Figure 7.1. Activity of Pt catalysts for low-temperature NO reduction by CO. Initial $^{13}CO_2$ production rate (red bars) and reaction rate after 700 s of time on stream (black bars) at 200 K.

Pt-CL was initially almost 4-fold more active toward $^{13}CO_2$ formation than the Pt-NP sample. On the other hand, no activity was observed on Pt-SA sample at the beginning of the reaction, but after 700s its $^{13}CO_2$ production was close to that of Pt-CL. The latter reflects the sintering of Pt single atoms to larger particles, further confirmed by HAADF-HRSTEM images.

7.3.2. Mechanism of the CO + NO reaction by Pt clusters.

To understand the reaction mechanism of low-temperature CO + NO reaction on Pt species with different particle sizes, theoretical calculations with four clusters of different atomicity, Pt_4, Pt_{10}, Pt_{13} and Pt_{38} were considered, together with a Pt atom placed in the cavity of MCM-22, and a slab model of the Pt(111) surface to represent Pt NPs. The following elementary steps in the mechanism of the CO+NO reaction were considered:

$$NO \rightarrow NO^* \quad (1)$$
$$CO \rightarrow CO^* \quad (2)$$
$$NO^* \rightarrow N^* + O^* \quad (3)$$
$$O^* + CO^* \rightarrow CO_2 \quad (4)$$
$$2N^* \rightarrow N_2 \quad (5)$$

Equations (1) and (2) refer to the adsorption of reactants and (3) is the dissociation of NO yielding atomic species. Equation (4) represents the reaction of CO with atomic O forming the CO_2 product, and (5) corresponds to the recombination of atomic N forming N_2. In addition, alternative pathways in which NO and CO react directly (6), or in which atomic N* reacts with CO to form NCO (7) or with NO to form N_2O (8) that subsequently reacts with CO yielding the N_2 and CO_2 products (9) were theoretically investigated over each of the catalyst models.

$$NO^* + CO^* \rightarrow N^* + CO_2 \quad (6)$$
$$N^* + CO \rightarrow NCO^* \quad (7)$$
$$N^* + NO \rightarrow N_2O^* \quad (8)$$
$$N_2O^* + CO^* \rightarrow N_2 + CO_2 \quad (9)$$

Adsorption of only one CO or NO molecule on a Pt atom stabilized in the MCM-22 zeolite model is clearly exothermic, with calculated adsorption energies of -95 and -79 kcal mol^{-1}, respectively, and lead to the formation of a complex with a linear arrangement of the framework O, the Pt atom and the C or N atom of the CO or NO molecule (Figure 7.2a,b). However, co-adsorption of two molecules on the same Pt atom, forming di-carbonyl, di-nitrosyl or a Pt-CO-NO complex, would weaken the interaction between Pt atom and the framework O atoms. As a result, the linear unit containing the Pt atom and the CO and NO molecules would move to the centre of the cavity of MCM-22. Aggregation of two such units is clearly exothermic, and would explain the formation of clusters observed by STEM in the Pt-SA sample under reaction conditions (Figure 7.2d).

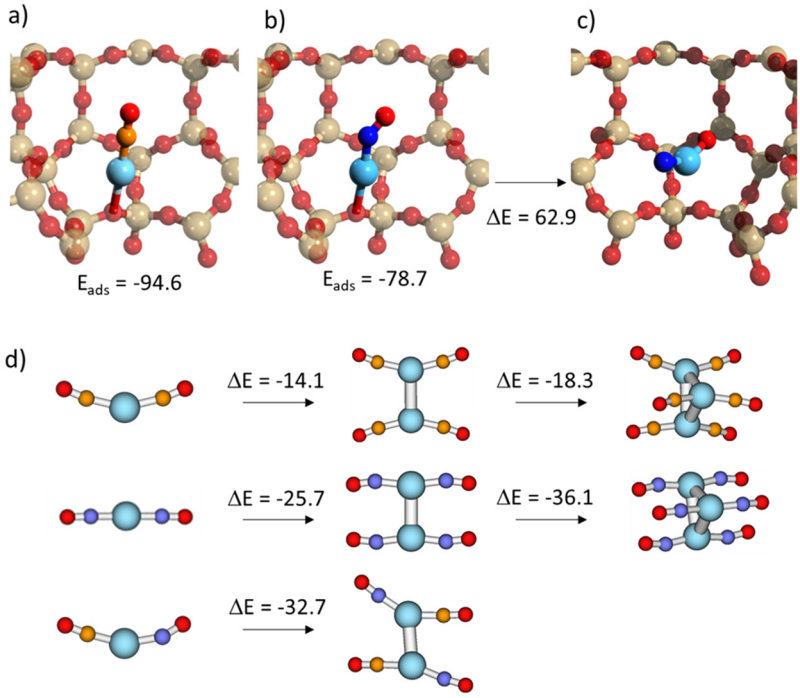

Figure 7.2. Optimized structures of a) adsorbed CO, b) adsorbed NO and c) product of NO dissociation on a Pt atom stabilized in MCM-22 zeolite. Adsorption (E_{ads}) and reaction energies (ΔE) are given in kcal mol^{-1}. d) Optimized structures of di-carbonyl, di-nitrosyl and Pt-CO-NO complexes and of the products of their aggregation, including the reaction energies involved (ΔE) in kcal mol^{-1}. Pt, N, C and O atoms are depicted in light blue, dark blue, orange and red, respectively.

In addition, the product of NO dissociation over a Pt atom in MCM-22 zeolite is more than 60 kcal mol^{-1} higher in energy than the corresponding initial reactant (Figure 7.2b,c), which would explain the initial lack of activity of the Pt-SA sample and confirms the previous hypothesis that Pt nanoclusters formed by agglomeration of Pt atoms are the working active species for the low-temperature CO + NO reaction.

In the case of subnanometric Pt clusters and Pt nanoparticles, CO preferentially adsorbs on top of low coordinated Pt atoms or in bridge positions between two Pt atoms, while NO forms a larger variety of complexes (Figures 7.3-7.4).

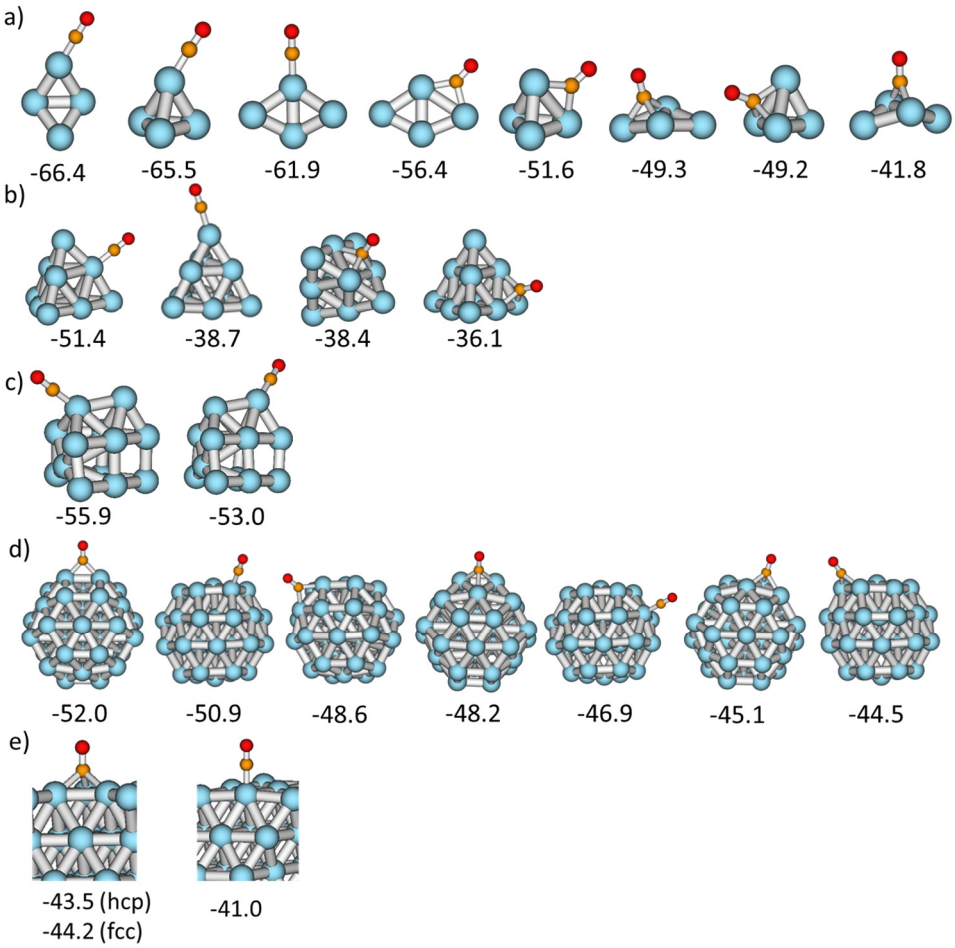

Figure 7.3. Optimized structures of the complexes formed by adsorption of CO on Pt_4 (a), Pt_{10} (b), Pt_{13} (c), Pt_{38} (d) and Pt(111) (e). Adsorption energies calculated as the energy difference in energy between the depicted adsorption complex and the sum of the energies of the clean particle and the CO molecule are given in kcal mol^{-1}. Pt, C and O atoms are depicted in light blue, orange and red, respectively.

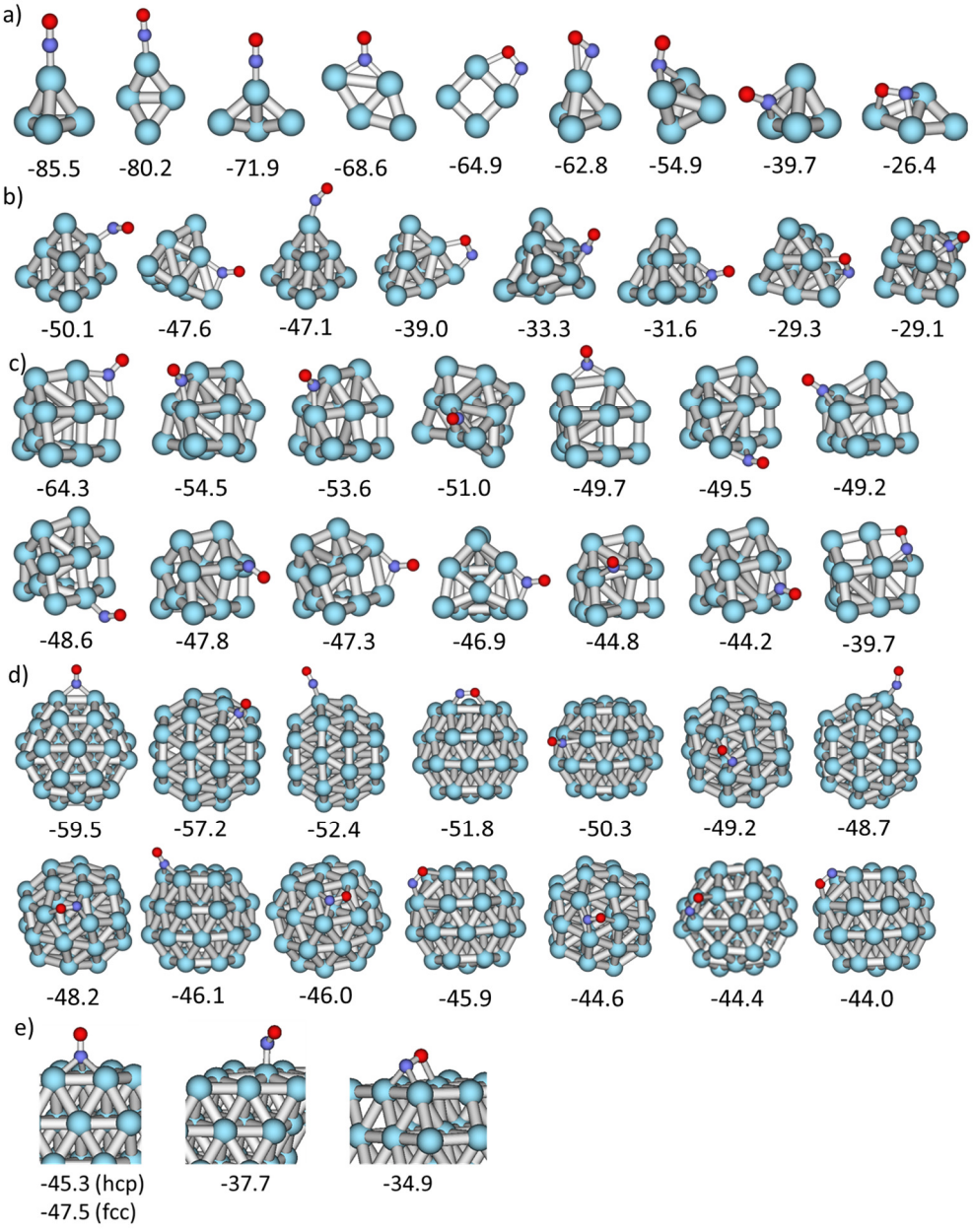

Figure 7.4. Optimized structures of the complexes formed by adsorption of NO on Pt_4(a), Pt_{10}(b), Pt_{13}(c), Pt_{38}(d) and Pt(111) (e). Adsorption energies calculated as the energy difference in energy between the depicted adsorption complex and the sum of the energies of the clean particle and the NO molecule are given in kcal mol^{-1}. Pt, N and O atoms are depicted in light blue, dark blue and red, respectively.

However, only some of these adsorption complexes, in particular bidentate species in which both N and O atoms are directly coordinated to Pt, lead to an adequate activation of the NO molecule and hence to its dissociation. The optimized structures of reactant $R_{(3)}$, transition state $TS_{(3)}$ and product $P_{(3)}$ involved in the unimolecular dissociation of NO over Pt clusters and nanoparticles are depicted in Figure 7.5, with the corresponding activation and reaction energies being summarized in Table 7.1 and Table 7.2.

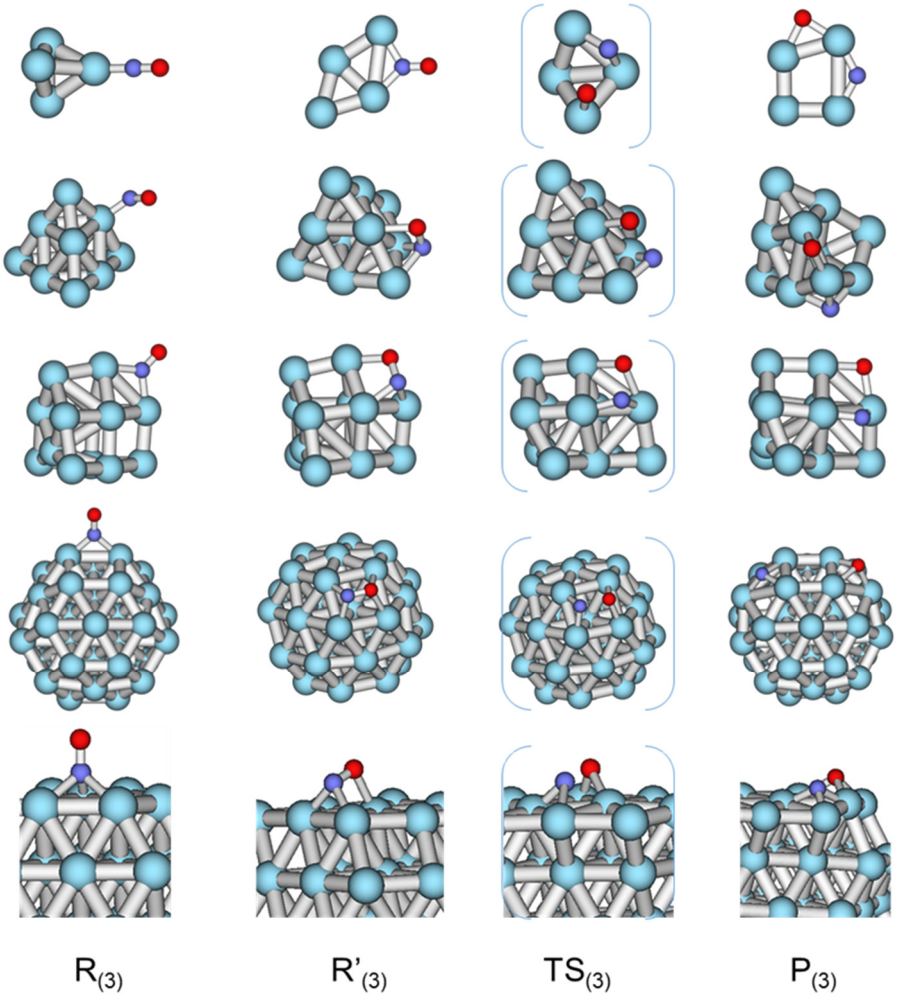

Figure 7.5. Optimized structures of reactant R, transition state TS and product P involved in the lowest energy pathways for NO dissociation (step 3) over Pt_4, Pt_{10}, Pt_{13} and Pt_{38} and Pt(111) catalyst models. Pt, N and O atoms are depicted in light blue, dark blue and red, respectively.

Table 7.1. Activation (ΔE_{act}) energies (in kcal mol^{-1}) for all elementary steps in the mechanism of CO + NO reaction over Pt clusters and nanoparticles, calculated as ΔE_{act} = E(TS) – E(R) (values in parenthesis are calculated as ΔE_{act} = E(TS)–E(R')). The structures involved are depicted in Figures 7.6, 7.8-7.10 and 7.12-7.15.

Step		Pt_4	Pt_{10}	Pt_{13}	Pt_{38}	Pt(111)
NO* → N* + O*	(3)	69.3 (52.5)	45.2 (24.4)	33.7 (9.1)	20.6 (7.1)	52.3 (39.7)
CO* + O* → CO_2	(4)	19.4	19.8	13.3	16.8	18.0
2N* → N_2	(5)	29.3 (22.2)	37.2 (27.2)	28.4 (22.0)	38.1 (5.8)	52.9 (21.5)
2N* → N_2 (high N*)	(5)			19.8	4.8	37.9
NO* + CO* → N* + CO_2	(6)	79.6	47.7	49.7	54.2	39.0
N* + CO* → NCO*	(7)	34.4 (29.8)	42.0	28.6	38.2 (24.9)	
N* + NO* → N_2O*	(8)	43.2 (25.1)	27.7	32.7 (19.1)	23.5 (22.5)	
N_2O* + CO* → N_2 + CO_2	(9)	33.1	33.1	33.8	26.8	

Table 7.2. Reaction (ΔE_{rea}) energies (in kcal mol^{-1}) for all elementary steps in the mechanism of CO + NO reaction over Pt clusters and nanoparticles, calculated as ΔE_{rea} = E(P) – E(R). The structures involved are depicted in Figures 7.6, 7.8-7.10 and 7.12-7.15.

Step		Pt_4	Pt_{10}	Pt_{13}	Pt_{38}	Pt(111)
NO* → N* + O*	(3)	17.4	4.6	15.7	-9.3	6.3
CO* + O* → CO_2	(4)	-0.3	0.4	-2.2	3.1	-15.4
2N* → N_2	(5)	-33.4	-44.6	-41.0	-10.3	-21.3
2N* → N_2 (high N*)	(5)			-71.9	-80.1	-104.1
NO* + CO* → N* + CO_2	(6)	48.8	18.5	23.2	3.3	0.6
N* + CO* → NCO*	(7)	1.5	11.4	9.1	20.0	
N* + NO* → N_2O*	(8)	32.3	-2.9	17.6	15.4	
N_2O* + CO* → N_2 + CO_2	(9)	-45.0	-30.9	-37.6	-35.8	

While in the most stable adsorption modes NO interacts with Pt only through the N atom forming one, two or three Pt-N bonds (structures $R_{(3)}$ in Figure 7.5), less stable conformations (structures $R'_{(3)}$ in Figure 7.5) in which O also interacts with Pt are always involved in the pathways for N-O bond dissociation. Such adsorption modes facilitate the transfer of electron density from the metal to the anti-bonding $2\pi^*$ orbital of NO, thus weakening the N-O bond and producing an elongation of the optimized NO distance from 1.17 Å in the gas phase to 1.21, 1.29, 1.32, and 1.34 and

1.25 Å on Pt_4, Pt_{10}, Pt_{13}, and Pt_{38} and Pt(111) models, respectively. In fact, an excellent linear correlation is obtained when activation energies for NO dissociation are plotted versus optimized NO distance in reactant structure $R'_{(3)}$ (Figure 7.6).

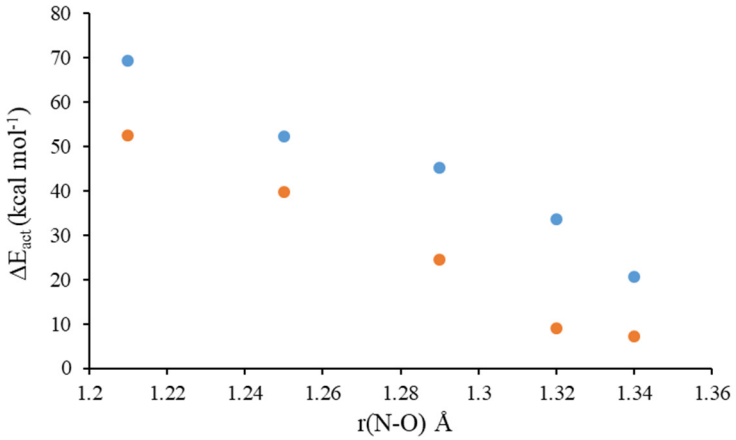

Figure 7.6. Correlation between the calculated activation energy for NO dissociation (from R (blue) and R' (orange)) over Pt models and the optimized NO bond length in the corresponding structure R'.

Moreover, in this conformation both O and N atoms are stabilized by the Pt surface in the transition states $TS_{(3)}$. Altogether, low activation energy barriers are obtained for Pt_{13} and Pt_{38} clusters when calculated with respect to $R'_{(3)}$ (E_{act} values in parenthesis in Table 7.2), while significantly higher values are found both on too small Pt_4 clusters and on large nanoparticles, in agreement with previous studies on Pt(111) catalysts[366,367]. It should be noted that when the E_{act} values are calculated with respect to the most stable adsorption complex $R_{(3)}$ the trend in the activation energies does not change, and intermediate Pt_{13} and Pt_{38} clusters are the most reactive. This trend is in excellent agreement with the IR *operando* results showing a faster ^{15}NO decomposition on Pt-CL as compared to Pt-NP. The reaction energies calculated with respect to the most stable $R_{(3)}$ system (Table 7.3) indicate that this step is exothermic only for Pt_{38}, and slightly endothermic for Pt_{10} and the Pt(111) surface model.

The second elementary step in the mechanism is the reaction of CO with adsorbed O atoms to form CO_2, step (4). In the reactant structure $R_{(4)}$, (Figure 7.7) CO adsorbs on the Pt atom directly in contact with a bi- or tri-coordinated O atom, and through a transition state structure $TS_{(4)}$ in which the O atom breaks one of the bonds with Pt while forms a new one with C, the product $P_{(4)}$ corresponding to a bent CO_2 molecule is obtained. The activation energies, between 13 and 20 kcal mol^{-1}, are lower than those previously obtained for NO dissociation (Table 7.2), indicating that the reaction of CO with adsorbed O is not the rate determining step of the process, while the

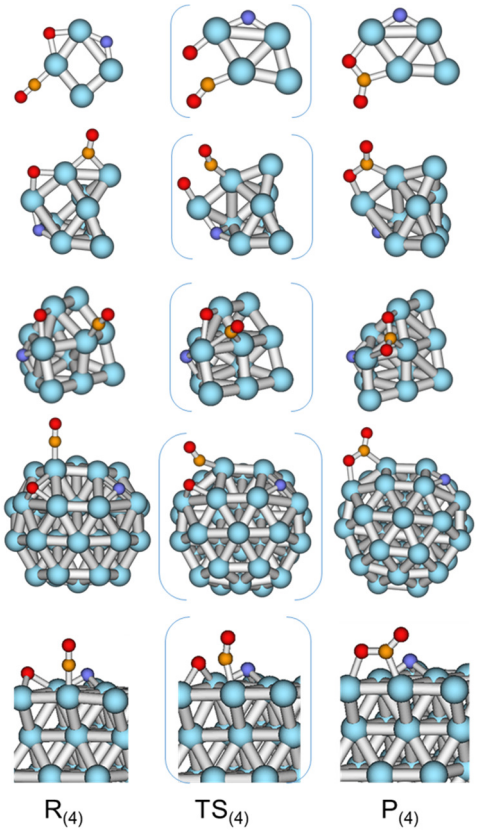

Figure 7.7. Optimized structures of reactant R, transition state TS and product P involved in the lowest energy pathways for CO reaction with atomic O (step 4) over Pt_4, Pt_{10}, Pt_{13}, Pt_{38} and Pt(111) catalyst models. Pt, N, C and O atoms are depicted in light blue, dark blue, orange and red, respectively.

calculated reaction energies indicate that this step is almost thermoneutral for all Pt catalyst models considered (Table 7.3). An alternative pathway involving the direct reaction of co-adsorbed NO and CO to produce, in one step, CO_2 and atomic N was also considered, as described in step (6). Starting from one CO and one NO molecule adsorbed close in stable conformations (structures labelled $R_{(6)}$ in Figure 7.8), transition states $TS_{(6)}$ were obtained in which the O atom of NO attacks the C atom of CO, forming a N-O-C-O system with strong interaction with Pt. The activation barriers for this processes are high, being close to 80 kcal mol^{-1} on the smallest Pt_4 cluster, around 50 kcal mol^{-1} on the rest of the clusters, and almost 40 kcal mol^{-1} on the Pt(111) model (Table 7.2). The calculated reaction energies indicate that this step becomes more thermodynamically favourable as the Pt particle size increases. In any case, except for the perfect Pt(111) surface, the calculated activation energies for step (6) are clearly higher than those previously obtained for the monomolecular NO dissociation according to (3), especially for Pt_{13} and Pt_{38} clusters, suggesting a low contribution of the bimolecular pathway to the activation and dissociation of NO over Pt catalysts.

To further clarify this point, the following experiments were performed in the coupled IR-MS system. Pt-CL and Pt-NP samples were exposed to ^{15}NO at 140 K for 30min, followed by evacuation at 10^{-5} mbar and annealing in vacuum at 213 K, until no IR bands associated to any adsorbed ^{15}NO species were observed in the IR spectra. Then the samples were cooled down to 140 K and subsequently exposed to ^{13}CO. $^{13}CO_2$ was immediately formed on both Pt-CL and Pt-NP samples, thus demonstrating that the presence of adsorbed O atoms unambiguously arises from ^{15}NO dissociation and can further react with ^{13}CO to form $^{13}CO_2$. These experiments confirm the contribution of the NO dissociative pathway in the reaction mechanism and that the

reaction of ^{13}CO with atomic O to form $^{13}CO_2$ is not the rds in the global reaction mechanism. Moreover, the $^{13}CO_2$ formation on the Pt-NP sample was found to be ~5-fold lower than on the Pt-CL sample, indicating a lower concentration of adsorbed O atoms on the Pt-NP, consistent with the higher activation barrier for NO dissociation obtained on Pt(111) model. To our knowledge, this is the first time where NO dissociation at such low temperature has been directly observed on metal catalysts.

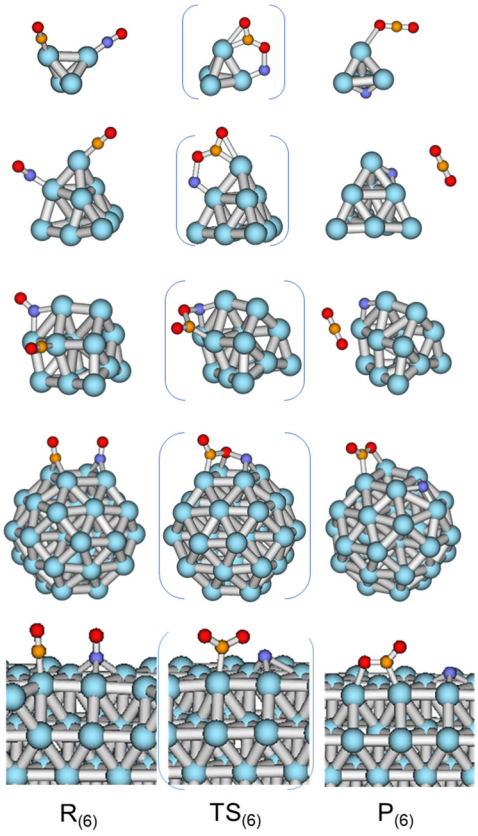

Figure 7.8. Optimized structures of reactant R, transition state TS and product P involved in the direct reaction between co-adsorbed NO and CO to produce CO_2 and atomic N (step 6) over Pt_4, Pt_{10}, Pt_{13}, Pt_{38} and Pt(111) catalyst models. Pt, N, C and O atoms are depicted in light blue, dark blue, orange and red, respectively.

The last step in the global mechanism is the recombination of two adsorbed N atoms to form N_2 and then desorption from the catalyst, as described by equation (5). The optimized structures of the species involved in this elementary step are depicted in Figure 7.9. In all cases, N atoms preferentially occupy distant 3-fold positions (bridge in the case of Pt_4) on the Pt cluster or nanoparticle surface, structures labelled $R_{(5)}$, and they have to become closer and move to bridge positions, structures labelled $R'_{(5)}$, in order to start the recombination process. The calculated activation energy over the smallest Pt_4 cluster is much lower than that found for NO dissociation, step (3), no matter whether it is related to minimum $R_{(5)}$ or $R'_{(5)}$. On the other catalysts, however, the activation barriers for N_2 formation are comparable to those obtained for NO dissociation, slightly lower on Pt_{10} and Pt_{13} clusters, higher on Pt_{38} model, and nearly the same on Pt(111) surface (Table 7.2), this last value being in excellent agreement with previous reports[367,368]. But in contrast to NO dissociation, the N_2 formation step is clearly exothermic for all catalyst models considered (Table 7.3). Taking into account the experimentally observed delay in the production of $^{15}N_2$ on Pt-CL sample, and the fact that gas phase production of $^{15}N_2$ is below the stoichiometric value, it seems that N_2 recombination and desorption is the rate determining step of the global process.

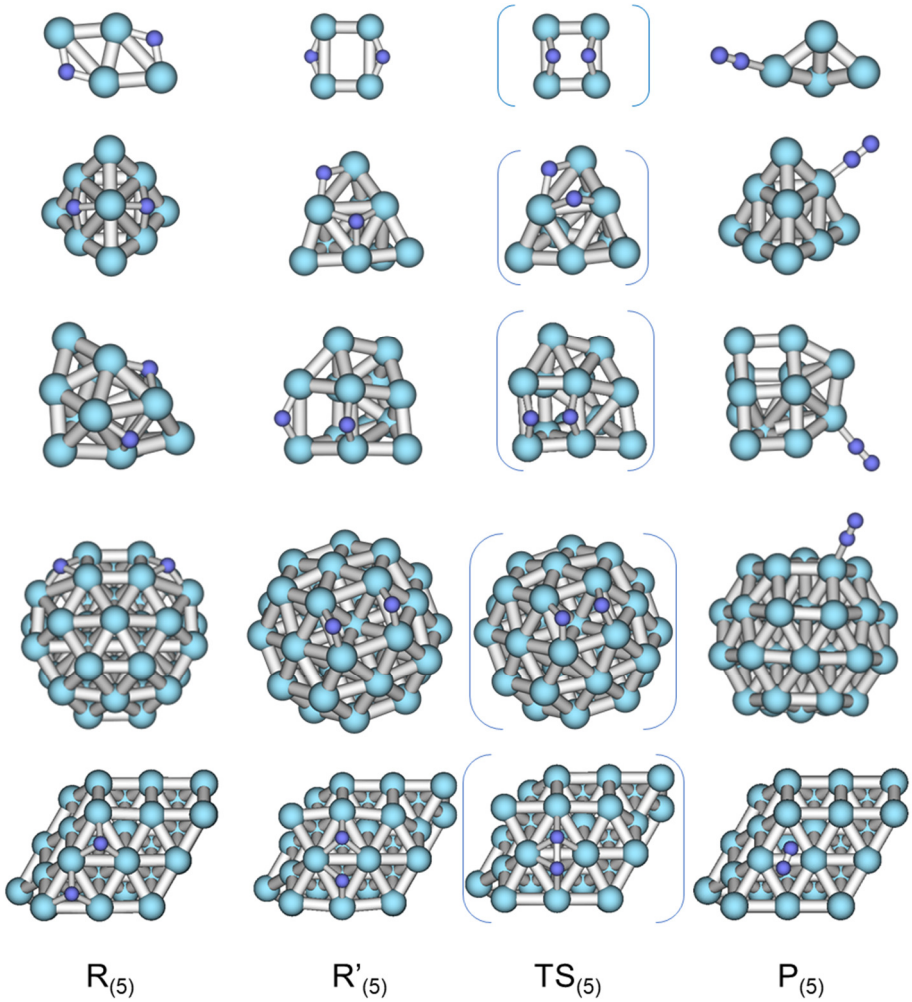

Figure 7.9. Optimized structures of reactant R and R', transition state TS and product P involved in the lowest energy pathways for recombination of atomic N to form N_2 (step 5) over Pt_4, Pt_{10}, Pt_{13}, Pt_{38} and Pt(111) catalyst models. Pt and N atoms are depicted in light and dark blue, respectively.

To prove that point, a N_2-desorption experiment with the Pt-CL sample was carried out. Firstly, the Pt-CL sample was exposed to ^{15}NO at 140 K for 30 min, and then evacuated at 10^{-5} mbar, and annealed in vacuum up to 213 K. Afterwards, the Pt-CL sample was again cooled down to 140 K and exposed to an Argon flow. Then the temperature was gradually increased with a rate of 2 K min^{-1} and gas phase species were analyzed by mass spectrometry. As shown in Figure 7.10, $^{15}N_2$ evolution was observed at 240 K, indicating that a slow N_2 recombination should be responsible for the observed delay in the $^{15}N_2$ production on the Pt-CL sample.

According to the pathway proposed by DFT, it is key to force N atoms to become closer in order to recombine into N_2, and a possible way to achieve that is increasing the surface coverage of adsorbed N* species. To check this point, additional calculations were performed for step (5) on Pt_{13}, Pt_{38} and Pt(111) catalyst models with a higher N* coverage (Figure 7.11).

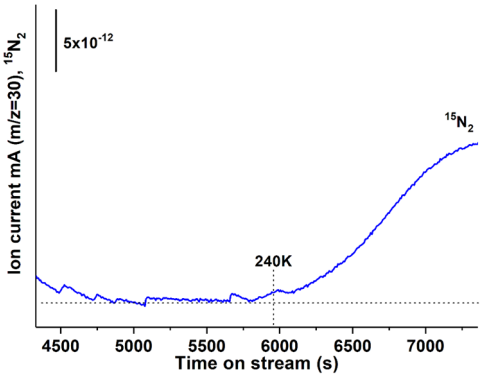

Figure 7.10. $^{15}N_2$ desorption experiment in the Pt-CL sample (see text for details).

As expected, the presence of other N species adsorbed close to the N atoms forces them to leave the stable 3-fold positions and approach each other, leading to a significant decrease in the activation energies and to a clear enhancement of the exothermicity of the process (Tables 7.2 and 7.3).

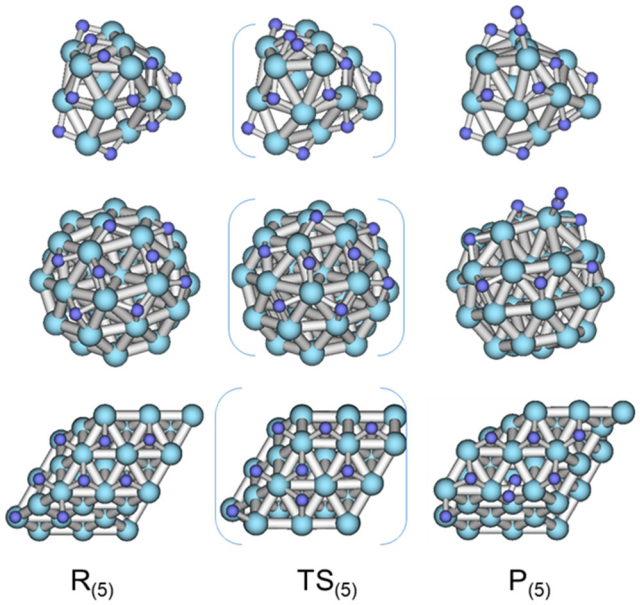

Figure 7.11. Optimized structures of reactant R, transition state TS and product P involved in the lowest energy pathways for recombination of atomic N to form N_2 (step 5) over Pt_{13}, Pt_{38} and Pt(111) catalyst models with a high surface N* coverage. Pt and N atoms are depicted as light and dark blue balls, respectively.

Since the catalyst surface becomes covered by atomic N in the first stage of the CO + NO reaction, we considered the possibility that adsorbed N atoms could react with CO yielding NCO (eq. (7)) or with NO to produce N_2O (eq. (8)) (Figures 7.12-7.13).

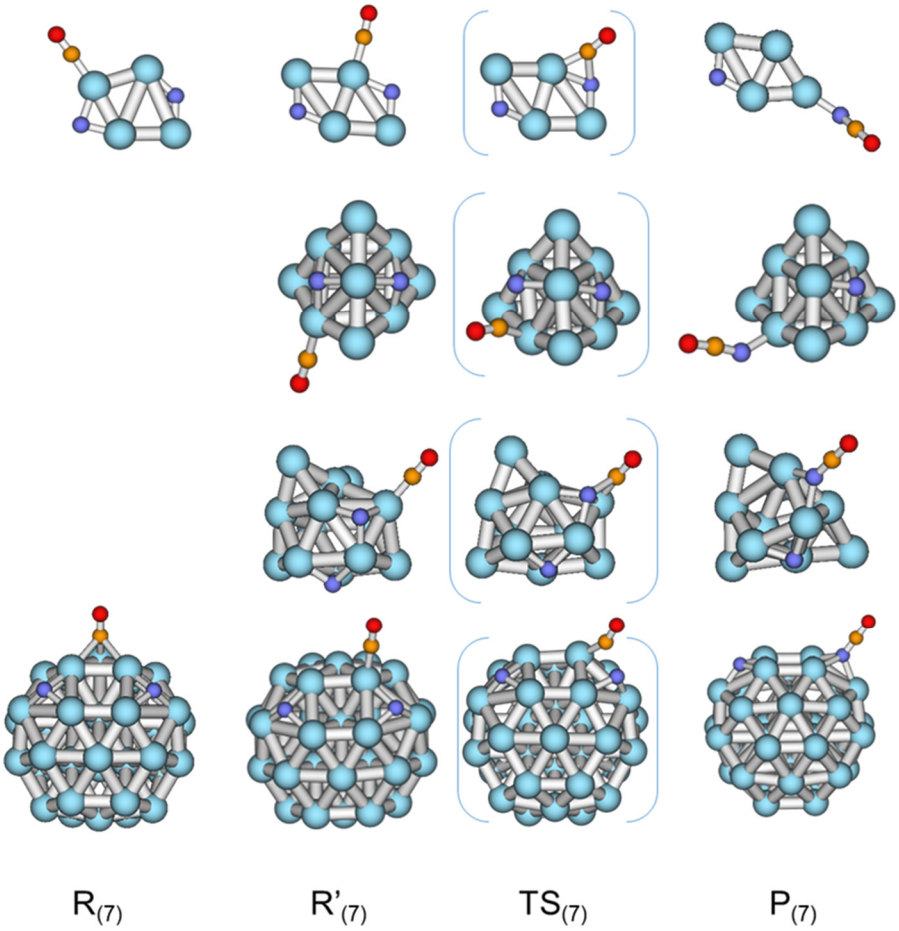

Figure 7.12. Optimized structures of reactant R and R', transition state TS and product P involved in the reaction of CO reaction with atomic N to form NCO (step 7) over Pt_4, Pt_{10}, Pt_{13} and Pt_{38} catalyst models. Pt, N, C and O atoms are depicted in light blue, dark blue, orange and red, respectively.

The activation energies for the reaction of CO with adsorbed N atoms are 15-20 kcal mol^{-1} higher than those previously reported for the reaction of CO with adsorbed O yielding CO_2 (Table 7.2) and the reaction energies are positive in all cases (Table 7.3), suggesting that formation of NCO will only occur in the absence of atomic O on the catalyst surface. In contrast, comparison of the activation and reaction energies obtained for NO reaction with N atoms with those calculated for NO dissociation according to equation (3) suggest that N_2O formation will be competitive on all Pt cluster models containing adsorbed N*. In fact, N_2O is observed in the *operando* IR study on all samples.

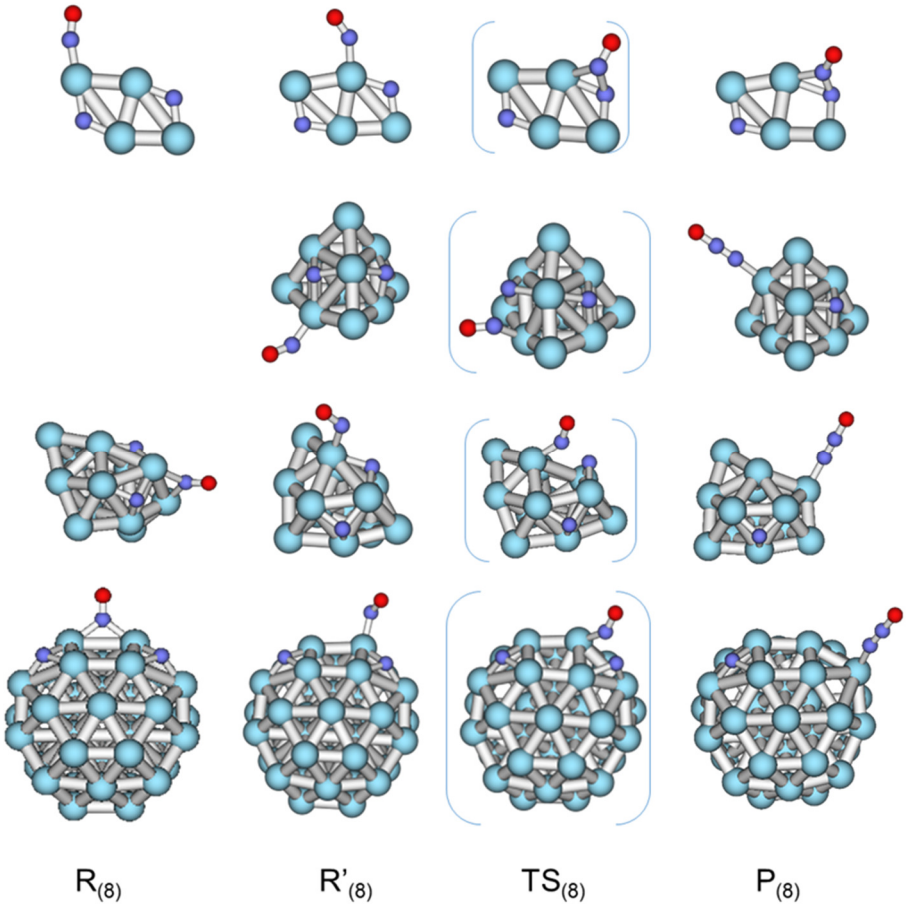

Figure 7.13. Optimized structures of reactant R and R', transition state TS and product P involved in the reaction of NO with atomic N to form N_2O (step 8) over Pt_4, Pt_{10}, Pt_{13} and Pt_{38} catalyst models. Pt, N and O atoms are depicted in light blue, dark blue and red, respectively.

The N_2O formed on the Pt clusters could further react with CO producing CO_2 according to equation (9). The process occurs, over all Pt cluster models, through a similar cyclic transition state in which the O atom of N_2O attacks the CO carbon atom bonded to one Pt site, while the terminal N atom of N_2O is attached to an adjacent Pt atom (Figure 7.14). The activation energies, around 30 kcal mol^{-1}, are only slightly higher than those involved in the formation of N_2O, and the step is clearly exothermic for all cluster with different sizes. Thus, the pathway involving the formation of N_2O according to (8) and its subsequent reaction with CO as described by (9) could also contribute to the overall reaction.

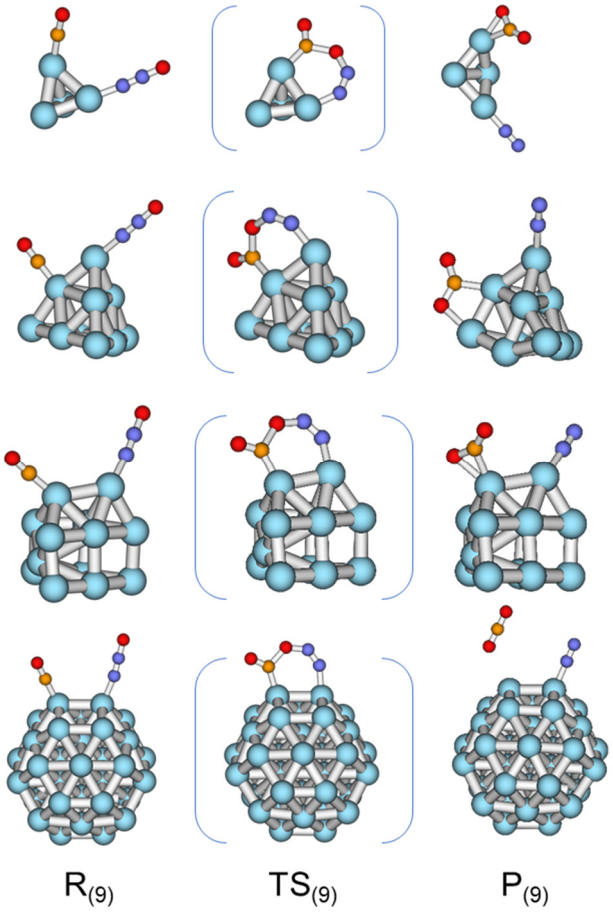

Figure 7.14. Optimized structures of reactant R, transition state TS and product P involved in the direct reaction of N_2O with CO to form N_2 and CO_2 (step 9) over Pt_4, Pt_{10}, Pt_{13} and Pt_{38} catalyst models. Pt, N, C and O atoms are depicted in light blue, dark blue, orange and red, respectively.

7.4. Conclusions.

According to DFT calculations it can be concluded that single atoms, too small clusters and too large nanoparticles cannot dissociate the NO molecule either monomolecularly (3) nor by direct reaction with CO (6), whereas medium-sized clusters can, with the monomolecular pathway being preferred.

The active clusters stabilize the NO molecule interacting not only with their N atom but also through their O atom, in (111) and (100) facets, thus activating the molecule and stabilizing the TS corresponding to its dissociation. In contrast, single atoms and

the smallest clusters cannot stabilize the TS nor the separated N nor O atoms, and larger particles do not interact as well with the molecule on their facets, leading to a smaller elongation of the NO bond and yielding significantly higher energy barriers.

The CO* + O* reaction (4) is easy on all Pt species, whereas the formation of N_2 via recombination of the adsorbed N* atoms produced in the dissociation of NO (5) is another difficult step of the mechanism. Indeed, for the active medium-sized clusters the latter is the rate-determining step of the CO + NO reaction.

Finally, the reaction of adsorbed N* atoms with NO to produce N_2O (8) and the subsequent reaction of the latter with CO (9) to produce CO_2 and N_2 is also possible in these medium-sized clusters, and hence might contribute to the global reaction.

All of these conclusions are consistent with the experimental results presented and, altogether, they show that the CO + NO reaction to produce CO_2 and N_2 can occur on stabilized Pt clusters at low temperature.

Conclusions

Regarding the studies on copper clusters, we firstly studied the adsorption and dissociation of the O_2 molecule in Cu_n clusters of size n=3-8, 13 and 38 at different computational levels (Chapter 3), showing that even using different methods trends are similar, ultimately reaching the same qualitative conclusions.

The O_2 interaction with copper clusters involves a transfer of electron density from the metal HOMO to the anti-bonding π^* of O_2, so that the O-O bond weakens and hence activates more the stronger the interaction. The calculated adsorption energies correlate with the HOMO energy of the isolated clusters, and the degree of O-O bond activation, indicated by the optimized r_{OO} distances or the shifts in the ν_{OO} vibrational frequencies, directly correlates with the net charge on adsorbed O_2. More importantly, the activation is determined by the mode of adsorption of O_2 on the copper clusters, for adsorption on 100 or 111 facets allows a larger degree of electron density transfer than adsorption at corners or edges in *bridge*, *mono* or *top* conformations.

The role of particle morphology is thus key because it determines the preferential mode of adsorption of O_2, with the most activating *h-100* and *h-111* modes being preferentially stabilized over 3D clusters. Since smaller clusters are planar, particle size affects because it implies changes to particle shape. Thus, Cu_3, Cu_4 and Cu_5, which are planar, present activation energies to dissociate O_2 larger than 40 kcal mol^{-1}, whereas barriers around ~ 15 kcal mol^{-1} are found for 3D clusters with n = 5-8, and decrease to 6-10 kcal mol^{-1} over larger Cu_{13} or Cu_{38} nanoparticles.

Theoretical kinetic studies and experimental XPS and SERS studies for Cu_5, Cu_8 and Cu_{13} further show the differential behaviour of small Cu_5 clusters, being less susceptible to be oxidized with respect to larger clusters, and also more easily reduced back to metallic copper. Therefore, it seems possible to stabilize metallic copper clusters under oxidizing reaction conditions by adjusting the atomicity of the copper cluster.

Similarly, theoretical and experimental data have shown that the reactivity of Cu_5 (and Cu_8) clusters toward oxygen dissociation is strongly enhanced in the presence of water. In the case of 3D Cu_5 the interaction of the resultant oxygen species with the copper cluster is in addition lower than for the rest, favouring oxygen recombination and O_2 desorption, in agreement with experiment.

Since Cu_5 clusters seem promising candidates for catalytic applications where stabilization of metallic copper species is required, we explored the CO oxidation reaction theoretically (Chapter 4), and it is concluded that all clusters studied, namely, planar Cu_5, 3D Cu_5 and Cu_8, are able to catalyze the CO oxidation reaction. The highest activation energy among the steps of the lowest energy pathway for each of them is similar and of about 16-18 kcal mol^{-1}. Planar Cu_5 presents the lowest barrier, but it will not represent a great difference in terms of efficiency. However, its reaction mechanism is different compared to that of 3D clusters.

In the mechanisms of 3D Cu_5 and Cu_8 the O_2 molecule is dissociated first, even in the presence of adsorbed CO, and then two CO molecules react with the resulting O atoms, and the second O + CO step is the rds. In contrast, since planar Cu_5 does not catalyze O_2 dissociation, the reaction proceeds forming a OOCO intermediate first, whose O-O bond is broken in a second step. The O atom that remains is bicoordinately adsorbed, which lowers the activation energy needed for the final O + CO ER step. As a result, the rds of the reaction is the formation of the OOCO intermediate instead.

It is also found that planar Cu_5 seems prone to deformation towards 3D Cu_5 with a high pressure of CO, although such effect would not diminish the catalytic activity of Cu_5 clusters, since 3D Cu_5 is equivalently active. For Cu_8 clusters, however, subsequent oxidation reactions at other available facets are likely to oxidize Cu_8 to a larger extent diminishing its catalytic activity.

Following this, planar and 3D Cu_5 were theoretically studied as possible catalysts for the propene epoxidation reaction. It is found that the first step leading to the OMC, determinant for the selectivity of the reaction, is somewhat favoured with respect to the undesired allyl on planar Cu_5, whereas 3D Cu_5 would perform worse because the adsorption of O_2 in an *h111* mode is enough to favour the reaction to allyl. Once the O_2 is dissociated, the preference for the allyl reaction is clear. However, it is also found that once the first PO molecule is produced on planar clusters, the remaining O atom, again bicoordinately adsorbed, still somewhat favours the OMC reaction, with the direct ER reaction being also energetically possible.
Secondary reactions towards PA or AC always presented higher barriers. As a result, planar Cu_5 clusters are indeed promising candidates to catalyze the propene epoxidation reaction with good selectivity to PO.

Using a support is required for the practical application of copper clusters but may produce a material with different properties. Therefore, we studied the effect of two supports, N-graphene and ceria, on the properties of copper clusters (Cu_n, n=5, 8 and 13) and, more specifically, on the O_2 dissociation by Cu_5 (Chapter 5).

The interaction between copper clusters and clean graphene or N-graphene is weak, losing Cu-C interactions in favour of Cu-Cu bonds with increasing size. Adding N to graphene enhances the interaction, but chemical adsorption is only achieved at the defects explored (C vacancies and three pyridinic N atoms sites). Nevertheless, the weak adsorption facilitates the deformation of clusters upon the adsorption of a molecule such as O_2, and interconversion of isomers is commonly observed during calculations, reflecting their fluxionality.

In spite of this, conclusions on N-graphene are very similar to gas phase results, i.e. planar clusters are favoured, adsorb O_2 in *bridge* modes and hence are less active

towards its dissociation. The three pyridinic atom site favours the 3D isomers thermodynamically, but interconversion from 3D to planar clusters was also produced.

Regarding $CeO_2(111)$, the hexagonal symmetry of the surface matches the geometry of planar Cu_5 or Cu_3, which adds to the strong O-Cu interaction, and larger clusters such as Cu_8 or Cu_{13} are found more stable forming a first layer of Cu_5 or Cu_3 islands connected through a second layer of copper atoms.

When clusters are adsorbed on ceria, they get oxidized and produce Ce^{3+} atoms on the surface, whose positions can greatly change the energy of the structure. However, the strong interaction and the symmetry matching produces very few geometries close in energy for the Cu_5 clusters, which do not deform into one another in the calculations. Planar clusters adsorb parallel to the surface, interacting with all five atoms, and the 3D cluster breaks one of its Cu-Cu bonds to interact with four atoms in a rhombus shape, leaving the remaining Cu atom on top of one of the facets, forming a tetrahedron.

Since planar clusters are not in an upright position anymore, the adsorption of O_2 at its edges is impeded. Instead, O_2 is able now to strongly adsorb at the planar Cu_5 *h111* facets, getting highly activated in the process. In contrast, the molecule prefers a *bridge* site on the opened 3D cluster, and even when an *h111* mode is close in energy, the copper atoms are not close enough to stabilize both O atoms at the TS, thus yielding a higher activation energy.

Therefore, on clean N-graphene the properties of the Cu_5 clusters observed from gas phase are kept, but supporting them on ceria produces reversed results: planar clusters are more resistant to oxidation and more easily reducible on N-graphene and gas phase, whereas 3D clusters are more resistant to oxidation on $CeO_2(111)$.

Regarding the independent studies, in Chapter 6 it is concluded that the Heck reaction is selectively catalyzed by subnanometer Pd and also by Pt clusters. The combined experimental and computational study shows that the oxidative addition does not limit the Heck coupling (nor other cross-coupling reactions) on clusters nor single atoms of neither palladium nor platinum, translating the rds of the coupling to a later step where the base actively participates. Computational calculations indicate that an adequate balance of the adsorption strength of the base and its facility to undergo the reductive elimination step is key to catalyze the Heck reaction.
With a suitable base, the ligand–free Pt–catalyzed Heck coupling of aryl iodides and bromides and the Pd–catalyzed Suzuki coupling of aryl chlorides were successfully carried out.

Finally, Chapter 7 shows that the CO + NO reaction to produce CO_2 and N_2 can occur on stabilized Pt clusters at low temperature. DFT calculations show that single

atoms, too small clusters and too large nanoparticles cannot dissociate the NO molecule neither monomolecularly nor by direct reaction with CO, whereas medium-sized clusters can, with the monomolecular pathway being preferred. In addition, for the active medium-sized clusters it is found that the rate-determining step of the CO + NO reaction is the formation of N_2 via recombination of the adsorbed N* atoms produced in the dissociation of NO, and that N_2O formation and its reaction with CO is competitive and might also contribute to the global reaction.

Summary

Due to their subnanometric size, metal clusters belong to the regime affected by quantum confinement, which makes them more "molecular" and less "metallic". As a result, they exhibit properties that differ with respect to those of larger particles of the same element, and which are often advantageous in the catalysis of specific reactions. Besides, their smaller size makes them more economic, with a greater surface exposed. All of this renders metal clusters very interesting options for catalysis, and their study, synthesis and application has steadily increased since their discovery in the 90s.

In this work we have mainly focused on copper, of which a fundamental study on the oxygen dissociation by clusters of different sizes is first presented. It is found that cluster morphology determines its reactivity towards O_2 dissociation, as 3D clusters are able to adsorb the molecule in highly activated *h111* and *h100* adsorption modes, whereas planar clusters stabilize O_2 in less activated *bridge* modes. Since clusters evolve from 2D to 3D with increasing atomicity, only small cluster sizes are not active for O_2 dissociation. Indeed, experimental results confirm that Cu_5 clusters are more resistant to oxidation and more easily reducible than Cu_8 or Cu_{13} clusters.

With that conclusion in mind, we studied next the catalysis of the CO oxidation reaction by planar Cu_5, 3D Cu_5 and Cu_8. Reaction mechanisms of similar low-energy barriers are found for all of them, but for 3D clusters the rds of the reaction is found in the last O + CO step, whereas for planar Cu_5 it is the formation of an OOCO intermediate, which arises due to the difficulty in dissociating the O-O bond directly.

Seeing this difference in the reaction mechanism, planar and 3D Cu_5 were studied for the propene epoxidation reaction, finally concluding that the first step leading to the OMC, which is determinant for the selectivity of the reaction, is favoured with respect to the undesired allyl for planar Cu_5 clusters. 3D Cu_5 would perform worse because the adsorption of O_2 in an *h111* mode is enough to favor the reaction to allyl. Once O_2 is dissociated, reaction to allyl predominates. However, it is also found that O atoms bicoordinately adsorbed in planar Cu_5 still favor the OMC reaction, with the direct ER reaction being also energetically possible. In addition to this, secondary reactions towards PA or AC always presented higher barriers. As a result, planar Cu_5 clusters are promising candidates to catalyze the propene epoxidation reaction with good selectivity to PO.

Since supporting the clusters is required for their application but may produce a material with different properties, we studied Cu_n (n=5, 8, 13) clusters supported on graphene sheets and on the $CeO_2(111)$ surface. The interaction of copper clusters with clean graphene or N-graphene is weak, whereas with defects (C vacancies and three pyridinic atoms sites) and ceria it is much stronger. Graphene sheets facilitate

the deformation of clusters upon the adsorption of a molecule such as O_2, (interconversion of isomers is observed during calculations, reflecting their fluxionality), whereas the strength of the Cu-O interactions on ceria impedes it.

In spite of this, conclusions on N-graphene regarding O_2 dissociation by Cu_5 are very similar to gas phase results, i.e. planar clusters are favoured, adsorb O_2 in *bridge* modes and hence are less active towards its dissociation. For ceria, the planar cluster adsorbs parallel to the surface, interacting with all its five atoms, and the 3D cluster breaks one of its Cu-Cu bond so that four of its atoms can interact with the surface. As a result, the planar cluster now preferentially stabilizes O_2 in highly activated *h111* modes, whereas 3D Cu_5 stabilizes bridge modes. Consequently, reversed results are obtained: 3D clusters are the ones more resistant to oxidation on CeO_2(111).

Finally, two other more specific studies are presented. In the first one it is concluded that the Heck reaction is selectively catalyzed by subnanometer Pd and also by Pt clusters. The combined experimental and computational study shows that the oxidative addition does not limit the Heck coupling (nor other cross-coupling reactions) on clusters nor single atoms of neither palladium nor platinum, translating the rds of the coupling to a later step where the base actively participates. Indeed, computational calculations indicate that an adequate balance of the adsorption strength of the base and its facility to undergo the reductive elimination step is key to catalyze the Heck reaction.

In the second one, it is shown that the CO + NO reaction to produce CO_2 and N_2 can occur on stabilized Pt clusters at low temperature. DFT calculations show that single atoms, too small clusters and too large nanoparticles cannot dissociate the NO molecule neither monomolecularly nor by direct reaction with CO, whereas medium-sized clusters can, with the monomolecular pathway being preferred. In addition, for the active medium-sized clusters it is found that the rate-determining step of the CO + NO reaction is the formation of N_2 via recombination of the adsorbed N* atoms produced in the dissociation of NO, and that N_2O formation and its reaction with CO is competitive and might also contribute to the global reaction.

Resumen

Dado su tamaño subnanométrico, los *clusters* metálicos están regidos por el confinamiento cuántico, lo que les hace más "moleculares" y menos "metálicos". En consecuencia, manifiestan propiedades que difieren con respecto a las de partículas más grandes del mismo elemento, y que a menudo son ventajosas para la catálisis de reacciones específicas. Además, su menor tamaño los hace más económicos, con una mayor superficie expuesta. Todo ello hace que los *clusters* sean opciones muy interesantes en catálisis, y su estudio, síntesis y aplicación ha crecido continuamente desde su descubrimiento en los años 90.

Esta tesis se ha centrado principalmente en el cobre, del que se presenta, en primer lugar, un estudio fundamental sobre la disociación de oxígeno por *clusters* de diferentes tamaños. Se encontró que la morfología del *cluster* determina su reactividad para la disociación de O_2, ya que los *clusters* 3D son capaces de adsorber la molécula en los modos de adsorción *h111* y *h100*, altamente activados, mientras que los *clusters* planos estabilizan el O_2 en modos *bridge* (puente), menos activados. Dado que los *clusters* evolucionan de 2D a 3D con el aumento de la atomicidad, sólo los *clusters* más pequeños son inactivos para la disociación de O_2. Ciertamente, los resultados experimentales confirman que los *clusters* de Cu_5 son más resistentes a la oxidación y más fácilmente reducibles que los *clusters* de Cu_8 o Cu_{13}.

Teniendo en cuenta esa conclusión, se pasó a estudiar la catálisis de la oxidación de CO por *clusters* planos y 3D de Cu_5 y por *clusters* de Cu_8. Se encuentran mecanismos de reacción de barreras bajas y parecidas para los tres, pero para los *clusters* 3D el paso determinante de la velocidad de reacción es el último paso de O + CO, mientras que para los *clusters* planos de Cu_5 es la formación del intermedio OOCO, que tiene lugar debido a la dificultad de romper el enlace O-O directamente.

Viendo esta diferencia en el mecanismo de reacción, se decidió estudiar la reacción de epoxidación de propeno en *clusters* planos y 3D de Cu_5, concluyendo que el primer paso que lleva al OMC, determinante para la selectividad de la reacción, está favorecido respecto a la reacción que lleva al alilo no deseado en los *clusters* planos de Cu_5. Los *clusters* 3D de Cu_5 funcionarían peor porque la adsorción de O_2 en modo *h111* es suficiente para favorecer la formación del alilo. Una vez que el O_2 es disociado, la reacción al alilo es predominante. Sin embargo, también se encuentra que los átomos de O bicoordinados en *clusters* planos de Cu_5 aún favorecen la reacción al OMC, para la que el paso directo tipo ER es también posible energéticamente. Además, las reacciones secundarias hacia PA o AC siempre presentan barreras más altas. Como resultado, los *clusters* planos de Cu_5 son candidatos prometedores para catalizar la epoxidación de propeno con una buena selectividad al PO.

Puesto que soportar los *clusters* es necesario para su aplicación pero puede producir un material con propiedades distintas, se estudiaron ahora *clusters* de Cu_n (n=5, 8,13)

soportados en láminas de grafeno y en la superficie de la ceria (CeO_2(111)). La interacción de los *clusters* de cobre con el grafeno o N-grafeno limpios es débil, mientras que con los defectos (vacante de C y sitio con tres N piridínicos) y la ceria es mucho más fuerte. Las láminas de grafeno facilitan la deformación de los *clusters* cuando se adsorbe una molécula como el O_2 (se observan interconversiones de los isómeros plano y 3D durante los cálculos, reflejando su fluxionalidad), mientras que la fuerza de las interacciones Cu-O en la ceria impiden estas deformaciones.

A pesar de ello, las conclusiones a las que se llega con N-grafeno sobre la disociación de O_2 por *clusters* de Cu_5 son muy similares a los resultados de fase gas, esto es, se favorecen los *clusters* planos que adsorben O_2 en modos *bridge* y por lo tanto lo activan menos para su disociación. En la ceria, el *cluster* plano se adsorbe paralelo a la superficie, interactuando con los cinco átomos de cobre, y el 3D rompe uno de sus enlaces Cu-Cu para que cuatro de sus átomos pueda interactuar con la superficie. En consecuencia, el *cluster* plano ahora adsorbe el O_2 preferentemente en modos *h111* altamente activados, mientras que el 3D estabiliza modos *bridge*, y se obtienen resultados contrarios a los del N-grafeno y fase gas: los *clusters* 3D son más resistentes a la oxidación que los planos.

Finalmente, se presentan también otros dos estudios más específicos. En el primero se concluye que la reacción de Heck es catalizada selectivamente por *clusters* de Pd y también de Pt de menos de 5 átomos. Los estudios experimental y computacional combinados muestran que la adición oxidativa no limita el acoplamiento de Heck (ni otras reacciones de acoplamientro cruzado (*cross-coupling*)), ni en clusters ni en átomos de Pt o Pd, trasladando el paso determinante de la velocidad de reacción a uno en el que la base participa. Ciertamente, los cálculos computacionales indican que un equilibrio adecuado entre la fuerza de adsorción de la base y su facilidad para llevar a cabo el paso de eliminación reductiva es clave para catalizar la reacción de Heck.

En el segundo, se muestra que la reacción CO + NO para producir CO_2 y N_2 puede darse en *clusters* de Pt a baja temperatura. Los cálculos DFT muestran que los átomos, los clusters demasiado pequeños y las nanoparticulas demasiado grandes no pueden disociar el NO ni monomolecularmente ni por reacción con CO, mientras que los clusters de tamaño mediano pueden, y lo hacen preferentemente siguiendo el camino monomolecular. Además, para los clusters activos de tamaño medio se encuentra que el paso determinante de la velocidad de reacción para la reacción de CO + NO es la formación de N_2 a través de la recombinación de los átomos de N* adsorbidos, producidos en la disociación de NO, y que la formación de N_2O y su reacción con CO es competitiva y podría contribuir a la reacción global.

Resum

Atès que són de grandària subnanomètrica, els *clusters* metàl·lics estan regits pel confinament quàntic, el qual els fa més "moleculars" i menys "metàl·lics". En conseqüència, manifesten propietats que són diferents a les de partícules més grans del mateix element, i que sovint són avantatjoses per a la catàlisi de reaccions específiques. A més a més, la seua menor grandària fa que siguen més econòmics, amb una major superfície exposada. Així, els *clusters* són una opció molt interesant en catàlisi, i el seu estudi, síntesi i aplicació ha crescut contínuament des del seu descobriment als anys 90.

Aquesta tesi s'ha centrat principalment en el coure, del qual es presenta, en primer lloc, un estudi fonamental sobre la dissociació de l'oxígen per *clusters* de diferents grandàries. Es va trobar que la morfologia del *cluster* determina la seua reactivitat per a la dissociació d'O_2, ja que els *clusters* 3D són capaços d'adsorbir la molècula en els modes d'adsorció *h111* i *h100*, altament activats, i els *clusters* plans estabilitzen l'O_2 en modes *bridge* (pont), menys activats. Com que els *clusters* evolucionen de 2D a 3D amb l'augment de l'atomicitat, només els *clusters* més menuts són inactius per a la dissociació d'O_2. Certament, els resultats experimentals confirmen que els *clusters* de Cu_5 són més resistents a l'oxidació i més fàcilment reduïbles que els *clusters* de Cu_8 o Cu_{13}.

Tenint en compte eixa conclusió, es va passar a estudiar la catàlisi de l'oxidació de CO per *clusters* plans i 3D de Cu_5 i per *clusters* de Cu_8. Es troben mecanismes de reacció de barreres baixes i paregudes per a tots tres, però pels *clusters* 3D el pas determinant de la velocitat de reacció és l'últim, la reacció O + CO, mentre que pels *clusters* plans de Cu_5 és la formació de l'intermedi OOCO, degut a la dificultat de trencar l'enllaç O-O directament.

En veient aquesta diferència en el mecanisme de reacció, es va decidir estudiar la reacció d'epoxidació de propè als *clusters* plans i 3D de Cu_5, concloent que el primer pas que porta a l'OMC, determinant per a la selectivitat de la reacció, està afavorit respecte a la reacció que porta a l'al·lil no desitjat als *clusters* plans. Els *clusters* 3D de Cu_5 funcionarien pitjor perquè l'adsorció d'O_2 en mode *h111* és suficient per afavorir la formació de l'al·lil. Una vegada que l'O_2 és dissociat, la reacció a l'al·lil és predominant. Això no obstant, també es troba que els àtoms d'O bicoordinats als *clusters* plans de Cu_5 encara afavoreixen la reacció a l'OMC, per a la qual el pas directe tipus ER és també possible energèticament. A més, les reaccions secundàries a PA o AC sempre presenten barreres més altes. Per consegüent, els *clusters* plans de Cu_5 són candidats prometedors per catalitzar l'epoxidació de propè amb una bona selectivitat a PO.

Com que suportar els *clusters* és necessari per a la seua aplicació però pot produir un material amb propietats distintes, es van estudiar *clusters* de Cu_n (n=5, 8, 13)

suportats en làmines de grafè i en la superfície de la cèria ($CeO_2(111)$). La interacció dels *clusters* de coure amb el grafè o N-grafè nets és dèbil, mentre que amb els defectes (vacant de C i lloc amb tres N piridínics) i la cèria és molt més forta. Les làmines de grafè faciliten la deformació dels *clusters* quan s'hi adsorbeix una molècula com l'O_2 (s'observen interconversions dels isòmers pla i 3D durant els càlculs, reflectint la seua fluxionalitat), mentre que la força de les interaccions Cu-O en la cèria impedeixen aquestes deformacions.

Malgrat això, les conclusions sobre la dissociació d'O_2 per *clusters* de Cu_5 suportats en N-grafè són molt paregudes als resultats de fase gas, és a dir, s'afavoreixen els *clusters* plans que adsorbeixen O_2 en modes *bridge* i per tant estan menys activats per a la seua dissociació. En la cèria, el *cluster* pla s'adsorbeix paral·lel a la superfície, interactuant amb els cinc àtoms de coure, i el 3D trenca ú dels seus enllaços Cu-Cu perquè quatre dels seus àtoms puguen interactuar amb la superfície. En conseqüència, el *cluster* pla ara adsorbeix l'O_2 preferentment en modes *h111* altament activats, mentre que el 3D estabilitza modes *bridge*, i s'obtenen resultats contraris als del N-grafè i fase gas: els *clusters* 3D són més resistents a l'oxidació que els plans.

Finalment, es presenten també altres dos estudis més específics. En el primer es conclou que la reacció de Heck és catalitzada selectivament per *clusters* de Pd i també de Pt de menys de 5 àtoms. Els estudis experimental y computacional combinats mostren que l'addició oxidativa no limita l'acoblament de Heck (ni d'altres reaccions d'acoblament creuat (*cross-coupling*)), ni als *clusters* ni als àtoms de Pt o Pd, traslladant el pas determinant de la velocitat de reacció a un posterior en el qual participa la base. Els càlculs computacionals indiquen que un equilibri adequat entre la força d'adsorció de la base i la seua facilitat per a dur a terme l'eliminació reductiva és clau per catalitzar la reacció de Heck.

En el segon, es mostra que la reacció CO + NO per produir CO_2 i N_2 pot ocórrer en *clusters* de Pt a baixa temperatura. Els càlculs DFT mostren que els àtoms, els *clusters* massa menuts i les nanoparticles massa grans no poden dissociar el NO ni monomolecularment ni per reacció amb CO, mentre que els *clusters* de grandària mitjana poden, i ho fan preferentment seguint el camí monomolecular. A més, pels *clusters* actius de grandària mitjana es troba que el pas determinant de la velocitat de reacció per a la reacció de CO + NO és la formació de N_2 mitjançant la recombinació dels àtoms de N* adsorbits, produïts en la dissociació de NO, i que la formació de N_2O i la seua reacció amb CO és competitiva i podria contribuir a la reacció global.

List of Publications

- Fernández, E.; Liu, L.; Boronat, M.; Arenal, R.; Concepción, P. and Corma, A., Low-temperature catalytic NO reduction with CO by subnanometric Pt clusters, **2019** (accepted in ACS Catalysis).

- Fernández, E.; Rivero-Crespo, M; Domínguez, I.; Rubio-Marqués, P.; Oliver-Meseguer, J.; Liu, L.; Cabrero-Antonino, M.; Gavara, R.; Hernandez-Garrido, J.; Boronat, M.; Leyva-Perez, A. and Corma, A., Base–controlled Heck, Suzuki and Sonogashira reactions catalyzed by ligand–free platinum or palladium single atom and sub–nanometer clusters, **2019**, *J. Am. Chem. Soc.*, 141, 5, 1928-1940.

- Fernandez, E. and Boronat, M., Subnanometer clusters in catalysis, **2018**, *J. Phys.: Condens. Matter*, 31, 013002.

- Fernandez, E.; Moreno-González, M.; Moliner, M.; Blasco, T.; Boronat, M. and Corma, A., Modelling of EPR parameters for Cu(II). Application to the Selective Reduction of NOx catalyzed by Cu-zeolite*s,* **2018**, *Top. Catal,* 61, 810-832.

- Concepción, P.; Boronat, M.; García, S.; Fernández, E. and Corma, A., Enhanced stability of copper clusters of low atomicity against oxidation. Effect on the catalytic redox process, **2017**, *ACS catalysis*, 7, 3560-3568.

- Fernandez, E.; Boronat, M. and Corma, A., Trends in the Reactivity of Molecular O_2 with Copper Clusters: Influence of Size and Shape, **2015**, *J. Phys. Chem. C*, 119, 19832-19846.

268

References

(1) Lindström, B.; Pettersson, L. J. A brief history of catalysis. *CATTECH* **2003,** *7*, 130-138.

(2) Li, Y.; Liu, J. H.-C.; Witham, C. A.; Huang, W.; Marcus, M. A.; Fakra, S. C.; Alayoglu, P.; Zhu, Z.; Thompson, C. M.; Arjun, A.et al. A Pt-Cluster-Based Heterogeneous Catalyst for Homogeneous Catalytic Reactions: X-ray Absorption Spectroscopy and Reaction Kinetic Studies of Their Activity and Stability against Leaching. *Journal of the American Chemical Society* **2011,** *133* (34), 13527-13533.

(3) Taylor, H. S. A Theory of the Catalytic Surface. *Proc. R. Soc. Lon. A.* **1925,** *108*, 105-111.

(4) Heiligtag, F. J.; Niederberger, M. The fascinating world of nanoparticle research. *Materials Today* **2013,** *16* (7), 262-271.

(5) Edwards, P. P.; Thomas, J. M. Gold in a Metallic Divided State—From Faraday to Present-Day Nanoscience. *Angewandte Chemie International Edition* **2007,** *46* (29), 5480-5486.

(6) Bogner, A.; Jouneau, P. H.; Thollet, G.; Basset, D.; Gauthier, C. A history of scanning electron microscopy developments: Towards “wet-STEM” imaging. *Micron* **2007,** *38* (4), 390-401.

(7) de Heer, W. A. The physics of simple metal clusters: experimental aspects and simple models. *Reviews of Modern Physics* **1993,** *65* (3), 611-676.

(8) Chisholm, M. H.; Newnham, L. L. o. Frank Albert Cotton. 9 April 1930 - 20 February 2007. *Biographical Memoirs of Fellows of the Royal Society* **2008,** *54*, 95-115.

(9) Muetterties, E. L.; Rhodin, T. N.; Band, E.; Brucker, C. F.; Pretzer, W. R. Clusters and surfaces. *Chemical Reviews* **1979,** *79* (2), 91-137.

(10) Gates, B. C. Supported metal-clusters: synthesis, structure and catalysis. *Chemical Reviews* **1995,** *95* (3), 511-522.

(11) Okrut, A.; Runnebaum, R. C.; Ouyang, X.; Lu, J.; Aydin, C.; Hwang, S.-J.; Zhang, S.; Olatunji-Ojo, O. A.; Durkin, K. A.; Dixon, D. A.et al. Selective molecular recognition by nanoscale environments in a supported iridium cluster catalyst. *Nature Nanotechnology* **2014,** *9* (6), 459-465.

(12) Femoni, C.; Iapalucci, M. C.; Ruggieri, S.; Zacchini, S. From Mononuclear Complexes to Molecular Nanoparticles: The Buildup of Atomically Precise Heterometallic Rhodium Carbonyl Nanoclusters. *Accounts of Chemical Research* **2018,** *51* (11), 2748-2755.

(13) Ekardt, W. Dynamical Polarizability of Small Metal Particles: Self-Consistent Spherical Jellium Background Model. *Physical Review Letters* **1984,** *52* (21), 1925-1928.

(14) Halperin, W. P. Quantum size effects in metal particles. *Reviews of Modern Physics* **1986,** *58* (3), 533-606.

(15) Henglein, A. Small-particle research: physicochemical properties of extremely small colloidal metal and semiconductor particles. *Chemical Reviews* **1989,** *89* (8), 1861-1873.

(16) Volokitin, Y.; Sinzig, J.; de Jongh, L. J.; Schmid, G.; Vargaftik, M. N.; Moiseevi, I. I. Quantum-size effects in the thermodynamic properties of metallic nanoparticles. *Nature* **1996,** *384* (6610), 621-623.

(17) Somorjai, G. A.; Carrazza, J. Structure sensitivity of catalytic reactions. *Industrial & Engineering Chemistry Fundamentals* **1986,** *25* (1), 63-69.

(18) Ransil, B. J. Studies in Molecular Structure. II. LCAO-MO-SCF Wave Functions for Selected First-Row Diatomic Molecules. *Reviews of Modern Physics* **1960,** *32* (2), 245-254.

(19) Frisch, M. J.; Trucks, G. W.; Schlegel, H. B.; Scuseria, G. E.; Robb, M. A.; Cheeseman, J. R.; Scalmani, G.; Barone, V.; Mennucci, B.; Petersson, G. A.et al. Gaussian 09, Revision C.01. *Gaussian, Inc., Wallingford CT* **2009**.

(20) Kresse, G.; Hafner, J. Ab initio hellmann-feynman molecular dynamics for liquid metals. *Journal of Non-Crystalline Solids* **1993,** *156*, 956-960.

(21) Kresse, G.; Hafner, J. Ab initio molecular dynamics simulation of the liquid metal amorphous semiconductor transition in germanium. *Physical Review B* **1994,** *49* (20), 14251-14269.

(22) Kresse, G.; Furthmuller, J. Efficient iterative schemes for ab initio total-energy calculations using a plane-wave basis set. *Physical Review B* **1996,** *54* (16), 11169-11186.

(23) Kresse, G.; Furthmuller, J. Efficiency of ab-initio total energy calculations for metals and semiconductors using a plane-wave basis set. *Computational Materials Science* **1996,** *6* (1), 15-50.

(24) Kresse, G.; Joubert, D. From ultrasoft pseudopotentials to the projector augmented-wave method. *Physical Review B* **1999,** *59* (3), 1758-1775.

(25) Heiz, U.; Sanchez, A.; Abbet, S.; Schneider, W. D. Catalytic Oxidation of Carbon Monoxide on Monodispersed Platinum Clusters: Each Atom Counts. *Journal of the American Chemical Society* **1999,** *121* (13), 3214-3217.

(26) Tsukuda, T.; Häkkinen, H. In *Frontiers of Nanoscience*; Tsukuda, T.;Häkkinen, H., Eds.; Elsevier, 2015; Vol. 9.

(27) Heiz, U.; Bullock, E. L. Fundamental aspects of catalysis on supported metal clusters. *Journal of Materials Chemistry* **2004,** *14* (4), 564-577.

(28) Boronat, M.; Leyva-Perez, A.; Corma, A. Theoretical and Experimental Insights into the Origin of the Catalytic Activity of Subnanometric Gold Clusters: Attempts to Predict Reactivity with Clusters and Nanoparticles of Gold. *Accounts of Chemical Research* **2014,** *47* (3), 834-844.

(29) Yoon, B.; Hakkinen, H.; Landman, U.; Worz, A. S.; Antonietti, J. M.; Abbet, S.; Judai, K.; Heiz, U. Charging effects on bonding and catalyzed oxidation of CO on Au-8 clusters on MgO. *Science* **2005,** *307* (5708), 403-407.

(30) Herzing, A. A.; Kiely, C. J.; Carley, A. F.; Landon, P.; Hutchings, G. J. Identification of active gold nanoclusters on iron oxide supports for CO oxidation. *Science* **2008,** *321* (5894), 1331-1335.

(31) Liu, Y.; Tsunoyama, H.; Akita, T.; Xie, S.; Tsukuda, T. Aerobic Oxidation of Cyclohexane Catalyzed by Size-Controlled Au Clusters on Hydroxyapatite: Size Effect in the Sub-2 nm Regime. *Acs Catalysis* **2011,** *1* (1), 2-6.

(32) Corma, A.; Concepcion, P.; Boronat, M.; Sabater, M. J.; Navas, J.; Yacaman, M. J.; Larios, E.; Posadas, A.; Arturo Lopez-Quintela, M.; Buceta, D.et al. Exceptional oxidation activity with size-controlled supported gold clusters of low atomicity. *Nature Chemistry* **2013,** *5* (9), 775-781.

(33) Oliver-Meseguer, J.; Leyva-Pérez, A.; Corma, A. Very Small (3–6 Atoms) Gold Cluster Catalyzed Carbon–Carbon and Carbon–Heteroatom Bond-Forming Reactions in Solution. *ChemCatChem* **2013,** *5* (12), 3509-3515.

(34) Oliver-Meseguer, J.; Cabrero-Antonino, J. R.; Dominguez, I.; Leyva-Perez, A.; Corma, A. Small Gold Clusters Formed in Solution Give Reaction Turnover Numbers of 10(7) at Room Temperature. *Science* **2012,** *338* (6113), 1452-1455.

(35) Lang, S. M.; Bernhardt, T. M.; Bakker, J. M.; Yoon, B.; Landman, U. Selective CH bond activation of ethane by free gold clusters. *International Journal of Mass Spectrometry* **2019,** *435*, 241-250.

(36) Lei, Y.; Mehmood, F.; Lee, S.; Greeley, J.; Lee, B.; Seifert, S.; Winans, R. E.; Elam, J. W.; Meyer, R. J.; Redfern, P. C.et al. Increased Silver Activity for Direct Propylene Epoxidation via Subnanometer Size Effects. *Science* **2010,** *328* (5975), 224-228.

(37) Maity, P.; Yamazoe, S.; Tsukuda, T. Dendrimer-Encapsulated Copper Cluster as a Chemoselective and Regenerable Hydrogenation Catalyst. *Acs Catalysis* **2013,** *3* (2), 182-185.

(38) Vidal, A. B.; Feria, L.; Evans, J.; Takahashi, Y.; Liu, P.; Nakamura, K.; Illas, F.; Rodriguez, J. A. CO2 Activation and Methanol Synthesis on Novel Au/TiC and Cu/TiC Catalysts. *The Journal of Physical Chemistry Letters* **2012,** *3* (16), 2275-2280.

(39) Liu, C.; Yang, B.; Tyo, E.; Seifert, S.; DeBartolo, J.; von Issendorff, B.; Zapol, P.; Vajda, S.; Curtiss, L. A. Carbon Dioxide Conversion to Methanol over Size-Selected Cu-4 Clusters at Low Pressures. *Journal of the American Chemical Society* **2015,** *137* (27), 8676-8679.

(40) Hirabayashi, S.; Ichihashi, M. Catalytic oxidation of CO with N2O on isolated copper cluster anions. *Physical Chemistry Chemical Physics* **2014,** *16* (48), 26500-26505.

(41) Torres, D.; Lopez, N.; Illas, F.; Lambert, R. M. Low-Basicity Oxygen Atoms: A Key in the Search for Propylene Epoxidation Catalysts. *Angewandte Chemie International Edition* **2007,** *46* (12), 2055-2058.

(42) Leyva-Pérez, A.; Oliver-Meseguer, J.; Rubio-Marqués, P.; Corma, A. Water-Stabilized Three- and Four-Atom Palladium Clusters as Highly Active Catalytic Species in Ligand-Free C□C Cross-Coupling Reactions. *Angewandte Chemie International Edition* **2013,** *52* (44), 11554-11559.

(43) Kaden, W. E.; Wu, T.; Kunkel, W. A.; Anderson, S. L. Electronic Structure Controls Reactivity of Size-Selected Pd Clusters Adsorbed on TiO2 Surfaces. *Science* **2009,** *326* (5954), 826-829.

(44) Thang, H. V.; Pacchioni, G. CO oxidation promoted by a Pt4/TiO2 catalyst: role of lattice oxygen at the metal/oxide interface. *Catalysis Letters* **2018,** *149*, 390-398.

(45) Vajda, S.; Pellin, M. J.; Greeley, J. P.; Marshall, C. L.; Curtiss, L. A.; Ballentine, G. A.; Elam, J. W.; Catillon-Mucherie, S.; Redfern, P. C.; Mehmood, F.et al. Subnanometre platinum clusters as highly active and selective catalysts for the oxidative dehydrogenation of propane. *Nature Materials* **2009,** *8* (3), 213-216.

(46) Yamamoto, K.; Imaoka, T.; Chun, W.-J.; Enoki, O.; Katoh, H.; Takenaga, M.; Sonoi, A. Size-specific catalytic activity of platinum clusters enhances oxygen reduction reactions. *Nature Chemistry* **2009,** *1* (5), 397-402.

(47) Qiao, Z.-A.; Zhang, P.; Chai, S.-H.; Chi, M.; Veith, G. M.; Gallego, N. C.; Kidder, M.; Dai, S. Lab-in-a-Shell: Encapsulating Metal Clusters for Size Sieving Catalysis. *Journal of the American Chemical Society* **2014,** *136* (32), 11260-11263.

(48) Wang, L.; Ma, S.; Jiao, Z.; Yuan, D. Capability of defective graphene-supported Co4 nanoparticle toward ammonia dehydrogenation. *Applied Surface Science* **2019,** *465*, 1-9.

(49) Halder, A.; Curtiss, L. A.; Fortunelli, A.; Vajda, S. Perspective: Size selected clusters for catalysis and electrochemistry. *The Journal of Chemical Physics* **2018,** *148* (11), 110901.

(50) Baletto, F. Structural properties of sub-nanometer metallic clusters. *Journal of Physics: Condensed Matter* **2019,** *31* (11), 113001.

(51) Kang, X.; Zhu, M. Tailoring the photoluminescence of atomically precise nanoclusters. *Chemical Society Reviews* **2019,** *48* (8), 2422-2457.

(52) Ferrari, P.; Vanbuel, J.; Janssens, E.; Lievens, P. Tuning the Reactivity of Small Metal Clusters by Heteroatom Doping. *Accounts of Chemical Research* **2018,** *51* (12), 3174-3182.

(53) Tyo, E. C.; Vajda, S. Catalysis by clusters with precise numbers of atoms. *Nature Nanotechnology* **2015,** *10* (7), 577-588.

(54) Liu, L.; Corma, A. Metal Catalysts for Heterogeneous Catalysis: From Single Atoms to Nanoclusters and Nanoparticles. *Chemical Reviews* **2018,** *118* (10), 4981-5079.

(55) Higaki, T.; Li, Q.; Zhou, M.; Zhao, S.; Li, Y.; Li, S.; Jin, R. Toward the Tailoring Chemistry of Metal Nanoclusters for Enhancing Functionalities. *Accounts of Chemical Research* **2018,** *51* (11), 2764-2773.

(56) Kwak, K.; Lee, D. Electrochemistry of Atomically Precise Metal Nanoclusters. *Accounts of Chemical Research* **2019,** *52* (1), 12-22.

(57) Yan, J.; Teo, B. K.; Zheng, N. Surface Chemistry of Atomically Precise Coinage–Metal Nanoclusters: From Structural Control to Surface Reactivity and Catalysis. *Accounts of Chemical Research* **2018,** *51* (12), 3084-3093.

(58) Tang, Q.; Hu, G.; Fung, V.; Jiang, D.-e. Insights into Interfaces, Stability, Electronic Properties, and Catalytic Activities of Atomically Precise Metal Nanoclusters from First Principles. *Accounts of Chemical Research* **2018,** *51* (11), 2793-2802.

(59) Ghosh, A.; Mohammed, O. F.; Bakr, O. M. Atomic-Level Doping of Metal Clusters. *Accounts of Chemical Research* **2018,** *51* (12), 3094-3103.

(60) Cook, A. W.; Hayton, T. W. Case Studies in Nanocluster Synthesis and Characterization: Challenges and Opportunities. *Accounts of Chemical Research* **2018,** *51* (10), 2456-2464.

(61) Buceta, D.; Piñeiro, Y.; Vázquez-Vázquez, C.; Rivas, J.; López-Quintela, M. Metallic Clusters: Theoretical Background, Properties and Synthesis in Microemulsions. *Catalysts* **2014,** *4* (4), 356.

(62) Alonso, J. A. Electronic and atomic structure, and magnetism of transition-metal clusters. *Chemical Reviews* **2000,** *100* (2), 637-677.

(63) Pyykko, P. Relativistic effects in structural chemistry. *Chemical Reviews* **1988,** *88* (3), 563-594.

(64) Häkkinen, H. Atomic and electronic structure of gold clusters: understanding flakes, cages and superatoms from simple concepts. *Chemical Society Reviews* **2008,** *37* (9), 1847-1859.

(65) Kalita, B.; Deka, R. C. Stability of small Pd(n) (n=1-7) clusters on the basis of structural and electronic properties: A density functional approach. *Journal of Chemical Physics* **2007,** *127* (24).

(66) Song, W.; Lu, W.-C.; Wang, C. Z.; Ho, K. M. Magnetic and electronic properties of the nickel clusters Nin (n⩽30). *Computational and Theoretical Chemistry* **2011,** *978* (1), 41-46.

(67) Chaves, A. S.; Rondina, G. G.; Piotrowski, M. J.; Tereshchuk, P.; Da Silva, J. L. F. The Role of Charge States in the Atomic Structure of Cu-n and Pt-n (n=2-14 atoms) Clusters: A DFT Investigation. *Journal of Physical Chemistry A* **2014,** *118* (45), 10813-10821.

(68) Fernandez, E.; Boronat, M.; Corma, A. Trends in the Reactivity of Molecular O-2 with Copper Clusters: Influence of Size and Shape. *Journal of Physical Chemistry C* **2015,** *119* (34), 19832-19846.

(69) Itoh, M.; Kumar, V.; Adschiri, T.; Kawazoe, Y. Comprehensive study of sodium, copper, and silver clusters over a wide range of sizes 2 <= N <= 75. *Journal of Chemical Physics* **2009,** *131* (17).

(70) Häkkinen, H.; Yoon, B.; Landman, U.; Li, X.; Zhai, H.-J.; Wang, L.-S. On the Electronic and Atomic Structures of Small AuN- (N = 4−14) Clusters: A Photoelectron Spectroscopy and Density-Functional Study. *The Journal of Physical Chemistry A* **2003,** *107* (32), 6168-6175.

(71) Häkkinen, H.; Landman, U. Gold clusters AuN (2<~N<~10) and their anions. *Physical Review B* **2000,** *62* (4), R2287-R2290.

(72) Lecoultre, S.; Rydlo, A.; Felix, C.; Buttet, J.; Gilb, S.; Harbich, W. Optical absorption of small copper clusters in neon: Cu-n, (n=1-9). *Journal of Chemical Physics* **2011,** *134* (7).

(73) Lin, C.-A. J.; Lee, C.-H.; Hsieh, J.-T.; Wang, H.-H.; Li, J. K.; Shen, J.-L.; Chan, W.-H.; Yeh, H.-I.; Chang, W. H. Synthesis of fluorescent metallic nanoclusters toward biomedical application: recent progress and present challenges. *Journal of Medical and Biological Engineering* **2009,** *29* (6), 276-283.

(74) Vázquez-Vázquez, C.; Bañobre-López, M.; Mitra, A.; López-Quintela, M. A.; Rivas, J. Synthesis of Small Atomic Copper Clusters in Microemulsions. *Langmuir* **2009,** *25* (14), 8208-8216.

(75) and, S. L.; El-Sayed, M. A. OPTICAL PROPERTIES AND ULTRAFAST DYNAMICS OF METALLIC NANOCRYSTALS. *Annual Review of Physical Chemistry* **2003,** *54* (1), 331-366.

(76) Eustis, S.; El-Sayed, M. A. Why gold nanoparticles are more precious than pretty gold: Noble metal surface plasmon resonance and its enhancement of the radiative and nonradiative properties of nanocrystals of different shapes. *Chemical Society Reviews* **2006,** *35* (3), 209-217.

(77) Zheng, J.; Zhou, C.; Yu, M.; Liu, J. Different sized luminescent gold nanoparticles. *Nanoscale* **2012,** *4* (14), 4073-4083.

(78) Zheng, J.; Zhang, C.; Dickson, R. M. Highly Fluorescent, Water-Soluble, Size-Tunable Gold Quantum Dots. *Physical Review Letters* **2004,** *93* (7), 077402.

(79) Vilar-Vidal, N.; Blanco, M. C.; Lopez-Quintela, M. A.; Rivas, J.; Serra, C. Electrochemical Synthesis of Very Stable Photoluminescent Copper Clusters. *Journal of Physical Chemistry C* **2010,** *114* (38), 15924-15930.

(80) Chaves, A. S.; Piotrowski, M. J.; Da Silva, J. L. F. Evolution of the structural, energetic, and electronic properties of the 3d, 4d, and 5d transition-metal clusters (30 TMn systems for n=2-15): a density functional theory investigation. *Physical Chemistry Chemical Physics* **2017,** *19* (23), 15484-15502.

(81) Yumura, T.; Kumondai, M.; Kuroda, Y.; Wakasugi, T.; Kobayashi, H. Utilizing super-atom orbital ideas to understand properties of silver clusters inside ZSM-5 zeolite. *RSC Advances* **2017,** *7* (9), 4950-4959.

(82) Copp, S. M.; Schultz, D.; Swasey, S.; Pavlovich, J.; Debord, M.; Chiu, A.; Olsson, K.; Gwinn, E. Magic Numbers in DNA-Stabilized Fluorescent Silver Clusters Lead to Magic Colors. *The Journal of Physical Chemistry Letters* **2014,** *5* (6), 959-963.

(83) Shayeghi, A.; Johnston, R. L.; Schäfer, R. Evaluation of photodissociation spectroscopy as a structure elucidation tool for isolated clusters: a case study of Ag4+ and Au4+. *Physical Chemistry Chemical Physics* **2013,** *15* (45), 19715-19723.

(84) Häkkinen, H.; Moseler, M.; Landman, U. Bonding in Cu, Ag, and Au Clusters: Relativistic Effects, Trends, and Surprises. *Physical Review Letters* **2002,** *89* (3), 033401.

(85) Lee, T. H.; Ervin, K. M. Reactions of Copper Group Cluster Anions with Oxygen and Carbon Monoxide. *The Journal of Physical Chemistry* **1994,** *98* (40), 10023-10031.

(86) Salisbury, B. E.; Wallace, W. T.; Whetten, R. L. Low-temperature activation of molecular oxygen by gold clusters: a stoichiometric process correlated to electron affinity. *Chemical Physics* **2000,** *262* (1), 131-141.

(87) Yoon, B.; Häkkinen, H.; Landman, U. Interaction of O2 with Gold Clusters: Molecular and Dissociative Adsorption. *The Journal of Physical Chemistry A* **2003,** *107* (20), 4066-4071.

(88) Zhai, H.; Alexandrova, A. N. Fluxionality of Catalytic Clusters: When It Matters and How to Address It. *ACS Catalysis* **2017,** *7* (3), 1905-1911.

(89) Popok, V. N.; Barke, I.; Campbell, E. E. B.; Meiwes-Broer, K.-H. Cluster-surface interaction: From soft landing to implantation. *Surface science reports* **2011,** *66* (10), 347-377.

(90) Wei, W. T.; Lu, Y. Z.; Chen, W.; Chen, S. W. One-Pot Synthesis, Photoluminescence, and Electrocatalytic Properties of Subnanometer-Sized Copper Clusters. *Journal of the American Chemical Society* **2011,** *133* (7), 2060-2063.

(91) Wu, Z.; Lanni, E.; Chen, W.; Bier, M. E.; Ly, D.; Jin, R. High Yield, Large Scale Synthesis of Thiolate-Protected Ag7 Clusters. *Journal of the American Chemical Society* **2009,** *131* (46), 16672-16674.

(92) Wei, C.; Shaowei, C. Oxygen Electroreduction Catalyzed by Gold Nanoclusters: Strong Core Size Effects. *Angewandte Chemie International Edition* **2009,** *48* (24), 4386-4389.

(93) Yasumatsu, H.; Kondow, T. Reactive scattering of clusters and cluster ions from solid surfaces. *Reports on Progress in Physics* **2003,** *66* (10), 1783-1832.

(94) Ji, Q.; Zhang, Y.; Zhang, Y.; Liu, Z. Chemical vapour deposition of group-VIB metal dichalcogenide monolayers: engineered substrates from amorphous to single crystalline. *Chemical Society Reviews* **2015,** *44* (9), 2587-2602.

(95) Tai, G.; Hu, T.; Zhou, Y.; Wang, X.; Kong, J.; Zeng, T.; You, Y.; Wang, Q. Synthesis of Atomically Thin Boron Films on Copper Foils. *Angewandte Chemie International Edition* **2015,** *54* (51), 15473-15477.

(96) Liu, X.; Astruc, D. Atomically precise copper nanoclusters and their applications. *Coordination Chemistry Reviews* **2018,** *359*, 112-126.

(97) Kurashige, W.; Niihori, Y.; Sharma, S.; Negishi, Y. Precise synthesis, functionalization and application of thiolate-protected gold clusters. *Coordination Chemistry Reviews* **2016,** *320-321*, 238-250.

(98) Fang, J.; Zhang, B.; Yao, Q.; Yang, Y.; Xie, J.; Yan, N. Recent advances in the synthesis and catalytic applications of ligand-protected, atomically precise metal nanoclusters. *Coordination Chemistry Reviews* **2016,** *322*, 1-29.

(99) Lu, Y.; Chen, W. Sub-nanometre sized metal clusters: from synthetic challenges to the unique property discoveries. *Chemical Society Reviews* **2012,** *41* (9), 3594-3623.

(100) Serna, P.; Gates, B. C. Molecular Metal Catalysts on Supports: Organometallic Chemistry Meets Surface Science. *Accounts of Chemical Research* **2014,** *47* (8), 2612-2620.

(101) Astruc, D.; Lu, F.; Aranzaes, J. R. Nanoparticles as recyclable catalysts: The frontier between homogeneous and heterogeneous catalysis. *Angewandte Chemie-International Edition* **2005,** *44* (48), 7852-7872.

(102) Reetz, M. T.; Helbig, W. Size-Selective Synthesis of Nanostructured Transition Metal Clusters. *Journal of the American Chemical Society* **1994,** *116* (16), 7401-7402.

(103) Rodríguez-Sánchez, M. L.; Rodríguez, M. J.; Blanco, M. C.; Rivas, J.; López-Quintela, M. A. Kinetics and Mechanism of the Formation of Ag Nanoparticles by Electrochemical Techniques: A Plasmon and Cluster Time-Resolved Spectroscopic Study. *The Journal of Physical Chemistry B* **2005,** *109* (3), 1183-1191.

(104) Santiago González, B.; Rodríguez, M. J.; Blanco, C.; Rivas, J.; López-Quintela, M. A.; Martinho, J. M. G. One Step Synthesis of the Smallest Photoluminescent and Paramagnetic PVP-Protected Gold Atomic Clusters. *Nano Letters* **2010,** *10* (10), 4217-4221.

(105) Vilar-Vidal, N.; Rivas, J.; López-Quintela, M. A. Size Dependent Catalytic Activity of Reusable Subnanometer Copper(0) Clusters. *ACS Catalysis* **2012,** *2* (8), 1693-1697.

(106) Huseyinova, S.; Blanco, J.; Requejo, F. G.; Ramallo-López, J. M.; Blanco, M. C.; Buceta, D.; López-Quintela, M. A. Synthesis of Highly Stable Surfactant-free Cu5 Clusters in Water. *The Journal of Physical Chemistry C* **2016,** *120* (29), 15902-15908.

(107) Concepcion, P.; Boronat, M.; Garcia-Garcia, S.; Fernandez, E.; Corma, A. Enhanced Stability of Cu Clusters of Low Atomicity against Oxidation. Effect on the Catalytic Redox Process. *Acs Catalysis* **2017,** *7* (5), 3560-3568.

(108) Brust, M.; Walker, M.; Bethell, D.; Schiffrin, D. J.; Whyman, R. Synthesis of thiol-derivatised gold nanoparticles in a two-phase Liquid–Liquid system. *Journal of the Chemical Society, Chemical Communications* **1994**, DOI:10.1039/C39940000801 10.1039/C39940000801(7), 801-802.

(109) Yang, H.; Wang, Y.; Zheng, N. Stabilizing subnanometer Ag(0) nanoclusters by thiolate and diphosphine ligands and their crystal structures. *Nanoscale* **2013,** *5* (7), 2674-2677.

(110) Yang, H.; Lei, J.; Wu, B.; Wang, Y.; Zhou, M.; Xia, A.; Zheng, L.; Zheng, N. Crystal structure of a luminescent thiolated Ag nanocluster with an octahedral Ag64+ core. *Chemical Communications* **2013,** *49* (3), 300-302.

(111) Sai Krishna, K.; Navin, C. V.; Biswas, S.; Singh, V.; Ham, K.; Bovenkamp, G. L.; Theegala, C. S.; Miller, J. T.; Spivey, J. J.; Kumar, C. S. S. R. Millifluidics for Time-resolved Mapping of the Growth of Gold Nanostructures. *Journal of the American Chemical Society* **2013,** *135* (14), 5450-5456.

(112) Olivares, A.; Laskin, J.; Johnson, G. E. Investigating the Synthesis of Ligated Metal Clusters in Solution Using a Flow Reactor and Electrospray Ionization Mass Spectrometry. *The Journal of Physical Chemistry A* **2014,** *118* (37), 8464-8470.

(113) Biswas, S.; Miller, J. T.; Li, Y.; Nandakumar, K.; Kumar, C. S. S. R. Developing a Millifluidic Platform for the Synthesis of Ultrasmall Nanoclusters: Ultrasmall Copper Nanoclusters as a Case Study. *Small* **2012,** *8* (5), 688-698.

(114) Navin Chelliah, V.; Krishna Katla, S.; Theegala Chandra, S.; Kumar Challa, S. S. R. In *Nanotechnology Reviews*, 2014; Vol. 3.

(115) Ran, R.; Sun, Q.; Baby, T.; Wibowo, D.; Middelberg, A. P. J.; Zhao, C.-X. Multiphase microfluidic synthesis of micro- and nanostructures for pharmaceutical applications. *Chemical Engineering Science* **2017,** *169*, 78-96.

(116) Gdowski, A.; Johnson, K.; Shah, S.; Gryczynski, I.; Vishwanatha, J.; Ranjan, A. Optimization and scale up of microfluidic nanolipomer production method for preclinical and potential clinical trials. *Journal of Nanobiotechnology* **2018,** *16* (1), 12.

(117) Guo, Y.; Zhang, Y.-W. Metal Clusters Dispersed on Oxide Supports: Preparation Methods and Metal-Support Interactions. *Topics in Catalysis* **2018,** *61* (9), 855-874.

(118) Muetterties, E. L.; Krause, M. J. Catalysis by Molecular Metal Clusters. *Angewandte Chemie International Edition in English* **1983,** *22* (2), 135-148.

(119) Gross, E.; Dean Toste, F.; Somorjai, G. A. Polymer-Encapsulated Metallic Nanoparticles as a Bridge Between Homogeneous and Heterogeneous Catalysis. *Catalysis Letters* **2015,** *145* (1), 126-138.

(120) Sanchez, A.; Abbet, S.; Heiz, U.; Schneider, W. D.; Häkkinen, H.; Barnett, R. N.; Landman, U. When Gold Is Not Noble: Nanoscale Gold Catalysts. *The Journal of Physical Chemistry A* **1999,** *103* (48), 9573-9578.

(121) Valden, M.; Lai, X.; Goodman, D. W. Onset of Catalytic Activity of Gold Clusters on Titania with the Appearance of Nonmetallic Properties. *Science* **1998,** *281* (5383), 1647.

(122) Chen, M. S.; Goodman, D. W. The structure of catalytically active gold on titania. *Science* **2004,** *306* (5694), 252-255.

(123) Chen, M.; Goodman, D. W. Catalytically Active Gold: From Nanoparticles to Ultrathin Films. *Accounts of Chemical Research* **2006,** *39* (10), 739-746.

(124) Matthey, D.; Wang, J. G.; Wendt, S.; Matthiesen, J.; Schaub, R.; Lægsgaard, E.; Hammer, B.; Besenbacher, F. Enhanced Bonding of Gold Nanoparticles on Oxidized TiO₂(110). *Science* **2007,** *315* (5819), 1692.

(125) Fortea-Pérez, F. R.; Mon, M.; Ferrando-Soria, J.; Boronat, M.; Leyva-Pérez, A.; Corma, A.; Herrera, J. M.; Osadchii, D.; Gascon, J.; Armentano, D.et al. The MOF-driven synthesis of supported palladium clusters with catalytic activity for carbene-mediated chemistry. *Nature Materials* **2017,** *16*, 760.

(126) Cheng, L.; Yin, C. R.; Mehmood, F.; Liu, B.; Greeley, J.; Lee, S.; Lee, B.; Seifert, S.; Winans, R. E.; Teschner, D.et al. Reaction Mechanism for Direct Propylene Epoxidation by Alumina-Supported Silver Aggregates: The Role of the Particle/Support Interface. *Acs Catalysis* **2014,** *4* (1), 32-39.

(127) Pulido, A.; Concepción, P.; Boronat, M.; Corma, A. Aerobic epoxidation of propene over silver (111) and (100) facet catalysts. *Journal of Catalysis* **2012,** *292*, 138-147.

(128) Boronat, M.; Pulido, A.; Concepcion, P.; Corma, A. Propene epoxidation with O2 or H2-O2 mixtures over silver catalysts: theoretical insights into the role of the particle size. *Physical chemistry chemical physics : PCCP* **2014,** *16* (48), 26600-12.

(129) Kim, I. S.; Li, Z.; Zheng, J.; Platero-Prats, A. E.; Mavrandonakis, A.; Pellizzeri, S.; Ferrandon, M.; Vjunov, A.; Gallington, L. C.; Webber, T. E.et al. Sinter-Resistant Platinum Catalyst Supported by Metal–Organic Framework. *Angewandte Chemie International Edition* **2018,** *57* (4), 909-913.

(130) Crabtree, R. H. Resolving Heterogeneity Problems and Impurity Artifacts in Operationally Homogeneous Transition Metal Catalysts. *Chemical Reviews* **2012,** *112* (3), 1536-1554.

(131) Lewis, L. N. Chemical catalysis by colloids and clusters. *Chemical Reviews* **1993,** *93* (8), 2693-2730.

(132) Phan, N. T. S.; Van Der Sluys, M.; Jones, C. W. On the Nature of the Active Species in Palladium Catalyzed Mizoroki–Heck and Suzuki–Miyaura Couplings – Homogeneous or Heterogeneous Catalysis, A Critical Review. *Advanced Synthesis & Catalysis* **2006,** *348* (6), 609-679.

(133) Astruc, D. Palladium Nanoparticles as Efficient Green Homogeneous and Heterogeneous Carbon−Carbon Coupling Precatalysts: A Unifying View. *Inorganic Chemistry* **2007,** *46* (6), 1884-1894.

(134) Narayanan, R.; Tabor, C.; El-Sayed, M. A. Can the Observed Changes in the Size or Shape of a Colloidal Nanocatalyst Reveal the Nanocatalysis Mechanism Type: Homogeneous or Heterogeneous? *Topics in Catalysis* **2008,** *48* (1), 60.

(135) Alley, W. M.; Hamdemir, I. K.; Johnson, K. A.; Finke, R. G. Ziegler-type hydrogenation catalysts made from group 8–10 transition metal precatalysts and AlR 3 cocatalysts: A critical review of the literature. *Journal of Molecular Catalysis A: Chemical $V 315* **2010,** (1), 1-27.

(136) Widegren, J. A.; Finke, R. G. A review of the problem of distinguishing true homogeneous catalysis from soluble or other metal-particle heterogeneous catalysis under reducing conditions. *Journal of Molecular Catalysis A: Chemical* **2003,** *198* (1), 317-341.

(137) Pagliaro, M.; Pandarus, V.; Ciriminna, R.; Béland, F.; Demma Carà, P. Heterogeneous versus Homogeneous Palladium Catalysts for Cross-Coupling Reactions. *ChemCatChem* **2012,** *4* (4), 432-445.

(138) Hagen, C. M.; Widegren, J. A.; Maitlis, P. M.; Finke, R. G. Is It Homogeneous or Heterogeneous Catalysis? Compelling Evidence for Both Types of Catalysts Derived from [Rh(η5-C5Me5)Cl2]2 as a Function of Temperature and Hydrogen Pressure. *Journal of the American Chemical Society* **2005,** *127* (12), 4423-4432.

(139) Bayram, E.; Linehan, J. C.; Fulton, J. L.; Roberts, J. A. S.; Szymczak, N. K.; Smurthwaite, T. D.; Özkar, S.; Balasubramanian, M.; Finke, R. G. Is It

Homogeneous or Heterogeneous Catalysis Derived from [RhCp*Cl2]2? In Operando XAFS, Kinetic, and Crucial Kinetic Poisoning Evidence for Subnanometer Rh4 Cluster-Based Benzene Hydrogenation Catalysis. *Journal of the American Chemical Society* **2011,** *133* (46), 18889-18902.

(140) Alves, L.; Ballesteros, B.; Boronat, M.; Cabrero-Antonino, J. R.; Concepción, P.; Corma, A.; Correa-Duarte, M. A.; Mendoza, E. Synthesis and Stabilization of Subnanometric Gold Oxide Nanoparticles on Multiwalled Carbon Nanotubes and Their Catalytic Activity. *Journal of the American Chemical Society* **2011,** *133* (26), 10251-10261.

(141) Heck, R. F. Palladium-catalyzed reactions of organic halides with olefins. *Accounts of Chemical Research* **1979,** *12* (4), 146-151.

(142) Miyaura, N.; Suzuki, A. Palladium-Catalyzed Cross-Coupling Reactions of Organoboron Compounds. *Chemical Reviews* **1995,** *95* (7), 2457-2483.

(143) Negishi, E.; Meijere, A. Handbook of Organopalladium Chemistry for Organic synthesis. *New York: Wiley* **2002**.

(144) Moreno-Mañas, M.; Pleixats, R. Formation of Carbon–Carbon Bonds under Catalysis by Transition-Metal Nanoparticles. *Accounts of Chemical Research* **2003,** *36* (8), 638-643.

(145) Liu, Y.; Jia, C.-J.; Yamasaki, J.; Terasaki, O.; Schüth, F. Highly Active Iron Oxide Supported Gold Catalysts for CO Oxidation: How Small Must the Gold Nanoparticles Be? *Angewandte Chemie International Edition* **2010,** *49* (33), 5771-5775.

(146) He, Q.; Freakley, S. J.; Edwards, J. K.; Carley, A. F.; Borisevich, A. Y.; Mineo, Y.; Haruta, M.; Hutchings, G. J.; Kiely, C. J. Population and hierarchy of active species in gold iron oxide catalysts for carbon monoxide oxidation. *Nat. Commun.* **2016,** *7*, 12905.

(147) Fernández, E.; Rivero-Crespo, M. A.; Domínguez, I.; Rubio-Marqués, P.; Oliver-Meseguer, J.; Liu, L.; Cabrero-Antonino, M.; Gavara, R.; Hernández-Garrido, J. C.; Boronat, M.et al. Base-Controlled Heck, Suzuki, and Sonogashira Reactions Catalyzed by Ligand-Free Platinum or Palladium Single Atom and Sub-Nanometer Clusters. *Journal of the American Chemical Society* **2019,** *141* (5), 1928-1940.

(148) Fernandez, E.; Liu, L.; Boronat, M.; Arenal, R.; Concepcion, P.; Corma, A. Low-temperature catalytic NO reduction with CO by subnanometric Pt clusters. *(accepted in ACS Catalysis)* **2019**.

(149) Fermi, E. Un Metodo Statistico per la Determinazione di alcune Prioprietà dell'Atomo. *Rendiconti: Accademia Nazionale dei Lincei* **1927,** *6*, 602-607.

(150) Thomas, L. H. The calculation of atomic fields. *Mathematical Proceedings of the Cambridge Philosophical Society* **1927,** *23* (5), 542-548.

(151) Dirac, P. A. M. Note on Exchange Phenomena in the Thomas Atom. *Mathematical Proceedings of the Cambridge Philosophical Society* **1930,** *26* (3), 376-385.

(152) Hohenberg, P. a. K., W. Inhomogeneous Electron Gas. *Phys. Rev. B* **1964,** *136*, 864-971.

(153) Kohn, W.; Sham, L. J. Self-Consistent Equations Including Exchange and Correlation Effects. *Physical Review* **1965,** *140* (4A), A1133-A1138.

(154) Martinez, J.-P. The Hartree-Fock method: from self-consistency to correct symmetry. *Annalen der Physik* **2017,** *529* (1-2), 1600328.

(155) Cramer, C. J. Essentials of Computational Chemistry: Theories and Models, 2nd Edition. *Wiley Ed.* **2004**.

(156) S.H. Vosko, L. W., M. Nusair. *Can. J. Phys.* **1980,** *58*, 1200-1211.

(157) Perdew, J. P.; Wang, Y. Accurate and simple analytic representation of the electron gas correlation energy. *Physical Review B* **1992,** *45* (23), 13244-13249.

(158) Perdew, J. P.; Burke, K.; Ernzerhof, M. Generalized Gradient Approximation Made Simple. *Physical Review Letters* **1996,** *77* (18), 3865-3868.

(159) J. P. Perdew, J. A. C., S. H. Vosko, K. A. Jackson, M. R. Pederson, D. J. Singh, and C. Fiolhais. Atoms, molecules, solids, and surfaces: Applications of the generalized gradient approximation for exchange and correlation. *Phys. Rev. B* **1992,** *46*, 6671-87.

(160) Becke, A. D. Density-functional thermochemistry III The role of the exact exchange. *J. Chem. Phys.* **1993,** *98*, 5648-5652.

(161) Grimme, S. Semiempirical GGA-type density functional constructed with a long-range dispersion correction. *Journal of Computational Chemistry* **2006,** *27* (15), 1787-1799.

(162) Penschke, C.; Paier, J.; Sauer, J. Oligomeric Vanadium Oxide Species Supported on the CeO2(111) Surface: Structure and Reactivity Studied by Density Functional Theory. *The Journal of Physical Chemistry C* **2013,** *117* (10), 5274-5285.

(163) Perdew, J. P.; Zunger, A. Self-interaction correction to density-functional approximations for many-electron systems. *Physical Review B* **1981,** *23* (10), 5048-5079.

(164) Dudarev, S. L.; Botton, G. A.; Savrasov, S. Y.; Humphreys, C. J.; Sutton, A. P. Electron-energy-loss spectra and the structural stability of nickel oxide: An LSDA+U study. *Physical Review B* **1998,** *57* (3), 1505-1509.

(165) Fabris, S.; Vicario, G.; Balducci, G.; de Gironcoli, S.; Baroni, S. Electronic and Atomistic Structures of Clean and Reduced Ceria Surfaces. *The Journal of Physical Chemistry B* **2005,** *109* (48), 22860-22867.

(166) Castleton, C. W. M.; Kullgren, J.; Hermansson, K. Tuning LDA+U for electron localization and structure at oxygen vacancies in ceria. *The Journal of Chemical Physics* **2007,** *127* (24), 244704.

(167) Slater, J. C. *Phys. Rev.* **1930,** *36*, 57.

(168) Boys, S. F. *Proc. royal Soc. London* **1950,** *258*, 402.

(169) W. J. Hehre, R. F. S., J. A. Pople. *J. Chem. Phys.* **1969,** *51*, 2657.

(170) Ditchfield, R.; Hehre, W. J.; Pople, J. A. Self-Consistent Molecular-Orbital Methods. IX. An Extended Gaussian-Type Basis for Molecular-Orbital Studies of Organic Molecules. *The Journal of Chemical Physics* **1971,** *54* (2), 724-728.

(171) Wachters, A. J. H. Gaussian Basis Set for Molecular Wavefunctions Containing Third-Row Atoms. *The Journal of Chemical Physics* **1970,** *52* (3), 1033-1036.

(172) Hay, P. J. Gaussian Basis Sets for Molecular Calculations - Representation of 3D Orbitals in Transition-Metal Atoms. *Journal of Chemical Physics* **1977,** *66* (10), 4377-4384.

(173) Weigend, F.; Ahlrichs, R. Balanced basis sets of split valence, triple zeta valence and quadruple zeta valence quality for H to Rn: Design and assessment of accuracy. *Physical Chemistry Chemical Physics* **2005,** *7* (18), 3297-3305.

(174) Weigend, F. Accurate Coulomb-fitting basis sets for H to Rn. *Physical Chemistry Chemical Physics* **2006,** *8* (9), 1057-1065.

(175) Hay, P. J.; Wadt, W. R. Ab Initio Effective Core Potentials for Molecular Calculations - Potentials for the Transition-Metal Atoms Sc to Hg. *Journal of Chemical Physics* **1985,** *82* (1), 270-283.

(176) Hay, P. J.; Wadt, W. R. Ab Initio Effective Core Potentials for Molecular Calculations - Potentials for K to Au including the Outermost Core Orbitals. *Journal of Chemical Physics* **1985,** *82* (1), 299-310.

(177) Monkhorst, H. J.; Pack, J. D. Special points for Brillouin-zone integrations. *Physical Review B* **1976,** *13* (12), 5188-5192.

(178) Blöchl, P. E. Projector Augmented-Wave Method. *Physical Review B* **1994,** *50* (24), 17953-17979.

(179) Schlegel, H. B. Optimization of equilibrium geometries and transition structures. *Journal of Computational Chemistry* **1982,** *3* (2), 214-218.

(180) Liu, D.; Nocedal, J. On the limited memory BFGS method for large-scale optimization. *Math. Program.* **1989,** *45*, 503-528.

(181) Pulay, P. Convergence acceleration of iterative sequences. the case of scf iteration. *Chemical Physics Letters* **1980,** *73* (2), 393-398.

(182) Hestenes, M. R.; Stiefel, E. Methods of Conjugate Gradients for Solving Linear Systems. *J. Res. Natl. Bur. Stand.* **1952,** *49* (6), 409.

(183) Peng, C.; Bernhard Schlegel, H. Combining Synchronous Transit and Quasi-Newton Methods to Find Transition States. *Israel Journal of Chemistry* **1993,** *33* (4), 449-454.

(184) Peng, C.; Ayala, P. Y.; Schlegel, H. B.; Frisch, M. J. Using redundant internal coordinates to optimize equilibrium geometries and transition states. *Journal of Computational Chemistry* **1996,** *17* (1), 49-56.

(185) Henkelman, G.; Jónsson, H. A dimer method for finding saddle points on high dimensional potential surfaces using only first derivatives. *J. Chem. Phys.* **1999,** *111*, 7010-7022.

(186) Heyden, A.; Bell, A. T.; Keil, F. J. Efficient methods for finding transition states in chemical reactions: Comparison of improved dimer method and partitioned rational function optimization method. *The Journal of Chemical Physics* **2005,** *123* (22), 224101.

(187) Henkelman, G.; Uberuaga, B. P.; Jónsson, H. A climbing image nudged elastic band method for finding saddle points and minimum energy paths. *The Journal of Chemical Physics* **2000,** *113* (22), 9901-9904.

(188) Reed, A. E.; Weinstock, R. B.; Weinhold, F. Natural population analysis. *The Journal of Chemical Physics* **1985,** *83* (2), 735-746.

(189) Tang, W.; Sanville, E.; Henkelman, G. A grid-based Bader analysis algorithm without lattice bias. *Journal of Physics: Condensed Matter* **2009,** *21* (8), 084204.

(190) Sanville, E.; Kenny, S. D.; Smith, R.; Henkelman, G. Improved grid-based algorithm for Bader charge allocation. *Journal of Computational Chemistry* **2007,** *28* (5), 899-908.

(191) Henkelman, G.; Arnaldsson, A.; Jónsson, H. A fast and robust algorithm for Bader decomposition of charge density. *Computational Materials Science* **2006,** *36* (3), 354-360.

(192) Bader, R. F. Atoms in Molecules. *Acounts of Chemical Research* **1985,** *18*, 9-15.

(193) Bader, R. F. W. *Atoms in Molecules: A Quantum Theory*; Oxford University Press: Oxford, 1990.

(194) Vukojevic, S.; Trapp, O.; Grunwaldt, J. D.; Kiener, C.; Schuth, F. Quasi-homogeneous methanol synthesis over highly active copper nanoparticles. *Angewandte Chemie-International Edition* **2005,** *44* (48), 7978-7981.

(195) Zhu, Y.; Kong, X.; Li, X.; Ding, G.; Zhu, Y.; Li, Y.-W. Cu Nanoparticles Inlaid Mesoporous Al2O3 As a High-Performance Bifunctional Catalyst for Ethanol Synthesis via Dimethyl Oxalate Hydrogenation. *Acs Catalysis* **2014,** *4* (10), 3612-3620.

(196) Estrella, M.; Barrio, L.; Zhou, G.; Wang, X. Q.; Wang, Q.; Wen, W.; Hanson, J. C.; Frenkel, A. I.; Rodriguez, J. A. In Situ Characterization of CuFe2O4 and Cu/Fe3O4 Water-Gas Shift Catalysts. *Journal of Physical Chemistry C* **2009,** *113* (32), 14411-14417.

(197) Sad, M. E.; Neurock, M.; Iglesia, E. Formation of C-C and C-O Bonds and Oxygen Removal in Reactions of Alkanediols, Alkanols, and Alkanals on Copper Catalysts. *Journal of the American Chemical Society* **2011,** *133* (50), 20384-20398.

(198) Bridier, B.; Hevia, M. A. G.; Lopez, N.; Perez-Ramirez, J. Permanent alkene selectivity enhancement in copper-catalyzed propyne hydrogenation by temporary CO supply. *Journal of Catalysis* **2011,** *278* (1), 167-172.

(199) Li, C. W.; Ciston, J.; Kanan, M. W. Electroreduction of carbon monoxide to liquid fuel on oxide-derived nanocrystalline copper. *Nature* **2014,** *508* (7497), 504-+.

(200) Salorinne, K.; Chen, X.; Troff, R. W.; Nissinen, M.; Häkkinen, H. One-pot synthesis and characterization of subnanometre-size benzotriazolate protected copper clusters. *Nanoscale* **2012,** *4* (14), 4095-4098.

(201) Vilar-Vidal, N.; Rivas, J.; Lopez-Quintela, M. A. Copper clusters as novel fluorescent probes for the detection and photocatalytic elimination of lead ions. *Physical Chemistry Chemical Physics* **2014,** *16* (48), 26427-26430.

(202) Baishya, K.; Idrobo, J. C.; Ogut, S.; Yang, M.; Jackson, K. A.; Jellinek, J. First-principles absorption spectra of Cu-n (n=2-20) clusters. *Physical Review B* **2011,** *83* (24).

(203) Ohshimo, K.; Akimoto, K.; Ogawa, M.; Iwasaki, W.; Yamamoto, H.; Tona, M.; Tsukamoto, K.; Nakano, M.; Misaizu, F. Correlation between Electronic Shell Structure and Inertness of Cun+ toward O2 Adsorption at n = 15, 21, 41, and 49. *The Journal of Physical Chemistry A* **2018,** *122* (11), 2927-2932.

(204) Poater, A.; Duran, M.; Jaque, P.; Toro-Labbe, A.; Sola, M. Molecular structure and bonding of copper cluster monocarbonyls CunCO (n=1-9). *Journal of Physical Chemistry B* **2006,** *110* (13), 6526-6536.

(205) Padilla-Campos, L. Theoretical study of the adsorption of carbon monoxide on small copper clusters. *Journal of Molecular Structure-Theochem* **2008,** *851* (1-3), 15-21.

(206) Florez, E.; Tiznado, W.; Mondragon, F.; Fuentealba, P. Theoretical study of the interaction of molecular oxygen with copper clusters. *Journal of Physical Chemistry A* **2005,** *109* (34), 7815-7821.

(207) Padilla-Campos, L. Theoretical investigation of the adsorption of oxygen on small copper clusters. *Journal of Molecular Structure-Theochem* **2007,** *815* (1-3), 63-69.

(208) Yuan, X.; Liu, L.; Wang, X.; Yang, M.; Jackson, K. A.; Jellinek, J. Theoretical Investigation of Adsorption of Molecular Oxygen on Small Copper Clusters. *Journal of Physical Chemistry A* **2011,** *115* (31), 8705-8712.

(209) Austin, N.; Mpourmpakis, G. Understanding the Stability and Electronic and Adsorption Properties of Subnanometer Group XI Monometallic and Bimetallic Catalysts. *Journal of Physical Chemistry C* **2014,** *118* (32), 18521-18528.

(210) Guvelioglu, G. H.; Ma, P. P.; He, X. Y.; Forrey, R. C.; Cheng, H. S. Evolution of small copper clusters and dissociative chemisorption of hydrogen. *Physical Review Letters* **2005,** *94* (2), 4.

(211) Chen, L.; Zhang, Q. F.; Zhang, Y. F.; Li, W. Z.; Han, B.; Zhou, C. G.; Wu, J. P.; Forrey, R. C.; Garg, D.; Cheng, H. S. A first principles study of water dissociation

on small copper clusters. *Physical Chemistry Chemical Physics* **2010,** *12* (33), 9845-9851.

(212) Wang, Y.; Wu, G.; Yang, M.; Wang, J. Competition between Eley-Rideal and Langmuir-Hinshelwood Pathways of CO Oxidation on Cu-n and CunO (n=6, 7) Clusters. *Journal of Physical Chemistry C* **2013,** *117* (17), 8767-8773.

(213) Takagi, N.; Nakagaki, M.; Ishimura, K.; Fukuda, R.; Ehara, M.; Sakaki, S. Electronic processes in NO dimerization on Ag and Cu clusters: DFT and MRMP2 studies. *Journal of Computational Chemistry* **2019,** *40* (1), 181-190.

(214) Gálvez-González, L. E.; Juárez-Sánchez, J. O.; Pacheco-Contreras, R.; Garzón, I. L.; Paz-Borbón, L. O.; Posada-Amarillas, A. CO2 adsorption on gas-phase Cu4−xPtx (x = 0–4) clusters: a DFT study. *Physical Chemistry Chemical Physics* **2018,** *20* (25), 17071-17080.

(215) Passalacqua, R.; Parathoner, S.; Centi, G.; Halder, A.; Tyo, E. C.; Yang, B.; Seifert, S.; Vajda, S. Electrochemical behaviour of naked sub-nanometre sized copper clusters and effect of CO2. *Catalysis Science & Technology* **2016,** *6* (18), 6977-6985.

(216) Reina, M.; Martínez, A. Cu, Ag and Au clusters as air pollutants hunters. *Computational and Theoretical Chemistry* **2018,** *1130*, 15-23.

(217) He, X. W.; Li, H.; Du, H. N.; Wang, J.; Zhang, H. X.; Xu, C. X. The stability of Cu clusters and their adsorption for CH4 and CH3 by first principle calculations. *The Journal of Chemical Physics* **2018,** *149* (20), 204310.

(218) Polynskaya, J. G.; Lebedev, A. V.; Knizhnik, A. A.; Sinitsa, A. S.; Smirnov, R. V.; Potapkin, B. V. Influence of charge state and active site structure of tetrahedral copper and silver clusters on the methane activation. *Computational and Theoretical Chemistry* **2019,** *1147*, 51-61.

(219) Zhao, B.; Zhang, R.; Huang, Z.; Wang, B. Effect of the size of Cu clusters on selectivity and activity of acetylene selective hydrogenation. *Applied Catalysis A: General* **2017,** *546*, 111-121.

(220) Zhang, X.; Liu, J.-X.; Zijlstra, B.; Filot, I. A. W.; Zhou, Z.; Sun, S.; Hensen, E. J. M. Optimum Cu nanoparticle catalysts for CO2 hydrogenation towards methanol. *Nano Energy* **2018,** *43*, 200-209.

(221) Zhang, R.; Peng, M.; Duan, T.; Wang, B. Insight into size dependence of C 2 oxygenate synthesis from syngas on Cu cluster: The effect of cluster size on the selectivity. *Applied Surface Science* **2017,** *407*, 282-296.

(222) Barabás, J.; Höltzl, T. Reaction of N2O and CO Catalyzed with Small Copper Clusters: Mechanism and Design. *The Journal of Physical Chemistry A* **2016,** *120* (44), 8862-8870.

(223) Jernigan, G. G.; Somorjai, G. A. Carbon Monoxide Oxidation over Three Different Oxidation States of Copper: Metallic, Copper (I) Oxide, and Copper (II) Oxide - A Surface Science and Kinetic Study. *J. Catal.* **1994,** *147*, 567-577.

(224) Xu, F.; Mudiyanselage, K.; Baber, A. E.; Soldemo, M.; Weissenrieder, J.; White, M. G.; Stacchiola, D. J. Redox-Mediated Reconstruction of Copper during Carbon Monoxide Oxidation. *Journal of Physical Chemistry C* **2014,** *118* (29), 15902-15909.

(225) Scuseria, G. E. Linear scaling density functional calculations with Gaussian orbitals. *Journal of Physical Chemistry A* **1999,** *103* (25), 4782-4790.

(226) Cramer, C. J.; Truhlar, D. G. Density functional theory for transition metals and transition metal chemistry. *Physical Chemistry Chemical Physics* **2009,** *11* (46), 10757-10816.

(227) Cohen, A. J.; Mori-Sanchez, P.; Yang, W. T. Challenges for Density Functional Theory. *Chemical Reviews* **2012,** *112* (1), 289-320.

(228) Corma, A.; Boronat, M.; Gonzalez, S.; Illas, F. On the activation of molecular hydrogen by gold: a theoretical approximation to the nature of potential active sites. *Chemical Communications* **2007,** *32*, 3371-3373.

(229) Jiang, T.; Mowbray, D. J.; Dobrin, S.; Falsig, H.; Hvolbæk, B.; Bligaard, T.; Nørskov, J. K. Trends in CO Oxidation Rates for Metal Nanoparticles and Close-Packed, Stepped, and Kinked Surfaces. *The Journal of Physical Chemistry C* **2009,** *113* (24), 10548-10553.

(230) Boronat, M.; Lopez-Ausens, T.; Corma, A. Making C-C Bonds with Gold Catalysts: A Theoretical Study of the Influence of Gold Particle Size on the Dissociation of the C-X Bond in Aryl Halides. *Journal of Physical Chemistry C* **2014,** *118* (17), 9018-9029.

(231) Hafner, J. Ab-initio simulations of materials using VASP: Density-functional theory and beyond. *Journal of Computational Chemistry* **2008,** *29* (13), 2044-2078.

(232) Becke, A. D. Density-Functional Exchange-Energy Approximation with Correct Asymptotic-Behavior. *Physical Review A* **1988,** *38* (6), 3098-3100.

(233) Binkley, J. S.; Pople, J. A.; Hehre, W. J. Self-Consistent Molecular-Orbital Methods. 21. Small Split-Valence Basis-Sets for First-Row Elements. *Journal of the American Chemical Society* **1980,** *102* (3), 939-947.

(234) Boys, S. F.; Bernardi, F. The calculation of small molecular interactions by the differences of separate total energies. Some procedures with reduced errors. *Molecular Physics* **1970,** *19* (4), 553-566.

(235) Boronat, M.; Corma, A. Oxygen activation on gold nanoparticles: separating the influence of particle size, particle shape and support interaction. *Dalton Transactions* **2010,** *39* (36), 8538-8546.

(236) Boronat, M.; Corma, A. Molecular approaches to catalysis: Naked gold nanoparticles as quasi-molecular catalysts for green processes. *Journal of Catalysis* **2011,** *284* (2), 138-147.

(237) Gruenert, W.; Hayes, N. W.; Joyner, R. W.; Shpiro, E. S.; Siddiqui, M. R. H.; Baeva, G. N. Structure, Chemistry, and Activity of Cu-ZSM-5 Catalysts for the Selective

Reduction of NOx in the Presence of Oxygen. *The Journal of Physical Chemistry* **1994,** *98* (42), 10832-10846.

(238) Vennestrøm, P. N. R.; Katerinopoulou, A.; Tiruvalam, R. R.; Kustov, A.; Moses, P. G.; Concepcion, P.; Corma, A. Migration of Cu Ions in SAPO-34 and Its Impact on Selective Catalytic Reduction of NOx with NH3. *ACS Catalysis* **2013,** *3* (9), 2158-2161.

(239) Briggs, D.; Seah, M. P. Practical Surface Analysis by Auger and X-ray Photoelectron Spectroscopy. *Ed. John Wiley & Sons* **1983**.

(240) Moretti, G.; Fierro, G.; Lo Jacono, M.; Porta, P. Characterization of CuO–ZnO catalysts by X-ray photoelectron spectroscopy: Precursors, calcined and reduced samples. *Surface and Interface Analysis* **1989,** *14* (6-7), 325-336.

(241) Choi, Y. M.; Abernathy, H.; Chen, H.-T.; Lin , M. C.; Liu, M. Characterization of O2–CeO2 Interactions Using In Situ Raman Spectroscopy and First-Principle Calculations. *ChemPhysChem* **2006,** *7* (9), 1957-1963.

(242) Root, D. E.; Mahroof-Tahir, M.; Karlin, K. D.; Solomon, E. I. Effect of Protonation on Peroxo−Copper Bonding: Spectroscopic and Electronic Structure Study of [Cu2((UN−O−)(OOH)]2+. *Inorganic Chemistry* **1998,** *37* (19), 4838-4848.

(243) Niaura, G. Surface-enhanced Raman spectroscopic observation of two kinds of adsorbed OH− ions at copper electrode. *Electrochimica Acta* **2000,** *45* (21), 3507-3519.

(244) Hibbitts, D.; Iglesia, E. Prevalence of Bimolecular Routes in the Activation of Diatomic Molecules with Strong Chemical Bonds (O-2, NO, CO, N-2) on Catalytic Surfaces. *Accounts of Chemical Research* **2015,** *48* (5), 1254-1262.

(245) Farrauto, R.; Hwang, S.; Shore, L.; Ruettinger, W.; Lampert, J.; Giroux, T.; Liu, Y.; Ilinich, O. New material needs for hydrocarbon fuel processing: Generating hydrogen for the PEM fuel cell. *Annual Review of Materials Research* **2003,** *33*, 1-27.

(246) Stratakis, M.; Garcia, H. Catalysis by Supported Gold Nanoparticles: Beyond Aerobic Oxidative Processes. *Chemical Reviews* **2012,** *112* (8), 4469-4506.

(247) Kummer, J. T. Catalysts for automobile emission control. *Progress in Energy and Combustion Science* **1980,** *6* (2), 177-199.

(248) Bowker, M. Automotive catalysis studied by surface science. *Chemical Society Reviews* **2008,** *37* (10), 2204-2211.

(249) Ji, J.; Lu, Z.; Lei, Y.; Turner, C. H. Theoretical Studies on the Direct Propylene Expocidation Using Gold-Based Catalysts: A Mini-Review. *Catalysts* **2018,** *8* (10), 421 (24).

(250) Lambert, R. M.; Williams, F. J.; Cropley, R. L.; Palermo, A. Heterogeneous alkene epoxidation: past, present and future. *Journal of Molecular Catalysis A: Chemical* **2005,** *228* (1), 27-33.

(251) Nijhuis, T. A.; Makkee, M.; Moulijn, J. A.; Weckhuysen, B. M. The Production of Propene Oxide: Catalytic Processes and Recent Developments. *Industrial & Engineering Chemistry Research* **2006,** *45* (10), 3447-3459.

(252) Huang, J.; Haruta, M. Gas-phase propene epoxidation over coinage metal catalysts. *Research on Chemical Intermediates* **2012,** *38* (1), 1-24.

(253) Lee, S.; Molina, L. M.; López, M. J.; Alonso, J. A.; Hammer, B.; Lee, B.; Seifert, S.; Winans, R. E.; Elam, J. W.; Pellin, M. J.et al. Selective Propene Epoxidation on Immobilized Au6–10 Clusters: The Effect of Hydrogen and Water on Activity and Selectivity. *Angewandte Chemie International Edition* **2009,** *48* (8), 1467-1471.

(254) Greiner, M. T.; Jones, T. E.; Johnson, B. E.; Rocha, T. C. R.; Wang, Z. J.; Armbrüster, M.; Willinger, M.; Knop-Gericke, A.; Schlögl, R. The oxidation of copper catalysts during ethylene epoxidation. *Physical Chemistry Chemical Physics* **2015,** *17* (38), 25073-25089.

(255) Marimuthu, A.; Zhang, J.; Linic, S. Tuning Selectivity in Propylene Epoxidation by Plasmon Mediated Photo-Switching of Cu Oxidation State. *Science* **2013,** *339* (6127), 1590-1593.

(256) Schaftenaar, G.; Noordik, J. H. Molden: a pre- and post-processing program for molecular and electronic structures*. *Journal of Computer-Aided Molecular Design* **2000,** *14* (2), 123-134.

(257) Jmol: un visor Java de código abierto para estructuras químicas en tres dimensiones. http://www.jmol.org/.

(258) Adrienko, G. A. Chemcraft. http://www.chemcraftprog.com.

(259) Gautam, S.; Dharamvir, K.; Goel, N. CO2 adsorption and activation over medium sized Cu-n (n=7, 13 and 19) clusters: A density functional study. *Computational and Theoretical Chemistry* **2013,** *1009*, 8-16.

(260) Pascucci, B.; Otero, G. S.; Belelli, P. G.; Illas, F.; Branda, M. M. Comparative density functional theory based study of the reactivity of Cu, Ag, and Au nanoparticles and of (111) surfaces toward CO oxidation and NO2 reduction. *Journal of Molecular Modeling* **2014,** *20* (9), 11.

(261) Mammen, N.; Spanu, L.; Tyo, E. C.; Yang, B.; Halder, A.; Seifert, S.; Pellin, M. J.; Vajda, S.; Narasimhan, S. Reversing Size-Dependent Trends in the Oxidation of Copper Clusters through Support Effects. *European Journal of Inorganic Chemistry* **2018,** *2018* (1), 16-22.

(262) Campbell, C. T. Electronic perturbations. *Nature Chemistry* **2012,** *4* (8), 597-598.

(263) Novoselov, K. S.; Geim, A. K.; Morozov, S. V.; Jiang, D.; Zhang, Y.; Dubonos, S. V.; Grigorieva, I. V.; Firsov, A. A. Electric Field Effect in Atomically Thin Carbon Films. *Science* **2004,** *306* (5696), 666.

(264) Castro Neto, A. H.; Guinea, F.; Peres, N. M. R.; Novoselov, K. S.; Geim, A. K. The electronic properties of graphene. *Reviews of Modern Physics* **2009,** *81* (1), 109-162.

(265) Guo, S.; Dong, S. Graphene nanosheet: synthesis, molecular engineering, thin film, hybrids, and energy and analytical applications. *Chemical Society Reviews* **2011,** *40* (5), 2644-2672.

(266) Kogan, E.; Silkin, V. M. Electronic structure of graphene: (Nearly) free electron bands versus tight-binding bands. *physica status solidi (b)* **2017,** *254* (9), 1700035.

(267) Liu, H.; Liu, Y.; Zhu, D. Chemical doping of graphene. *Journal of Materials Chemistry* **2011,** *21* (10), 3335-3345.

(268) Wang, H.; Maiyalagan, T.; Wang, X. Review on Recent Progress in Nitrogen-Doped Graphene: Synthesis, Characterization, and Its Potential Applications. *ACS Catalysis* **2012,** *2* (5), 781-794.

(269) Błoński, P.; Tuček, J.; Sofer, Z.; Mazánek, V.; Petr, M.; Pumera, M.; Otyepka, M.; Zbořil, R. Doping with Graphitic Nitrogen Triggers Ferromagnetism in Graphene. *Journal of the American Chemical Society* **2017,** *139* (8), 3171-3180.

(270) Lv, R.; Li, Q.; Botello-Méndez, A. R.; Hayashi, T.; Wang, B.; Berkdemir, A.; Hao, Q.; Elías, A. L.; Cruz-Silva, R.; Gutiérrez, H. R.et al. Nitrogen-doped graphene: beyond single substitution and enhanced molecular sensing. *Scientific Reports* **2012,** *2*, 586.

(271) Lu, X.; Wang, D.; Ge, L.; Xiao, L.; Zhang, H.; Liu, L.; Zhang, J.; An, M.; Yang, P. Enriched graphitic N in nitrogen-doped graphene as a superior metal-free electrocatalyst for the oxygen reduction reaction. *New Journal of Chemistry* **2018,** *42* (24), 19665-19670.

(272) Cao, Y.; Si, W.; Zhang, Y.; Hao, Q.; Lei, W.; Xia, X.; Li, J.; Wang, F. Nitrogen-doped graphene: Effect of graphitic-N on the electrochemical sensing properties towards acetaminophen. *FlatChem* **2018,** *9*, 1-7.

(273) Schiros, T.; Nordlund, D.; Palova, L.; Zhao, L.; Levendorf, M.; Jaye, C.; Reichman, D.; Park, J.; Hybertsen, M.; Pasupathy, A. Atomistic Interrogation of B–N Co-dopant Structures and Their Electronic Effects in Graphene. *ACS Nano* **2016,** *10* (7), 6574-6584.

(274) Shahrokhi, M.; Léonard, C. Tuning the band gap and optical spectra of silicon-doped graphene: Many-body effects and excitonic states. *Journal of Alloys and Compounds* **2016,** *693*.

(275) Choudhary, A.; Malakkal, L.; Siripurapu, R. K.; Szpunar, B.; Szpunar, J. First principles calculations of hydrogen storage on Cu and Pd-decorated graphene. *International Journal of Hydrogen Energy* **2016,** *41* (39), 17652-17656.

(276) Bulushev, D. A.; Chuvilin, A. L.; Sobolev, V. I.; Stolyarova, S. G.; Shubin, Y. V.; Asanov, I. P.; Ishchenko, A. V.; Magnani, G.; Riccò, M.; Okotrub, A. V.et al. Copper on carbon materials: stabilization by nitrogen doping. *J. Mater. Chem. A* **2017,** *5* (21), 10574-10583.

(277) Ni, S.; Li, Z.; Yang, J. Oxygen molecule dissociation on carbon nanostructures with different types of nitrogen doping. *Nanoscale* **2012,** *4* (4), 1184-1189.

(278) Faisal, S. N.; Haque, E.; Noorbehesht, N.; Zhang, W.; Harris, A. T.; Church, Tamara L.; Minett, A. I. Pyridinic and graphitic nitrogen-rich graphene for high-performance supercapacitors and metal-free bifunctional electrocatalysts for ORR and OER. *RSC Advances* **2017,** *7* (29), 17950-17958.

(279) Zhang, L.; Xia, Z. Mechanisms of Oxygen Reduction Reaction on Nitrogen-Doped Graphene for Fuel Cells. *The Journal of Physical Chemistry C* **2011,** *115* (22), 11170-11176.

(280) Farmer, J. A.; Campbell, C. T. Ceria Maintains Smaller Metal Catalyst Particles by Strong Metal-Support Bonding. *Science* **2010,** *329* (5994), 933-936.

(281) Paier, J.; Penschke, C.; Sauer, J. Oxygen Defects and Surface Chemistry of Ceria: Quantum Chemical Studies Compared to Experiment. *Chemical Reviews* **2013,** *113* (6), 3949-3985.

(282) Li, P.; Chen, X.; Li, Y.; Schwank, J. W. A review on oxygen storage capacity of CeO2-based materials: Influence factors, measurement techniques, and applications in reactions related to catalytic automotive emissions control. *Catalysis Today* **2019,** *327*, 90-115.

(283) Fu, Q.; Saltsburg, H.; Flytzani-Stephanopoulos, M. Active nonmetallic Au and Pt species on ceria-based water-gas shift catalysts. *Science* **2003,** *301* (5635), 935-938.

(284) Gorte, R. J. Ceria in catalysis: From automotive applications to the water–gas shift reaction. *AIChE Journal* **2010,** *56* (5), 1126-1135.

(285) López-Ausens, T.; Boronat, M.; Concepción, P.; Chouzier, S.; Mastroianni, S.; Corma, A. A heterogeneous mechanism for the catalytic decomposition of hydroperoxides and oxidation of alkanes over CeO2 nanoparticles: A combined theoretical and experimental study. *Journal of Catalysis* **2016,** *344*, 334-345.

(286) Laursen, S.; Combita, D.; Hungría, A. B.; Boronat, M.; Corma, A. First-Principles Design of Highly Active and Selective Catalysts for Phosgene-Free Synthesis of Aromatic Polyurethanes. *Angewandte Chemie International Edition* **2012,** *51* (17), 4190-4193.

(287) Sharma, S.; Hu, Z.; Zhang, P.; McFarland, E. W.; Metiu, H. CO2 methanation on Ru-doped ceria. *Journal of Catalysis* **2011,** *278* (2), 297-309.

(288) Rodriguez, J. A.; Liu, P.; Hrbek, J.; Evans, J.; Perez, M. Water gas shift reaction on Cu and Au nanoparticles supported on CeO2(111) and ZnO(000(1)over-bar): Intrinsic activity and importance of support interactions. *Angewandte Chemie-International Edition* **2007,** *46* (8), 1329-1332.

(289) Wang, S.; Zheng, M.; Li, M.; Wu, X.; Xia, C. Synergistic effects towards H2 oxidation on the Cu-CeO2 electrode: a combination study with DFT calculations and experiments. *J. Mater. Chem. A* **2016,** *4* (15), 5745-5754.

(290) Yang, Z.; Xie, L.; Ma, D.; Wang, G. Origin of the High Activity of the Ceria-Supported Copper Catalyst for H2O Dissociation. *The Journal of Physical Chemistry C* **2011,** *115* (14), 6730-6740.

(291) Wang, W.-W.; Yu, W.-Z.; Du, P.-P.; Xu, H.; Jin, Z.; Si, R.; Ma, C.; Shi, S.; Jia, C.-J.; Yan, C.-H. Crystal Plane Effect of Ceria on Supported Copper Oxide Cluster Catalyst for CO Oxidation: Importance of Metal–Support Interaction. *ACS Catalysis* **2017,** *7* (2), 1313-1329.

(292) Du, L.; Wang, W.; Yan, H.; Wang, X.; Jin, Z.; Song, Q.; Si, R.; Jia, C. Copper-ceria sheets catalysts: Effect of copper species on catalytic activity in CO oxidation reaction. *Journal of Rare Earths* **2017,** *35* (12), 1186-1196.

(293) An, J.; Wang, Y.; Lu, J.; Zhang, J.; Zhang, Z.; Xu, S.; Liu, X.; Zhang, T.; Gocyla, M.; Heggen, M.et al. Acid-Promoter-Free Ethylene Methoxycarbonylation over Ru-Clusters/Ceria: The Catalysis of Interfacial Lewis Acid–Base Pair. *Journal of the American Chemical Society* **2018,** *140* (11), 4172-4181.

(294) Ren, Z.; Peng, F.; Chen, B.; Mei, D.; Li, J. A combined experimental and computational study of water-gas shift reaction over rod-shaped Ce0.75M0.25O2 (M = Ti, Zr, and Mn) supported Cu catalysts. *International Journal of Hydrogen Energy* **2017,** *42* (51), 30086-30097.

(295) Branda, M. M.; Hernández, N. C.; Sanz, J. F.; Illas, F. Density Functional Theory Study of the Interaction of Cu, Ag, and Au Atoms with the Regular CeO2 (111) Surface. *The Journal of Physical Chemistry C* **2010,** *114* (4), 1934-1941.

(296) Ren, Z.; Liu, N.; Chen, B.; Li, J.; Mei, D. Nucleation of Cun (n = 1–5) Clusters and Equilibrium Morphology of Cu Particles Supported on CeO2 Surface: A Density Functional Theory Study. *The Journal of Physical Chemistry C* **2018,** *122* (48), 27402-27411.

(297) Song, E. H.; Wen, Z.; Jiang, Q. CO Catalytic Oxidation on Copper-Embedded Graphene. *Journal of Physical Chemistry C* **2011,** *115* (9), 3678-3683.

(298) Esrafili, M. D.; Mousavian, P. A DFT study on the possibility of using a single Cu atom incorporated nitrogen-doped graphene as a promising and highly active catalyst for oxidation of CO. *International Journal of Quantum Chemistry* **2019,** *119* (7).

(299) Sun, W.; Shi, R.; Wang, X.; Liu, S.; Han, X.; Zhao, C.; Li, Z.; Ren, J. Density-functional theory study of dimethyl carbonate synthesis by methanol oxidative carbonylation on single-atom Cu1/graphene catalyst. *Applied Surface Science* **2017,** *425*, 291-300.

(300) Nakada, K.; Ishii, A. DFT Calculation for Adatom Adsorption on Graphene. *Graphene Simulation* **2011,** *IntechOpen Ed.*

(301) Valencia, H.; Gil, A.; Frapper, G. Trends in the Adsorption of 3d Transition Metal Atoms onto Graphene and Nanotube Surfaces: A DFT Study and Molecular Orbital Analysis. *The Journal of Physical Chemistry C* **2010,** *114* (33), 14141-14153.

(302) García-Rodríguez, D. E.; Mendoza-Huizar, L. H.; Díaz, C. A DFT study of Cu nanoparticles adsorbed on defective graphene. *Applied Surface Science* **2017,** *412*, 146-151.

(303) Zhang, P.; Wang, Q.-N.; Yang, X.; Wang, D.; Li, W.-C.; Zheng, Y.; Chen, M.; Lu, A.-H. A Highly Porous Carbon Support Rich in Graphitic-N Stabilizes Copper Nanocatalysts for Efficient Ethanol Dehydrogenation. *ChemCatChem* **2017,** *9* (3), 505-510.

(304) Yang, Y.; Reber, A. C.; Gilliland, S. E.; Castano, C. E.; Gupton, B. F.; Khanna, S. N. Donor/Acceptor Concepts for Developing Efficient Suzuki Cross-Coupling Catalysts Using Graphene-Supported Ni, Cu, Fe, Pd, and Bimetallic Pd/Ni Clusters. *The Journal of Physical Chemistry C* **2018,** *122* (44), 25396-25403.

(305) He, H.; Morrissey, C.; Curtiss, L. A.; Zapol, P. Graphene-Supported Monometallic and Bimetallic Dimers for Electrochemical CO2 Reduction. *The Journal of Physical Chemistry C* **2018,** *122* (50), 28629-28636.

(306) Kaur, G.; Gupta, S.; Dharamvir, K. Energetics of Small Clusters of Group IB Metals (Cu, Ag, and Au) Adsorbed on Graphene. *AIP Conference Proceedings* **2013,** *1536*, 331-332.

(307) Agarwal, S.; Lefferts, L.; Mojet, B. L.; Ligthart, D. A. J. M.; Hensen, E. J. M.; Mitchell, D. R. G.; Erasmus, W. J.; Anderson, B. G.; Olivier, E. J.; Neethling, J. H.et al. Exposed Surfaces on Shape-Controlled Ceria Nanoparticles Revealed through AC-TEM and Water–Gas Shift Reactivity. *ChemSusChem* **2013,** *6* (10), 1898-1906.

(308) Pulido, A.; Boronat, M.; Corma, A. Theoretical investigation of gold clusters supported on graphene sheets. *New Journal of Chemistry* **2011,** *35* (10), 2153-2161.

(309) http://www.p4vasp.at.

(310) Momma, K.; Izumi, F. VESTA 3 for three-dimensional visualization of crystal, volumetric and morphology data. *J. Appl. Crystallogr.* **2011,** *44*, 1272-1276.

(311) Rêgo, C. R. C.; Tereshchuk, P.; Oliveira, L. N.; Da Silva, J. L. F. Graphene-supported small transition-metal clusters: A density functional theory investigation within van der Waals corrections. *Physical Review B* **2017,** *95* (23), 235422.

(312) Jia, T.-T.; Lu, C.-H.; Ding, K.-N.; Zhang, Y.-F.; Chen, W.-K. Oxidation of Pdn (n=1–5) clusters on single vacancy graphene: A first-principles study. *Computational and Theoretical Chemistry* **2013,** *1020*, 91-99.

(313) Zhao, C.; Wu, H. Density functional investigation of mercury and arsenic adsorption on nitrogen doped graphene decorated with palladium clusters: A promising heavy metal sensing material in farmland. *Applied Surface Science* **2017,** *399*, 55-66.

(314) Jalili, S.; Goliaei, E. M.; Schofield, J. Silver cluster supported on nitrogen-doped graphene as an electrocatalyst with high activity and stability for oxygen reduction reaction. *International Journal of Hydrogen Energy* **2017,** *42* (21), 14522-14533.

(315) Meeprasert, J.; Junkaew, A.; Rungnim, C.; Kunaseth, M.; Kungwan, N.; Promarak, V.; Namuangruk, S. Capability of defective graphene-supported Pd13 and Ag13 particles for mercury adsorption. *Applied Surface Science* **2016,** *364*, 166-175.

(316) Lim, D.-H.; Wilcox, J. DFT-Based Study on Oxygen Adsorption on Defective Graphene-Supported Pt Nanoparticles. *The Journal of Physical Chemistry C* **2011,** *115* (46), 22742-22747.

(317) Fadlallah, M. M.; Abdelrahman, A. G.; Schwingenschlögl, U.; Maarouf, A. A. Graphene and graphene nanomesh supported nickel clusters: electronic, magnetic, and hydrogen storage properties. *Nanotechnology* **2019,** *30* (8), 085709.

(318) Corbet, J.-P.; Mignani, G. Selected Patented Cross-Coupling Reaction Technologies. *Chemical Reviews* **2006,** *106* (7), 2651-2710.

(319) Magano, J.; Dunetz, J. R. Large-Scale Applications of Transition Metal-Catalyzed Couplings for the Synthesis of Pharmaceuticals. *Chemical Reviews* **2011,** *111* (3), 2177-2250.

(320) José Climent, M.; Corma, A.; Iborra, S. Homogeneous and heterogeneous catalysts for multicomponent reactions. *RSC Advances* **2012,** *2* (1), 16-58.

(321) Wu, X.-F.; Anbarasan, P.; Neumann, H.; Beller, M. From Noble Metal to Nobel Prize: Palladium-Catalyzed Coupling Reactions as Key Methods in Organic Synthesis. *Angewandte Chemie International Edition* **2010,** *49* (48), 9047-9050.

(322) Miyaura, N. Cross-coupling reaction of organoboron compounds via base-assisted transmetalation to palladium(II) complexes. *Journal of Organometallic Chemistry* **2002,** *653* (1), 54-57.

(323) Chinchilla, R.; Nájera, C. The Sonogashira Reaction: A Booming Methodology in Synthetic Organic Chemistry. *Chemical Reviews* **2007,** *107* (3), 874-922.

(324) Balanta, A.; Godard, C.; Claver, C. Pd nanoparticles for C–C coupling reactions. *Chemical Society Reviews* **2011,** *40* (10), 4973-4985.

(325) Reetz, M. T.; de Vries, J. G. Ligand-free Heck reactions using low Pd-loading. *Chemical Communications* **2004,** *14*, 1559-1563.

(326) Kelkar, A. A. The vinylation of aryl iodides using homogeneous platinum complex catalyst. *Tetrahedron Letters* **1996,** *37* (49), 8917-8920.

(327) Bhanage, B. M.; Zhao, F. G.; Shirai, M.; Arai, M. Comparison of activity and selectivity of various metal-TPPTS complex catalysts in ethylene glycol · toluene biphasic Heck vinylation reactions of iodobenzene. *Tetrahedron Letters* **1998,** *39* (51), 9509-9512.

(328) Kantam, M. L.; Roy, M.; Roy, S.; Subhas, M. S.; Sreedhar, B.; Choudary, B. M. Layered Double Hydroxide-Supported Nanoplatinum: An Efficient and Reusable Ligand-Free Catalyst for Heck and Stille Coupling of Iodoarenes. *Synlett* **2006,** *14*, 2266-2268.

(329) Lee, C. T.; Yang, W. T.; Parr, R. G. Development of the Colle-Salvetti Correlation-Energy Formula into a Functional of the Electron-Density. *Physical Review B* **1988,** *37* (2), 785-789.

(330) Wu, Y.; Cai, S.; Wang, D.; He, W.; Li, Y. Syntheses of Water-Soluble Octahedral, Truncated Octahedral, and Cubic Pt–Ni Nanocrystals and Their Structure–Activity Study in Model Hydrogenation Reactions. *Journal of the American Chemical Society* **2012,** *134* (21), 8975-8981.

(331) Shen, Z.; Matsuki, Y.; Shimoda, T. Preparation of large thermally stable platinum nanocubes by using solvent-thermal reaction. *Chemical Communications* **2010,** *46* (45), 8606-8608.

(332) Beletskaya, I. P.; Cheprakov, A. V. The Heck Reaction as a Sharpening Stone of Palladium Catalysis. *Chemical Reviews* **2000,** *100* (8), 3009-3066.

(333) Oliver-Meseguer, J.; Dominguez, I.; Gavara, R.; Leyva-Pérez, A.; Corma, A. Disassembling Metal Nanocrystallites into Sub-nanometric Clusters and Low-faceted Nanoparticles for Multisite Catalytic Reactions. *ChemCatChem* **2017,** *9* (8), 1429-1435.

(334) Campos, J.; Ortega-Moreno, L.; Conejero, S.; Peloso, R.; López-Serrano, J.; Maya, C.; Carmona, E. Reactivity of Cationic Agostic and Carbene Structures Derived from Platinum(II) Metallacycles. *Chemistry – A European Journal* **2015,** *21* (24), 8883-8896.

(335) Tagge, C. D.; Simpson, R. D.; Bergman, R. G.; Hostetler, M. J.; Girolami, G. S.; Nuzzo, R. G. Synthesis of a Novel Volatile Platinum Complex for Use in CVD and a Study of the Mechanism of Its Thermal Decomposition in Solution. *Journal of the American Chemical Society* **1996,** *118* (11), 2634-2643.

(336) Kayahara, E.; Iwamoto, T.; Takaya, H.; Suzuki, T.; Fujitsuka, M.; Majima, T.; Yasuda, N.; Matsuyama, N.; Seki, S.; Yamago, S. Synthesis and physical properties of a ball-like three-dimensional π-conjugated molecule. *Nat. Commun.* **2013,** *4*, 2694.

(337) Liberman-Martin, A. L.; Bergman, R. G.; Tilley, T. D. A Remote Lewis Acid Trigger Dramatically Accelerates Biaryl Reductive Elimination from a Platinum Complex. *Journal of the American Chemical Society* **2013,** *135* (26), 9612-9615.

(338) Joost, M.; Zeineddine, A.; Estévez, L.; Mallet−Ladeira, S.; Miqueu, K.; Amgoune, A.; Bourissou, D. Facile Oxidative Addition of Aryl Iodides to Gold(I) by Ligand Design: Bending Turns on Reactivity. *Journal of the American Chemical Society* **2014,** *136* (42), 14654-14657.

(339) González-Arellano, C.; Abad, A.; Corma, A.; García, H.; Iglesias, M.; Sánchez, F. Catalysis by Gold(I) and Gold(III): A Parallelism between Homo- and Heterogeneous Catalysts for Copper-Free Sonogashira Cross-Coupling Reactions. *Angewandte Chemie International Edition* **2007,** *46* (9), 1536-1538.

(340) Boronat, M.; Combita, D.; Concepción, P.; Corma, A.; García, H.; Juárez, R.; Laursen, S.; de Dios López-Castro, J. Making C–C Bonds with Gold: Identification of Selective Gold Sites for Homo- and Cross-Coupling Reactions between Iodobenzene and Alkynes. *The Journal of Physical Chemistry C* **2012,** *116* (47), 24855-24867.

(341) Young, G. B.; Whitesides, G. M. Oxidative addition and reductive elimination reactions involving platinum metallacycles. *Journal of the American Chemical Society* **1978,** *100* (18), 5808-5815.

(342) Low, J. J.; Goddard, W. A. Theoretical studies of oxidative addition and reductive elimination. 3. Carbon-hydrogen and carbon-carbon reductive coupling from palladium and platinum bis(phosphine) complexes. *Journal of the American Chemical Society* **1986,** *108* (20), 6115-6128.

(343) Müller, C.; Iverson, C. N.; Lachicotte, R. J.; Jones, W. D. Carbon−Carbon Bond Activation in Pt(0)−Diphenylacetylene Complexes Bearing Chelating P,N- and P,P-Ligands. *Journal of the American Chemical Society* **2001,** *123* (39), 9718-9719.

(344) Braunstein, P.; Knorr, M.; Stährfeldt, T. Heterobimetallic templates for Carbon–Carbon bond formation by migratory insertion reactions involving CO, isonitriles or olefins. *Journal of the Chemical Society, Chemical Communications* **1994,** *17*, 1913-1914.

(345) Hill, R. H.; Puddephatt, R. J. Mechanism and energetics of the ligand-induced reductive elimination of hydrogen from a binuclear platinum hydride. *Journal of the American Chemical Society* **1983,** *105* (18), 5797-5804.

(346) Morris, R. H. Brønsted–Lowry Acid Strength of Metal Hydride and Dihydrogen Complexes. *Chemical Reviews* **2016,** *116* (15), 8588-8654.

(347) Frasco, D. A.; Mukherjee, S.; Sommer, R. D.; Perry, C. M.; Lambic, N. S.; Abboud, K. A.; Jakubikova, E.; Ison, E. A. Nondirected C–H Activation of Arenes with Cp*Ir(III) Acetate Complexes: An Experimental and Computational Study. *Organometallics* **2016,** *35* (15), 2435-2445.

(348) Granger, P.; Parvulescu, V. I. Catalytic NOx Abatement Systems for Mobile Sources: From Three-Way to Lean Burn after-Treatment Technologies. *Chemical Reviews* **2011,** *111* (5), 3155-3207.

(349) Liu, L.; Arenal, R.; Meira, D. M.; Corma, A. Generation of gold nanoclusters encapsulated in an MCM-22 zeolite for the aerobic oxidation of cyclohexane. *Chemical Communications* **2019,** *55* (11), 1607-1610.

(350) Liu, L.; Díaz, U.; Arenal, R.; Agostini, G.; Concepción, P.; Corma, A. Generation of subnanometric platinum with high stability during transformation of a 2D zeolite into 3D. *Nature Materials* **2016,** *16*, 132.

(351) Chen, H.; Wang, X.; Pan, Z.; Xu, H. Numerical Simulation and Experimental Study on Commercial Diesel Reforming Over and Advanced Pt/Rj Three-Way Catalyst. *Catalysts* **2019,** *9*, 590-607.

(352) Yoshida, H.; Kakei, R.; Kuzuhara, Y.; Misumi, S.; Machida, M. A comparative study on TWC reactions over Rh thin films and supported Rh nanoparticles under lean conditions. *Catalysis Today* **2019,** *332*, 245-250.

(353) Yentekakis, I. V.; Vernoux, P.; Goula, G.; Caravaca, A. Electropositive Promotion by Alkalis or Alkaline Earths of Pt-Group Metals in Emissions control Catalysis: A Status Report. *Catalysts* **2019,** *9* (157-231).

(354) Holles, J. H.; Switzer, M. A.; Davis, R. J. Influence of Ceria and Lanthana Promoters on the Kinetics of NO and N2O Reduction by CO over Alumina-Supported Palladium and Rhodium. *Journal of Catalysis* **2000,** *190* (2), 247-260.

(355) Ozawa, M.; Okouchi, T.; Haneda, M. Three way catalytic activity of thermally degenerated Pt/Al2O3 and Pt/CeO2–ZrO2 modified Al2O3 model catalysts. *Catalysis Today* **2015,** *242*, 329-337.

(356) Koga, H.; Hayashi, A.; Ato, Y.; Tada, K.; Hosokawa, S.; Tanaka, T.; Okumura, M. Effect of ceria and zirconia supports on NO reduction over platinum-group metal catalysts: A DFT study with comparative experiments. *Catalysis Today* **2019,** *332*, 236-244.

(357) Wörz, A. S.; Judai, K.; Abbet, S.; Heiz, U. Cluster Size-Dependent Mechanisms of the CO + NO Reaction on Small Pdn (n ≤ 30) Clusters on Oxide Surfaces. *Journal of the American Chemical Society* **2003,** *125* (26), 7964-7970.

(358) Judai, K.; Abbet, S.; Wörz, A. S.; Heiz, U.; Henry, C. R. Low-Temperature Cluster Catalysis. *Journal of the American Chemical Society* **2004,** *126* (9), 2732-2737.

(359) Fukuda, R. Electronic Origin of Catalytic Nitric Oxide Reduction upon Small Rhodium and Copper Clusters. *Journal of Computer Chemistry, Japan* **2018,** *advpub*.

(360) Gao, H. Theoretical analysis of CO+NO reaction mechanism on the single Pd atom embedded in γ-Al2O3 (110) surface. *Applied Catalysis A: General* **2017,** *529*, 156-166.

(361) Tang, Y. A.; Chen, W. G.; Zhou, J. C.; Chai, H. D.; Li, Y.; Cui, Y. Q.; Feng, Z.; Dai, X. Q. Mechanistic insight into the selective catalytic oxidation for NO and CO on co-doping graphene sheet: A theoretical study. *Fuel* **2019,** *253*, 1531-1544.

(362) Liu, C.-G.; Sun, C.; Jiang, M.-X.; Zhang, L.-L.; Sun, M.-J. Calculations of NO reduction with CO over a Cu1/PMA single-atom catalyst: a study of surface oxygen species, active sites, and the reaction mechanism. *Physical Chemistry Chemical Physics* **2019,** *21* (19), 9975-9986.

(363) Avogadro: an open-source molecular builder and visualization tool. Version 1.2.0. http://avogadro.cc/.

(364) Hanwell, M. D.; Curtis, D. E.; Lonie, D. C.; Vandermeersch, T.; Zurek, E.; Hutchison, G. R. Avogadro: an advanced semantic chemical editor, visualization, and analysis platform. *Journal of Cheminformatics* **2012,** *4* (1), 17.

(365) Leonowicz, M. E.; Lawton, J. A.; Lawton, S. L.; Rubin, M. K. MCM-22: A Molecular Sieve with Two Independent Multidimensional Channel Systems. *Science* **1994,** *264* (5167), 1910.

(366) Backus, E. H. G.; Forsblom, M.; Persson, M.; Bonn, M. Highly Efficient Ultrafast Energy Transfer into Molecules at Surface Step Sites. *The Journal of Physical Chemistry C* **2007,** *111* (17), 6149-6153.

(367) Gonzalez, J. D.; Shojaee, K.; Haynes, B. S.; Montoya, A. The effect of surface coverage on N2, NO and N2O formation over Pt(111). *Physical Chemistry Chemical Physics* **2018,** *20* (39), 25314-25323.

(368) Ma, H.; Schneider, W. F. Structure- and Temperature-Dependence of Pt-Catalyzed Ammonia Oxidation Rates and Selectivities. *ACS Catalysis* **2019,** *9* (3), 2407-2414.

Si tanque els ulls recorde tot el que he estimat
i escolte com el cor em torna a bategar.
L'alegria senzilla, l'emoció compartida
pel demà que encara hem de guanyar.

Obrint Pas, "Si tanque els ulls" *Coratge*.